Surface Chemical Composition, Atomic Structure and Oxidation of the Ga_3Ni_2 Intermetallic Catalyst

Thesis submitted in accordance with the requirements of the University of Liverpool for the degree of Doctor in Philosophy by

Oscar Shedwick

May, 2025

Abstract

This thesis presents an investigation into the surface properties of three Ga_3Ni_2 intermetallic samples, each cut along the (001), (100), and $(2\bar{1}0)$ crystallographic planes. Surface characterisation was performed using X-ray photoelectron spectroscopy (XPS), low-energy electron diffraction (LEED), scanning tunnelling microscopy (STM), and ultraviolet photoelectron spectroscopy (UPS).

All three of the surfaces exhibited preferential sputtering of Ga from the surface caused by Ga having a lower surface free energy compared to Ni. After annealing, the Ga concentration recovered and then exceeded the amount expected from the bulk composition in all three surfaces, showing that Ga is segregating from the bulk to the surface. This is also attributed to Ga having a lower surface free energy. The (001) and (100) surfaces after annealing showed the (1×1) surface unit cell with no surface reconstruction observed. The $(2\bar{1}0)$ surface, however, at temperatures exceeding 500°C undergoes c(2×2) reconstruction below this temperature, a (1×1) surface unit cell is observed instead.

The (001) surface contained both Ga and Ni bonded together, confirmed by STM images and low energy ion scattering (LEIS), specific step heights were observed which apply to the distance between Ga - Ga planes or the Ni - Ni planes from the Ga_3Ni_2. The $(2\bar{1}0)$ wide scan showed the expected step heights from the model with only one possible termination plane, and the c(2×2) reconstruction was resolved from the surface at higher annealing temperatures. No bias dependency recorded for all surfaces.

After exposing the (001) surface to pure O_2, the effects it had on the surface were studied via XPS. Ga oxidises as O_2 increases, with the formation of multiple Ga oxides. The Ni did not react with the oxygen, as no change in peak shape or position was seen, with the only change being a decrease in the amount of Ni recorded, shown by a decrease in the atomic composition.

The (001) surface underwent ultraviolet photoelectron spectroscopy scans to record the valence band region to confirm the density of state calculations performed by collaborators at Tribhuvan University. Results showed that the largest orbital contributions came from Ni, as expected from the surface, as Ni is the catalytically active element of the intermetallic compound. Each of the peaks from the density of state results was mapped onto the UPS results, demonstrating that these density of state calculations are accurate representations of experimental results.

In Memoriam

This thesis is dedicated to the memory of my dad, Alan Shedwick, who sadly passed away during the final months of this thesis.

You kept me going when times were tough and were always a constant font of love, warmth and humour. Rest in peace Dad you will always be missed and never forgotten.

"To say that it was wondrous would be to say that the universe is quite a big place." —Robert Rankin.

Acknowledgments

Compiling the past four years of work into a single thesis caused me to reflect on my time at the University of Liverpool. Initially, I arrived to complete my Bachelor's degree in physics and am leaving after completing my PhD, a feat I never thought I would be able to do. During my time here, there have been challenges and tasks which never seemed to have an end, but I am happy to say that it has been a rewarding four years. I wish to thank Dr Hem Raj Sharma and Prof. Ronan McGrath for inviting me into their group. Your expertise and support have been invaluable over this PhD, and the welcoming atmosphere you fostered both in the office and outside with group lunches and dinners made everyone in the group relax and open up.

A monumental thank you must go to Dr Sam Haq for his help and support with the experimental side of this work. His expertise in surface science and experimental equipment was vital to many of the results obtained over this PhD, and learning how to look after the equipment is a skill I will never forget. Special thank you to Dr Julian Ledieu and Dr Vincent Fournée for your time and expertise while I was visiting the Institut Jean Lamour, and the data we obtained during that visit has been invaluable to this thesis. Also, a big thank you to ECMetAC, who funded the trip to the Institut Jean Lamour and for hosting the ECMetAC Days, where I was able to share my work through both poster and oral presentation. Finally, a big thank you to the EPSRC and the University of Liverpool for funding this thesis.

Finally, a thank you to the people in my life who have kept me going over this PhD, kept me motivated to push onwards, asked questions and listened to my many hour-long talks about surface physics. To my friends, you have been a rock and a lifeline. You did so much that words can not describe. Ryan and Emma, thank you for both being there and having to deal with my monologues about my research. To Anthony and Lucas, you made the many long nights easier by being there to talk to and keeping me company, sane and laughing. To my Mum and Dad, I do not think any of us saw this coming when I left for university all those years ago, but I could not have done this without you and the love and support you have always given. Thank you.

Contents

List of Terms and Abbreviations **1**

1 Introduction **2**

2 Background **5**

2.1 Introduction 5

2.2 Crystals and Crystallography 5

2.2.1 Crystals 5

2.2.2 Crystallography 6

2.2.3 Complex Metallic Alloys 7

2.3 Intermetallics 8

2.4 Quasicrystals 9

2.5 Catalysis 10

2.5.1 Heterogeneous Catalysts 12

2.5.2 Intermetallic Compounds as Catalysts 12

2.5.3 Examples of Compound Catalysts 14

2.5.4 Summary of Prior GaNi Research 23

3 Experimental Methods **29**

3.1 Introduction 29

3.2 Ultra High Vacuum 29

3.2.1 Vacuum Pumps 31

3.2.2 Bakeout Procedure 34

3.2.3 Pressure Measurement 35
3.2.4 Surface Preparation 36
3.3 Surface Analysis Techniques 39
3.3.1 Low Energy Electron Diffraction (LEED) 39
3.3.2 Scanning Tunnelling Microscopy (STM) 44
3.3.3 X-ray Photoelectron Spectroscopy (XPS) 53
3.3.4 Ultraviolet Photoelectron Spectroscopy (UPS) 56
3.4 Growth, Phase Diagram and Structure of Ga_3Ni_2 58

4 Surface Chemical Composition of Ga_3Ni_2 62

4.1 Introduction 62
4.2 Experimental Details 62
4.3 Results and Discussion 63
4.3.1 Influence of Air Exposure, Sputtering and Annealing 63
4.3.2 Atomic Composition 68
4.3.3 Depth Profile 69
4.3.4 Comparison of the (001) surfaces for Ga_3Ni_2 and In_3Ni_2 78
4.4 Summary 80

5 Surface Atomic Structure of Ga_3Ni_2 81

5.1 Introduction 81
5.2 Experimental Details 81
5.3 Results and Discussion 83
5.3.1 Surface Model Structure 83
5.3.2 Ga_3Ni_2 (001) Surface 85

5.3.3 Ga_3Ni_2 $(2\bar{1}0)$ surface 96
5.3.4 Ga_3Ni_2 (100) surface 100
5.3.5 A Comparison of all Three Ga_3Ni_2 Surfaces 101
5.4 Summary 113

6 Surface Oxidation Studied by XPS **115**
6.1 Introduction 115
6.2 Experimental Details 115
6.3 Results and Discussion 116
6.3.1 The Clean Surface 116
6.3.2 Effects on the Gallium Peaks 118
6.3.3 Effects on the Nickel Peaks 122
6.3.4 Effects on the Total Atomic Composition 123
6.3.5 Comparison of Oxidation on Ga_3Ni_2 and In_3Ni_2. 124
6.4 Summary 126

7 Valence Band Structure **128**
7.1 Introduction 128
7.2 Experimental Details 129
7.3 Results and Discussion 130
7.3.1 UPS Results 130
7.3.2 Comparison of UPS with the DoS Calculations 131
7.4 Summary 134

8 Summary and Outlook **135**
8.1 Conclusions and Further Studies 135

Bibliography **138**

Conferences and Publications **151**

List of Figures

2.1 A model of X-ray diffraction using the Laue method, in which an X-ray is fired at a crystal and the scattered X-rays are recorded on a photographic plate or phosphorescent screen [13]. 6

2.2 A model showing possible ways for two metals to alloy together [16]. . . . 7

2.3 A large single crystal of the icosahedral quasicrystal Ho-Mg-Zn [32]. . . . 9

2.4 A diagram showing the effects of catalysis on a reaction. The catalysed reaction in red has a much lower change in energy (ΔG) compared to the uncatalysed reaction in black [39]. 11

2.5 A model of a chemical reaction using a heterogeneous catalyst. (1 and 2) The two reactants, green and yellow, adsorb to the surface. (3) The reaction undergoes a chemical transformation facilitated by the surface, forming the product. (4) The product desorbs from the surface [42]. . . . 12

2.6 A periodic table with the catalytically active transition elements highlighted in red, and the secondary metals typically used in IMCs highlighted in teal [47]. 13

2.7 (A) An STM image of the ZnPd alloy formed after depositing Zn onto Pd(111), adopted from [2]. (B) The model of ZnPd with Zn atoms in silver and Pd in purple. 16

2.8 (A) The model structure of Ga_7Pd3, where the Pd atoms are in silver and Ga atoms are in green. Adopted and edited from [57]. (B) The XPS data of the Ga $2p3/2$ peak from GaPd after being air milled: (a) untreated, (b) after H_2 treatment at 573 K, (c) after H_2 treatment at 673 K, (d) after ion scattering spectroscopy (ISS) [57]. 17

2.9 (A) A LEED image of the (010) Al13Fe4 surface with a beam energy of 50 eV. (B) STM image (30×30 nm^2) showing step terraces formed after annealing at 600°C. (A) and (B) adopted from [64], (C) from [65], and (D) from [66]. 19

2.10 (A) The unit cell of In_3Ni_2. (B) Side view of In_3Ni_2 (001), showing the stacking of five atomic layers labelled 0 to 4, with each plane separation shown [72]. 20

2.11 (A) Surface chemical composition of the In_3Ni_2 (001) surface after sputtering and annealing, recorded via XPS. (B) LEIS spectra recorded from the In_3Ni_2 (001) surface after sputtering and annealing at 400°C for two hours using a 3 keV He^+ beam. Both images adopted from [72]. 21

2.12 STM image of the clean In_3Ni_2 (001) surface after annealing at 550°C (400 Å × 400 Å, +0.866 V, 0.645 nA), showing step heights and a line scan along the blue line [72]. 22

2.13 Surface chemical composition of the In_3Ni_2 (001) surface upon increasing exposure to O_2, measured via XPS. Adopted from [72]. 23

2.14 (A) Two unit cells of Ga_3Ni_2 showing the structural isolation of the Ni atoms (in silver) by a shell of Ga atoms (in green). (B) The phase diagram shows all of the possible GaNi phases [83]. 26

2.15 High-resolution XPS spectra showing several depths of the Ga $2p3/2$ peak after oxidation (A) and after annealing at 600°C (B). The corresponding Ni $2p3/2$ peaks after oxidation and annealing are shown in (C) and (D). Adopted from [10]. 27

3.1 How altering the pressure affects the time to form one monolayer in Equation 3.1, where the sticking coefficient (S) is treated as 1. 30

3.2 The UHV chamber used for all of the experiments at the University of Liverpool. Each key part is labelled with (A) being the front side of the detector and (B) being the rear side. 32

3.3 A diagram of (A) a rotary vane pump, (B) a turbo molecular pump and (C) an ion pump. Reproduced from [90]. 33

3.4 A graph showing the effect a bakeout has on the pressure in a chamber over time [91]. 34

3.5 A diagram of (A) Pirani gauge and (B) an ionisation gauge. Reproduced from [90]. 36

3.6 (A) The effects of Ar^+ sputtering, the green atoms are the bulk materials with orange circles to represent contamination on the surface. Black Ar^+ atoms are fired at the surface to remove the contamination. (B) The effects of annealing the sputtered surface. By heating the sputtered surface, the roughness caused by the Ar^+ sputtering is corrected back to an atomically flat surface with any Ar atoms embedded into the surface desorbed. 38

3.7 A model of the Davisson-Germer Experiment. The entire experiment is housed in a vacuum chamber to ensure that the emitted electrons could diffract from the Ni target [96]. 39

3.8 A model of a 2D Ewald sphere showing for an incident vector K_0 how a reciprocal lattice is constructed with the diffracted waves K_i and K_d with the red points that intersect the circle, O and P. 41

3.9 A Universal Curve showing how the electron energy affects the Inelastic Mean free path. The equation used is modified from [98] equation [5]. . . 42

3.10 A schematic of a LEED set-up (A) and a (1×1) LEED image from Al(111) (B). (A) is from [90]. 43

3.11 (A) a schematic model of an STM set-up and (B) an energy diagram showing the quantum mechanical tunnelling of the STM tip to the surface. E_{F_1} and E_{F_2} are the Fermi energies of the surface and tip, respectively. ϕ_1 and ϕ_2 are the work functions of both the sample and tip, V is the bias voltage, d is the tunnelling gap and ϕ_b is the effective barrier height. Taken from [90]. 44

3.12 A model showing quantum mechanical tunnelling where a particle can transfer through a potential barrier from the sample to an STM tip. Image was adapted from [101]. 45

3.13 A model of the two modes of scanning with STM. (A) shows a constant current mode where the Z-axis height is altered to maintain a constant tunnelling current, while (B) shows a constant height mode where the change in tunnelling current is recorded. From [90]. 46

3.14 (A) A model of a raster scan showing the movement of an STM tip from left to right before moving onto the next layer below and starting again. (B) FFT of an STM image from the Ga_3Ni_2 (001) surface showing the skewed hexagon caused by drift. 48

3.15 (A) A model showing the effect of creep for a piezoelectric actuator. As the voltage is applied, the displacement X occurs within less than a millisecond, after which the secondary displacement in red, ΔX_{cr}, occurs over a longer period, causing creep to distort the frame being recorded [110]. (B) A diagram showing the effect of hysteresis, with the black dashed line showing the ideal linear relationship between the applied voltage and the piezoelectric movement and the red lines representing the non-linear relationship which occurs [111]. 49

3.16 (A) A 20×20 nm^2 STM image of the Ga_3Ni_2 (001) surface. (B) The FFT of (A) shows all of the bright spots coming from a repeating feature. (C) The inverse FFT of (D) shows the real space repeating features, which is a rhombic unit cell. (D) A filtered version of (B) filtering out the six brightest spots. (E) The Inverse FFT of (F) showing the long-range information from the centre of the FFT (F) A filtered version of (B) filtering the information from the centre containing the long-range non-repeating information. (G) The Inverse FFT of (H), enhancing the repeating features from (C) and combined with (E), shows how the repeating features look with the larger surface structure. (H) A filtered version of (B) combining (D) and (F). 52

3.17 A diagram of the photoelectron process (A) with a model XPS set-up shown in (B) [90]. 54

3.18 (A) An XPS spectrum taken from Ga_3Ni_2 (001) with the largest peaks at the core level highlighted by black lines. (B) A UPS spectrum taken from Ga_3Ni_2 (001). 55

3.19 XPS spectrum from CasaXPS showing the Ga $2p_{3/2}$ peak from the Ga_3Ni_2 (001) surface. All the key features for peak analysis are shown from regions and components to the residual standard deviation value (SDV), a value representing how close the fitted peak matches the results. 57

3.20 (A) A diagram of the Czochralski method. (B) Ga_3Ni_2 crystal pulled along a 3-fold rotational axis. (C) Ga_3Ni_2 structure showing the Ni atoms, silver, being isolated from other Ni atoms by the Ga atoms, green. 61

4.1 XPS spectra from the (001) surface after exposure to air, sputtering for thirty minutes and annealing at 560°C for ninety minutes taken with an Al (K_α) source. Vertical black lines are placed at the elemental binding energies of expected elements on the surface [125]. 64

4.2 (A) XPS spectra from the air-exposed surface. (B) XPS spectra from the clean surface (B). The binding energy for elemental Ga has been highlighted. The binding energy was taken from [125]. (A) required two peaks to fit, showing the presence of both the intermetallic Ga and Ga_2O_3 and after sputtering, only one peak was required (B). A Shirley background was used. 65

4.3 The XPS of on the Ga $2p_{1/2}$ and Ga $2p_{3/2}$ peaks. Black vertical lines show the literature binding energies for Ga $2p_{1/2}$ and Ga $2p_{3/2}$ [126]. The figure shows the air-exposed, sputtering and annealing. 66

4.4 XPS spectra for both the Ni $2p_{1/2}$ and Ni $2p_{3/2}$ peaks from air exposure after sputtering and annealing. Vertical black lines show the binding energy values of elemental Ni $2p_{1/2}$ and Ni $2p_{3/2}$. 67

4.5 Altering the scanning angles affects the depth of the sample being measured using XPS. θ is the angle between the detector and the surface normal. By increasing the angle between the detector and the surface normal, the probing depth is reduced [134]. 70

4.6 (A) The atomic composition of the (001) surface determined via XPS as a function of sputtering and annealing. The bulk composition is highlighted by the dotted lines. (B) The atomic composition of the (001) surface determined via XPS as a function of the scanning angle after annealing to 335°C. The bulk composition is highlighted by the dotted lines. 71

4.7 (A) The atomic composition of the $(2\bar{1}0)$ surface determined via XPS as a function of sputtering and annealing. The bulk composition is highlighted by the dotted lines. (B) The atomic composition of the $(2\bar{1}0)$ surface was determined via XPS as a function of scanning angle. The bulk composition is highlighted by the dotted lines. 75

4.8 (A) The atomic composition of the (100) surface determined via XPS as a function of sputtering and annealing. The bulk composition is highlighted by the dotted lines. (B) The atomic composition of the (100) surface determined via XPS as a function of scanning angle after being annealed to 410°C. The bulk composition is highlighted by the dotted lines. 77

4.9 The atomic composition of the (001) surface for both Ga_3Ni_2 (A) and In_3Ni_2 (B) both determined via XPS as a function of annealing temperature. (B) was adapted from [72]. 79

5.1 Model structures of all the Ga_3Ni_2 surfaces, with the nearest neighbour bonds shown. Ga atoms are in green and Ni atoms are in silver. (A) and (B) show the side profile, with the step heights given, and the top view, with the unit cell dimensions of the (001) surface. (C) and (D) show the side profile, with the step heights given, and the top view, with the unit cell dimensions of the (100) surface. (E) and (F) show the side profile, with the step heights given, and the top view, with the unit cell dimensions of the $(2\bar{1}0)$ surface. 83

5.2 (A) The Model of Al (111) showing the surface unit cell. (B) LEED image of Al (111) at 74 eV with Bragg peaks highlighted by white circles. . 85

5.3 LEED patterns for Ga_3Ni_2 (001) surface after sputtering (A) and annealing at 335°C (B) and 525°C (C). The beam energy is 74 eV for all patterns. Spots are highlighted by circles. 86

5.4 (A) A 400×400 nm^2 STM image from the (001) surface. (B) Height histogram from the section of (A) marked by the black square, showing three different step heights (4.89 Å, 1.35 Å and 3.51 Å). The histogram underwent 3-point levelling to reduce the noise present, producing cleaner peaks. (C) A 3D section of (A) marked by the black square showing the miniature steps that make up the larger steps. The substeps are marked and their average heights given, plus error. 88

5.5 (A) 20×20 nm^2 STM image of the Ga_3Ni_2 (001) surface. A row of dots is visible running diagonally across the surface, showing structure on the surface. White patches are randomly dotted over the surface. (B) FFT of (A) with the peaks attributed to the noise highlighted in green and those from the surface in white. 89

5.6 (A) The inverse FFT of Figure 5.5 (A). (B) The filtered FFT used to produce (A). All six of the brightest maxima were selected in addition to the background in the centre. (C) The filtered FFT converted back to real space showing the (1×1) structure on the (001) surface. 90

5.7 (A) The FFT of a high resolution STM image from the (001) surface showing the six bright spots from the (1×1) structure and the twelve diffuse spots resulting from a weak superstructure. (B) The reciprocal space of a three-domain $c(2\sqrt{3} \times 4)$ superstructure, where different colours represent the reciprocal space of three different domains. (C) The inverse FFT of selected superstructure spots shown in (D) with a selected superstructure domain highlighted. (D) The Filtered FFT showing one example of the selected domain. 91

5.8 The model structure of vertically stacked (001) planes with the three proposed surface termination models, the expected step heights for each model are shown. Model One shows the surface termination with the Ni atoms on the surface, marked by the planes 1 and 4 in blue. Model Two shows the surface termination with Ga atoms on the surface, marked by the planes 0 and 3 in red. Model Three, the Ga surface termination utilises all of the Ga layers, marked by the planes 0, 2 and 3 in magenta. 93

5.9 LEIS spectra recorded from the Ga_3Ni_2 (001) surface after sputtering and annealing at 480°C. Each peak is highlighted with the corresponding element. The y-axis is set to a natural log scale. 94

5.10 LEED patterns for Ga_3Ni_2 $(2\bar{1}0)$ surface after sputtering (A) and annealing at 320°C (B) and 525°C (C). The beam energy is 50 eV for all patterns. The white circles correspond to the (1 × 1) structure with the cyan circles corresponding to the c(2 × 2) superstructure. 96

5.11 (A) The main window from the LEEDPat [144] LEED modelling software shows the input parameters and the type of reconstruction selected, with the real space results on the left and the reciprocal space results on the right. (B) The model $(2\bar{1}0)$ plane with the c(2 × 2) reconstruction highlighted with the purple atoms. The unit cell dimensions are given. . 97

5.12 (A) 100×100 nm^2 STM image of the Ga_3Ni_2 $(2\bar{1}0)$ surface. (B) The 3D view of the black square in (A). Each plane is labelled with either a red arrow or a black arrow. Black arrows represent the unit cell height a which is 4.05 Å and the red arrows represent $a/2$ which is 2.03 Å. 98

5.13 (A) 20×20 nm^2 STM image of the Ga_3Ni_2 $(2\bar{1}0)$ surface. A row of dots is visible running diagonally across the surface. White patches are visible and randomly dotted over the surface. (B) FFT of (A) with the spots highlighted by white circles and the surface unit cell outlined with white lines. (C) A model c(2 × 2) reconstruction overlaid onto an inverse FFT of a section of (A). 99

5.14 LEED patterns for Ga_3Ni_2 (100) surface after sputtering (A) and annealing at 410°C (B) and 494°C (C). The beam energy is 50 eV for all patterns. Spots are highlighted by white circles. 100

5.15 The LEED patterns from the Ga_3Ni_2 (100) surface at five different temperatures recorded with a beam energy between 35 - 67 eV. This image is from Dr Ahmna Alofie's thesis [145]. 101

5.16 A series of LEED images taken from all three surfaces from sputtered to annealed at two increasing temperatures, with the Bragg peaks highlighted. (A), (B) and (C) are from the (001) surface and consist of the sputtered surface. The surface was annealed at 320°C and 500°C, respectively, with the Bragg peaks of interest highlighted in white. (D), (E) and (F) are from the (100) surface and consist of the sputtered surface and the surface annealed at 414°C and 495°C, respectively, with the Bragg peaks of interest highlighted in red. (G), (H) and (I) are from the $(2\bar{1}0)$ surface and consist of the sputtered surface, and the surface annealed at 325°C and 508°C respectively with the Bragg peaks of interest highlighted in blue showing the appearance of the c(2×2) reconstruction. 104

5.17 (A) A 400×400 nm^2 STM image of the (001) surface. (B) A 100×100 nm^2 STM image of the $(2\bar{1}0)$ surface. 106

5.18 (A) A 3D image of the (001) surface with the step heights shown to confirm Ni termination. (B) A 3D image of the $(2\bar{1}0)$ surface with the average step height displayed. 107

5.19 STM images of the (001) and $(2\bar{1}0)$ surface. (A) 30nm×30 nm^2 section of the (001) surface equalised to highlight surface structure. (B) 35×35 nm^2 section of the $(2\bar{1}0)$ surface equalised to highlight surface structure. (C) An FFT of (A) with the noise removed to enhance the peaks and noise. Peaks of interest are highlighted by white circles. (D) An FFT of (B) with the noise removed to enhance the peaks and noise to show the central peak indicative of c(2×2) reconstruction. Peaks of interest are highlighted by white circles. (E) A filtered section of (A) showing atoms forming the (1×1) expected surface structure. (F) A filtered section of (B) showing atoms forming the c(2×2) reconstruction observed through LEED. 109

5.20 The LEED pattern from the (001) surface of In_3Ni_2, after annealing (A) and after hydrogen exposure (B), and Ga_3Ni_2 after annealing over 500°C. (A) and (B) adopted from [72]. 110

5.21 3D STM images of the (001) surface from In_3Ni_2 (A) and Ga_3Ni_2 (B). The model structures of both In_3Ni_2 (C) and Ga_3Ni_2 (D) with the distance between each layer are given. 111

6.1 The wide XPS scan of the (001) surface after being annealed at 520°C. (A) The entire spectrum of the (001) surface in 0.5 eV steps with the key peaks highlighted and labelled. (B) Shows the 200 - 0 eV range in 0.5 eV steps with each key peak identified. (C) The Ga and Ni peaks after air exposure and cleaning to show the effects on the elements observed. (D) The contamination peaks after air exposure and cleaning, that C, N and O are all removed after sputtering and annealing. 117

6.2 XPS spectra of the Ga $2p_{1/2}$ and Ga $2p_{3/2}$ as O_2 exposure was increased, for the Ga_3Ni_2 (001) surface prepared by annealing at 571°C. The formation of a shoulder towards higher binding energy can be observed at higher exposures. Vertical lines mark the binding energy of elemental Ga $2p_{1/2}$ and Ga $2p_{3/2}$ adopted from [125], [126]. 118

6.3 XPS spectra from the Ga_3Ni_2 (001) surface after exposure to O_2 (13300 L). The binding energy for elemental Ga has been highlighted, the binding energy was taken from [125]. The Ga peaks required two peaks to fit one from intermetallic Ga and the other from Ga in Ga_2O_3. 119

6.4 (A) The FWHM of the Ga oxides $2p_{1/2}$ and Ga oxides $2p_{1/2}$ as a function of O_2 exposure. (B) The peak position of the Ga oxides $2p_{1/2}$ and Ga oxides $2p_{1/2}$ as a function of O_2 exposure. 120

6.5 The composition of the Ga $2p_{1/2}$ and Ga $2p_{3/2}$ peaks from the (001) surface as exposure to O_2 increases taken from XPS results. The intermetallic Ga peaks and the Ga in Ga_2O_3 are labelled. 121

6.6 XPS spectra of the Ni doublet peak as O_2 exposure is increased. 122

6.7 The atomic composition of the surface as a function of O_2 exposure showing all the key elements, Ga, Ni, O, C and $Ni(OH)_2$. 124

6.8 The atomic composition as a function of oxygen exposure for Ga_3Ni_2 (A) and In_3Ni_2 (B). (B) is adopted from [72]. 124

7.1 Schematic illustration of the valence and conduction bands in insulators, metals, and semiconductors. The Fermi level corresponds to the highest occupied electronic state at absolute zero [154]. 129

7.2 UPS spectrum of the Ga_3Ni_2(001) surface after annealing at 414°C for ninety minutes, taken using a He_2 source, with the Fermi edge marked by a vertical dotted line. 130

7.3 The UPS spectrum from Figure 7.2 (upper), the total DoS calculations (Lower). Each peak has been labelled, and the Fermi edge is denoted by a vertical dashed line. Both of the graphs have the same X-axis range (-4 eV to 0.25 eV). 132

7.4 Three UPS spectra for (A) Elemental Ni, (B) Elemental Ga and (C) the Ga_3Ni_2. (A) and (B) are from The XPS Library with both samples being scraped and etched, while (C) is from the UPS study performed on Ga_3Ni_2. 133

List of Terms and Abbreviations

STM Scanning Tunnelling Microscope

LEED Low Energy Electron Diffraction

XPS X-ray Photoelectron Spectroscopy

UPS Ultraviolet Photoelectron Spectroscopy

LEIS Low Energy Ion Scattering

UHV Ultra High Vacuum

UHVC Ultra High Vacuum Chamber

IMC Intermetallic Compound

DFT Density Functional Theory

FFT Fast Fourier Transform

DOS Density of States

Chapter 1

Introduction

Intermetallic compounds (IMCs) are a type of material composed of two or more elemental metals [1], which exhibit different crystal structures and properties than the parent elements. This has made them of particular interest in the field of catalysis due to their higher selectivity for reactions, high corrosion resistance, and ability to replace rare earth metals with more common and abundant alternatives [2]–[5]. Binary alloys are a subset of IMCs in which only two elemental metals are used to form a new intermetallic compound. The spatial separation and site isolation of the catalytically active elements exhibited by IMCs are thought to be responsible for their higher selectivity, improved thermal stability, and corrosion resistance when compared to other metallic catalysts typically used in reactions [6].

Catalysis is a fundamental aspect of industrial chemistry, with roughly 90% of all industrial reactions involving catalysts [7]. A catalyst is a substance that increases the rate of a reaction without being consumed during the reaction and without affecting the Gibbs free energy of the system [8]. Although well-studied, catalysis remains a complex field, and gaining a fundamental understanding of catalytic behaviour continues to be challenging.

This has led to trial-and-error methods being used to understand and refine the conditions necessary to optimise catalytic activity. Simple and well-defined model systems are employed to investigate the physical parameters affecting catalysis. For heterogeneous catalysts, a single crystal of the material is often grown and cut along specific crystallographic faces to serve as model catalysts. Using surface physics techniques such as scanning tunnelling microscopy (STM), X-ray photoelectron spectroscopy (XPS), ultraviolet photoelectron spectroscopy (UPS), and low-energy electron diffraction (LEED), the atomic and electronic properties of the sample can be characterised. By introducing key reactants, it is possible to observe how these surfaces behave in relevant chemical reactions [9].

In this thesis, we exclusively study the Ga_3Ni_2 intermetallic compound. Three different samples, each cut along a distinct crystallographic orientation—(001), (100), and $(2\bar{1}0)$—were analysed. A variety of surface analysis techniques were employed to build a comprehensive understanding of each sample's surface.

Chapter 2 provides a literature review on intermetallic compounds, detailing their importance to the field of catalysis. Chapter 3 describes the experimental techniques used in this thesis, covering both theoretical background and practical equipment. It begins with a detailed overview of one of the Ultra-High Vacuum (UHV) chambers used in this work, explaining why a UHV environment is essential, how the chamber is evacuated and maintained at low pressure, and the equipment housed within it.

The theory and experimental setup for each of the methods used in this thesis are discussed in turn. These include Low-Energy Electron Diffraction (LEED), X-ray Photoelectron Spectroscopy (XPS), Ultraviolet Photoelectron Spectroscopy (UPS), and Scanning Tunnelling Microscopy (STM).

The results chapters, Chapters 4, 5, 6, and 7, present the individual projects undertaken. Chapter 4 presents XPS data collected from all three Ga_3Ni_2 surfaces to understand the surface chemical composition and how it is influenced by the preparation conditions. Chapter 5 focuses on the surface atomic structure, using LEED and STM to observe the reconstruction of the $(2\bar{1}0)$ surface as a function of annealing temperature. STM images—both wide-scan and atomic-resolution—for the $(2\bar{1}0)$ and (001) surfaces are used to identify surface termination and corroborate the LEED data.

Chapter 6 presents XPS results on the oxidation of the (001) surface. These findings are compared to a previous oxidation study on powdered GaNi [10]. Controlled exposure allowed for the observation of oxide formation and provided insight into how the surface might behave in industrial environments.

Chapter 7 describes a collaborative project with Tribhuvan University, Nepal. Theoretical density of states (DOS) calculations produced by the collaborators were validated using UPS measurements obtained from the Ga_3Ni_2 (001) surface in Nancy. The peaks observed in the UPS spectra were matched to those in the DOS predictions, confirming the accuracy of the theoretical results.

Finally, Chapter 8 summarises the findings from each project and evaluates the overall progress made in understanding and characterising the surface of Ga_3Ni_2. Future directions are proposed to build on this research.

Chapter 2

Background

2.1 Introduction

This literature review will summarise crystals and crystallography with a focus on large unit-cell alloys and intermetallic compounds. This will be followed by an explanation of catalysis, with a focus on heterogeneous catalysts. Finally, a summary of four different intermetallic compounds will be presented, focusing on their catalytic properties and prior surface physics research, culminating in an overview of the crystal structure and previous work on the GaNi system of intermetallic compounds.

2.2 Crystals and Crystallography

2.2.1 Crystals

Crystals have fascinated humanity for centuries, from the large crystal caves of Naica, Mexico, to the microscopic salt crystals used all over the world. The first study that would lead to crystallography dates back to 1669, when Niels Steensen observed that the angles between the faces of a crystal are consistent within a species of crystal. This observation became known as Steensen's Law and eventually formed the basis for the first law of crystallography [11].

Over the years, the study of crystallography has expanded, and the definition of what constitutes a crystal has evolved to incorporate new discoveries. A crystal can be broadly defined as a material whose atoms are arranged in a three-dimensional, repeating periodic pattern [12].

2.2.2 Crystallography

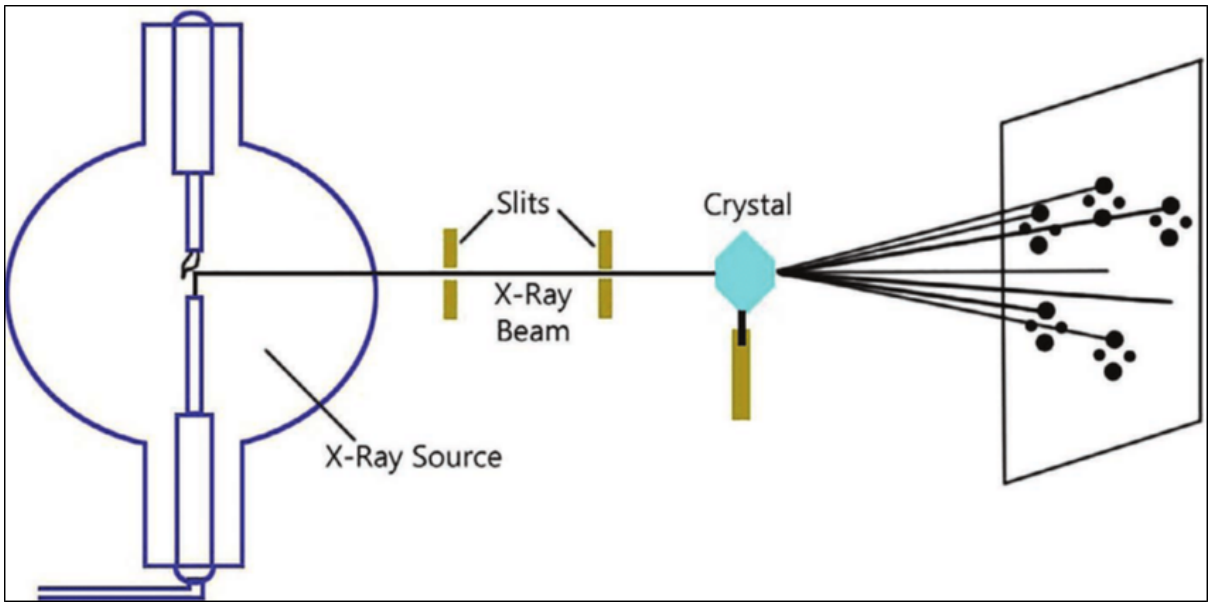

Figure 2.1: A model of X-ray diffraction using the Laue method, in which an X-ray is fired at a crystal and the scattered X-rays are recorded on a photographic plate or phosphorescent screen [13].

While there had been work on the study of crystals before 1912, it was the discovery of X-ray diffraction by Friedrich, Knipping, and Laue that launched the field of crystallography. By diffracting X-rays through a large crystal sample, they observed a diffraction pattern, shown in Figure 2.1, and confirmed that X-rays exhibited wave-like behaviour. Dr. Max von Laue was awarded the Nobel Prize in 1914 for his discovery of the diffraction of X-rays by crystals. The revelation of the atomic arrangement and bonding within crystalline solids, as well as the geometric structure of crystal lattices, propelled the field of crystallography forward.

Crystal System	Number of Lattices	Restriction on Cell Axes	Restriction on Cell Angles
Triclinic	1	$a \neq b \neq c$	$\alpha \neq \beta \neq \gamma$
Monoclinic	2	$a \neq b \neq c$	$\alpha = \gamma = 90°, \beta \neq 90°$
Orthorhombic	4	$a \neq b \neq c$	$\alpha = \beta = \gamma = 90°$
Tetragonal	2	$a = b \neq c$	$\alpha = \beta = \gamma = 90°$
Trigonal	1	$a = b = c$	$\alpha = \beta = \gamma < 120° \neq 90°$
Hexagonal	1	$a = b \neq c$	$\alpha = \beta = 90°, \gamma = 120°$
Cubic	3	$a = b = c$	$\alpha = \beta = \gamma = 90°$

Table 2.1: A table showing the seven crystal systems along with the conditions required to fulfil each system [14].

The unit cell is the smallest repeating unit that makes up a crystal and falls into one of the seven crystal systems listed in Table 2.1. The dimensions of the crystal are given by the lengths a, b, and c, while the three angles are represented by α, β, and γ.

Understanding the unit cell of each material and surface is important, as it allows us to confirm the orientation by matching the recorded unit cell to a theoretical model. The unit cell is used in LEED analysis to identify the surface symmetry observed, along with reconstructions, through deviations from the expected model [15].

2.2.3 Complex Metallic Alloys

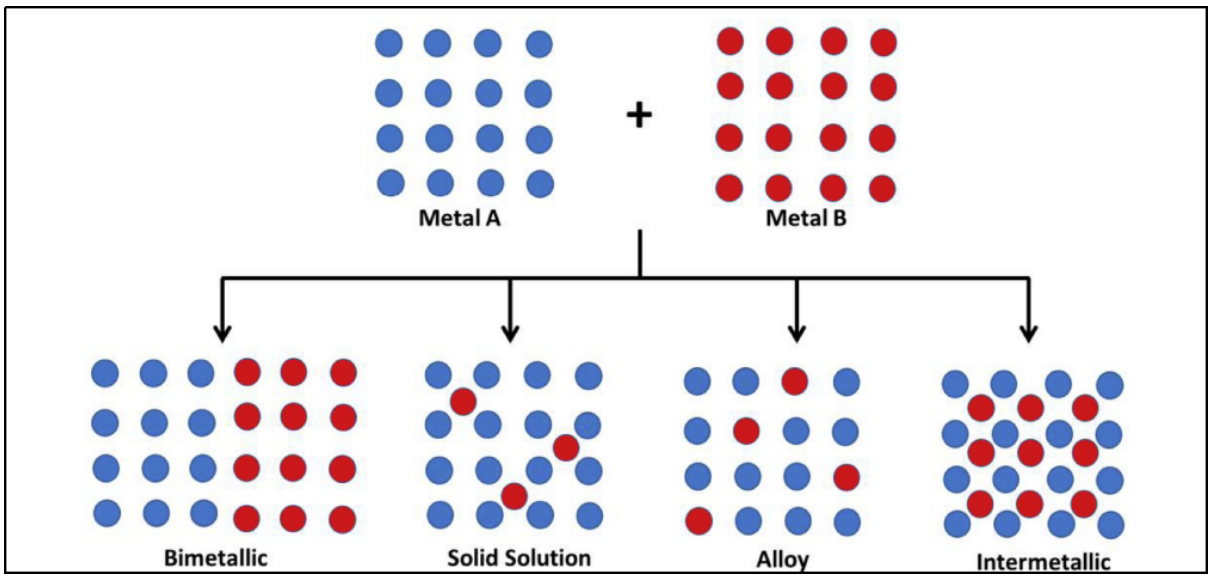

Figure 2.2: A model showing possible ways for two metals to alloy together [16].

Complex metallic alloys (CMAs) are a broad category of crystalline materials consisting of metal compounds alloyed together, as shown in Figure 2.2 [16]. CMAs are typically characterised by three traits: first, the presence of a large unit cell, which can contain anywhere from ten to several thousand atoms. As quasicrystalline materials are aperiodic and theoretically infinite in unit cell size, the lower bound for CMAs has been conventionally set at more than twelve atoms per unit cell [17].

Secondly, there is a variety of atomic clusters present within the unit cell, with these clusters often beginning to form icosahedral phases. Finally, their chemical formulas are as complex as their structures, often involving three, four, or five elemental metals. Examples include Ag-Yb-In and Ho-Mg-Zn. With continued research, binary complex metallic alloys have also been discovered.

CMAs have a wide range of applications, as they can be designed and tailored to achieve specific properties [18]. Due to their resistance to high temperatures and radiation, many CMAs are used in aerospace engineering and nuclear reactors, where materials are subjected to extreme environments [17], [19], [20].

CMAs can also exhibit chemical and wear resistance, making them suitable for use in environments exposed to corrosive substances or in high-performance machinery where durability is essential [16], [17], [19], [20].

Another area where CMAs have shown promise is as heterogeneous catalysts. Compared to more expensive elements such as palladium—used in many non-catalytic applications as well [21]—CMAs offer a lower-cost alternative for many catalytic reactions, making them appealing for industrial chemical processes. By understanding the surface physics of these alloys, scientists can adopt a more research-driven approach to catalyst design, moving away from trial-and-error methods.

Due to the broad scope of CMAs, the following sections will focus on the two principal areas of current research: intermetallic compounds and quasicrystals. Both are subcategories within the broader field of complex metallic alloys.

2.3 Intermetallics

Intermetallic compounds (IMC) are a class of materials composed of two or more elemental metals. The resulting IMC has an ordered structure distinct from the component elements, as shown in Figure 2.2, with the ordered and periodic distribution of the two metals compared to an alloy or solid solution [22].

Intermetallic compounds have been studied across many fields of research over the past few decades. For chemists, their application as a new form of nanoparticle and heterogeneous catalyst has been of great interest [23], [24]. Physicists have measured a broad range of their electronic properties, including magnetic and superconducting behaviours [25], [26]. Large and complex structures have attracted the attention of many crystallographers, who have observed large unit cells containing over 23,000 atoms [27].

IMCs are often synthesised by bulk-melting one metal and then adding the additional metals until the desired ratio is achieved. This process allows the metals to diffuse into each other [28]. By manipulating the ratio of added metals, bulk crystals of specific compositions can be reliably and repeatedly grown, allowing these crystals to be tailored for specific traits and properties [29], [30]. With their defined crystal structure and specific atomic composition, IMCs are used in several applications [31].

2.4 Quasicrystals

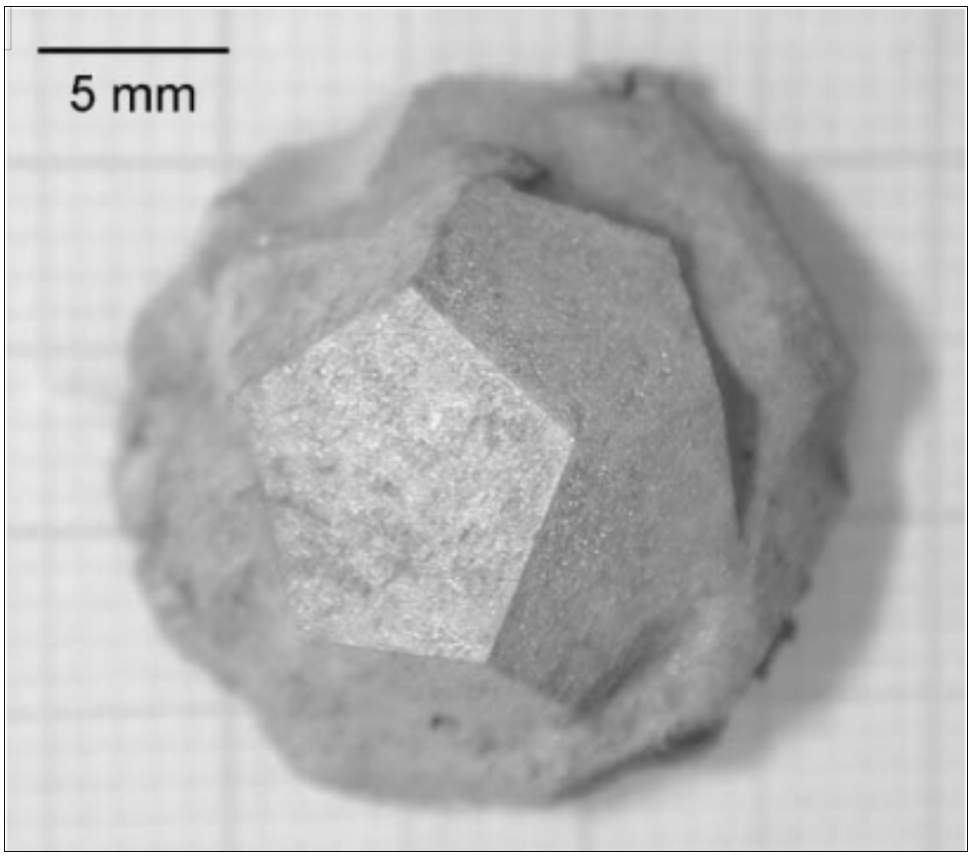

Figure 2.3: A large single crystal of the icosahedral quasicrystal Ho-Mg-Zn [32].

Quasicrystals were discovered by Dr Dan Shechtman in 1982 [33] while studying an aluminium and manganese alloy, Al_6Mn. He observed a 10-fold electron diffraction pattern. Before this discovery, 10-fold rotations were considered forbidden by the crystallographic restriction theorem, which stated that a crystal was limited to 2-fold, 3-fold, 4-fold, or 6-fold symmetries [34], [35].

These materials were labelled as quasicrystals and are a new class of materials known for exhibiting long-range order without periodicity. By forming large tiling patterns, such as Penrose tiling, non-overlapping polygons can be arranged to exhibit these forbidden symmetries, such as 5-fold rotational symmetry [36].

The discovery of quasicrystals opened up a new family of materials to explore, and over the years, many more quasicrystalline materials have been uncovered [37]. Figure 2.3 shows an icosahedral crystal of Ho-Mg-Zn. Table 2.2 shows a comparison between quasicrystalline materials and regular metals, highlighting potential applications for quasicrystals due to their hardness, low friction coefficient, and corrosion resistance [16].

Metallic systems property	**Metals**	**Quasicrystals**
Mechanical	Ductility Malleability	Brittle
Tribological	Relatively Soft Easy Corrosion	Very Hard Low Friction Coefficient Corrosion Resistant
Electrical	High Conductivity Resistivity Increases With Temperature Small Thermopower	Moderate to Low Conductivity Resistivity Decreases With Temperature Large Thermopower
Magnetic	Paramagnetic	Diamagnetic
Thermal	High Conductivity High Specific Heat Values High Melting Points	Very Low Conductivity Low Specific Heat Values
Optical	Metallic Luster Drude Peak	Metallic Luster IR Absorption

Table 2.2: A comparison of quasicrystals and metallic systems [16].

2.5 Catalysis

Catalysts are a vital area of study across many fields of science, particularly within chemistry, dating back to 1835 when Jöns Jakob Berzelius coined the term "catalyst" [38]. A catalyst is a material that increases the rate of a reaction, is not consumed during the reaction, and does not alter the equilibrium constant [38], [39].

To increase the rate of a reaction, catalysts lower the activation energy required for the reaction to take place, as shown in Figure 2.4. This does not affect the thermodynamics of the reaction, as the catalyst is not consumed during the process and only facilitates kinetically favourable reactions for both the forward and reverse directions, leaving the equilibrium constant unchanged.

Catalysts are used in reactions of all scales, from small laboratory experiments to large-scale industrial manufacturing [40]. At industrial scales, catalysis is essential for ensuring sufficient product yield. However, rare earth materials, commonly used as catalysts, can be expensive. This has led to the optimisation of catalyst surfaces through surface physics to reduce costs without affecting product yield [7], [41].

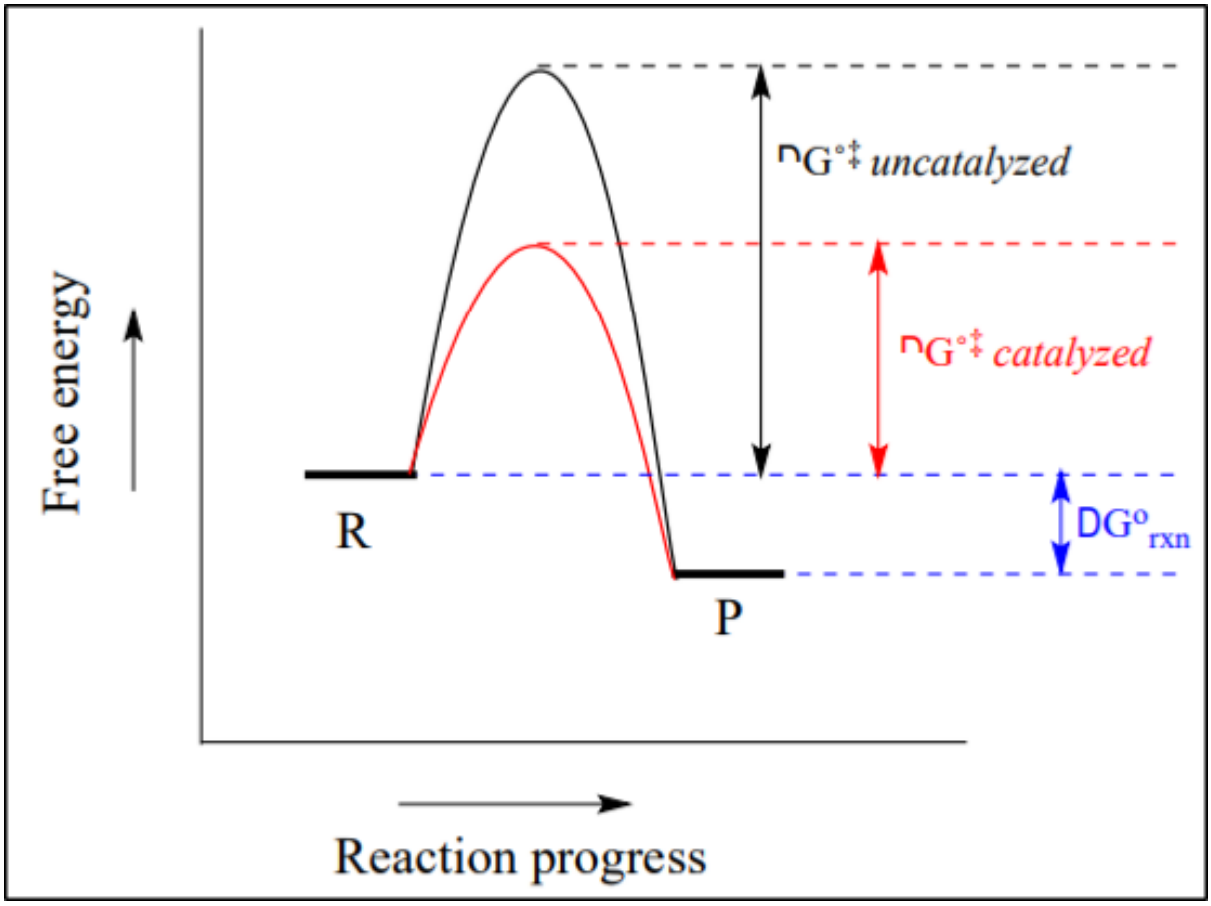

Figure 2.4: A diagram showing the effects of catalysis on a reaction. The catalysed reaction in red has a much lower change in energy (ΔG) compared to the uncatalysed reaction in black [39].

2.5.1 Heterogeneous Catalysts

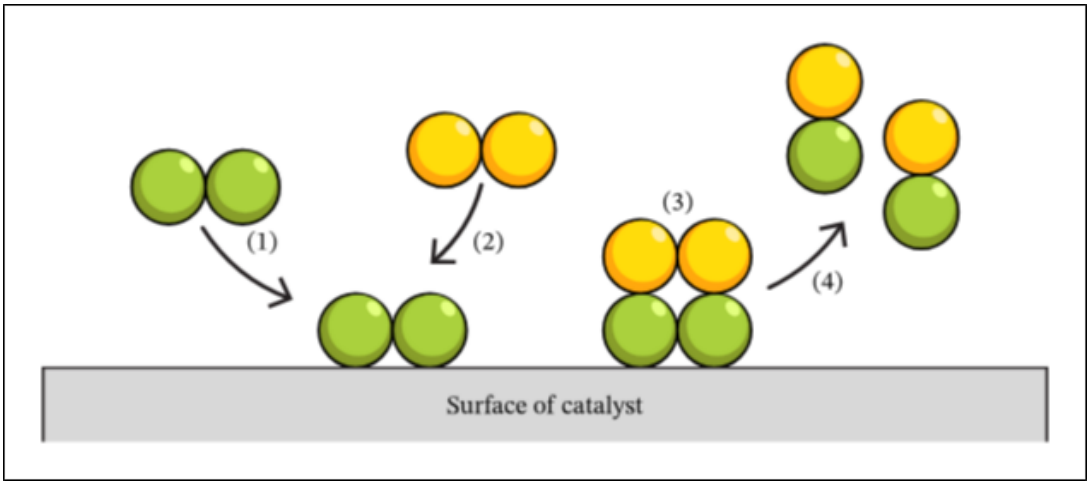

Figure 2.5: A model of a chemical reaction using a heterogeneous catalyst. (1 and 2) The two reactants, green and yellow, adsorb to the surface. (3) The reaction undergoes a chemical transformation facilitated by the surface, forming the product. (4) The product desorbs from the surface [42].

Heterogeneous catalysts are a type of catalyst that exists in a different phase than the reactants. Typically, this is seen with solid metallic catalysts used in environments containing gaseous or aqueous reactants, as shown in Figure 2.5 [43]. As all catalytic reactions occur at the interface between the catalyst and the reactants, understanding the physics of the catalyst surface is vital. Any changes to the surface will directly affect catalytic properties, either positively or negatively, with many heterogeneous catalysts having applications in green technologies and a sustainable future [44].

Surface physics and chemistry involve the study of physical changes and chemical interactions that occur at interfaces. This makes heterogeneous catalysts ideal candidates for study, as understanding their surface structure will help improve and refine their catalytic performance.

2.5.2 Intermetallic Compounds as Catalysts

Intermetallic compounds are of great interest for their use as catalysts. They exhibit increased catalytic activity, stability, and selectivity when compared to previous catalysts that typically used a single metal [1], [45].

Typically, intermetallic compounds contain a catalytically active element, e.g., Au, Pt, Pd, Ni, Rh, Co, Ru, and Fe [46]. The other metals should ideally be either early transition metals or other metals separate from the catalytically active elements. Figure 2.6 shows a periodic table where the catalytically active elements are highlighted in red and the secondary elements in teal. This refines the number of elements that can form an intermetallic compound [23].

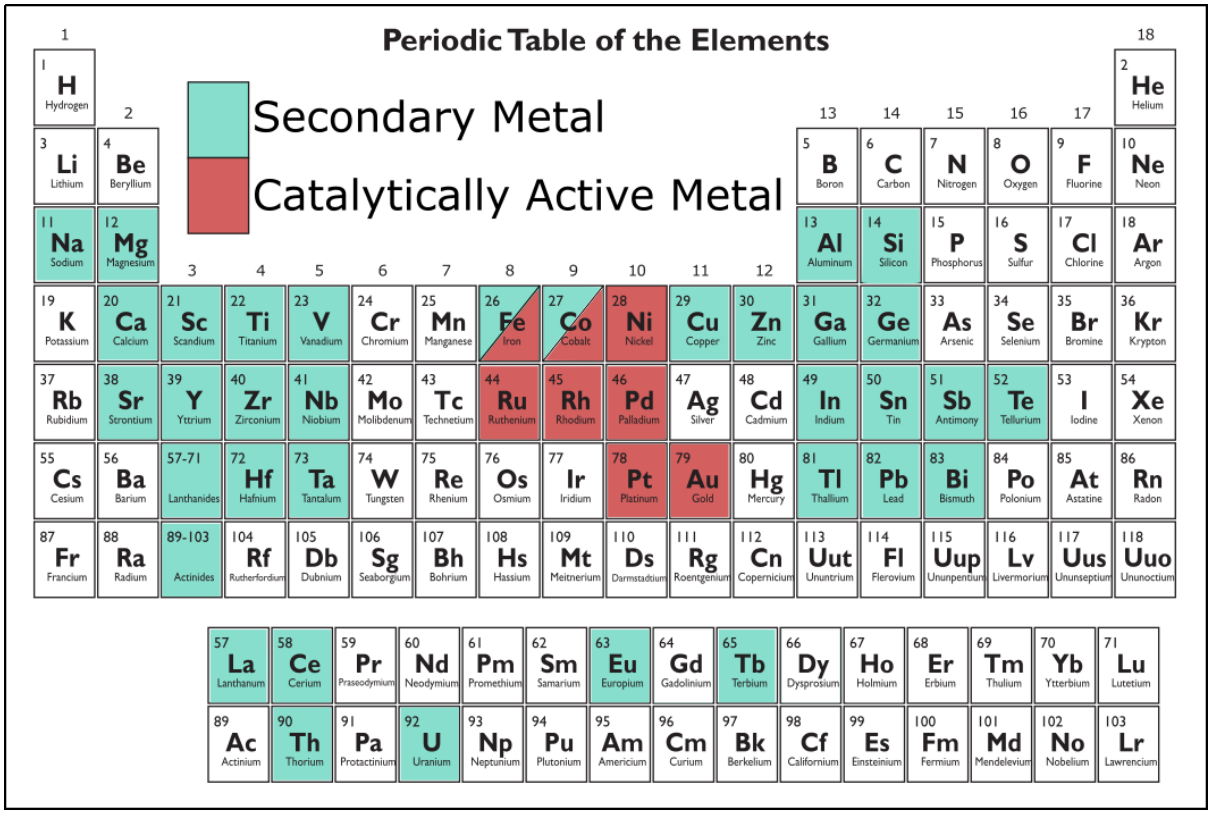

Figure 2.6: A periodic table with the catalytically active transition elements highlighted in red, and the secondary metals typically used in IMCs highlighted in teal [47].

Another application of intermetallic compounds as catalysts is in replacing certain elements in key reactions. One example is catalytic converters, found in all petrol and diesel cars, which use platinum, palladium, and rhodium to convert NO, CO, and HC into N_2, CO_2, and H_2O [48].

These metals are expensive and in high demand, and as such, are prime targets to be replaced with more readily available materials. CeNi is an intermetallic compound of interest due to its ability to oxidise CO into CO_2 [49], which could make it a potential replacement for palladium in new catalytic converters.

ZnPd has also been used as a replacement for Cu in the methanol steam reforming reaction [3], for which Cu is commonly used. Both have similar valence electron densities. This suggests that the catalytic function for methanol steam reforming is dependent primarily on the valence band structure. This implies that other intermetallic compounds with similar valence band structures could be found or synthesised and used in place of Cu as a catalyst.

The ability to design and grow these compounds for selective reactions [22] means that rare earth and expensive materials, which are typically used as catalysts, can be replaced by these new materials made from cheaper metals. This is of interest to the industry, especially as chemical reactions are scaled up for large-scale production [10]. One challenge currently limiting wide-scale application is the preparation required for intermetallic compounds. Controlling the structure, purity, and morphology of the crystals being grown is difficult, and variations in these factors influence catalytic performance.

2.5.3 Examples of Compound Catalysts

In the following section, we will examine research conducted on four intermetallic compounds that have specific applications as industrial catalysts. We will begin by discussing the catalytic reactions these intermetallic compounds are involved in, followed by a summary of any surface physics studies conducted on each IMC.

By considering a broad range of catalytically active elements, in addition to GaNi, we can contrast key features and traits among them and gain insights into how to prepare and image the surface of Ga_3Ni_2.

ZnPd

In a world where most energy is currently produced through the burning of fossil fuels, finding a method of producing CO_2-neutral energy is vital [2]. Hydrogen is a popular fuel source, but it has a storage issue. Storing hydrogen in its elemental form is both costly and difficult. It is possible to store hydrogen chemically in the form of methanol due to its high hydrogen content and safe handling properties.

ZnPd is one of many intermetallic compounds of interest as a potential catalyst in the methanol steam reforming reaction. In this reaction, methanol is placed in a steam-pressurised reactor, where it decomposes into CO, which then reacts with steam to produce CO_2 and H_2 [50].

$$\mathsf{CH_3OH} \longleftrightarrow \mathsf{CO} + 2\,\mathsf{H_2} \tag{2.1}$$

$$\mathsf{CO} + \mathsf{H_2O} \longleftrightarrow \mathsf{CO_2} + \mathsf{H_2} \tag{2.2}$$

Cu would be the catalyst of choice for this reaction, as it is one of the best catalysts at lower temperatures [51]. However, at higher temperatures, Cu is susceptible to sintering, which reduces catalytic activity. ZnPd is a desirable alternative to Cu, as it is resistant to sintering at high temperatures and other forms of corrosion [3].

ZnPd exhibits a tetragonal system with a P4/mmm space group, similar to the CuTi structure [52]. The lattice parameters are $a = 4.1$ Å, $b = 4.1$ Å, and $c = 3.35$ Å, with the unit cell consisting of layers of Pd and Zn atoms, as shown in Figure 2.7 (B).

Once synthesised, the surface is prepared under ultra-high vacuum (UHV) by sputtering and annealing at 240°C for half an hour, followed by annealing at 220°C overnight. The surface was then studied using XPS, STM, LEED, and photoemission electron microscopy (PEEM).

LEED and PEEM were used to determine surface features, such as domain structures and crystallite sizes. PEEM images revealed three distinct contrasts, indicating three different surface orientations [2].

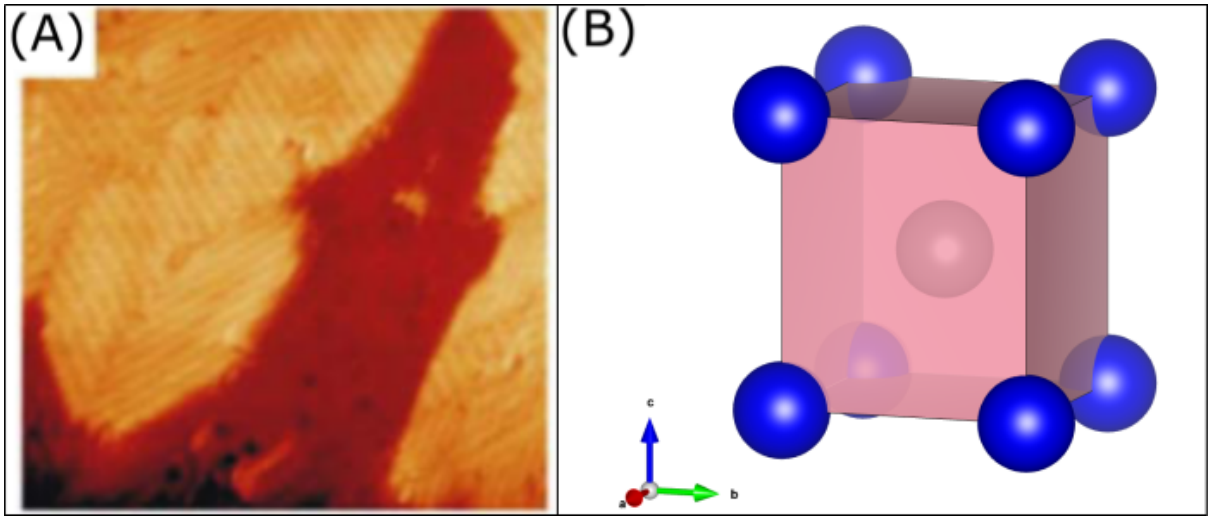

Figure 2.7: (A) An STM image of the ZnPd alloy formed after depositing Zn onto Pd(111), adopted from [2]. (B) The model of ZnPd with Zn atoms in silver and Pd in purple.

XPS was employed to analyse the surface chemical composition of the ZnPd alloy and how the surface responded to sputtering and annealing. The atomic composition, shown in Table 2.3 [2], indicates that sputtering preferentially removes Zn, while annealing restores the Zn percentage to approximately the bulk composition. Since Zn is the lighter element in the alloy and has a lower surface free energy, this suggests that Zn is prone to preferential sputtering [53].

Preparation State	Zn (at%)	Pd (at%)
Sputtered	38.6	61.4
Annealed	50.5	49.5

Table 2.3: The change in atomic composition, measured by XPS, for the ZnPd surface. Adopted from [54]. Each value has an estimated 5% uncertainty.

STM images were taken of the ZnPd surface to observe surface phenomena. The atomic structure of the thin film displayed several surfaces: (110), (101), (111), and (114). The surface appeared to be Pd-terminated, as confirmed by the density of states (DOS) calculations [55]. The DOS calculations show only contributions from Pd around the Fermi level, which is consistent with the STM observations [56].

This was expected, as Pd is the catalytically active element within the alloy, and its presence on the surface is crucial for achieving the ideal level of catalytic activity required for industrial applications [41].

GaPd

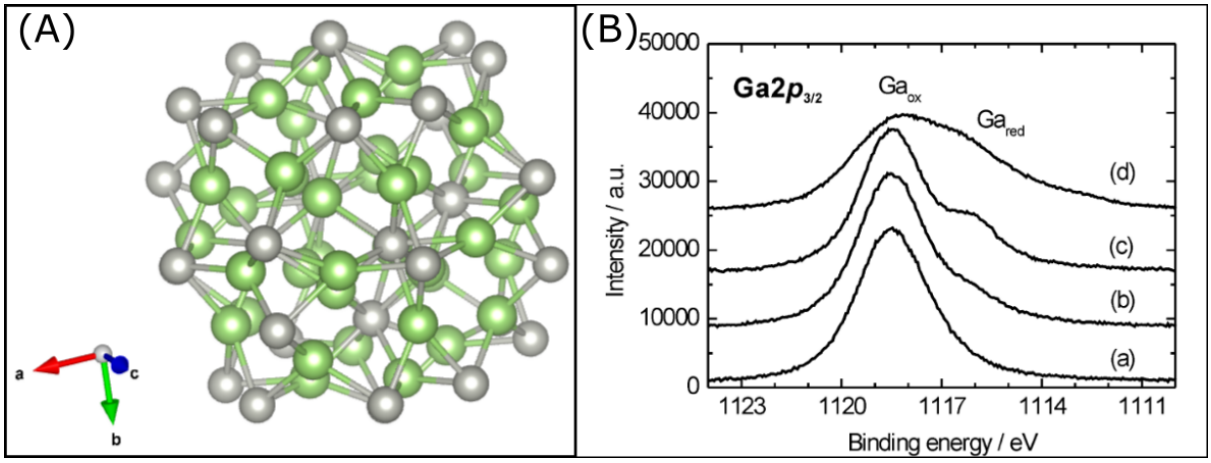

Figure 2.8: (A) The model structure of Ga_7Pd3, where the Pd atoms are in silver and Ga atoms are in green. Adopted and edited from [57]. (B) The XPS data of the Ga $2p3/2$ peak from GaPd after being air milled: (a) untreated, (b) after H_2 treatment at 573 K, (c) after H_2 treatment at 673 K, (d) after ion scattering spectroscopy (ISS) [57].

GaPd and Ga_7Pd_3 are highly selective intermetallic compound catalysts for the hydrogenation of acetylene into ethylene [57], which is a key step in removing acetylene from the feed material in the production of polyethylene [57]–[59].

$$C_2H_2 + H_2 \longrightarrow C_2H_4 \tag{2.3}$$

Figure 2.8 (A) shows the model structure of Ga_7Pd_3, where the Ga atoms are in green and the Pd atoms are in silver. Each Pd atom is encapsulated by Ga atoms, isolating it from neighbouring Pd atoms. This site isolation has beneficial effects on the long-term stability and selectivity of the catalyst [60].

In addition, the covalent bonding between Ga and Pd atoms affects the chemistry of the alloy, resulting in notable differences between GaPd and pure Pd as catalysts [57]. This is due to the inability of sub-surface hydrides to form, reducing the amount of hydrogen available for undesired hydrogenation reactions.

Ga_7Pd_3 crystals were grown by melting the required amounts of pure Pd and Ga under an inert Ar^+ atmosphere in a high-frequency furnace. The phase purity of the ingot was monitored using X-ray powder diffraction [57].

The topmost layers of the crystals were scanned using XPS, with the results showing covalent bonding interactions between Ga and Pd atoms. These interactions are attributed to the high selectivity of these catalysts [61]. At the Fermi energy, there is a significant contribution from the Pd $4d$ orbital, confirmed through density of states calculations [61], [62]. The catalytically active element being highly present at the Fermi level is expected for intermetallic compounds, as the valence electrons of the active element facilitate catalytic reactions at the surface [16].

After air milling, the exposed surface was measured via XPS before undergoing H_2 treatments to clean the surface. Figure 2.8 (B) shows that, before treatment, a substantial presence of oxidised Ga species was observed around 1118.5 eV. This signal diminished with treatment, indicating a surface Ga oxide layer had formed, which reduced the observed presence of Pd.

Elemental Pd has a higher electron density around the Fermi level compared to Ga_7Pd_3, which is significantly lower. The addition of Ga causes the Pd d-band orbital to become filled, shifting this band away from the Fermi level [62]. This reduces subsurface hydride formation—an essential process for the hydrogenation of acetylene—making Ga_7Pd_3 a more selective and desirable catalyst compared to the commercially used Pd/Al_2O_3 catalysts [57], [63].

AlFe

Fe has many applications as a heterogeneous catalyst, notably in the Haber process, which converts N_2 into NH_3 [67], commonly used in agricultural fertilisers. It can also be used in a variety of hydrogenation reactions, where Fe may replace other less efficient and practical metals currently used in industrial catalytic processes. Of particular interest is the potential for Fe to replace Pd and Ni in hydrogenation reactions [65], as illustrated in Equation 2.5.

Currently, PdNi is the catalyst of choice for many hydrogenation reactions. Pd is an expensive and rare metal with broad applications across fuel cells, catalysts, and electronics [68].

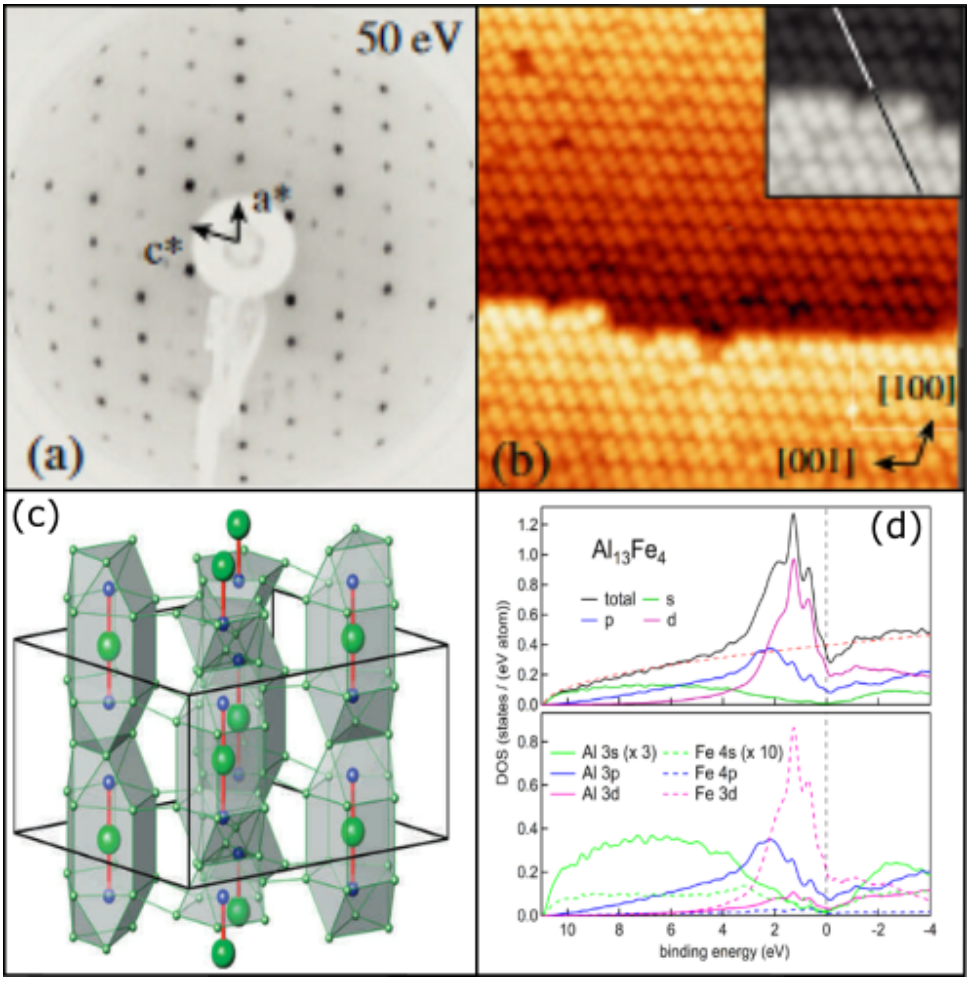

Figure 2.9: (A) A LEED image of the (010) Al13Fe4 surface with a beam energy of 50 eV. (B) STM image (30×30 nm^2) showing step terraces formed after annealing at 600°C. (A) and (B) adopted from [64], (C) from [65], and (D) from [66].

By substituting Pd with the more abundant and affordable Fe, it becomes feasible for industries to scale up catalyst usage. Ni, while a common catalyst, suffers from several limitations with prolonged use, including sintering (which disrupts surface order and reduces catalytic activity), poisoning (which deactivates the catalyst over time), and carbon formation (which builds up and hinders catalytic performance) [69], [70].

Figure 2.9 (C) shows that $Al_{13}Fe_4$ possesses a large unit cell comprising 137 atoms, with lattice parameters of $a = 15.49$ Å, $b = 8.09$ Å, and $c = 12.48$ Å, and angles $\alpha = 90.00°$ and $\beta = 107.67°$ [64]. The (010) plane was studied to determine whether its surface structure is due to the strong Fe–Al–Fe bonding predicted by quantum chemical calculations [64].

STM analysis (Figure 2.9 (B)) indicates that the $Al_{13}Fe_4$ surface is Fe-terminated, with the exposed Fe atoms anchored by subsurface Al atoms [64], maintaining a bipyramidal structure [71]. Since Fe is the catalytically active element, its isolation on the surface is expected and beneficial.

Density of states (DOS) calculations in Figure 2.9 (D) reveal that Fe $3d$ orbitals are the primary contributors to the total DOS, followed by Al $3p$ orbitals due to the presence of a pseudogap [65]. These DOS findings support the STM results indicating a Fe-terminated surface [64].

InNi

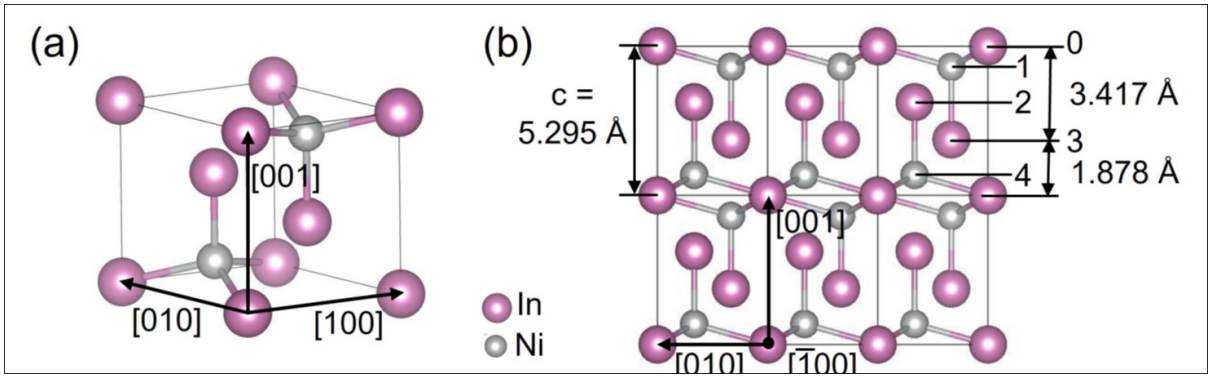

Figure 2.10: (A) The unit cell of In_3Ni_2. (B) Side view of In_3Ni_2 (001), showing the stacking of five atomic layers labelled 0 to 4, with each plane separation shown [72].

InNi is a member of the AlNi family of catalysts, all of which have applications as effective environmental catalysts. With Ni as the catalytic element in the alloy, InNi is used in reactions involving C–C double bonds [73]. It has been studied as a catalyst in the reverse water-gas shift reaction [74], for converting acetic acid into ethanol [75], and for the dry reforming of methane [76], in which two greenhouse gases—CO_2 and CH_4—are converted into hydrogen gas and carbon monoxide, as shown in Equation 2.4 (1). Ni catalysts, however, tend to deposit more carbon during methane cracking (Equation 2.4 (2)) and the carbon monoxide disproportionation reaction (Equation 2.4 (3)).

This results in a gradual decline in catalytic activity—an inherent limitation of Ni-based catalysts. However, smaller Ni particles exhibit greater resistance to carbon deposition. By using a binary alloy such as InNi, the size of the exposed Ni particles can be controlled, enabling the design of an ideal catalyst [76].

Typically, catalysts used in dry reforming of methane face severe coking issues, which hinder their industrial implementation. To address this, several InNi catalysts have been designed with improved resistance to coking [76].

$$\begin{aligned} CH_4 + CO_2 &\longleftrightarrow 2\,CO + 2\,H_2 \ (1) \\ CH_4 &\longrightarrow C + 2\,H_2 \ (2) \\ 2\,CO &\longrightarrow C + CO_2 \ (3) \end{aligned} \tag{2.4}$$

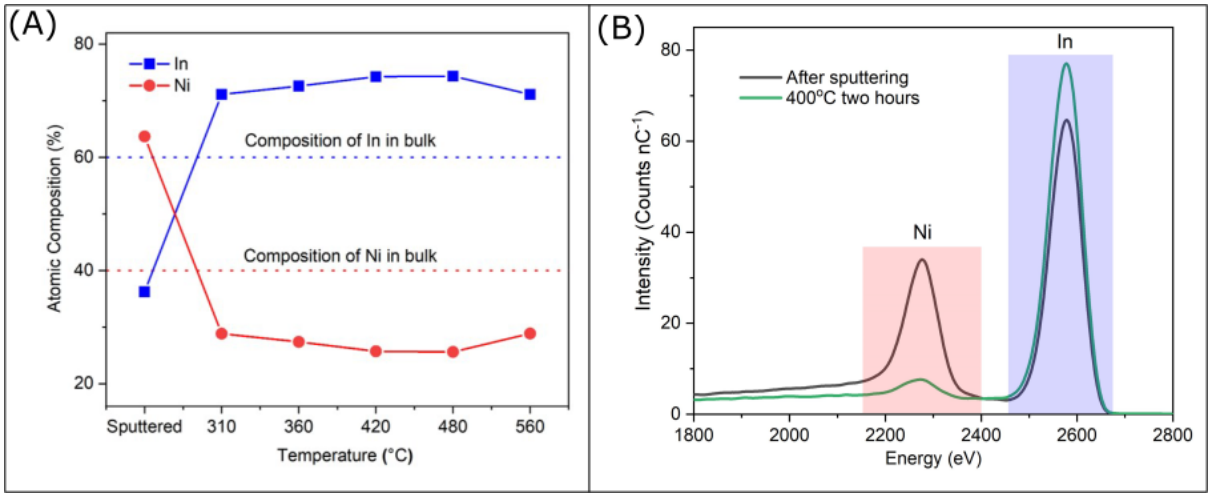

Figure 2.11: (A) Surface chemical composition of the In_3Ni_2 (001) surface after sputtering and annealing, recorded via XPS. (B) LEIS spectra recorded from the In_3Ni_2 (001) surface after sputtering and annealing at 400°C for two hours using a 3 keV He^+ beam. Both images adopted from [72].

To study the surface of InNi, a sample of In_3Ni_2 was grown using the Czochralski method [77] and cut into three samples along the (001), (100), and $(2\bar{1}0)$ surfaces. Each surface was prepared via Ar^+ sputtering and annealing, and then analysed using XPS, LEED, LEIS, and STM.

The surface chemical composition in Figure 2.11 (A) shows preferential sputtering of In from the surface, due to In's lower surface free energy compared to Ni [78]. Preferential sputtering of the heavier element is a surprising phenomenon, further explained in Section 3.2.4. After annealing at 310°C, the In content increases to approximately 71

Figure 2.11 (B) shows the Low Energy Ion Scattering (LEIS) results, probing the outermost atomic layer after sputtering and after annealing at 400°C for two hours. After sputtering, the Ni intensity increases significantly.

Following annealing, In intensity increases slightly, while the Ni intensity decreases sharply. These results corroborate the XPS findings, confirming preferential sputtering of In, followed by surface segregation of In upon annealing. Both results support the hypothesis that In's low surface free energy drives segregation.

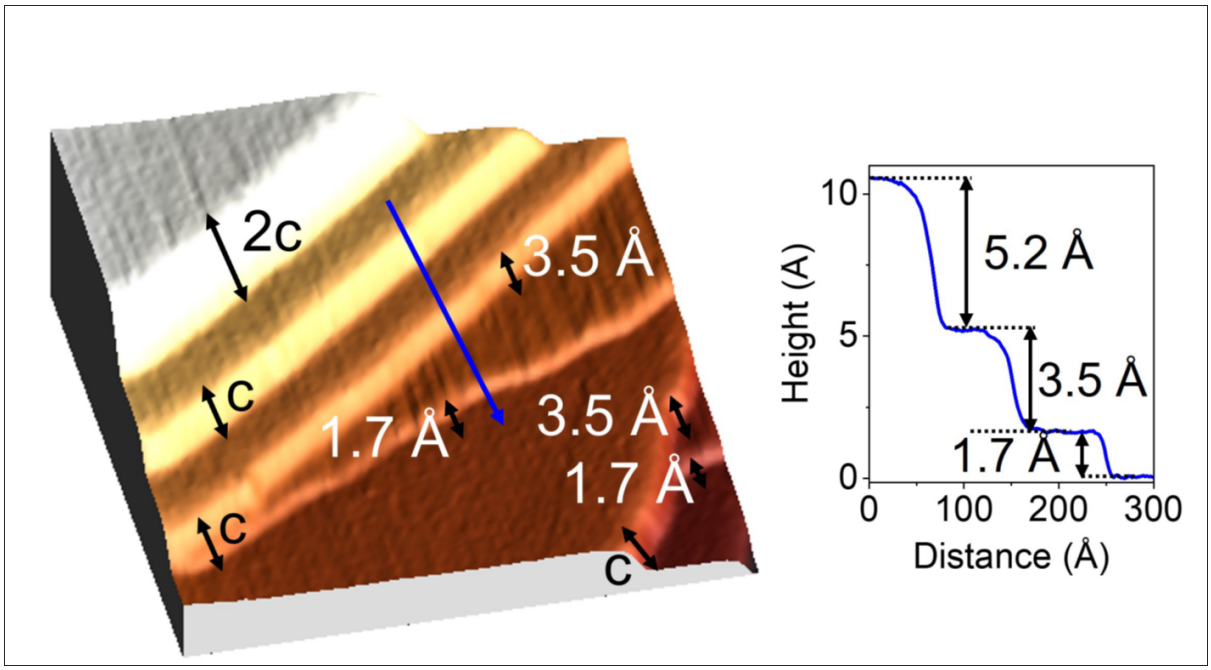

Figure 2.12: STM image of the clean In_3Ni_2 (001) surface after annealing at 550°C (400 Å × 400 Å, +0.866 V, 0.645 nA), showing step heights and a line scan along the blue line [72].

After annealing the In_3Ni_2 (001) surface to 560°C for 2 hours, large step terraces formed, as shown in Figure 2.12. In addition to the expected step height (5.3 Å), corresponding to the unit cell height, sub-steps were observed at 3.5 Å and 1.7 Å.

These sub-steps match the buckled planes 0 and 3 in Figure 2.10 (B), and are supported by surface energy calculations. This suggests that In is bonded with Ni at the surface, as observed in AlFe, which terminates on both elements [79], rather than on just one. A similar phenomenon is observed in ZnPd, where dual-element surface terminations are more stable than single-element ones [80].

The surface oxidation behaviour of InNi was studied by exposing the clean In_3Ni_2 (001) surface to incremental doses of pure O_2. As shown in Figure 2.13, both In and Ni form oxides upon oxygen exposure. At 900 L, a higher proportion of In had oxidised compared to Ni.

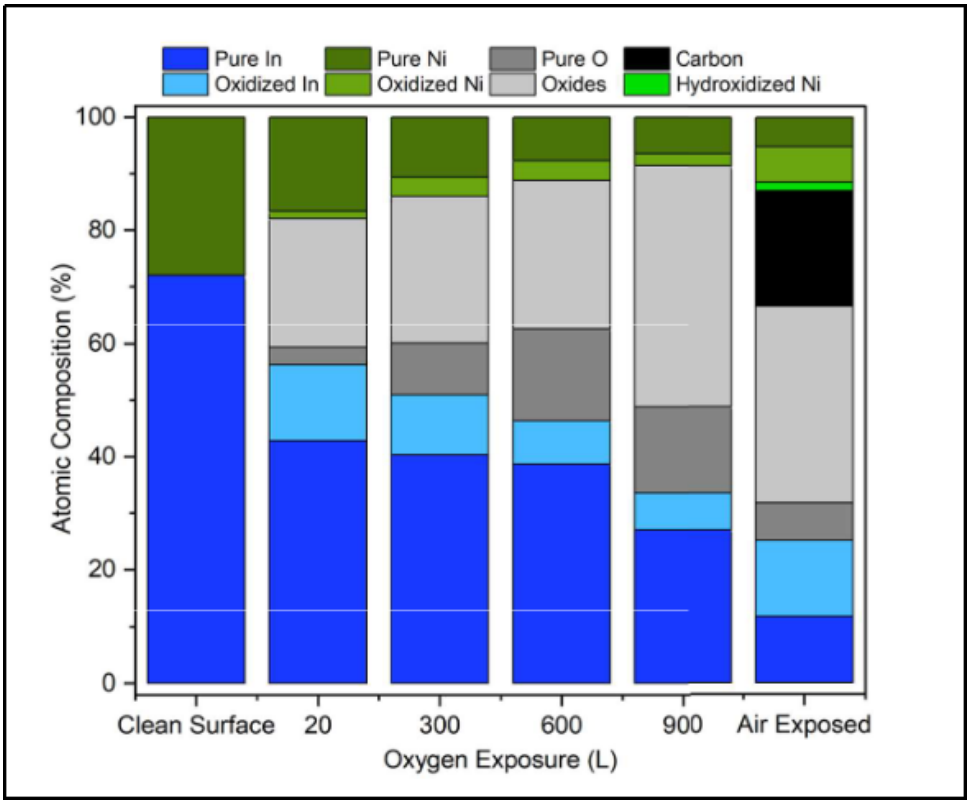

Figure 2.13: Surface chemical composition of the In_3Ni_2 (001) surface upon increasing exposure to O_2, measured via XPS. Adopted from [72].

This indicates that the (001) surface contains In. As O_2 exposure increases, the Ni signal decreases as oxidised In forms a surface layer, attenuating the Ni photoelectrons. Nevertheless, some Ni remains capable of oxidising, suggesting it is less reactive than Ga in Ga_3Ni_2, where Ga rapidly oxidises while Ni remains largely unaffected [10].

2.5.4 Summary of Prior GaNi Research

In nature, CO_2 can be reduced photochemically to store energy. This process has become a scientific challenge to replicate artificially. One method involves generating H_2 molecules, which can then be used to reduce CO_2 gas into liquid methanol [16], [81]. This would offer a sustainable method to convert a greenhouse gas into a liquid fuel source. Current industrial processes require the products to be produced in large facilities and kept under high pressure (around 100 bar), with no potential for miniaturisation unless a different catalyst is used in place of the current $Pt/Cu/ZnO/Al_2O_3$ system.

At lower pressure, more CO is produced, which poisons the currently used catalysts. Studies have determined that GaNi shows promise in the reduction of CO_2 at ambient pressure [81]. As mentioned, at ambient pressure, there is an increase in the quantity of CO produced, which is why GaNi was chosen as an intermetallic catalyst (IMC) for this reaction. Ni is resistant to coking and will not become poisoned by the increased CO concentration. By converting CO_2 into mostly methanol and water, both of which can be used as fuels for fuel cells, this reaction is of great interest to many industries [10], [30], [81].

$$\begin{aligned} H_2 + CO_2 &\longleftrightarrow CO + H_2O \ (1) \\ 4\,H_2 + CO_2 &\longleftrightarrow CH_4 + 2\,H_2O \ (2) \\ 3\,H_2 + CO_2 &\longleftrightarrow CH_3OH + H_2O \ (3) \end{aligned} \tag{2.5}$$

The fundamental hydrogenation reactions for CO_2 to produce methanol and water using a GaNi catalyst are shown in Equation 2.5.4 [30], [81]. Equation 2.5.4 (1) represents the reverse water-gas shift reaction, where the H_2 molecule begins to break down CO_2 into CO and water.

This reaction is not ideal, as the CO produced would poison the catalyst [82]. Equation 2.5.4 (2) is the methanation reaction, where CO_2 is decomposed into methane and water [30], [81]. Equation 2.5.4 (3) is the methanol synthesis reaction, where CO_2 is decomposed into water and methanol. This is the ideal reaction, as both products are usable as fuel sources while converting an abundant greenhouse gas [6], [10].

GaNi IMCs have attracted interest due to their high activity and selectivity for the hydrogenation of carbon dioxide into methanol, as shown in Equation 2.5.4. The phase diagram shown in Figure 2.14 (B) [83] presents multiple possible Ga and Ni combinations that can be grown. Initially, Ga_3Ni_5 was tested due to its high selectivity and catalytic activity [81]; however, it cannot be grown from a binary liquid phase [30]. There was one compound with the desired fixed stoichiometry for a catalyst, Ga_3Ni_2, which is in equilibrium with the binary Ga–Ni melt. For this reason, Ga_3Ni_2 was selected to be grown and used for subsequent experiments to study its catalytic activity.

Figure 2.14 (A) shows a single unit cell of Ga_3Ni_2. The Ga atoms are in green and the Ni atoms are in silver. Ga_3Ni_2 crystallizes into the Al_3Ni_2-type structure, exhibiting a trigonal structure with a $P\bar{3}m1$ space group and lattice parameters $a = 4.05$ Å and $c = 4.89$ Å [30]. From Figure 2.14 (A), it can be seen that the Ni atoms are bonded only to neighbouring Ga atoms, forming a tetragonal pyramid, thus isolating the Ni atoms. This trait is shared by Ga_3Ni_2, Al_3Ni_2, and In_3Ni_2. This isolation of the Ni atoms from neighbouring Ni atoms contributes to the selectivity of the Ga_3Ni_2 IMC for the hydrogenation of CO_2 into methanol.

The Ga_3Ni_2 crystals used in all experiments were grown using the Czochralski method with a Ga_3Ni_2 seed crystal [30], [84]. The resulting ingot was cut along high-symmetry planes and mechanically polished with diamond paste to produce an atomically flat surface with a mirror-like shine [30], [85], [86].

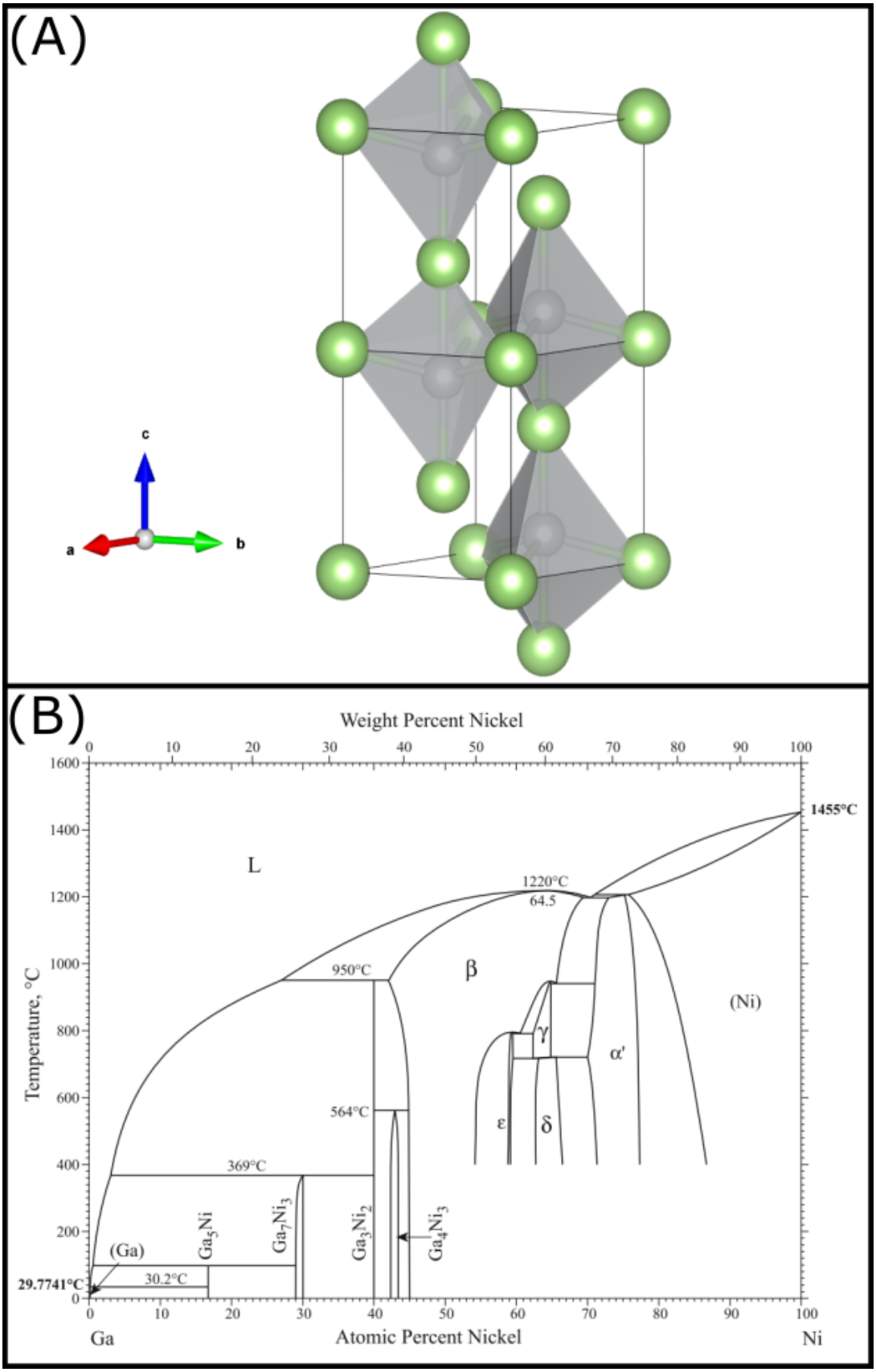

Figure 2.14: (A) Two unit cells of Ga_3Ni_2 showing the structural isolation of the Ni atoms (in silver) by a shell of Ga atoms (in green). (B) The phase diagram shows all of the possible GaNi phases [83].

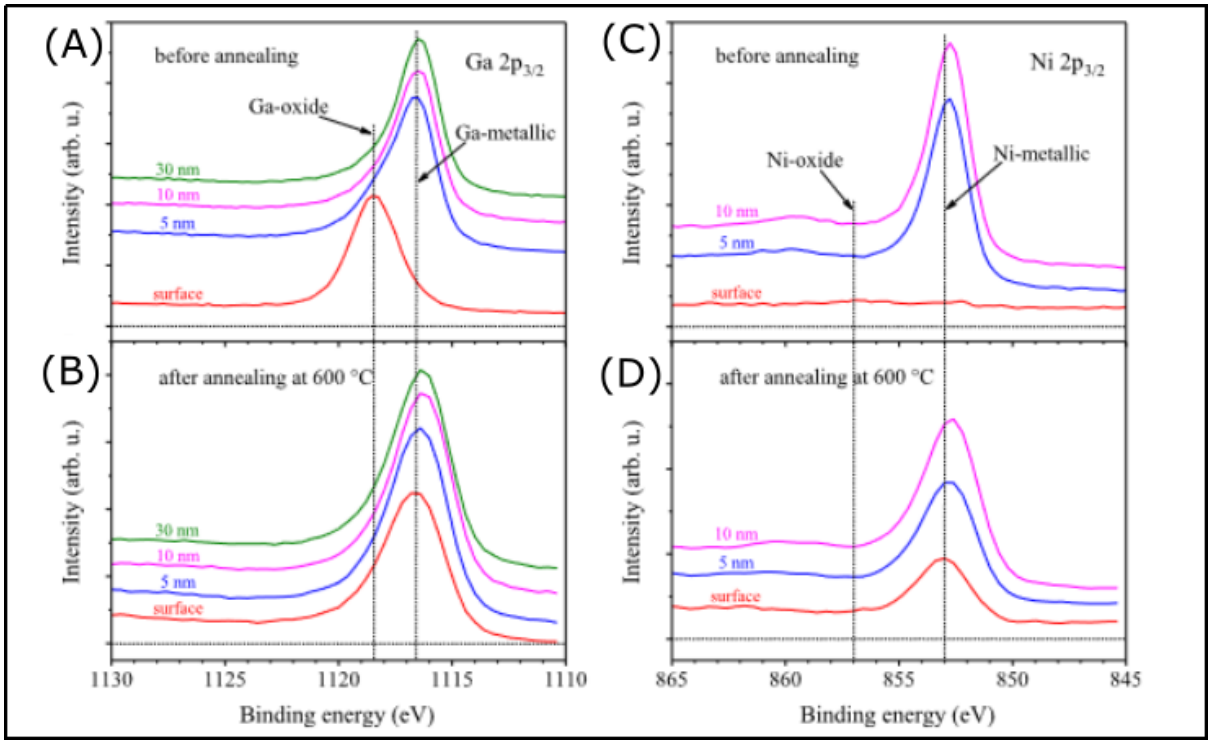

Figure 2.15: High-resolution XPS spectra showing several depths of the Ga $2p3/2$ peak after oxidation (A) and after annealing at 600°C (B). The corresponding Ni $2p3/2$ peaks after oxidation and annealing are shown in (C) and (D). Adopted from [10].

When a catalyst is used in industrial environments, it must be assumed that oxygen will be present. Understanding how oxygen affects the catalytic properties is crucial for determining whether a given intermetallic compound is suitable for industrial applications [10], [30]. The effect of surface oxidation on the catalytic properties of Ga_3Ni_2 was studied by exposing powdered Ga_3Ni_2 to pure O_2 [10].

Once the Ga_3Ni_2 powder was exposed to oxygen, the Ga present on the surface oxidised, and the surface composition showed a distinct shift in the binding energy, as seen in Figure 2.15 (A), which was also observed in Figure 2.8 (B) with Ga oxidation. The Ni peak was not discernible from the background (Figure 2.15 (B)), indicating that the Ga oxide (likely Ga_2O_3) had formed on the surface, as Ga_2O_3 is the most common Ga oxide [87].

The subsurface showed the presence of intermetallic Ga and Ni, further confirming that the Ga oxide is confined to the topmost surface layer and that O_2 had not reached the subsurface. After annealing at 600°C, the oxide peaks were no longer visible (Figures 2.15 (C) and (D)), indicating that the oxides had evaporated.

The effect of annealing the Ga_3Ni_2 catalyst to 600°C increased the amount of CO_2 converted into methanol while maintaining higher selectivity. This suggests that the Ga oxide layer affects the catalytic properties, as the Ni on the surface is covered by the oxide, but the Ga oxides can be removed by annealing at a sufficiently high temperature.

There are no prior surface science studies that have been carried out on GaNi intermetallic compounds. The results of this thesis will help build upon existing GaNi research to improve our understanding of these intermetallic surfaces and develop insights into their catalytic properties.

Chapter 4 covers how the surface chemical composition of three Ga_3Ni_2 surfaces is affected by sputtering, annealing, and scanning angle, providing insight into the topmost layer composition and how preparation conditions could influence catalytic activity.

Chapter 5 presents LEED and STM results from all three Ga_3Ni_2 surfaces. Using LEED, surface reconstructions can be observed, along with the conditions (annealing temperature and/or time) that induce them. Wide-scan STM images are used to determine step heights on large terraces, identifying if the surface is terminated on bonded Ga–Ni planes similar to In_3Ni_2. Atomic-resolution results will show surface features and the surface unit cell, which are important to record, as the surface is the interface for catalytic activity [88].

Chapter 6 discusses how the atomic composition of the Ga_3Ni_2 (001) surface changes upon exposure to pure O_2, confirming results from powdered Ga_3Ni_2 studies [10] and contrasting them with In_3Ni_2 to observe how the change in the secondary element affects oxide formation. Since many industrial catalysts operate in oxygen-rich environments, recording how the surface oxidises and at what exposure levels is critical.

Chapter 3

Experimental Methods

3.1 Introduction

In this chapter, the experimental methods used to measure and characterise the surfaces of the three orientations of the Ga_3Ni_2 binary alloy are described.

Firstly, I will present an explanation of Ultra High Vacuum (UHV) chambers, the necessity of such an environment, the processes required to achieve UHV, the types of pumps needed to reach and maintain UHV, and the additional attachments to the chamber that are used in research.

Secondly, each of the surface analysis techniques will be discussed, from the theoretical background to the experimental setup used in this thesis, culminating in a discussion about peak fitting in the XPS software, including how we identified, isolated, and fitted all of the peaks from the XPS and UPS results presented in the corresponding chapters.

3.2 Ultra High Vacuum

An ultra-high vacuum is broadly defined as an environment with a pressure below approximately 10^{-9} mbar. Table 3.1 shows the pressure ranges for each type of vacuum. Such an extreme environment is required in surface physics to characterise the surface of a solid sample. By reducing the pressure inside the chamber to such a low range, we minimise the rate at which surface contamination occurs, as demonstrated by the time taken to contaminate a surface with one monolayer of adsorbates.

$$T = \frac{3 \times 10^{-6} \times S}{P} \tag{3.1}$$

Where T is the time taken in seconds for one monolayer to adsorb, S is the sticking coefficient treated as 1, assuming each O_2 molecule adheres to the surface, and P is the pressure in mbar in Equation 3.1.

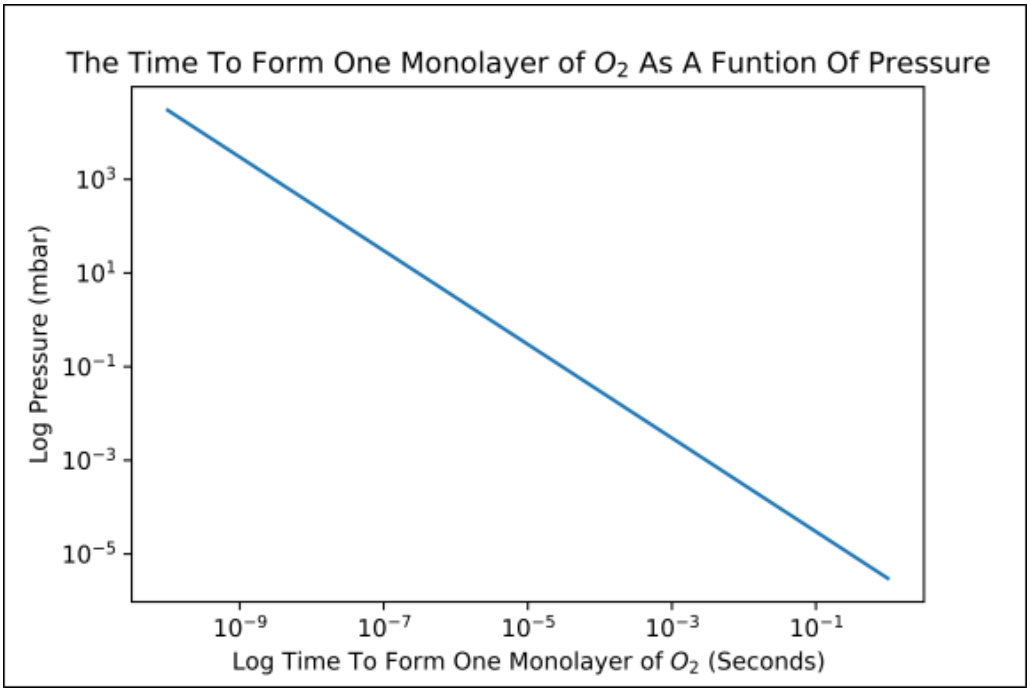

Figure 3.1: How altering the pressure affects the time to form one monolayer in Equation 3.1, where the sticking coefficient (S) is treated as 1.

Figure 3.1 shows how increasing the pressure directly affects the time taken to form one monolayer, as given in Equation 3.1. The pressure begins at 1×10^{-10} mbar, which corresponds to an ultra-high vacuum pressure (see Table 3.2), where the time to form one monolayer is approximately 30,000 seconds (8.3 hours). Increasing the pressure causes the time to form one monolayer to decrease exponentially, dropping to 3,000 seconds (0.83 hours). This further decreases to 300 seconds (0.08 hours) at 1×10^{-8} mbar, which is the upper limit of the ultra-high vacuum range.

This illustrates why maintaining extremely low pressures is vital for creating an environment in which surface contamination is delayed, which is essential for STM, LEED, and XPS research, where the goal is to observe the surface structure of the samples. Figure 3.1 highlights that even within the UHV range, the contamination time is significantly affected by small pressure changes, so achieving the lowest feasible pressure is always the objective. Outside the UHV range, monolayer formation occurs so rapidly that conducting any meaningful surface analysis becomes virtually impossible.

Low Vacuum	Atmospheric pressure to 1 mbar
Medium Vacuum	1 to 1×10^{-3} mbar
High Vacuum	1×10^{-3} to 1×10^{-8} mbar
Ultra High Vacuum	1×10^{-8} to 1×10^{-12} mbar
Extreme High Vacuum	Less than 1×10^{-12} mbar

Table 3.1: Classification of the levels of vacuum. Adapted from [89].

In addition to reducing the rate of surface contamination, lowering the pressure in the chamber increases the mean free path of an electron, λ, as shown in Equation 3.2. Since Low Energy Electron Diffraction (LEED), X-ray Photoelectron Spectroscopy (XPS), Ultraviolet Photoelectron Spectroscopy (UPS), and Scanning Tunnelling Microscopy (STM) all rely on the emission of electrons, a UHV environment is required. The mean free path, λ, can be calculated using Equation 3.2, where k_B is the Boltzmann constant, T is the temperature, d is the molecular diameter, and P is the pressure in mbar:

$$\lambda = \frac{k_B T}{\sqrt{2}\pi d^{\,2}\, P} \tag{3.2}$$

3.2.1 Vacuum Pumps

In this section, the core components that comprise a UHV setup will be discussed. A general overview of the steps required to reach the UHV range from atmospheric pressure will be provided. The systems within the UHV chamber used for data acquisition will then be described. Figure 3.2 shows a UHV chamber with all components labelled.

To reach UHV pressures, a sealed chamber designed to achieve and maintain such low pressures is required. Additionally, the chamber must be made from a material that can withstand the temperatures reached during the bakeout process, discussed later in this section, and must exhibit low outgassing properties. The main chamber is typically made from stainless steel, as it meets all of these requirements. Components are attached to the main chamber via flanges secured with a ring of bolts. The flanges are sealed using a copper gasket, where a knife edge on each flange cuts into the gasket when tightened, forming a highly secure seal.

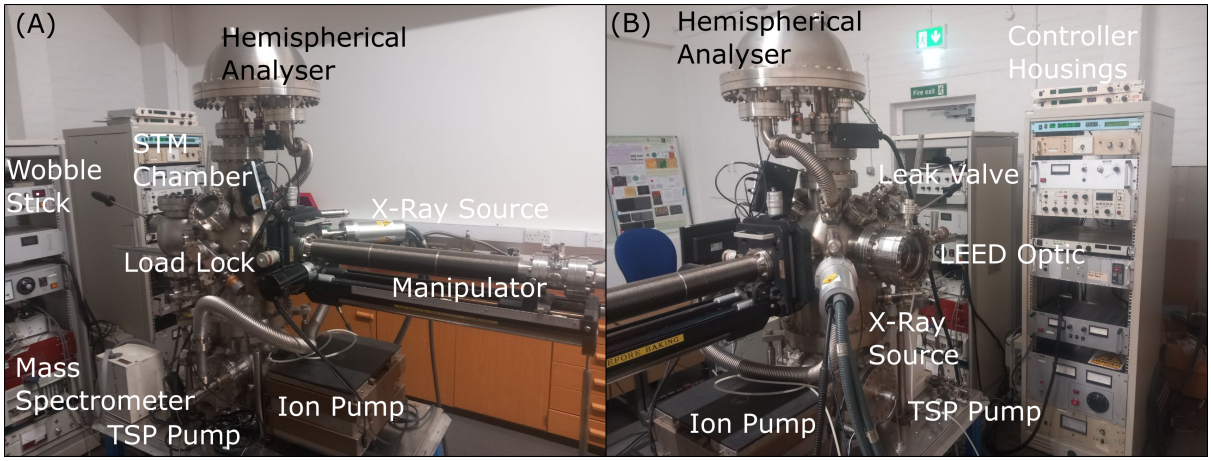

Figure 3.2: The UHV chamber used for all of the experiments at the University of Liverpool. Each key part is labelled with (A) being the front side of the detector and (B) being the rear side.

Attached to the main chamber is a large manipulator, which can move the sample across the entire chamber and adjust its angle for LEED, XPS, and transfer to the STM chamber. Transferring the sample from the manipulator to the STM chamber is done via the wobble stick, which can pick up the sample plates and either place them into the STM housing or a carousel for internal storage. The load lock is attached to a tube where samples can be loaded into the chamber. Depressurising a smaller volume is safer and more efficient than depressurising the entire chamber to insert or remove a sample.

A sapphire-seated leak valve is used to introduce gases from an external source—typically Ar^+ for sputtering or O_2 for dosing—in a controlled manner. The Ar^+ inlet valve is connected to a rotary pump to expel any Ar^+ and other contaminants from the polythene tubes. The hemispherical analyser and X-ray source were added to enable XPS studies within this UHV chamber. The analyser channels the emitted photoelectrons from the surface to the detector, as shown in Figure 3.2(B). The X-ray source is water-cooled to prevent overheating, which could damage both the source and the associated electronics.

Pumps

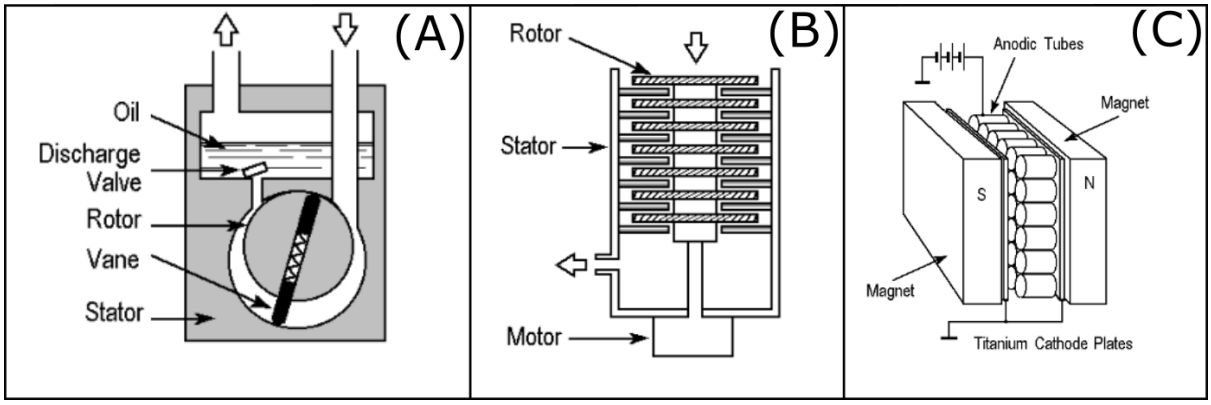

Figure 3.3: A diagram of (A) a rotary vane pump, (B) a turbo molecular pump and (C) an ion pump. Reproduced from [90].

To reduce the pressure from atmospheric levels to the ultra-high vacuum (UHV) range, a series of pumps must be operated in sequence. The initial pump used to bring the UHV chamber from atmospheric pressure down to a rough vacuum of approximately 1×10^{-3} mbar is a rotary vane pump. This is a mechanical compression pump consisting of a circular rotor offset within a larger circular cavity. This design creates a periodic change in volume at both the inlet and outlet, facilitating the removal of gases from the chamber. Figure 3.3(A) shows a diagram of the rotary vane pump, where gas enters the inlet and is compressed as it is pushed along. Upon reaching the outlet valve, the gas exits the system, typically via an oil reservoir.

To transition from a rough vacuum to an ultra-high vacuum environment (1×10^{-3} to 1×10^{-9} mbar), a turbomolecular pump is employed. Using a series of angled fan blades rotating at high speed, the pump imparts kinetic energy to gas molecules, pushing them further through the pump until they are expelled through the outlet. Turbomolecular pumps typically operate between 1×10^{-3} and 1×10^{-10} mbar, so a partial vacuum is required before they can be used. Figure 3.3(B) shows a diagram of the turbomolecular pump.

An ion pump is also used to attain and maintain UHV pressures. It consists of two titanium cathode plates surrounded by an array of tubular anodes. When a high voltage is applied, the resulting electric discharge ionises residual gas molecules in the chamber, which are then attracted to the cathode.

A magnetic field is applied at right angles to the cathode plates, causing the electrons to follow a helical path. This increases the rate of ionisation, allowing more of the remaining gas molecules to be captured on the cathode plates. Ion pumps must operate at low pressures, so they can only be used once a turbomolecular pump is already in operation. Figure 3.3(C) shows a schematic of an ion pump.

The final pump used is a titanium sublimation pump, which coats the walls of the UHV chamber with a thin layer of titanium. Any gas molecules adhering to the chamber walls are chemisorbed by the titanium and retained as stable compounds. The pumps described above are those used in the UHV chambers for this thesis. Other configurations can also be employed to reach UHV pressures.

3.2.2 Bakeout Procedure

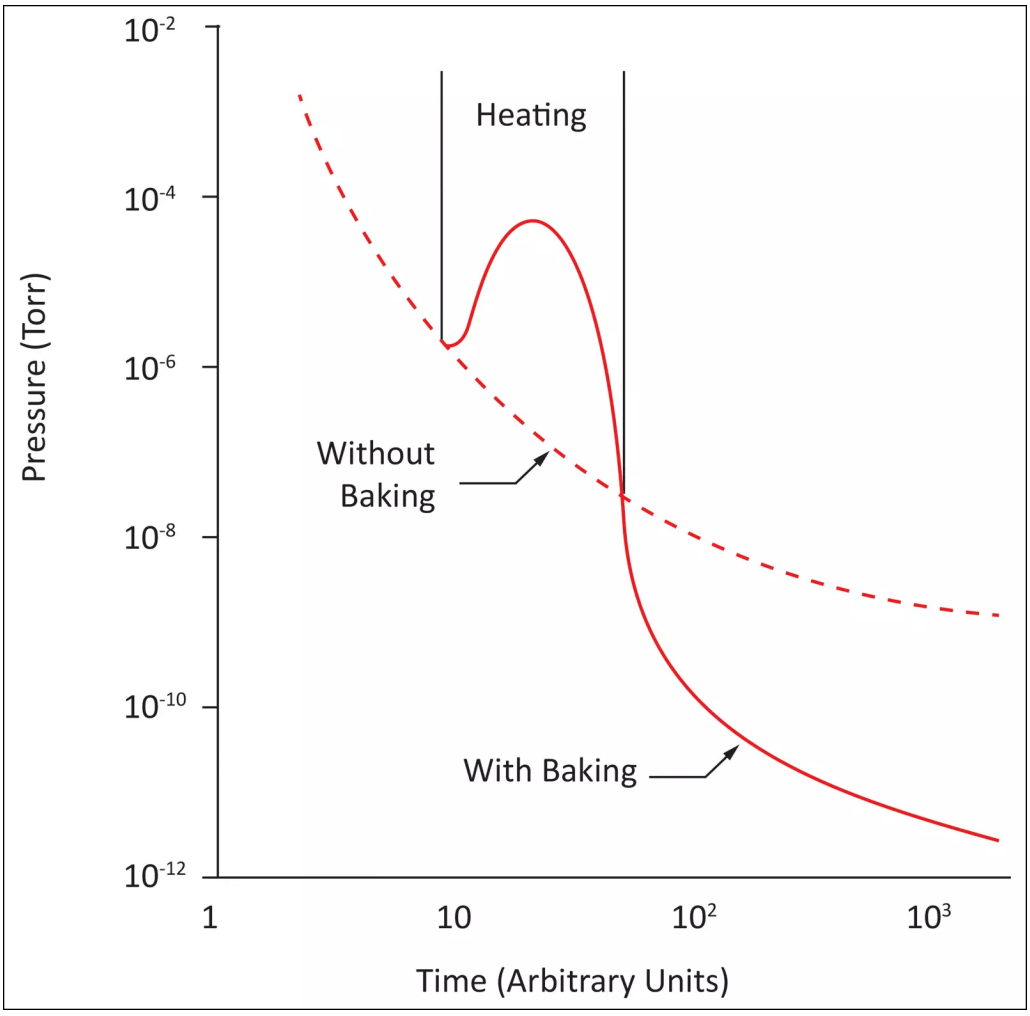

Figure 3.4: A graph showing the effect a bakeout has on the pressure in a chamber over time [91].

To begin the process of attaining UHV, the chamber is first evacuated using a rotary vane pump to reach the low vacuum range. The turbomolecular pump is then engaged to bring the chamber down to the medium vacuum range (Table 3.1). A bakeout procedure is also performed while the turbomolecular pump is running. This involves heating the entire chamber to between 120°C and 200°C using ceramic heaters and insulating panels that cover the chamber for over 12 hours. This accelerates the desorption of water molecules from the internal walls of the chamber (Figure 3.4). Instruments connected to the chamber are operated under normal conditions during the bakeout to degas them and remove any adsorbed gases. After more than 12 hours of baking, and once each instrument has degassed, the chamber should be under UHV conditions, which is confirmed using an ionisation gauge.

3.2.3 Pressure Measurement

Pressure management is vital for maintaining any vacuum environment, as even a small leak can raise the pressure above the UHV threshold. For pressures in the low vacuum range, Pirani gauges are used to monitor the backing pressures for the rotary and turbomolecular pumps. Pirani gauges work by detecting changes in the temperature of a filament within the vacuum region. This is typically done by measuring the change in resistance of the filament, from which the corresponding pressure in mbar can be determined.

In higher vacuum regions, ionisation gauges are used. The ionisation gauges in the UHV chamber (Figure 3.2) consist of a cathode filament, an anode, and an ion collector. The filament is heated, causing the thermal emission of electrons, which are accelerated towards the anode due to the potential difference. These electrons ionise any gas particles they encounter. The resulting ions are collected, and the current produced is used to infer the density of gas particles and the pressure within the chamber.

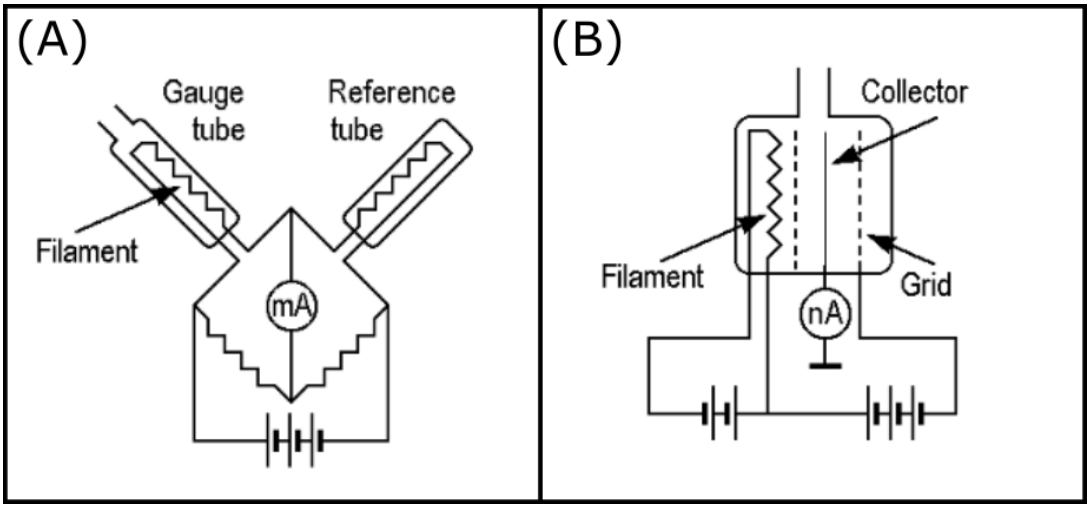

Figure 3.5: A diagram of (A) Pirani gauge and (B) an ionisation gauge. Reproduced from [90].

3.2.4 Surface Preparation

This section will cover how each of the three samples was prepared before and after being placed into the UHV chamber.

Ex-situ Preparation

The sample was grown via the Czochralski method by Dr. Peter Gille at Ludwig-Maximilians-Universität München. Once the crystal had cooled to room temperature, it was cut along the (001), (100), and $(2\bar{1}0)$ planes using a 50 μm thick tungsten wire with boron carbide powder (800 mesh) in a glycerol suspension [30]. The orientations of the crystals were confirmed using Laue backscattering. After cutting, each surface was mechanically polished using diamond grit paste of decreasing grain sizes down to 0.25 μm. Any remaining paste was removed by washing the sample in methanol using an ultrasonic bath.

In-situ Preparation

Once a sample was introduced into the UHV chamber via the load lock, it underwent in-situ preparation through multiple cycles of sputtering and annealing. Sputtering involves bombarding the surface with charged noble gas ions (Ar^+ was used for all experiments in this thesis) to remove surface contaminants (Figure 3.6).

Argon gas was introduced into the UHV chamber through a leak valve to a pressure of 2.5×10^{-5} mbar. An ion gun heats a filament to emit electrons toward an anode, ionising the Ar gas. The Ar^+ ions are then accelerated toward the sample using a negatively biased grid, where they impact the surface, removing contaminants and some sample material. This bombardment causes the surface structure to deteriorate, as seen in Figure 3.6 (A), since the Ar^+ ions effectively sandblast the surface. Annealing is required to allow the sample to regain a flat, ordered surface. The sample is grounded during sputtering to prevent charge buildup.

Figure 3.6 (A) shows some of the bulk material being removed from the surface during sputtering. If the Ar^+ ions have sufficient kinetic energy, they can eject atoms from the surface of the sample. Three factors are key to understanding whether specific elements are preferentially sputtered from the surface [92], [93]. These are atomic weight, surface free energy, and bonding strength.

Lighter elements require less energy to sputter than heavier elements. Elements with low surface free energy tend to segregate to the surface and are more easily removed during sputtering. Finally, the higher the bonding energy between atoms, the greater the energy required to remove that element from the surface.

For intermetallic compounds, which are composed of two or more elements, these three factors determine which element is preferentially sputtered. It has been previously reported that heavier elements with lower surface free energy can be preferentially sputtered. For example, In is preferentially sputtered from the surface of In_3Ni_2 [72]; In is heavier than Ni but has a lower surface free energy. Similarly, the heavier elements In and Yb are preferentially sputtered from the surface of the quasicrystal Ag-In-Yb, due to their lower surface free energy compared to Ag [94].

Annealing involves heating the sample to a desired temperature for a specific period. A general guideline is to anneal at a maximum of approximately two-thirds of the bulk melting temperature in kelvin. This limit is used because, compared to the bulk, surface atoms have lower coordination numbers, meaning less energy is required to induce surface melting. Annealing is typically performed using a resistive heating element, usually a ceramic component, where the temperature is controlled by adjusting the input current and voltage via a high-voltage power supply.

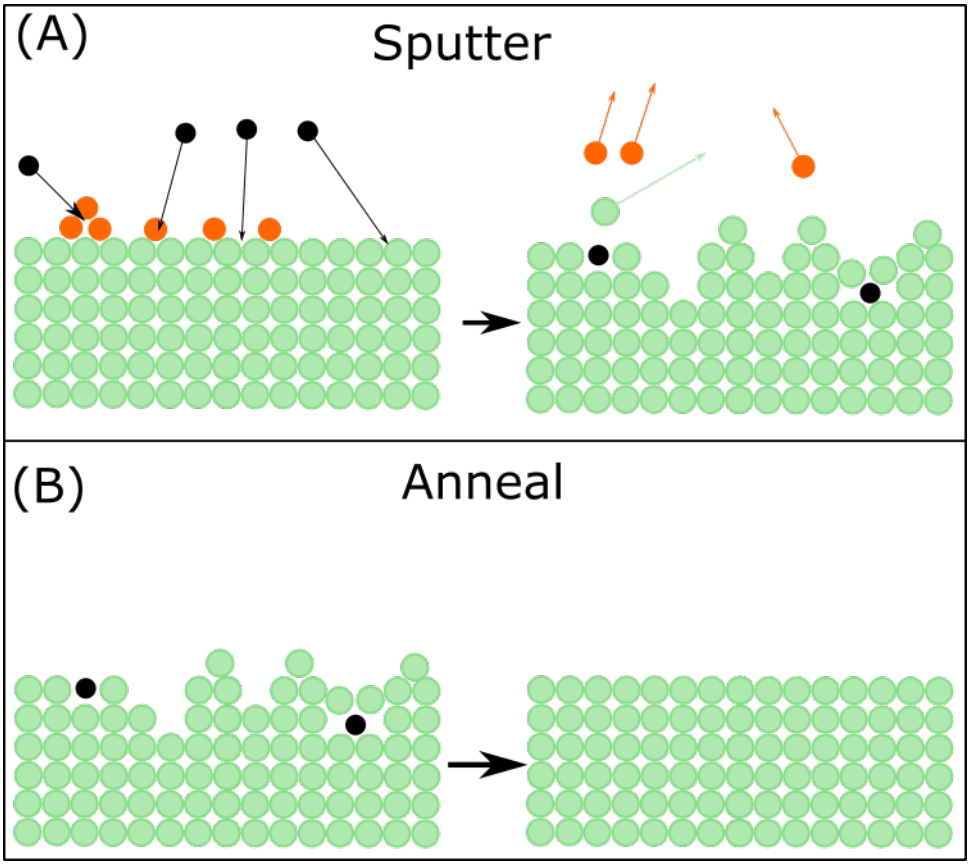

Figure 3.6: (A) The effects of Ar^+ sputtering, the green atoms are the bulk materials with orange circles to represent contamination on the surface. Black Ar^+ atoms are fired at the surface to remove the contamination. (B) The effects of annealing the sputtered surface. By heating the sputtered surface, the roughness caused by the Ar^+ sputtering is corrected back to an atomically flat surface with any Ar atoms embedded into the surface desorbed.

If the resistive heating element is insufficient to reach the desired temperature, electron bombardment can be employed to further increase the sample's temperature. Electron bombardment involves using an electron gun to direct electrons toward the back of the sample plate [95]. These electrons transfer their energy to the sample in the form of heat.

Annealing not only aids in the removal of any Ar^+ ions that may have adsorbed onto the surface, but it is also essential after sputtering to promote the diffusion of atoms to the surface. This restores the surface stoichiometry and atomic order, resulting in a clean and atomically flat surface—an ideal condition for surface studies.

3.3 Surface Analysis Techniques

In this section, we will discuss each of the surface analysis techniques used in this thesis: low energy electron diffraction (LEED), X-ray photoelectron spectroscopy (XPS), ultraviolet photoelectron spectroscopy (UPS), and scanning tunnelling microscopy (STM), including the theory behind each technique and the experimental equipment used.

3.3.1 Low Energy Electron Diffraction (LEED)

History

Low Energy Electron Diffraction is the oldest diffraction technique by which the surface symmetry of a crystalline material can be directly observed on a phosphorescent screen. The origin of LEED as a diffraction technique can be traced back to the Davisson–Germer experiment conducted between 1923 and 1928.

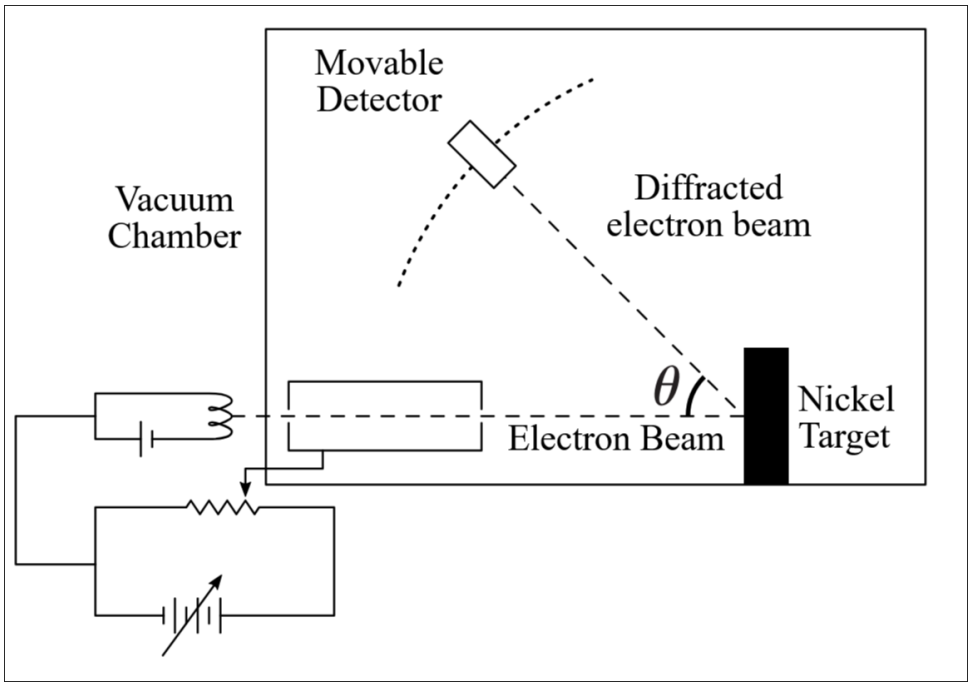

Figure 3.7: A model of the Davisson-Germer Experiment. The entire experiment is housed in a vacuum chamber to ensure that the emitted electrons could diffract from the Ni target [96].

The Davisson–Germer experiment was a series of experiments in which a narrow beam of electrons was first directed at a single crystal of nickel held normal to the electron gun [96].

A movable detector was used to detect the scattered electrons from the target. It was discovered that at certain angles, there was a peak in the number of electrons recorded, as well as troughs, suggesting the electrons exhibited wave-like behaviour as proposed by Louis de Broglie. This discovery of electron diffraction, confirmed through Bragg's law, experimentally observed de Broglie's hypothesis of wave-particle duality.

Physical Principle

Diffraction techniques utilise the elastic scattering of particles/waves to probe the surface structure of a crystal [97]. After interacting with the sample, the scattered waves interfere constructively and destructively, forming maxima and minima.

Low-energy electron diffraction uses 10 - 200 eV electrons to probe the surface structure. The intensity and distribution of the diffracted beams contain information about the atomic arrangement and spatial distribution of the sample. A diffraction pattern is related to the reciprocal lattice of the sample:

$$K - K_0 = G_{hkl} \tag{3.3}$$

where K is the scattered wave vector, K_0 is the incident wave vector, and G_{hkl} is the reciprocal lattice vector. Since the scattering is elastic, $|K| = |K_0| = (2\pi/\lambda)$, as conservation of energy is applied. G_{hkl} is the reciprocal lattice vector defined by:

$$G_{hkl} = hA + kB + lC \tag{3.4}$$

where h, k, and l are the Miller indices, and A, B, and C are the reciprocal lattice vectors of the real-space lattice vectors a, b, and c. The real-space and reciprocal-space lattice vectors are related by:

$$A = \frac{2\pi b \times c}{a \cdot (b \times c)} \quad B = \frac{2\pi c \times a}{b \cdot (c \times a)} \quad C = \frac{2\pi a \times b}{c \cdot (a \times b)} \tag{3.5}$$

Ewald Sphere

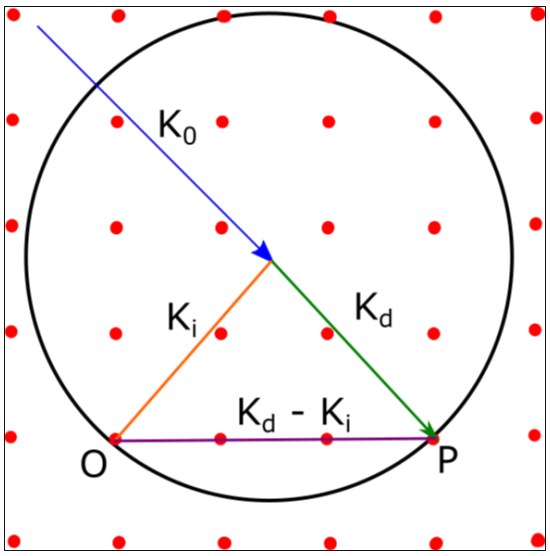

Figure 3.8: A model of a 2D Ewald sphere showing for an incident vector K_0 how a reciprocal lattice is constructed with the diffracted waves K_i and K_d with the red points that intersect the circle, *O* and *P*.

An Ewald construction is typically used to model the diffraction process observed through LEED. For a 2D Ewald sphere, the reciprocal lattice points are considered perpendicular to the surface because there is infinite periodicity along that direction, denoted by the series of red points in Figure 3.8. Any red points that intersect the circle, the size of which is determined by the incident K_0 vector, will result in a diffracted wave. These diffracted waves would be visible as bright spots on the LEED optic.

By increasing the size of the Ewald sphere, through increasing the incident wave vector (beam energy), more points will intersect with the circle and be visible, which can be confirmed from higher beam energy LEED images, which show additional spots.

Inelastic Mean Free Path

The inelastic mean free path is the average distance an electron can travel through a given medium before losing energy. For an electron, the inelastic mean free path (IMFP) can be modelled using a universal curve shown in Figure 3.9 [98]. As the electron energy increases, the IMFP decreases until it reaches a minimum, after which the IMFP increases in a linear relationship with electron energy:

$$\lambda = \frac{143}{E^2} + 0.054 \times \sqrt{E} \tag{3.6}$$

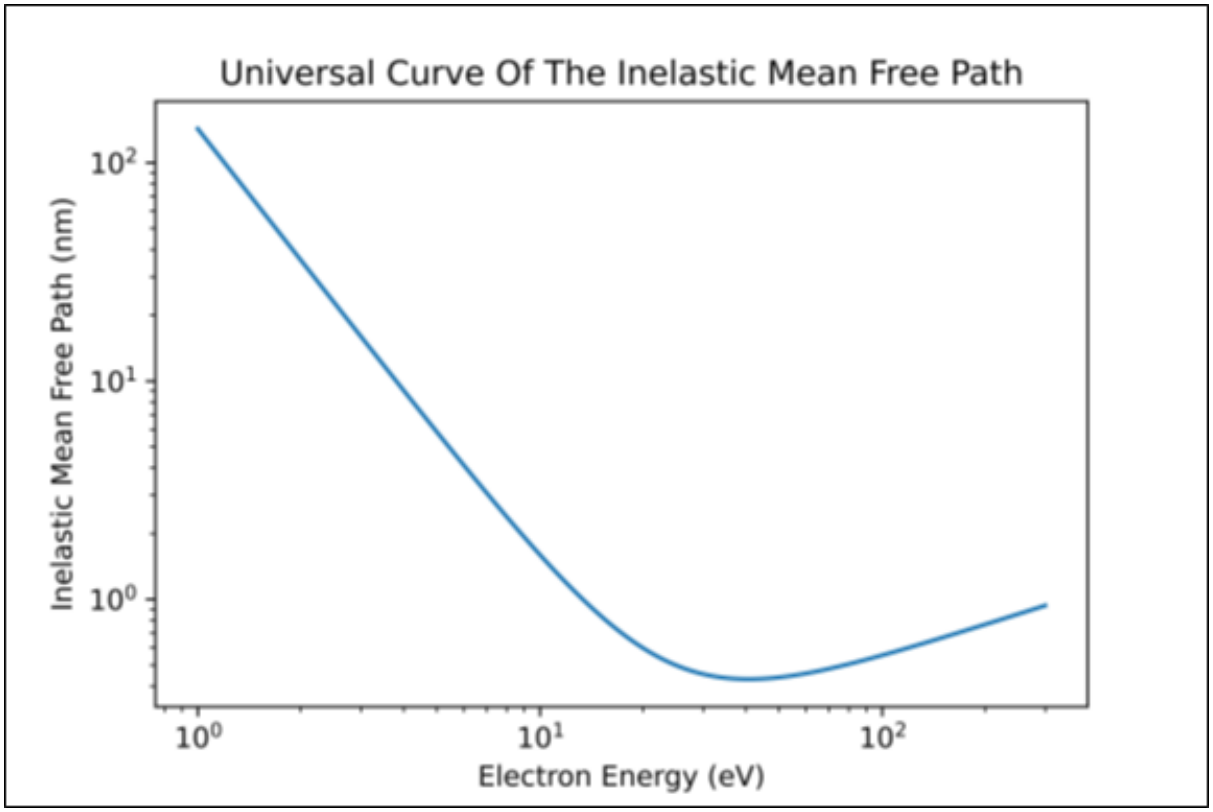

Figure 3.9: A Universal Curve showing how the electron energy affects the Inelastic Mean free path. The equation used is modified from [98] equation [5].

Here, E is the electron energy and λ is the inelastic mean free path [98]. At the lowest energy, the electrons are not probing the topmost layer of any material. For Ga_3Ni_2, a range of 1 - 200 eV was chosen. This range covers the surface sensitive range (40 - 100 eV) to far into the bulk, 120+ eV.

Equation 3.6 is a modified version of Equation [5] from Quantitative electron spectroscopy of surfaces: A standard database for electron inelastic mean free paths in solids [98] where the terms A_i and B_i were substituted for values that would apply to a vacuum environment given in Table 3.1.

Experimental Set-Up

Figure 3.10 (A) shows a schematic of a LEED setup. An electron gun generates electrons by heating the cathode filament, which is used in Chapter 5. The electrons pass through a Wehnelt cylinder to focus them, then through several lenses, which accelerate the electrons through potential differences. After being emitted, the accelerated electrons impinge on the surface and backscatter towards the hemispherical fluorescent screen and a series of grids.

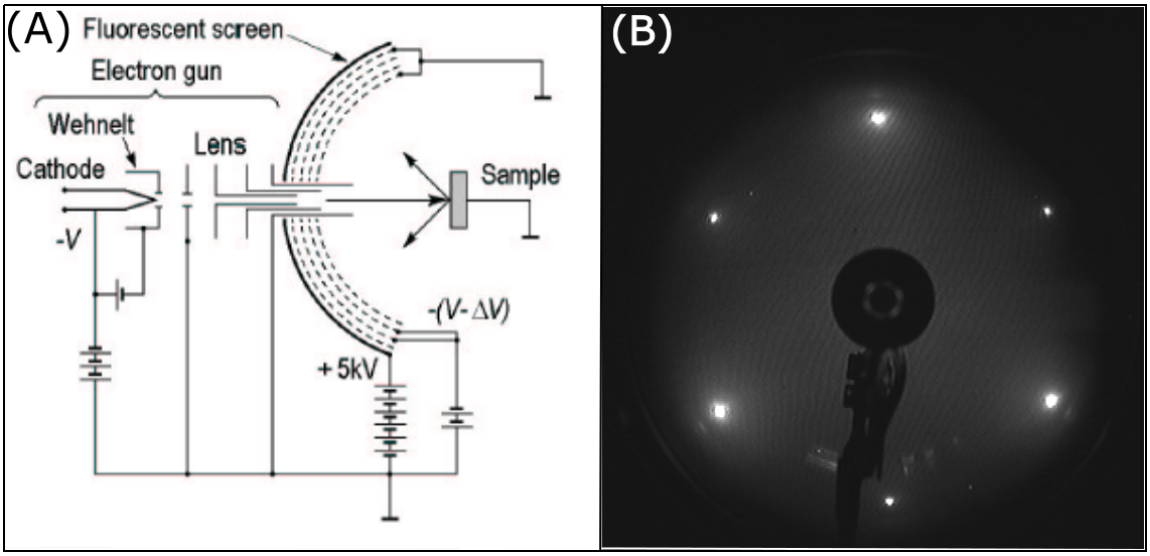

Figure 3.10: A schematic of a LEED set-up (A) and a (1×1) LEED image from Al(111) (B). (A) is from [90].

The first grid is grounded to remove any field between the sample and the grid, ensuring the electron path in the region is unaffected. The second and third grids use negative potential differences to suppress the inelastic backscattered electrons. The final grid accelerates the remaining electrons towards the screen to cause fluorescence. Each grid can have its input voltage altered to adjust the contrast of the LEED screen to ensure the best images. This setup ensures that only elastically scattered electrons are observed on the fluorescent screen, which represents the surface symmetry of the sample in reciprocal space.

In addition to the reciprocal lattice information LEED images provide, we can also obtain the geometrical arrangement of the diffraction spots and infer information from the sharpness and brightness of the spots in the LEED images and the presence of background noise. A clean and well-ordered surface will display sharp points on the LEED optic with minimal background (Figure 3.10 (B)). If the Bragg peaks are broadening with an increase in the background, this would suggest the surface is rough and there may be defects or contaminants affecting the surface order.

If no peaks are observed, it means the surface is disordered. LEED can, and often is, used to monitor the surface preparation process, typically after cycles of sputtering and annealing or material deposition on the surface. LEED can also indicate reconstruction on the surface of a sample by the presence of additional spots.

3.3.2 Scanning Tunnelling Microscopy (STM)

History

Scanning Tunnelling Microscopy (STM) was invented by Dr. Gerd Binnig and Dr. Heinrich Rohrer in 1981 at IBM Zurich [99], and they were awarded the Nobel Prize in Physics in 1986 for this discovery. Using a sharp tip close to the surface of the sample, information regarding the structural features and topography of the surface can be recorded. STM utilises the quantum tunnelling effect, as the tip is brought to within 5 - 10 Å of the surface, and the wave functions from the atom at the point of the tip and the atoms on the surface will overlap.

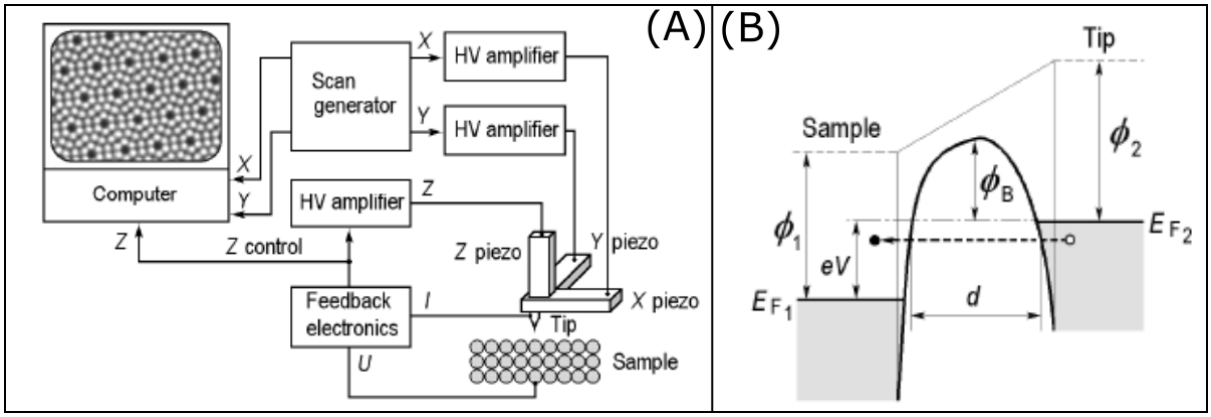

Figure 3.11: (A) a schematic model of an STM set-up and (B) an energy diagram showing the quantum mechanical tunnelling of the STM tip to the surface. E_{F_1} and E_{F_2} are the Fermi energies of the surface and tip, respectively. ϕ_1 and ϕ_2 are the work functions of both the sample and tip, V is the bias voltage, d is the tunnelling gap and ϕ_b is the effective barrier height. Taken from [90].

Quantum mechanical tunnelling occurs when a particle passes through a potential energy barrier that is larger than the total energy of the particle [100]. A property of matter having wavelike properties means there is a possibility of it existing outside of the potential energy barrier, allowing the particle to tunnel through the energy barrier without going over, as classical physics would require, as shown in Figure 3.12. As mentioned previously, quantum tunnelling is vital for STM to function, as the electrons tunnel from the tip to the surface, or from the surface to the tip. The tunnelling current can be measured, or the z-axis position of the tip can be adjusted to produce an image of the surface at an atomic level.

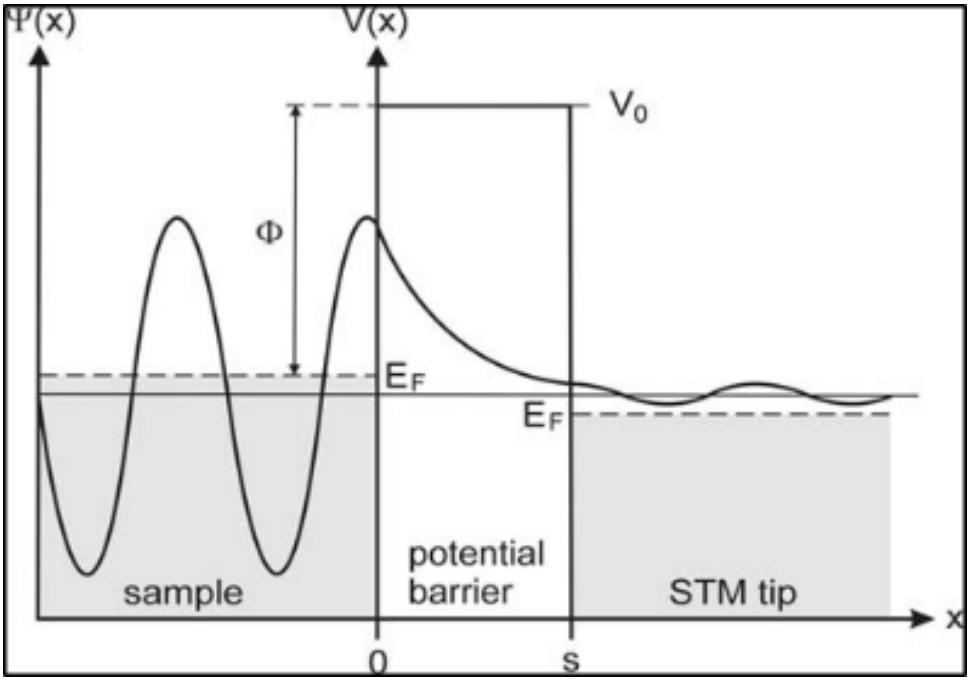

Figure 3.12: A model showing quantum mechanical tunnelling where a particle can transfer through a potential barrier from the sample to an STM tip. Image was adapted from [101].

Physical Principle

By applying a bias voltage between the surface and the tip, we allow electrons to tunnel across the gap between the tip and surface. A negative bias voltage applied to the tip causes electrons to tunnel from the tip to the surface, probing the unoccupied states, while a positive bias voltage applied to the tip causes electrons to tunnel from the surface to the tip, probing the occupied states. The tunnelling current is given by:

$$j = \frac{D(V)V}{d} \times exp(-A{\phi_\mathrm{b}}^{1/2}d). \tag{3.7}$$

D(V) represents the electron state densities of the tip and the sample, V is the bias voltage, d is the effective tunnelling gap, ϕ_B is the effective barrier height, and A is a constant. Equation 3.7 shows an exponential relationship between j and d, so a minor change in the tip-sample distance, from a protrusion or depression, will result in a substantial change in the tunnelling current.

Experimental Set-Up

Figure 3.11 (A) shows a simplified model set-up of an STM. An atomically sharp tip, typically made of tungsten, is housed in the scanning stage, which is suspended above the sample. Copper fins are located at regularly spaced intervals around the scanning stage, which, when lowered, fall between two powerful magnets suspending the stage freely, preventing any mechanical vibrations from being transferred to the tip.

A coarse positioning system is used to move the tip to and from the surface and across the surface to different areas. In contrast, a series of piezoelectric ceramics are used for the fine control of the tip in the x, y, and z directions by applying electrical signals across the ceramic to expand or contract the piezoelectric [102].

A complex series of feedback electronics (Figure 3.11 (A)) are used to monitor the tunnelling current and the tip-to-sample distance. The position and tunnelling current are converted into an image on a computer, where other parameters such as bias voltage, scan size, feedback control, etc., can be adjusted [103].

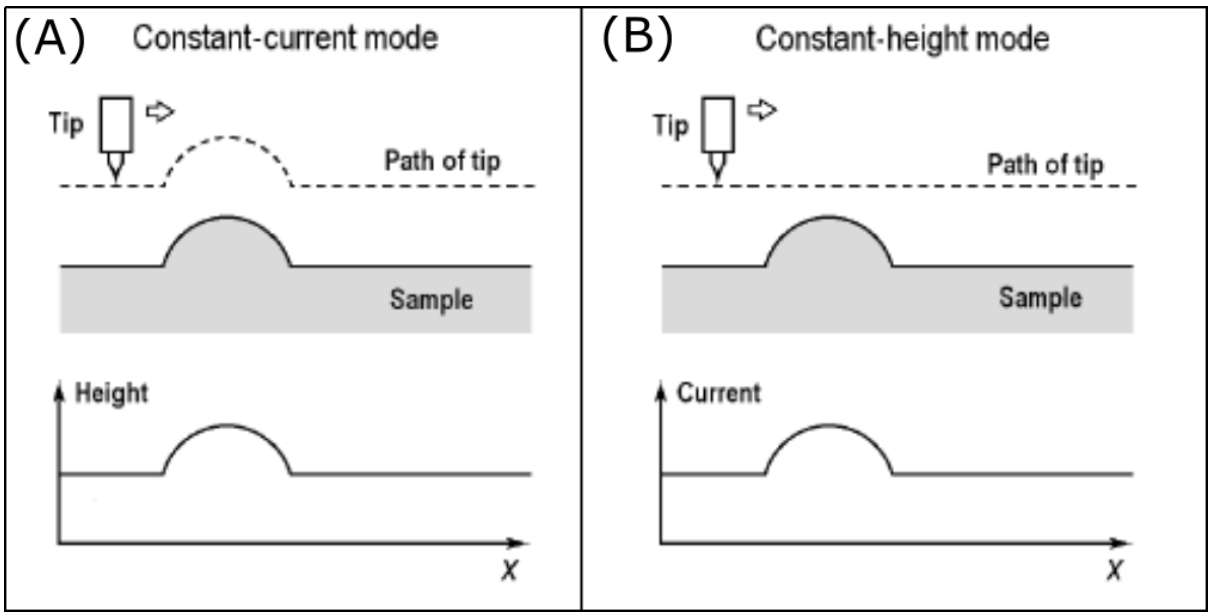

Figure 3.13: A model of the two modes of scanning with STM. (A) shows a constant current mode where the Z-axis height is altered to maintain a constant tunnelling current, while (B) shows a constant height mode where the change in tunnelling current is recorded. From [90].

There are two modes for STM operation: constant current and constant height. Constant current mode maintains the tunnelling current at a set value by adjusting the Z-axis piezoelectric element during scanning. This results in an image formed from changes in the x, y, and z directions of the piezoelectric movement [104] (Figure 3.13 (A)). This method produces images more slowly than constant height mode but allows the tip to adapt to sudden changes in surface topography, either avoiding protrusions to protect the tip or lowering into depressions to maintain signal.

Constant height mode fixes the position of the Z-axis piezoelectric during scanning and records variations in the tunnelling current to generate an image based on changes in the x and y axes and tunnelling current [104]. This method acquires images more quickly, as the tip does not move in the z direction; however, it does not respond to sudden height variations, increasing the risk of tip damage if it encounters a protrusion or step edge. For this reason, constant current mode was selected for all STM results in this thesis.

STM is an exceedingly sensitive surface analysis technique, meaning that distortions can occur in the data that may not correspond to actual surface features. Two software packages, WSXM [105] and Gwyddion [106], were used to correct these distortions. Plane levelling is applied to correct for slope artefacts due to tip-sample misalignment, using different methods depending on whether the image is atomically flat or contains steps of varying height. Scan line defects, resulting from line-by-line image acquisition, as well as corrupted lines, are removed through a scar removal process.

Due to the small scan area on the sample surface—ranging from 400×400 nm^2 to 20×20 nm^2 in this thesis—subtle and otherwise imperceptible effects, such as drift, thermal drift, and creep, can be observed in the STM images.

Thermal drift arises from differences in the thermal expansion coefficients of the various materials in physical contact with the STM tip and the sample surface [104], [107]. Temperature fluctuations cause these materials to expand and contract at different rates, leading to relative motion between the tip and the sample. In this thesis, only STM systems without active temperature control were used. As a result, thermal drift could not be stabilised and thus remained a persistent influence on the acquired data, necessitating correction during image processing.

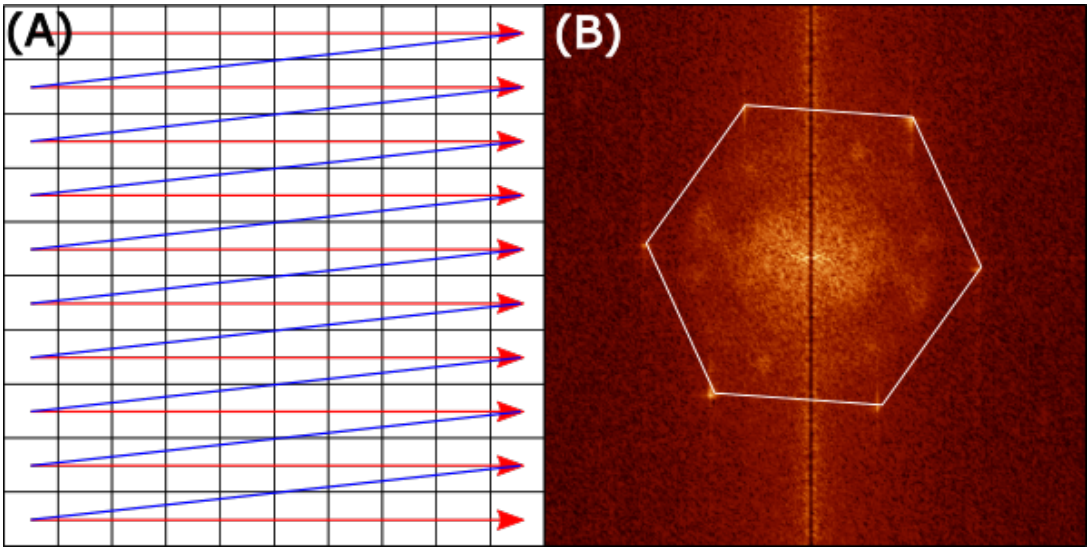

Figure 3.14: (A) A model of a raster scan showing the movement of an STM tip from left to right before moving onto the next layer below and starting again. (B) FFT of an STM image from the Ga_3Ni_2 (001) surface showing the skewed hexagon caused by drift.

Understanding how thermal drift affects an image during scanning is important. Typically, a raster scan is used to collect an image, as shown in Figure 3.14 (A), where the tip moves from left to right, recording the change in height/current as a function of position, then increments downward to the next line and continues [108]. The scan speed in the X-direction is therefore much faster than the overall scan speed in the Y-direction, meaning that thermal drift will have a more pronounced effect in the X-direction due to its higher scan speed. Figure 3.14 (B) shows an FFT image of the Ga_3Ni_2 (001) surface. The six bright points should form a hexagon, but due to drift, the hexagon had to be skewed vertically to align properly.

As thermal drift is a constant presence, drift correction will be applied to all high-resolution STM images. If the expected symmetry of the surface is known—for example, a hexagonal pattern as seen in Figure 3.14 (B) the FFT image can be adjusted by rotating, skewing, and scaling the image vertically and horizontally until the observed symmetry matches the expected one. To correct the real-space image, the corrections made in reciprocal space are used: any horizontal skewing applied in reciprocal space corresponds to vertical skewing in real space, and vice versa. Similarly, any scaling adjustments in reciprocal space must be inverted when applied to the real-space image [109].

Creep is observed as the continued motion of a scanner following a rapid change in voltage, such as when the scanning position is altered. Piezoelectric materials do not respond to voltage changes instantaneously. The initial movement occurs in less than a millisecond and then gradually reaches the final position asymptotically, as shown in Figure 3.15. This asymptotic movement is referred to as creep [110]. Creep distorts the surface, making features appear either smaller or elongated in one direction. This effect is especially noticeable after zooming into a region or moving to a new area of the surface, although any recent tip movement will contribute to creep.

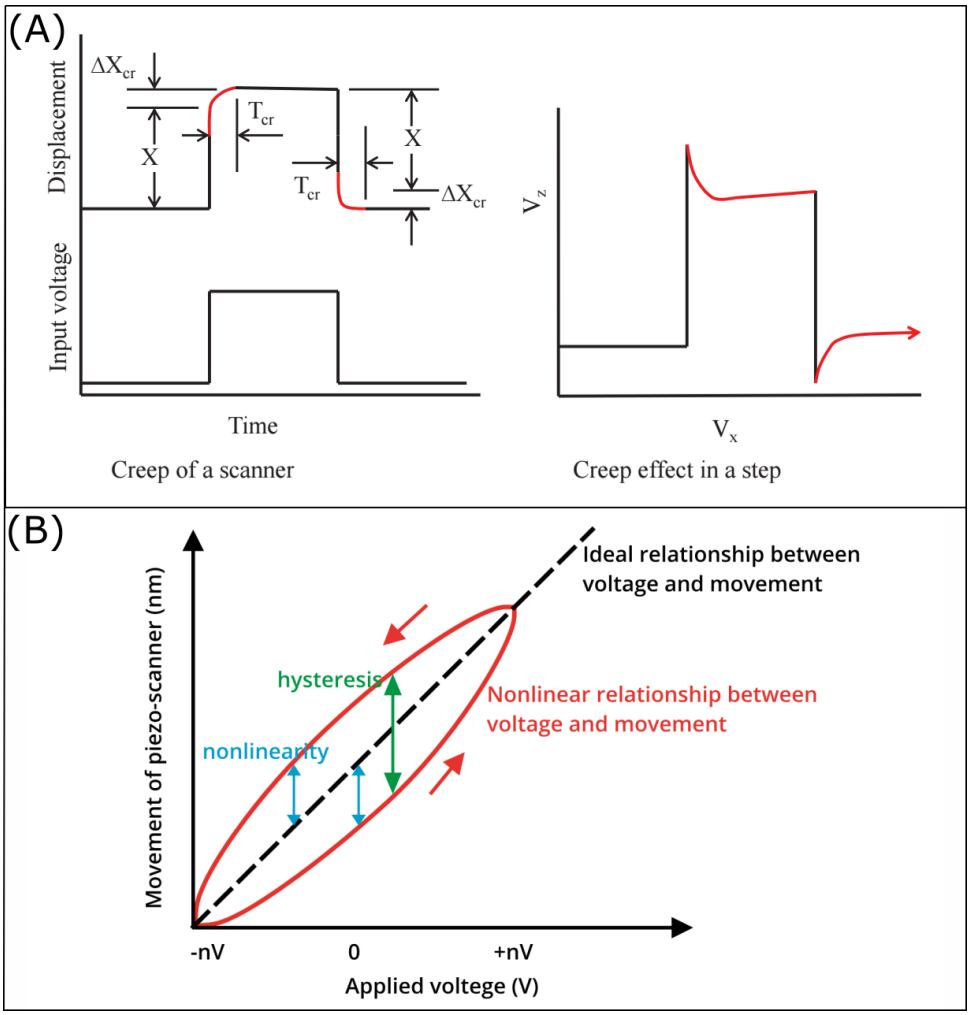

Figure 3.15: (A) A model showing the effect of creep for a piezoelectric actuator. As the voltage is applied, the displacement X occurs within less than a millisecond, after which the secondary displacement in red, ΔX_{cr}, occurs over a longer period, causing creep to distort the frame being recorded [110]. (B) A diagram showing the effect of hysteresis, with the black dashed line showing the ideal linear relationship between the applied voltage and the piezoelectric movement and the red lines representing the non-linear relationship which occurs [111].

Creep can be resolved by allowing the tip to scan the surface a few times to allow the piezoelectric to settle before recording or using a coarse motor for larger movements when applicable. Piezoelectric actuator hysteresis occurs when the change in the piezoelectric actuators does not follow an ideal linear path, as shown in Figure 3.15 when a voltage is applied, which will distort the image recorded [112]. Typically, this occurs when changing the scan size or moving the scan window and will only affect the first set of lines scanned. Rescanning the window or lowering the scan speed is used to reduce the effect of the hysteresis on images.

After the STM results have been corrected, any drift measurements can be taken directly from the image. Line profiles are commonly used to measure the change in the Z-axis height or tunnelling current along the selected line, allowing for the step height between terraces and the height of other features to be measured. A height histogram can also be used to measure step heights. There are two other image analysis techniques used regularly in STM analysis: the Fast Fourier Transformation (FFT) and autocorrelation. Both of these allow for the inherent order present in an image to be measured and assessed when it might not be easy to see by the eye initially.

An FFT converts an image into its harmonic components, which are sums of sine and cosine functions with several frequencies and amplitudes. These harmonic components are represented in the Fourier domain, where points in this domain correspond with key frequencies contained within the real-space image. This allows any order within the image to be easily observed, even if it is not discernible by the naked eye.

Figure 3.16 (A) shows a real image of the Ga_3Ni_2 (001) surface recorded via STM, while Figure 3.16 (B) shows the 2D FFT of Figure 3.16 (A). Periodic features in real space are observed in the Fourier domain by bright points where multiple frequencies overlap. This can be seen through the six bright spots that form a hexagon, in addition to two points at the top and bottom of the image, which are attributed to noise.

Filtering out these high-intensity spots and applying an inverse FFT means that these features can be observed in real space, as shown in Figures 3.16 (D) and (C) respectively. These repeated features can now be observed, measured, and adjusted to correct for drift.

The central region of the FFT corresponds to low frequencies, which are associated with larger, non-repeating features; this is evident from the absence of distinct bright spots near the centre. When filtering both the bright spots and a portion of the centre of the FFT (Figure 3.16 (H)), we can enhance the repeating features, as shown in Figure 3.16 (G).

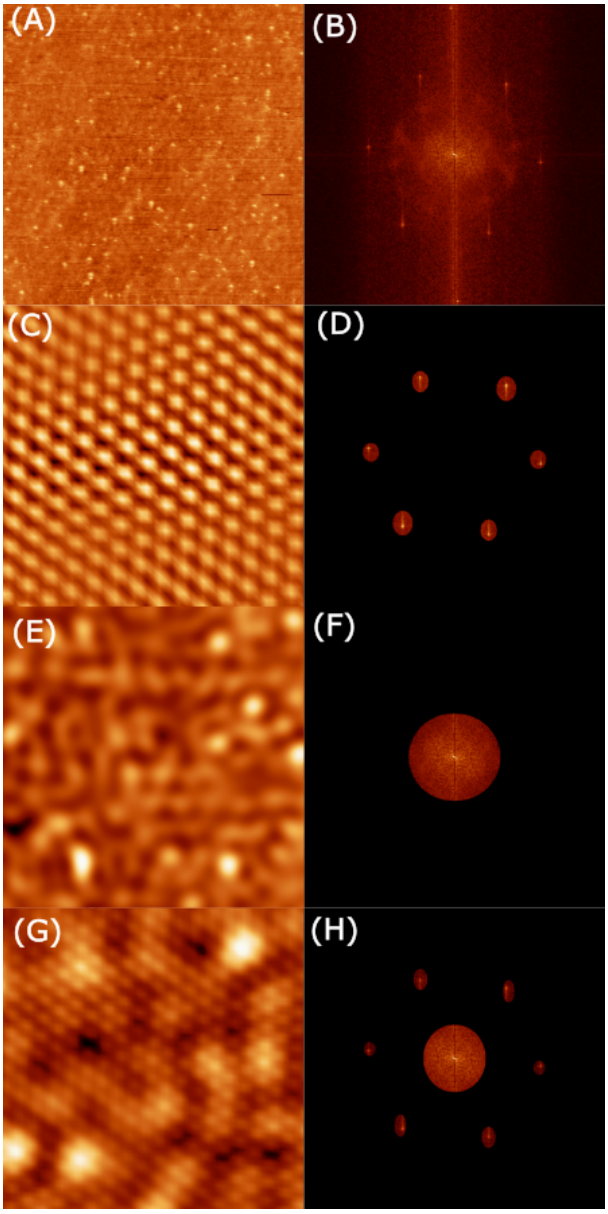

Figure 3.16: (A) A 20×20 nm^2 STM image of the Ga_3Ni_2 (001) surface. (B) The FFT of (A) shows all of the bright spots coming from a repeating feature. (C) The inverse FFT of (D) shows the real space repeating features, which is a rhombic unit cell. (D) A filtered version of (B) filtering out the six brightest spots. (E) The Inverse FFT of (F) showing the long-range information from the centre of the FFT (F) A filtered version of (B) filtering the information from the centre containing the long-range non-repeating information. (G) The Inverse FFT of (H), enhancing the repeating features from (C) and combined with (E), shows how the repeating features look with the larger surface structure. (H) A filtered version of (B) combining (D) and (F).

3.3.3 X-ray Photoelectron Spectroscopy (XPS)

History

The photoelectric effect is at the core of all methods of photoelectron spectroscopy. The photoelectric effect is the emission of electrons from a material after exposure to light [113]. The history of the photoelectric effect can be traced back to Heinrich Rudolf Hertz [114], who was the first person to confirm Maxwell's theory of electromagnetic radiation in 1886. Maxwell proposed that light was an electromagnetic wave which propagated at the speed of light. This experiment used sparking electrodes to produce light, which could be measured, and in addition, it was also noted by Hertz that while exposing these electrodes to ultraviolet light, they became notably easier to create electric sparks from.

Hertz's discovery was an important first step into the history of the photoelectric effect and was further developed upon by Philipp Eduard Anton von Lenard, who studied how the intensity of the light affected the emitted photoelectrons [115]. Under classical electromagnetic theory by altering the light intensity the kinetic energy of the electrons from the material would also increase and vice versa using a dim light there would be a delay from the light hitting the surface to the emission of an electron as a wave the light was assumed to be transferring the energy to the election [116]. Lenard discovered that by doubling the intensity of a light source facing a material, you did not increase the energy of the emitted electrons, but doubled the number of electrons being emitted from the surface, and the maximum kinetic energy was dependent upon the material.

Albert Einstein proposed a solution to Lenard's discovery. Building upon Max Planck's hypothesis that the energy carried by electromagnetic waves must be released in "packets" of energy Einstein published a paper proposing that light energy is carried as a quantised pack of energy which has an energy hv where h is Planck's constant [117] and v is the frequency of the electromagnetic radiation.

$$E = h\nu \tag{3.8}$$

As the light hits the surface, Einstein predicted that these photons were imparting all of their energy into the surface electrons [118]. Some of this initial energy is lost in allowing the electron to overcome the bond it has to the material, and the rest is given to the electron [119].

$$K_E = h\nu - \phi \tag{3.9}$$

As all photoelectron spectroscopy work utilises the emission of photons from the surface of a material, utilising a source of electromagnetic radiation, be it X-ray or ultraviolet light, this field of study would not be possible without Max Planck and Albert Einstein's contributions to physics.

Physical Principle

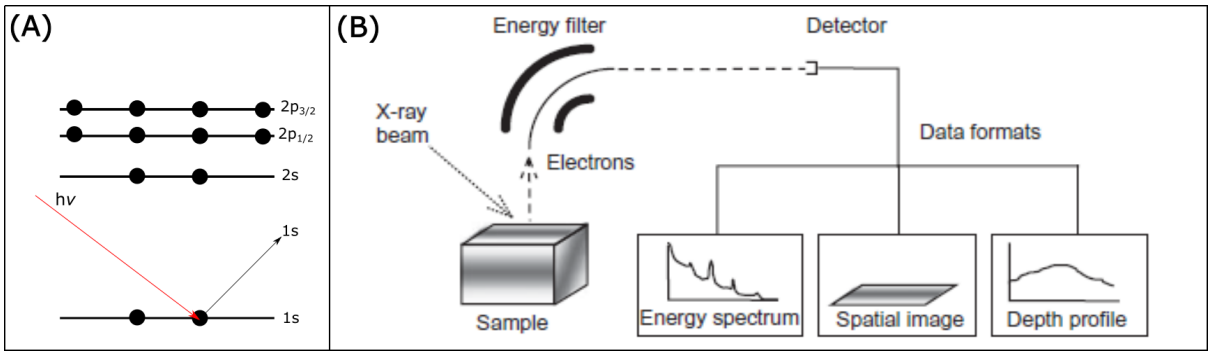

Figure 3.17: A diagram of the photoelectron process (A) with a model XPS set-up shown in (B) [90].

Dr. Kai Siegbahn was awarded the Nobel Prize in Physics in 1981 for the development of X-ray photoelectron spectroscopy. XPS uses X-rays to liberate an electron bound to an atom until it is emitted from the surface, where the kinetic energy of those emitted electrons is recorded (Figure 3.17). XPS is effective at probing the topmost layers of a sample (1 - 10 nm). The kinetic energy of an electron is a function of the electron's binding energy, which is element-specific (Equation 3.10).

$$h\nu = BE + KE + \Phi \tag{3.10}$$

Where ϕ is the work function of the spectrometer, which is a constant value. Typically,

ϕ would represent the work function of the material experiencing the photoelectric effect, but as the sample and the spectrometer are in electrical contact, their Fermi levels are aligned, so the work function of the spectrometer can be used. The binding energy can be calculated using Equation 3.10 and is independent of the X-ray source used to eject the photoelectron. XPS is used in the identification of elements from a sample and quantifying the chemical composition, discussed further in Chapter 3.

Experimental Set-Up

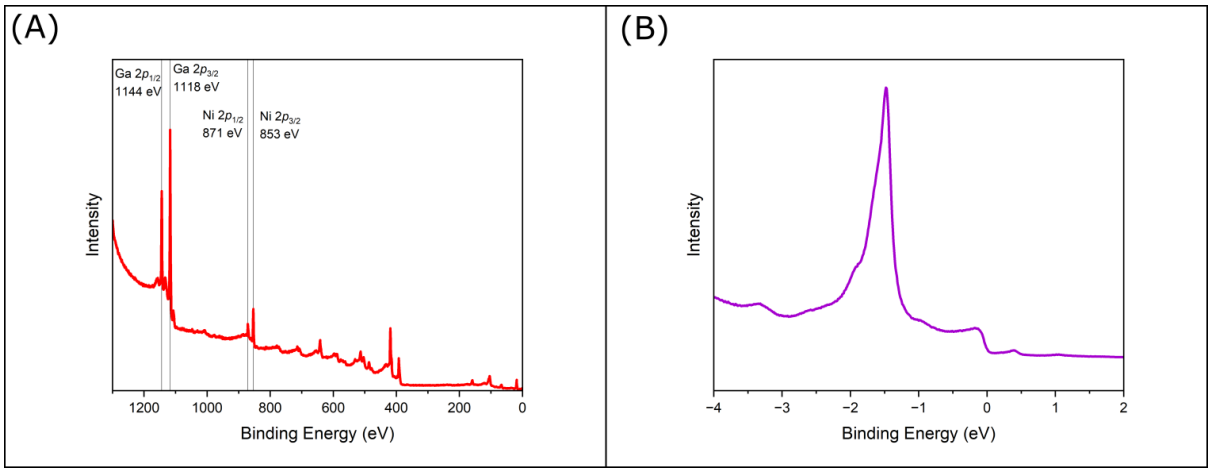

Figure 3.18: (A) An XPS spectrum taken from Ga_3Ni_2 (001) with the largest peaks at the core level highlighted by black lines. (B) A UPS spectrum taken from Ga_3Ni_2 (001).

Figure 3.17 (B) shows a model of an XPS set-up. An incident X-ray beam excites an electron from a sample into a detector. The X-rays are typically produced from either an Mg or an Al anode, with high-energy electrons being targeted at a cooled Al or Mg anode to produce incident X-rays of known energy.

Both Mg and Al X-rays have noticeable doublet emission peaks from the electron vacancies in the K-shell, producing two peaks, K_α and K_β. This will cause the "satellite" peaks to be observed within the spectra, where photoelectrons from both K_α and K_β are recorded.

A monochromator can be used to rectify this problem by filtering out the undesired photons, or software can be used to remove these peaks. For this thesis, each source used will be mentioned for each sample, and the sources will not be monochromatic. Once an electron is emitted from the surface, a series of lenses collects it into the hemi-

spherical detector. The electron detector measures the current from the incident electrons, but the current from a single electron would be too small to accurately measure.

By applying a high voltage to a tube within the detector with a high-resistance coating, the emitted electron will be absorbed and emit a shower of secondary electrons, multiplying the initial reading of one electron into a cascade of electrons, increasing the amplitude of the signal recorded.

The shower of electrons is then passed through the hemispherical analyser. The analyser consists of an inner and outer dome where the electron travels between the two. Each of the hemispheres is set to different voltages, producing an electromagnetic field that will only allow electrons of a given energy to pass through onto the detectors [120]. By altering the voltages and the pass energy over a range, it is possible to develop an XPS spectrum for a sample.

The XPS spectrum is a plot of the number of recorded electrons for each binding energy bin; the energy step range determines the bin size. When enough energy is provided to emit photoelectrons from core levels, they appear as peaks, as seen in Figure 3.18 (A). By noting the binding energy of each peak, the elemental makeup of the surface can be determined. Figure 3.18 (A) has peaks for Ga and Ni. By taking the area of each peak minus the background, it is possible to obtain the composition of the surface of the sample, which is discussed in more detail in Chapter 4.

3.3.4 Ultraviolet Photoelectron Spectroscopy (UPS)

The experimental set-up for UPS is similar to that shown in Figure 3.17 (A). Typically, a differentially pumped helium discharge lamp is used as the radiation source, which produces photons at two energies, He^1 at 21.2 eV and He^2 at 40.4 eV, which arise from the decay of the $1s$ and $2p$ states. The UV photoelectron interacts with the topmost layers of the surface, causing the valence electron to be ejected towards the analyser, and the single electron is multiplied into a cascade in the detector as described above.

For this thesis, a He^1 source was used, and it is not monochromatic, meaning satellite peaks will be present in the UPS results. Figure 3.18 (B) shows the results of a UPS scan. The range of binding energy is limited by the photon energies to the valence band electrons. Density of states calculations are used to model the orbital contribu-

tions, which are used to identify peaks in the UPS spectrum.

Software and Peak Analysis

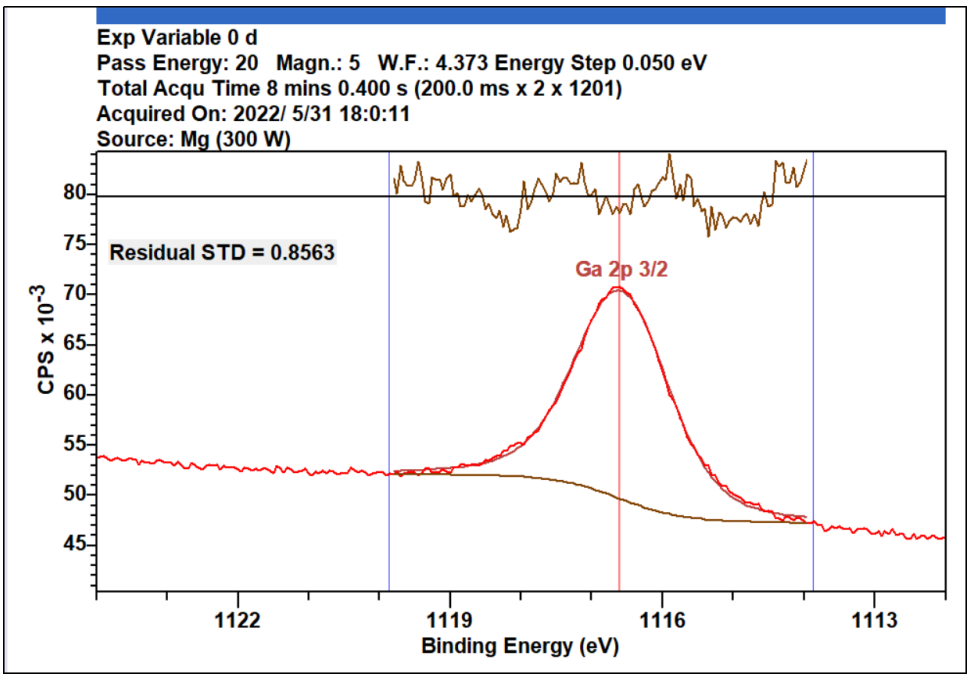

Figure 3.19: XPS spectrum from CasaXPS showing the Ga $2p_{3/2}$ peak from the Ga_3Ni_2 (001) surface. All the key features for peak analysis are shown from regions and components to the residual standard deviation value (SDV), a value representing how close the fitted peak matches the results.

CasaXPS was used to analyse all of the XPS and UPS data in this thesis. After opening an XPS or UPS file, the first step is to highlight and identify all of the peaks present. Peaks are highlighted using a region, denoted by two vertical blue lines.

An appropriate background type is selected, as shown in Figure 3.19. For this thesis, a Shirley background was selected unless otherwise stated. After finding the peak position, a library of all element peaks can be used to identify which element and orbital this peak represents.

A line shape is used to fit a peak. Fitting provides the line shape of the peak, confirms if multiple peaks are required due to other contributors, and accounts for high-energy tails. For this thesis, a mixture of GL(Z) and A(X, Y, 0) GL(Z) line shapes are used. GL(Z) is a Gaussian/Lorentz line shape where Z is a value from 0 to 100, with 0 representing a pure Gaussian peak and 100 representing a pure Lorentzian peak. A(X, Y, 0) is an addition to the GL(Z) line shape that adds asymmetry to the peaks to account

for high-energy tails. X can be any value between 0 and 1, and Y can be any positive value.

By adjusting the values in the line shape, changing the type of line shape used, or adding more peaks within a region, we can reduce the residual standard deviation value (STD) seen in Figure 3.19 to close to unity.

The residual standard deviation value is an estimation of the noise alongside the residual trace produced by fitting the peak. As Poisson statistics are present, an STD value approaching 1 is considered optimal; by altering the parameters of the fit, we can approach unity. To produce the most optimal line shapes, each value (X, Y, Z) is put through a Monte Carlo simulation where the value is varied between a given range. The results that produce the lowest residual STD are then selected.

Using this Monte Carlo method, we can determine if secondary, tertiary, etc., peaks are required to fit the measured data. This may indicate the presence of an oxide or another element, as discussed in Chapter 6.

3.4 Growth, Phase Diagram and Structure of Ga_3Ni_2

This section covers the methods used to grow all three Ga_3Ni_2 samples studied in this thesis. The samples were grown by Prof. Peter Gille [30] and provided for study. The Czochralski method is one of many techniques that can be used to grow crystals, as shown in Figure 3.20 (A). By placing a seed crystal into a crucible containing the molten alloy, a large single crystal can be grown.

The Czochralski method produces a large single ingot of the desired crystalline material using an extremely slow pull rate while gently rotating the crystal to achieve the desired solid-liquid interface [121]. The process is widely used to grow large single crystals of semiconductor wafers, as well as binary alloys used for catalysis. The method is named after Jan Czochralski, who discovered it in 1915 [122].

For Ga–Ni intermetallic compounds, a bulk melt of Ga is used, into which Ni is introduced to reach the desired atomic percentage. Ga_3Ni_2 is the only configuration from which a single crystal can be grown. Figure 2.8 (B) shows that Ga_3Ni_2 can be crystallised from a Ga-rich solution between 369°C and 950°C. The maximum annealing

temperature is used because the accumulation of liquid Ga during the experiment can cause the temperature to decrease, resulting in Ga-rich inclusions if the drop is drastic.

A macroscopic seed crystal is used to initiate sample growth in the Czochralski method. If no seed crystal is present, the literature offers several alternatives. One method involves using a refractory material such as tantalum, which has a high melting point [29].

A second option is to use a ceramic tip to induce spontaneous nucleation [123]. A third option is to use a similar material or one of the alloy's constituent elements [30]. For Ga_3Ni_2, a Ni seed was used since its melting point (1455°C) is well above that of the melt used to grow the crystal. Although there is no thermodynamic equilibrium between Ni and Ga_3Ni_2, the goal of using Ni as a seed is to provide a nucleation site for a single Ga_3Ni_2 crystal once the seed is wetted, from which the rest of the crystal can grow.

Once the seed crystal was placed into the melt, extraction began at a rate of 0.1 mm/hr to form the crystal neck. After three days, the rate was reduced to 0.05 mm/hr and finally to 0.025 mm/hr, allowing the crystal to grow over 22 days. The crucible was rotated at a constant 6.7 rpm, while the crystal was counter-rotated at 70 rpm to aid material transport at the growth interface [30]. This entire process took place in a sealed metal chamber under UHV to prevent oxygen contamination, and the crystal was grown under an Ar^+ environment [29].

After twenty two days, the Ga_3Ni_2 crystal shown in Figure 3.20 (B) was cooled to room temperature at a rate of 150 K/hr before being sliced into three samples, each with a different crystallographic orientation: (001), (100), and $(2\bar{1}0)$. Each orientation was confirmed through Laue diffraction. Each surface was mechanically polished using diamond grit paste of decreasing grain size from 6m to 0.25m, with methanol cleanings in an ultrasonic bath between each grit.

The phase diagram for Ga–Ni (Figure 2.8 (B)) shows four possible compounds: Ga_5Ni, Ga_7Ni_3, Ga_4Ni_3, and Ga_3Ni_2. Only Ga_3Ni_2 is in equilibrium with the Ga–Ni melt, making it the only phase from which a single crystal can be grown [30]. Ga_3Ni_2 is grown at the highest annealing temperature of 950°C, as no other Ga–Ni alloy can be crys-

tallised from the melt at that temperature, reducing the risk of inclusions from other alloys if the melt composition changes.

The phase diagram does not show a homogeneity band for the Ga_3Ni_2 intermetallic compound. Ga_3Ni_2 crystallises in the Al_3Ni_2 structure type, which includes Al_3Ni_2, Ga_3Ni_2, and In_3Ni_2, with a $P\bar{3}m1$ space group and lattice parameters of $a = 4.06$ Å and $c = 4.89$ Å [30].

The Al_3Ni_2 structure exhibits trigonal symmetry, as shown in Figure 3.20 (C). This symmetry isolates the Ni atoms (in silver) by surrounding them with four Ga atoms (in green). This site isolation is believed to contribute to the high selectivity of this intermetallic compound [124].

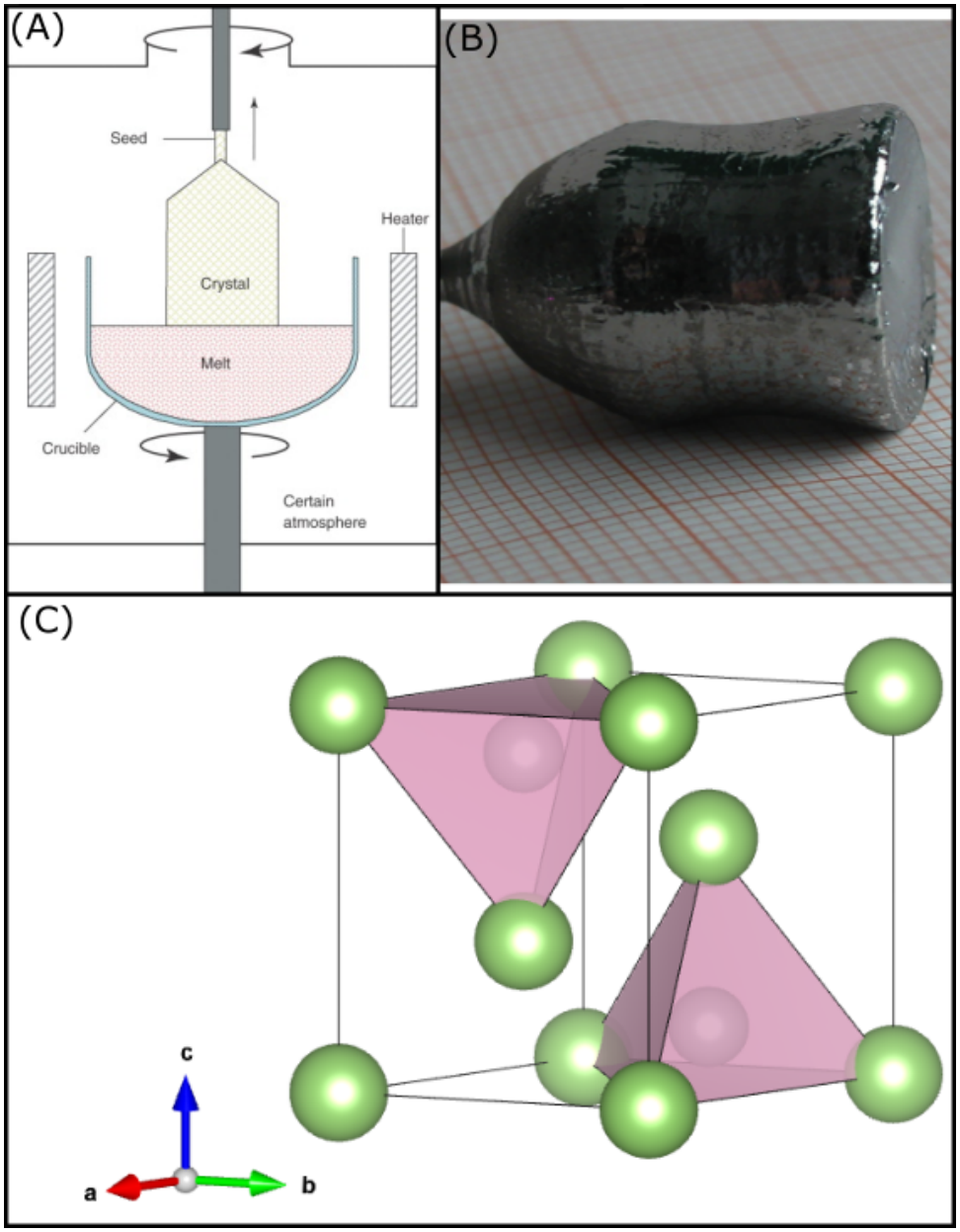

Figure 3.20: (A) A diagram of the Czochralski method. (B) Ga_3Ni_2 crystal pulled along a 3-fold rotational axis. (C) Ga_3Ni_2 structure showing the Ni atoms, silver, being isolated from other Ni atoms by the Ga atoms, green.

Chapter 4

Surface Chemical Composition of Ga_3Ni_2

4.1 Introduction

In this chapter, three sets of results will be presented. Firstly, the Ga_3Ni_2 (001) XPS spectra are shown after air exposure, followed by sputtering and annealing. Secondly, the atomic composition changes for all three Ga_3Ni_2 surfaces (001), $(2\bar{1}0)$, and (100) are examined as a function of sputtering and annealing temperature. Thirdly, the variation in atomic composition for all three Ga_3Ni_2 surfaces as a function of scanning angle is discussed.

With no prior research into the surface preparation of Ga_3Ni_2, understanding how sputtering and annealing affect the surface of each sample is important. By observing changes in the spectrum and the atomic composition, ideal preparation conditions for all three samples are identified.

4.2 Experimental Details

A single grain sample of Ga_3Ni_2 was grown via the Czochralski method [30]. Each sample was cut along a different surface: (001), $(2\bar{1}0)$, and (100), and polished using progressively smaller grains of diamond paste, from 6 μm to 0.25 μm. All three surfaces underwent standard surface preparation procedures in the UHV chamber. The surfaces were sputtered using argon ions (Ar^+, thirty minutes, 2 keV ($\approx 2.5\times10^{-5}$ mbar, drain current $\approx$ 28 μA) and then annealed (500°C, ninety minutes) until no contamination was detected.

The Ga_3Ni_2 (001) surface was studied at the University of Liverpool Surface Science Research Center, and all three surfaces—(100), (001), and $(2\bar{1}0)$—were investigated at the Institut Jean Lamour in Nancy. The surface preparation conditions were identical between the two institutes.

The surfaces were characterised by XPS using an Al (Kα) source in Liverpool (base pressure 1×10^{-9} mbar) and a Mg (Kα) source in Nancy (base pressure 4.7×10^{-10} mbar). At L'Institut Jean Lamour, the (100), (001), and $(2\bar{1}0)$ samples were studied in two different UHV chambers, which had different source-detector geometry setups for XPS in collaboration with Dr. Vincent Fournee, Dr. Julian Ledieu, and Wilfried Bajoun Mbajoun. Each of the surfaces underwent XPS scans after sputtering, annealing at different temperatures, and air exposure to study any changes in the surface chemical composition due to these treatments.

4.3 Results and Discussion

4.3.1 Influence of Air Exposure, Sputtering and Annealing

Before being introduced into the UHV chamber, each of the Ga_3Ni_2 samples had been exposed to air for a prolonged period, saturating the surface with oxygen and other contaminants. XPS was used to identify the constituent elements of the sample and any contaminants, as well as to investigate how the surface reacts to sputtering and annealing. Figure 4.1 shows survey scans from the air-exposed, sputtered, and annealed surface of the (001) surface, where the principal peaks of all constituent elements have been marked and labelled.

The air-exposed surface shows the presence of oxygen and carbon. After sputtering, the O 1s and C 1s peaks are no longer present. The spectrum taken from the surface after annealing (560°C) is identical in shape and position to the sputtered surface. The binding energies and profiles of each principal peak of Ni and Ga were then investigated. To determine the binding energy, the peaks were fitted using an asymmetric Gaussian and Lorentzian product line shape with a Shirley-type background. Several background types were tested, but the Shirley background was selected as it reliably produced the best fits. An example of fitting is shown in Figure 4.2 (A) and (B).

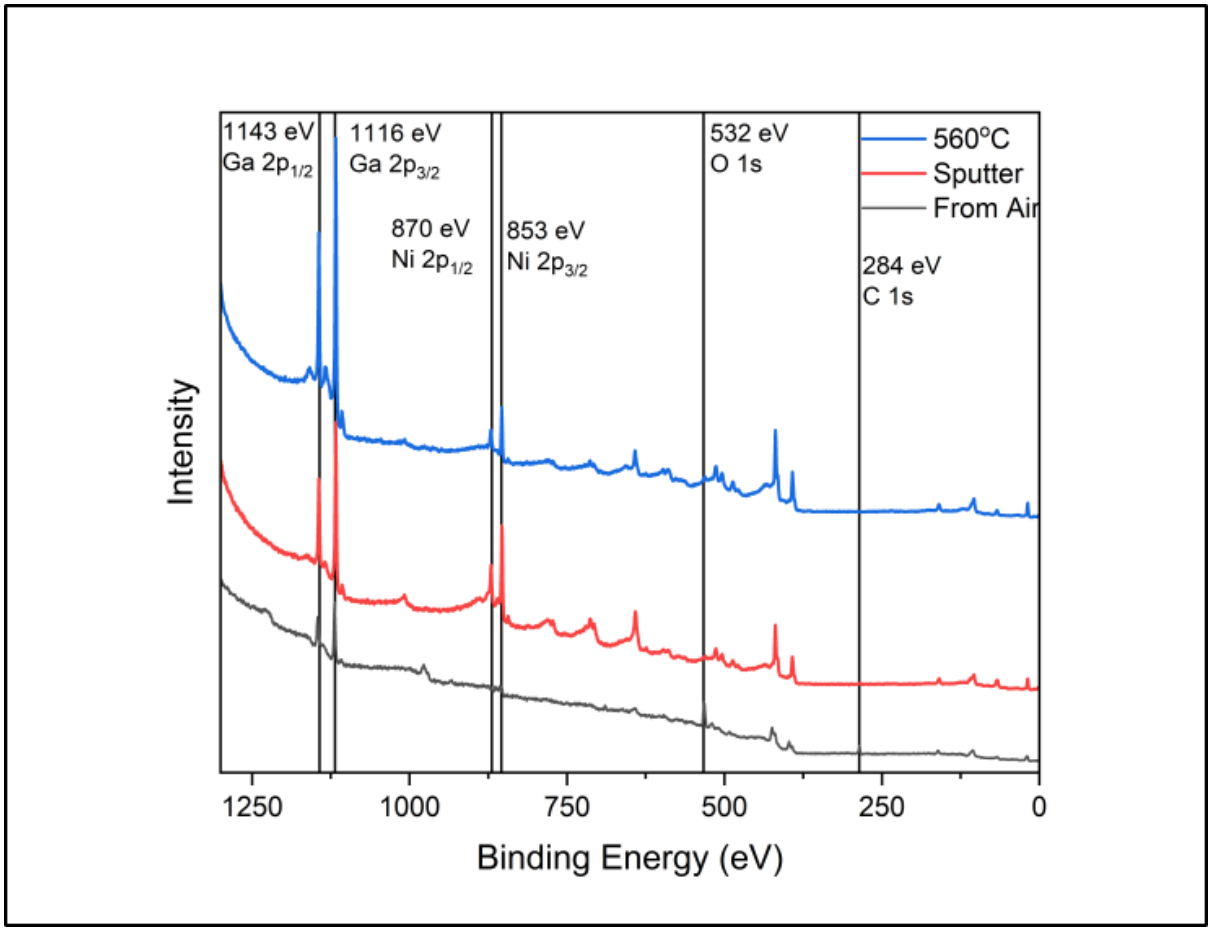

Figure 4.1: XPS spectra from the (001) surface after exposure to air, sputtering for thirty minutes and annealing at 560°C for ninety minutes taken with an Al (K_α) source. Vertical black lines are placed at the elemental binding energies of expected elements on the surface [125].

The Ga $2p3/2$ peak after air exposure was fitted using two peaks at 1119.2 eV and 1117.0 eV, as shown in Figure 4.2 (A) and Table 4.1. The peak at the higher binding energy corresponds to Ga in $Ga2O_3$ [126], whereas the peak at the lower binding energy is from intermetallic Ga [125].

A majority of Ga near the surface has been oxidized, with the oxide peak making up 94% of the total area, calculated by taking the ratio of the area of each component peak against the . After a single cycle of sputtering, all of the oxide present on the surface was removed, as the Ga $2p$ peaks after sputtering only required a single asymmetric Gaussian and Lorentzian line shape to fit (Figure 4.2 (B)).

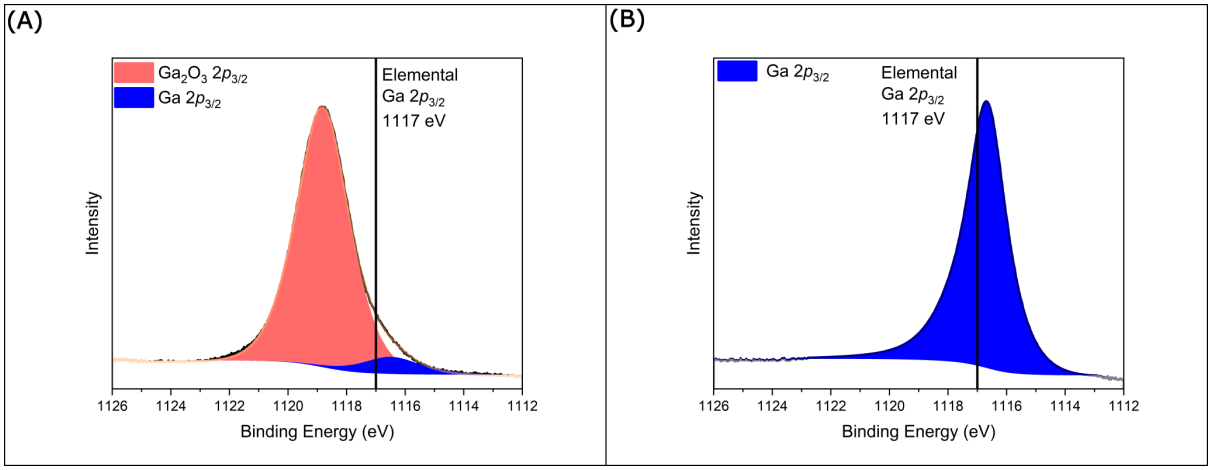

Figure 4.2: (A) XPS spectra from the air-exposed surface. (B) XPS spectra from the clean surface (B). The binding energy for elemental Ga has been highlighted. The binding energy was taken from [125]. (A) required two peaks to fit, showing the presence of both the intermetallic Ga and Ga_2O_3 and after sputtering, only one peak was required (B). A Shirley background was used.

	Experimental Value	Literature Value
Pure Ga	1116.8	1117.0 [125]
Ga in Ga_2O_3	1118.8	1119.2 [126]

Table 4.1: The binding energy of the Ga $2p_{3/2}$ and Ga in Ga_2O_3 $2p_{3/2}$ compared to literature values.

Gallium 2*p*

Figure 4.3 compares the Ga 2p peaks from the air-exposed surface and the surface after sputtering and annealing at 560°C. The air exposure has oxidized a majority of the Ga on the surface. The XPS results from the sputtered surface show that the Ga 2p peaks have shifted to a lower binding energy, close to that of pure Ga, confirming the removal of Ga2O3. After annealing the surface at 560°C (Figure 4.3), there is no change in the position or shape of the Ga 2p1/2 and Ga 2p3/2 peaks, showing that the surface is not contaminated again after annealing.

The Ga 2p peaks are consistently 27 eV apart, as expected from the literature [126], due to them being doublet peaks. As this is a constant, all Ga 2p1/2 and Ga 2p3/2 peaks will be set 27 eV apart for all further analysis.

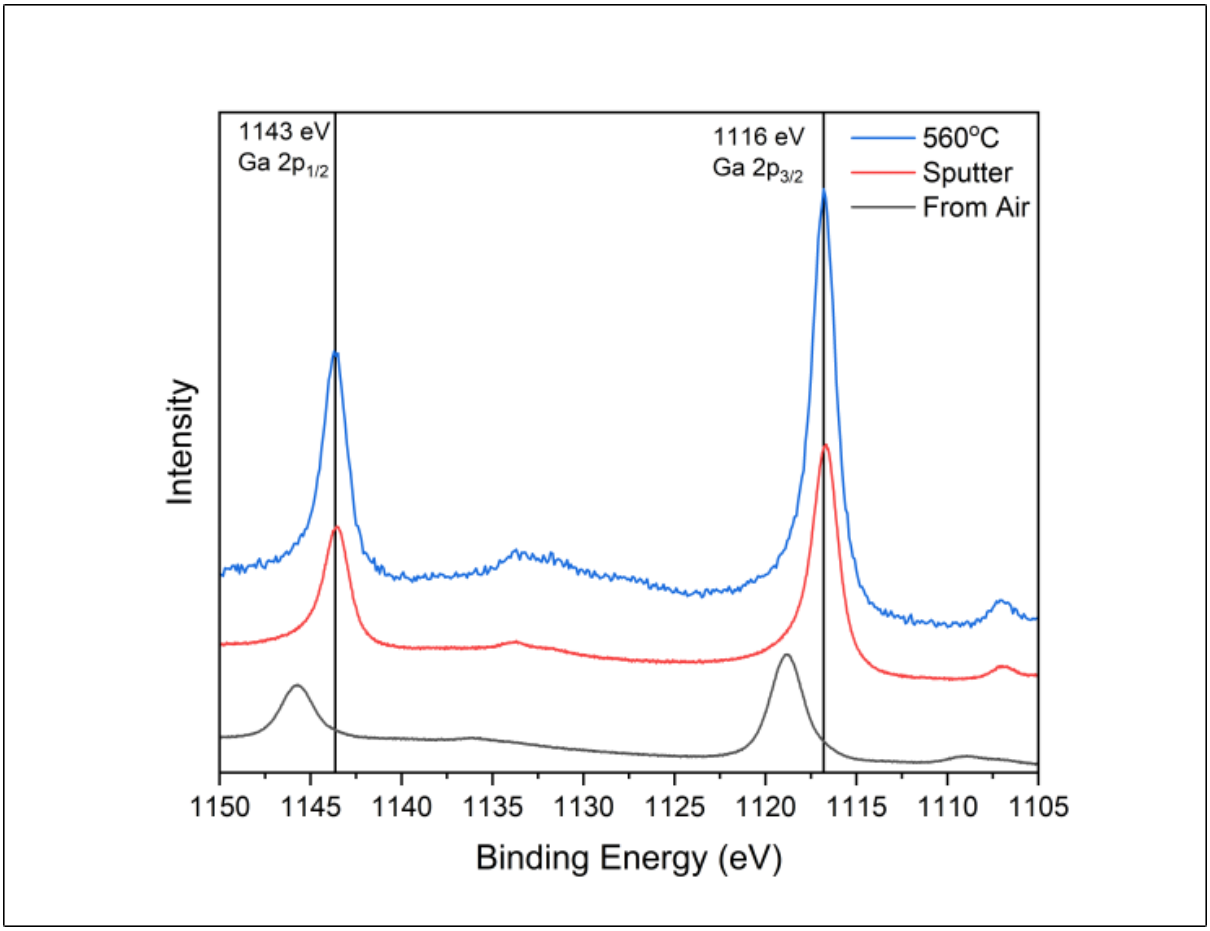

Figure 4.3: The XPS of on the Ga $2p_{1/2}$ and Ga $2p_{3/2}$ peaks. Black vertical lines show the literature binding energies for Ga $2p_{1/2}$ and Ga $2p_{3/2}$ [126]. The figure shows the air-exposed, sputtering and annealing.

Data Set	Binding Energy (eV)		
	Ga $2p_{1/2}$	Ga $2p_{3/2}$	Difference
Air Exposed	1145.7	1118.8	26.9
Sputtered	1143.5	1116.7	26.8
560°C	1143.7	1116.7	27.0
Elemental [125]	1144.0	1117.0	27.0

Table 4.2: A table showing the change in binding energy for the Ga $2p_{1/2}$, Ga $2p_{3/2}$ in addition to the difference between the two peaks. The elemental values are from literature [126] and are present for reference.

Nickel 2*p*

We will now compare the Ni 2p peaks from the air-exposed surface, after sputtering, and after annealing at 560°C, as shown in Figure 4.4. The Ni 2p air-exposed results in Figure 4.4 only show the binding energy region around the Ni 2p3/2 peak. Two peaks are observed: the lower binding energy peak at 853 eV is close to the literature value for Ni 2p3/2 [125] in Table 4.3, and the peak at the higher binding energy, at 856.0 eV, is consistent with the presence of $Ni(OH)_2$ [127]. No peak at 854.4 eV is observed, which would confirm the lack of NiO on the surface [126].

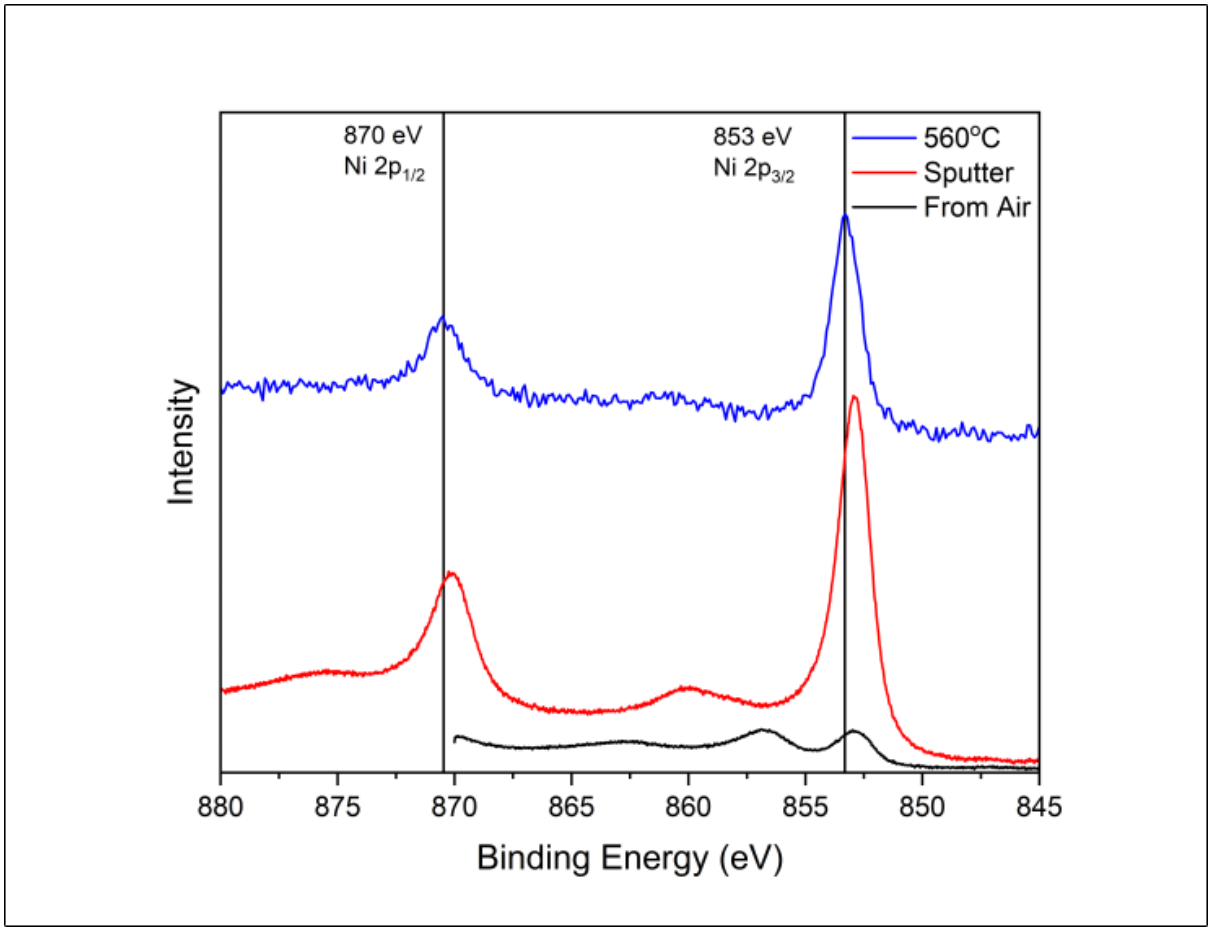

Figure 4.4: XPS spectra for both the Ni $2p_{1/2}$ and Ni $2p_{3/2}$ peaks from air exposure after sputtering and annealing. Vertical black lines show the binding energy values of elemental Ni $2p_{1/2}$ and Ni $2p_{3/2}$.

After sputtering, the Ni(OH)2 peak was completely removed, as no visible shoulder or peak was found. Both the Ni $2p_{1/2}$ and Ni $2p_{3/2}$ peaks were fitted using a single line shape, as with the Ga results. The shape and position of the peaks do not change after annealing.

The data indicate that Ni on the surface appears to be inert towards oxygen, as no oxide was found, whereas it forms a hydroxide on the surface when exposed to air. On the other hand, the majority of the Ga on the surface is oxidised after air exposure. Sputtering and annealing remove the contaminants from the surface.

Data Set	Binding Energy (eV)		
	Ni $2p_{1/2}$	Ni $2p_{3/2}$	$Ni(OH)_2$
Air Exposed	N/A	825.8	856.7
Sputtered	870.2	852.9	N/A
560°C	870.5	853.1	N/A
Elemental [125]	870.1	852.7	856.7

Table 4.3: A table showing the change in binding energy for the Ni $2p_{1/2}$, Ni $2p_{3/2}$ and the $Ni(OH)_2$ peaks due to the preparation conditions. The elemental values are from literature [126] and are present for reference.

4.3.2 Atomic Composition

The atomic composition of the surface was calculated after sputtering for a series of annealing temperatures: 335°C, 400°C, 410°C, 414°C, 441°C, 492°C, 502°C, and 508°C.

$$(1) : \text{Corrected Area (CA)} = \frac{\text{Area} - \text{Background}}{\text{Number of Scans}}$$

$$(2) : \text{Normalised Area (NA)} = \left(\frac{CA}{PC \times IMFP \times ATF} \right)$$

$$(3) : \text{Atomic Composition (AC)} = \frac{\sum \text{NA of one element}}{\sum \text{NA of all elements}} \times 100$$

The corrected area is normalised by three factors: the photoionisation cross section **(PC)**, the inelastic mean free path **(IMFP)**, and the analyser transmission function **(ATF)**. The photoionisation cross section values are taken from the literature, appropriate for the X-ray source employed [128].

$$ATF = (\frac{a^2}{a^2 + \frac{E_k}{E_p}^2})^b \tag{4.1}$$

The inelastic mean free path (IMFP) for Ga_3Ni_2 at the binding energies corresponding to the Ga and Ni peaks was calculated using formula proposed by Tanuma, Powell, and Penn (TPP) TPP-2M [129], [130]. The analyser transmission function (ATF) is specific to each detector and depends on the analyser parameters [131], as described by Equation 4.1, where a and b are detector-specific constants, and E_k and E_p are the kinetic energy of the measured peaks and the pass energy of the XPS scan, respectively.

After normalisation, the atomic composition is determined by calculating the ratio of the normalised area of a given peak to the total normalised area of all detected peaks, expressed as a percentage.

4.3.3 Depth Profile

Typically, XPS measurements are performed with the sample oriented normal to the detector to maximise signal intensity and minimise statistical error. In this geometry, photoelectrons originating from a few nanometres beneath the surface can escape and be detected. For the Ga_3Ni_2 surface, the probing depth under normal emission was estimated to be approximately 24 nm, providing sufficient surface sensitivity. This value was approximated as 3λ [132], where λ is the inelastic mean free path (IMFP) for Ga_3Ni_2, calculated using the TPP-2M method [129].

To further enhance surface sensitivity, the sample can be rotated to increase the emission angle relative to the surface normal, thus making XPS more surface-specific [133], although this comes at the cost of reduced signal intensity. Our experimental setup enables measurements at grazing angles by rotating the sample accordingly (Figure 4.5).

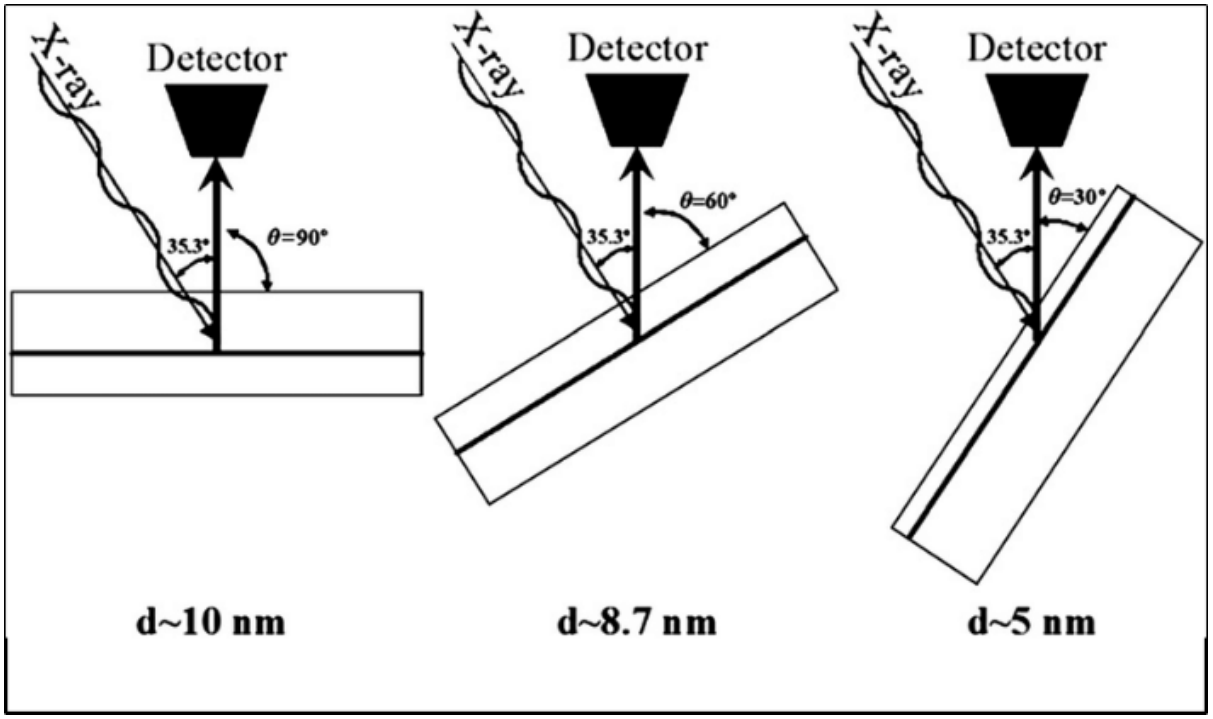

Figure 4.5: Altering the scanning angles affects the depth of the sample being measured using XPS. θ is the angle between the detector and the surface normal. By increasing the angle between the detector and the surface normal, the probing depth is reduced [134].

Atomic Composition As A Function Of Temperature

By measuring the surface chemical composition after sputtering and annealing at increasing temperatures for all three surfaces, we can observe the effects that the preparation conditions have on the Ga and Ni concentrations.

(001) Surface

The results for the (001) surface, shown in Figure 4.6 (A), provide the atomic percentage after each surface treatment. Sputtering induces a significant shift in the atomic composition, with Ga accounting for only 30% of the total atomic composition, compared to the 60% expected from the bulk composition. In contrast, Ni comprises 70% of the surface chemical composition, whereas the expected bulk composition is only 40%.

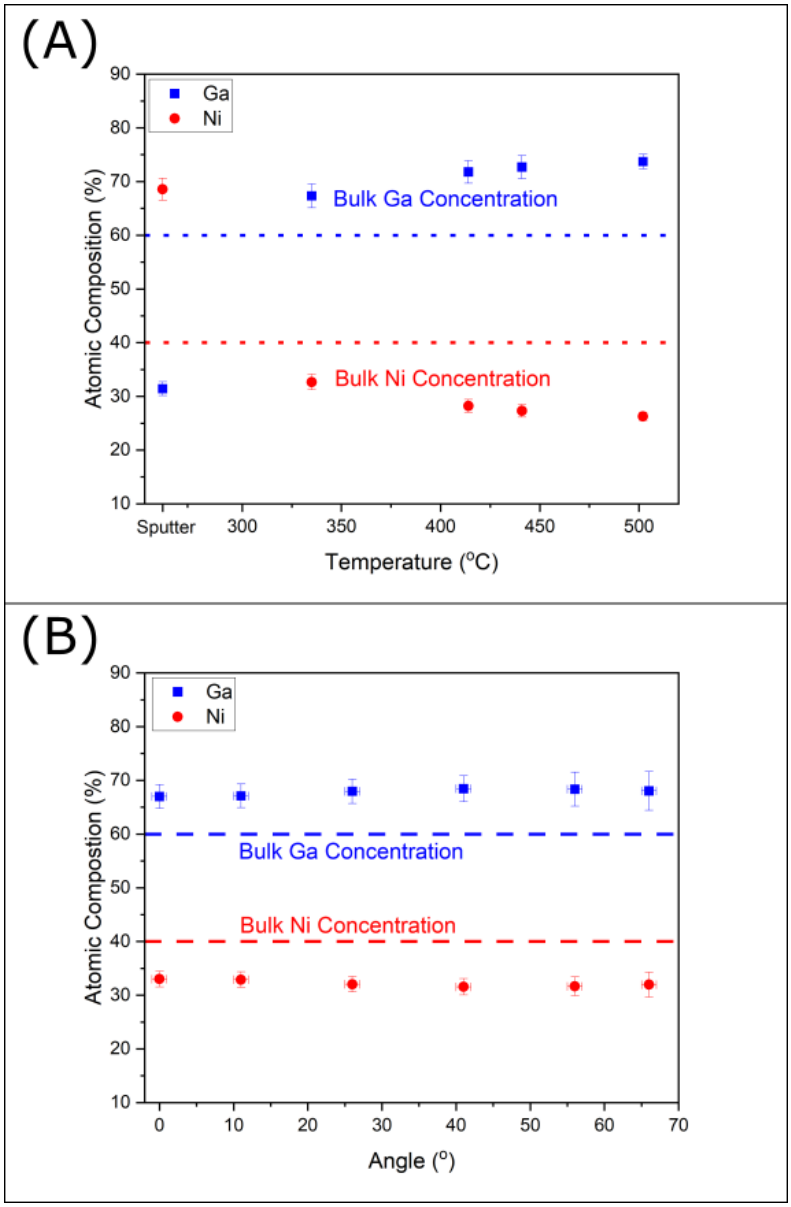

Figure 4.6: (A) The atomic composition of the (001) surface determined via XPS as a function of sputtering and annealing. The bulk composition is highlighted by the dotted lines. (B) The atomic composition of the (001) surface determined via XPS as a function of the scanning angle after annealing to 335°C. The bulk composition is highlighted by the dotted lines.

The data in Figure 4.6 (A) show a clear decrease in the Ga percentage in the topmost layers after sputtering, with a rapid increase following annealing, whereas the inverse trend is observed for Ni. As illustrated in Figure 2.14 (A), the model indicates that Ni atoms are isolated from neighboring Ni atoms by being encapsulated by four Ga atoms. The increase in Ni observed after sputtering could be attributed to the disruption of these Ga cages, exposing more Ni atoms as the surface becomes roughened by sputtering with Ar^+ ions. As the surface is annealed and order is restored, the exposed Ni atoms are re-encapsulated by Ga atoms, as evidenced by the increase in the Ga percentage after annealing.

The decrease in Ga and the subsequent increase in Ni could also indicate that the sputtering process preferentially removes Ga from the surface, resulting in an excess of Ni observed at the surface. Three factors influence the preferential sputtering of an element within an intermetallic compound (IMC): atomic weight, surface free energy, and bonding energy. An element with lower atomic weight, lower surface energy, and lower bonding energy is more likely to be preferentially sputtered [92], [93], [135], [136]. Since Ga is heavier than Ni, atomic weight is not the dominant factor responsible for the preferential sputtering.

When comparing the surface free energy of the constituent elements, Ga has a lower surface free energy than Ni. The surface free energy of the close-packed surface of body-centered tetragonal Ga is 0.661 J/m^2, while that of the close-packed surface of face-centered cubic Ni is 2.011 J/m^2 [78]. This significant difference in surface free energy suggests that Ga, despite being the heavier element, is preferentially sputtered from the surface. This phenomenon has also been observed in the isostructural binary alloy In_3Ni_2, where the heavier In has a lower surface free energy and is preferentially sputtered, as well as in the quasicrystal Ag-In-Yb, where In and Yb, having lower surface free energies, are preferentially sputtered [72], [94], [137].

The In_3Ni_2 (001) surface may provide additional insights into the surface composition of this family of IMCs. Both the (001) surfaces exhibit similar trends in atomic composition after sputtering and annealing, with the secondary element having a lower surface free energy.

Results from the In_3Ni_2 (001) surface, which show preferential sputtering of the non-catalytically active element, align with the findings from the Ga_3Ni_2 (001) surface. This suggests that the preferential sputtering of Ga from the surface could explain the observed results. A similar trend has been noted in Ag-In-Yb and ZnPd, where the heavier elements with lower surface free energy are preferentially sputtered from the surface [80], [137].

After annealing at 335°C, the percentage of Ga increases to 67%, while the percentage of Ni decreases to 33%. This is significantly higher than the bulk composition at a relatively low annealing temperature, with further annealing showing minimal changes in atomic composition. This suggests that the surface has become saturated. These composition changes imply that annealing causes Ga to segregate from the bulk to the surface. Surface segregation in an alloy is defined as the enrichment of the surface by one of the alloy's constituent elements [138], as observed in Figure 4.6 (A).

Surface segregation is driven by three factors in the alloy: the difference in surface energy between the components, the difference in atomic radius, and the bonding energy [139]. Typically, the element with the lower surface energy will segregate to the surface. This effect is more pronounced in interstitial materials rather than crystalline materials, as the atoms in crystalline materials are tightly bound within the crystal lattice, which overcomes the difference in surface free energy.

Both Ga and Ni have similar atomic sizes, so the difference in atomic radius required for Ga segregation is unlikely [139]. The XPS results confirm Ga segregation for all three surfaces, suggesting that the segregation of Ga to the surface is due to Ga having a lower surface free energy compared to Ni. The preferential sputtering and segregation of the heavier element within an IMC due to annealing were also observed in In_3Ni_2 [72].

As In is heavier than Ga, all of the concerns regarding Ga being preferentially sputtered from the surface are also present for In_3Ni_2. However, the results observed in Ga_3Ni_2 matched those from In_3Ni_2, so we can attribute the same conclusion regarding a negative heat solution to both IMCs.

At 335°C, Figure 4.6 (B) shows no change in the atomic composition with the change in grazing angle, with any observed changes falling within experimental error. At 0°, Ga is 6% and Ni is 33%, and at 66°, Ga remains at 67% with Ni still at 33%. This indicates an even distribution of Ga and Ni among the top layers. The increase in the size of the error bars suggests a decrease in the number of photoelectrons being detected.

(2$\bar{1}$0) Surface

Figure 4.7 (A) shows the atomic composition of the (2$\bar{1}$0) surface. After sputtering, the atomic composition reveals that Ga and Ni have similar surface concentrations, with Ga making up 45%, with Ni comprising the remaining 55%. Annealing the surface increases the percentage of Ga to 60% at 402°C and 78% at 508°C. Similar to the (001) surface, Ga segregates from the bulk to the surface. At 400°C, the surface composition is approximately equivalent to that of the bulk, with a ratio of 60% Ga to 40% Ni.

In Figure 4.7 (B), the atomic percentages from the (2$\bar{1}$0) surface are plotted as a function of grazing angle. A reduced angle range was used due to the difference in source-detector geometry of the UHV chamber.

The results in Figure 4.7 (B) show little change in the atomic composition as the grazing angle increases. These results suggest that Ga is evenly distributed among the top layers of the surface, similar to the (001) surface, as seen in Figure 4.6 (B). However, due to the shallow angle range used, any potential Ga enrichment at the topmost layer may not have been detected.

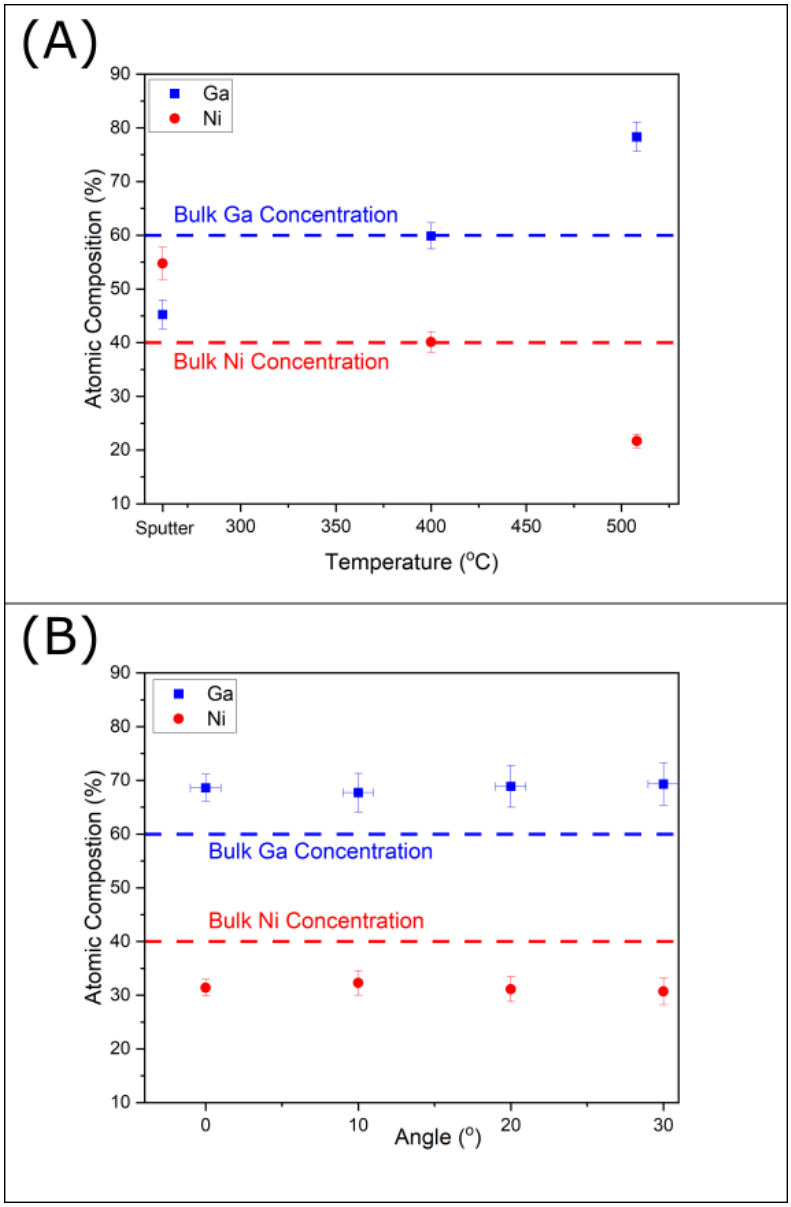

Figure 4.7: (A) The atomic composition of the $(2\bar{1}0)$ surface determined via XPS as a function of sputtering and annealing. The bulk composition is highlighted by the dotted lines. (B) The atomic composition of the $(2\bar{1}0)$ surface was determined via XPS as a function of scanning angle. The bulk composition is highlighted by the dotted lines.

(100) Surface

Figure 4.8 (A) shows the change in the atomic composition of the (100) surface after sputtering and annealing at increasing temperatures. After sputtering, the surface consists of 50% Ga and 50% Ni. Comparing this result to the other two Ga_3Ni_2 surfaces, we can observe that Ga is preferentially sputtered from all three surfaces.

For the (100) surface, we were able to record lower annealing temperatures, starting at 250°C. At this temperature, the Ga% begins to increase, approaching the bulk composition, as denoted by the blue and red dashed lines in Figure 4.8 (A). The surface chemical composition matches the bulk composition after annealing at 300°C. Increasing the annealing temperature further causes the Ga% to increase and the Ni% to decrease, surpassing the bulk composition, with Ga composing over 73% of the surface after annealing at 500°C.

Figure 4.8 (B) shows the atomic composition of the surface after annealing at 410°C at grazing angles of 0°, 11°, 26°, 41°, and 56°, which was the maximum angle at which the sample could be tilted further without the risk of the sample falling out of the manipulator. These results were recorded separately from the temperature-dependent data and are not included in Figure 4.8 (B). The atomic composition does not change as the grazing angle increases from 0° to 41°, with a slight increase in Ga from 83

The increase in Ga by 2% is within experimental error for XPS results, especially considering the reduction in intensity recorded at such extreme angles. The results from Figure 4.8 (B) show that Ga and Ni are evenly distributed among the top few nanometers of the (100) surface, which is consistent across all three surfaces.

The (001), $(2\bar{1}0)$, and (100) surfaces all show Ga segregating from the bulk to the surface after being sputtered away. With the results of all three surfaces being consistent, it can be concluded that Ga is preferentially sputtered from the surface and then segregates to the surface after annealing.

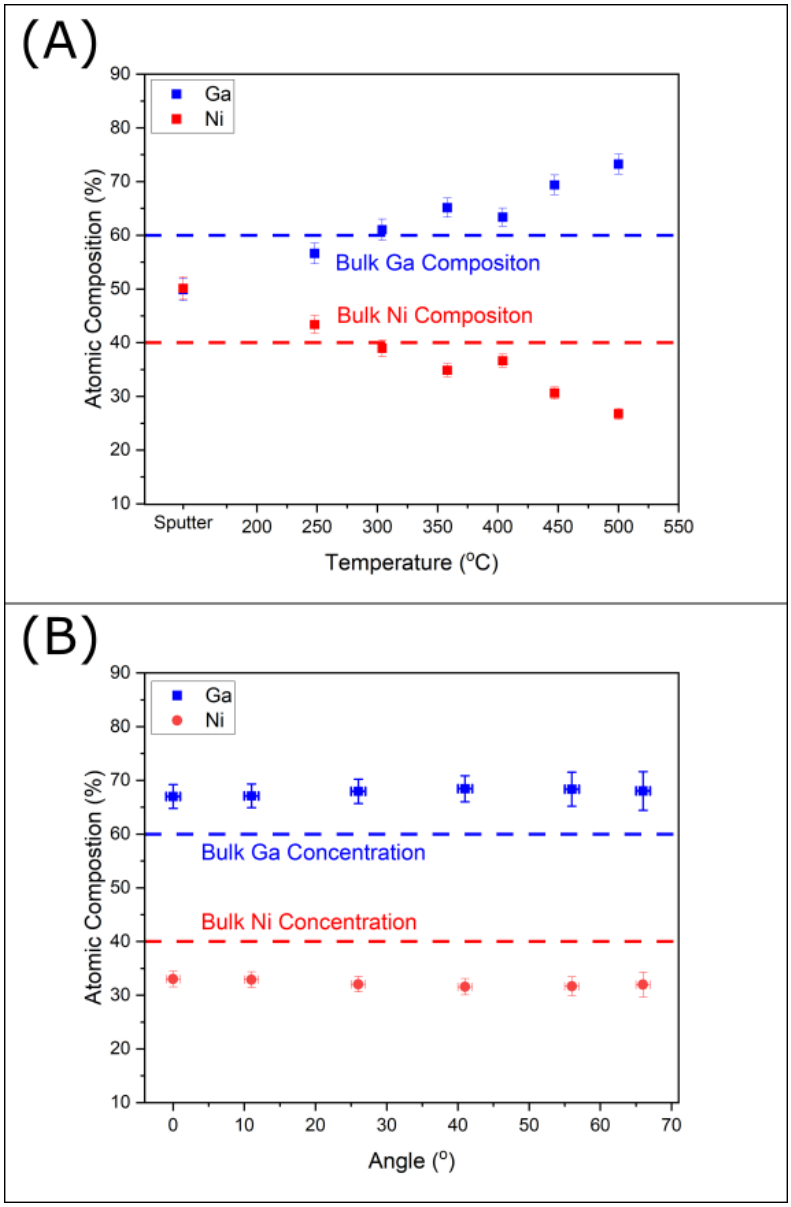

Figure 4.8: (A) The atomic composition of the (100) surface determined via XPS as a function of sputtering and annealing. The bulk composition is highlighted by the dotted lines. (B) The atomic composition of the (100) surface determined via XPS as a function of scanning angle after being annealed to 410°C. The bulk composition is highlighted by the dotted lines.

4.3.4 Comparison of the (001) surfaces for Ga_3Ni_2 and In_3Ni_2

In_3Ni_2 is an isostructural crystal to Ga_3Ni_2, which is also part of the Al_3Ni_2 family of catalysts discussed in Chapter 2. It has been studied by a fellow PhD student at the University of Liverpool. All of the In_3Ni_2 results are attributed to Ahowd Youssef Alfahad and sourced from [72].

By comparing the (001) surface of both Ga_3Ni_2 and In_3Ni_2, we can see how the secondary elements present within these intermetallic compounds affect the (001) surface, and which phenomena are intrinsic to the Al_3Ni_2 family of catalysis and which ones can be related to the presence of Ga or In within the intermetallic compound.

Figure 4.9 (A) and (B) show how the atomic composition changes as a function of annealing temperature. From Chapter 4, it was confirmed that Ga segregates from the bulk to the surface after annealing for all three surfaces. Figure 4.9 (B) shows that for In_3Ni_2, after sputtering, Ni constitutes approximately 60% of the surface composition, indicating that In is also preferentially sputtered from the surface. After annealing to 310°C for ninety minutes, the composition of the surface shifts to In, composing over 70% of the surface.

Both In and Ga segregate from the bulk to the surface for the (001) surface, which is attributed to the surface free energy of both In and Ga being lower than that of Ni [140]. Both surfaces terminate on the bonded Ni planes, so both Ga/In and Ni are present in the topmost layers, confirmed through angle-resolved XPS on both surfaces and LEIS in In_3Ni_2 [72].

Both samples reach a plateau in secondary element composition, with only minor fluctuations recorded within experimental error. The angle-resolved results shown in Figure 4.6 (B) indicate that Ga is evenly distributed among the top layers.

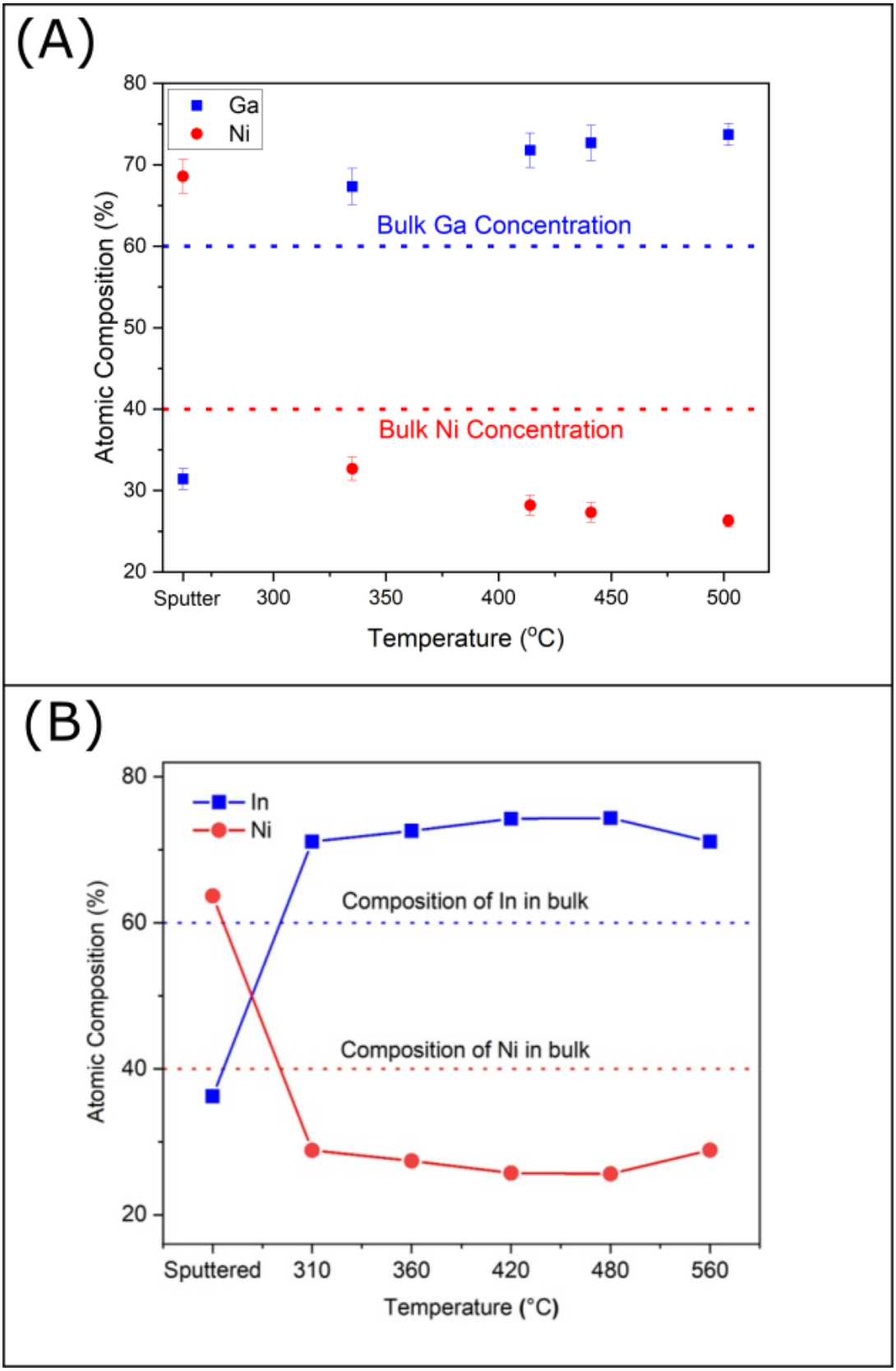

Figure 4.9: The atomic composition of the (001) surface for both Ga_3Ni_2 (A) and In_3Ni_2 (B) both determined via XPS as a function of annealing temperature. (B) was adapted from [72].

4.4 Summary

This chapter investigates the effects of the preparation conditions on the surface chemical composition of all three Ga_3Ni_2 surfaces.

Sputtering increases the percentage of Ni visible on all three Ga_3Ni_2 surfaces beyond the bulk composition, as shown in Figures 4.6 (A), 4.8 (A), and 4.7 (A). This has been attributed to the preferential sputtering of Ga from the surface due to Ga having a lower surface free energy than Ni. The phenomenon of the heavier element with the lower surface free energy being preferentially sputtered from the surface has been observed in In_3Ni_2, where In is preferentially sputtered from the surface [72], and in Ag-In-Yb [137], where preferential sputtering of the heavier elements, In and Yb, with lower surface free energies has also been observed.

Annealing the surfaces caused Ga from the bulk to segregate to the surface in all cases, as seen in Figures 4.6 (A), 4.8 (A), and 4.7 (A), which is also attributed to Ga having a lower surface free energy. Similar results were observed from the In_3Ni_2 (001) surface as well, where In segregated to the surface after annealing.

The angle dependant results shown in Figures 4.6 (B), 4.8 (B), and 4.7 (B) showed that all three samples have Ga and Ni evenly distributed among the topmost layers. This can not confirm the presence of both Ga and Ni on the topmost layer. A low energy ion scattering (LEIS) study performed on the (001) surface by Ahowd Alfahad, discussed in Chapter 5 and shown in Figure 5.9, confirmed that the topmost surface layers contain both Ga and Ni atoms.

To achieve a surface composition similar to that of the bulk and to observe the (1×1) bulk unit cell through LEED, each of the Ga_3Ni_2 surfaces would need to be annealed to different temperatures. For the $(2\bar{1}0)$ surface, annealing at 400°C for ninety minutes, as shown in Figure 4.7 (A), produced a surface composition akin to the bulk. The (001) surface will require annealing at 300°C for ninety minutes to achieve bulk composition, as shown in Figure 4.8 (A). For the (001) surface, a lower range of annealing temperatures is required to determine when the surface composition matches the bulk composition, as the Ga% exceeded 65% after annealing at 335°C, the lowest recorded temperature.

Chapter 5

Surface Atomic Structure of Ga_3Ni_2

5.1 Introduction

This chapter presents the atomic structure of Ga_3Ni_2 (001), $(2\bar{1}0)$, and (100) surfaces studied by LEED and STM. LEED results demonstrate how the LEED images are affected by sputtering and annealing at different temperatures. The XPS results presented in Chapter 4 revealed Ga segregation from the bulk to the surface during annealing. Here, we will investigate how this segregated Ga influences the surface symmetry.

STM results for the Ga_3Ni_2 (001) and $(2\bar{1}0)$ surfaces will be discussed. We begin by calculating the step height for each surface to understand surface morphology and identify which plane the surface terminates on. The step height and features observed in the high-resolution STM images will be compared with the model structures. In Chapter 4, it was shown that Ga segregates from the bulk to the surface after annealing.

5.2 Experimental Details

Single grain samples were grown by the Czochralski method [30] and cut to expose the (001), $(2\bar{1}0)$, and (100) surfaces. After being manually polished using progressively smaller grits of diamond paste from 6 μm to 0.25 μm, each sample was prepared under UHV with several cycles of sputtering (Ar^+, thirty minutes, 2 keV, drain current 6 μA / 28 μA) and annealing (525°C, ninety minutes), where the annealing temperature was recorded through an optical pyrometer at an emissivity of 0.2.

LEED patterns were recorded after sputtering and annealing over a range of temperatures (335°C - 525°C). A series of LEED patterns were recorded with an electron beam energy from 1 - 200 eV every 1 eV (base pressure 1×10^{-9} mbar). Covering the 1 - 200 eV range ensures that the most surface-sensitive LEED images will be recorded.

The quality of the surface was checked via LEED. These STM experiments were conducted in two laboratories: the University of Liverpool, where the base pressure while scanning was 2×10^{-9} mbar, and the Institut Jean Lamour, Nancy, where the base pressure while scanning was 4.7×10^{-10} mbar. Both experiments used the same preparation method as discussed above and the same Ga_3Ni_2 samples.

The STM images used in this thesis were recorded in two laboratories, Institut Jean Lamour in Nancy and the Surface Science Research Center in Liverpool. To ensure the results are accurate, all of the STM apparatus were calibrated using a material with known dimensions, which was easy to scan via STM. HOPG was used as it is a well-researched surface [141], ensuring we were able to calibrate the surface before scanning each of the surfaces.

To prepare the surface sufficiently to produce high-quality STM images, each sample must be annealed at temperatures where Ga segregation has occurred. The abundance of Ga on the surface caused issues with obtaining STM images, especially at the atomic scale. After pulsing the tip, the image quality would drastically decrease as the tip pulled weakly bonded materials from the surface, ruining the prepared tip. After further pulsing to sharpen the tip, large blobs of material would be deposited over the surface.

5.3 Results and Discussion

5.3.1 Surface Model Structure

Figure 5.1 shows the unit cell of all three Ga_3Ni_2 surfaces with a side-on view followed by a head-on view of all three surfaces. By adding the bonds between the nearest-neighbour atoms, Figure 5.1 shows that the Ni atoms are only connected to the nearest Ga atoms and vice versa; the surrounding Ga atoms are only bonded to Ni atoms. This suggests that the Ni atoms are anchored into the unit cell by the Ga atoms, which encompass the Ni atoms in a tetrahedral shell seen in Figure 3.20 (C).

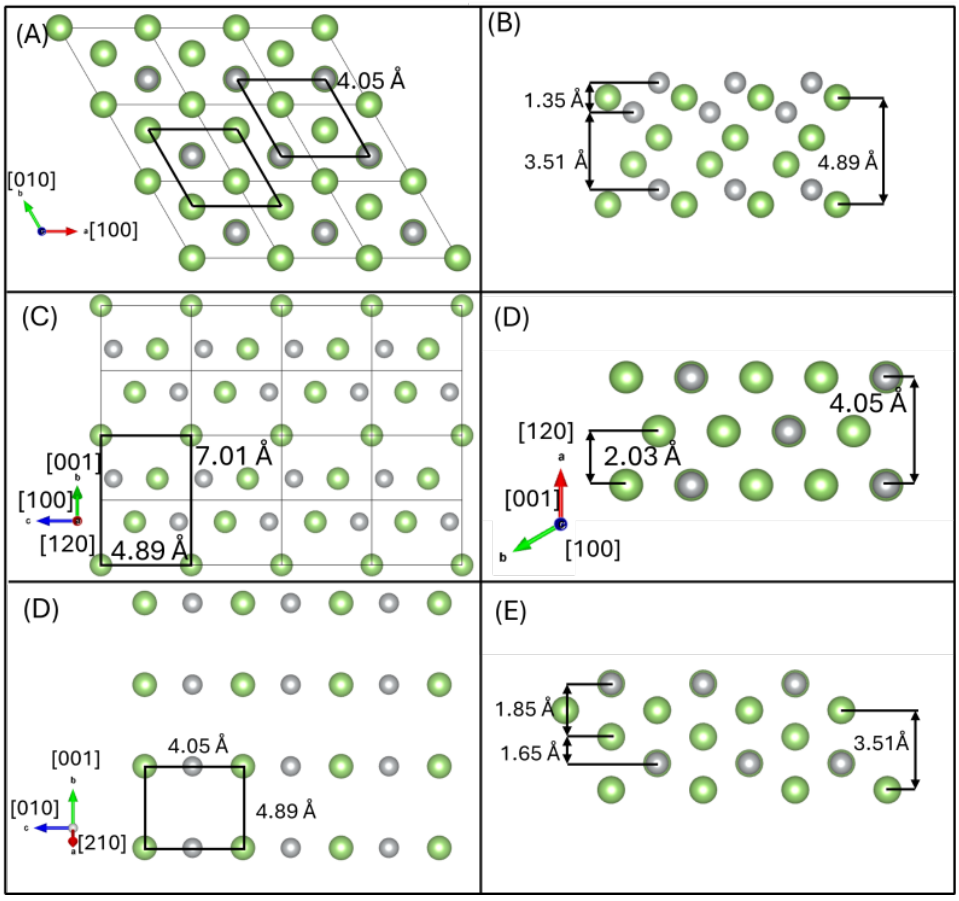

Figure 5.1: Model structures of all the Ga_3Ni_2 surfaces, with the nearest neighbour bonds shown. Ga atoms are in green and Ni atoms are in silver. (A) and (B) show the side profile, with the step heights given, and the top view, with the unit cell dimensions of the (001) surface. (C) and (D) show the side profile, with the step heights given, and the top view, with the unit cell dimensions of the (100) surface. (E) and (F) show the side profile, with the step heights given, and the top view, with the unit cell dimensions of the $(2\bar{1}0)$ surface.

Figure 5.1 (A) shows a Model of the (001) surface, which exhibits a rhombus unit cell with a dimension of 4.05 Å which can be mapped over both the Ga and Ni layers. Figure 5.1 (B) shows several (001) layers stacked vertically, showing the slight offset of the Ga and Ni atoms. The surface can be considered a buckled layer consisting of the topmost Ni and Ga layers.

Two of the three distances given, on the left, are the distances between the pure Ni planes, while the value on the right is the height of the unit cell. From the STM results, it was concluded that the Ni to Ni steps were being observed in addition to the unit cell height.

Figure 5.1 (C) shows the $(2\bar{1}0)$ surface unit cell showing a large rectangle with sides of 7.01 Å and 4.89 Å. Figure 5.1 (D) shows three $(2\bar{1}0)$ planes stacked vertically, each plane is identical being a mixture of Ga and Ni atoms, each plane being equidistant from each other at 2.03 Å or $a/2$ where a the corresponding lattice parameter equal to 4.05 Å.

The Model of the Ga_3Ni_2 plane (100) shown in Figure 5.1 (E) shows the (1×1) rectangular unit cell with sides of 4.05 Å and 4.89 Å. Figure 5.1 (F) shows several (100) planes stacked vertically, the planes are either pure Ni, pure Ga or a mixed Ga and Ni plane, as shown in Figure 5.1 (E). The distances provided show the distance between each of the individual planes starting from the pure Ni and Ga planes.

5.3.2 Ga_3Ni_2 (001) Surface

Surface Structure by LEED

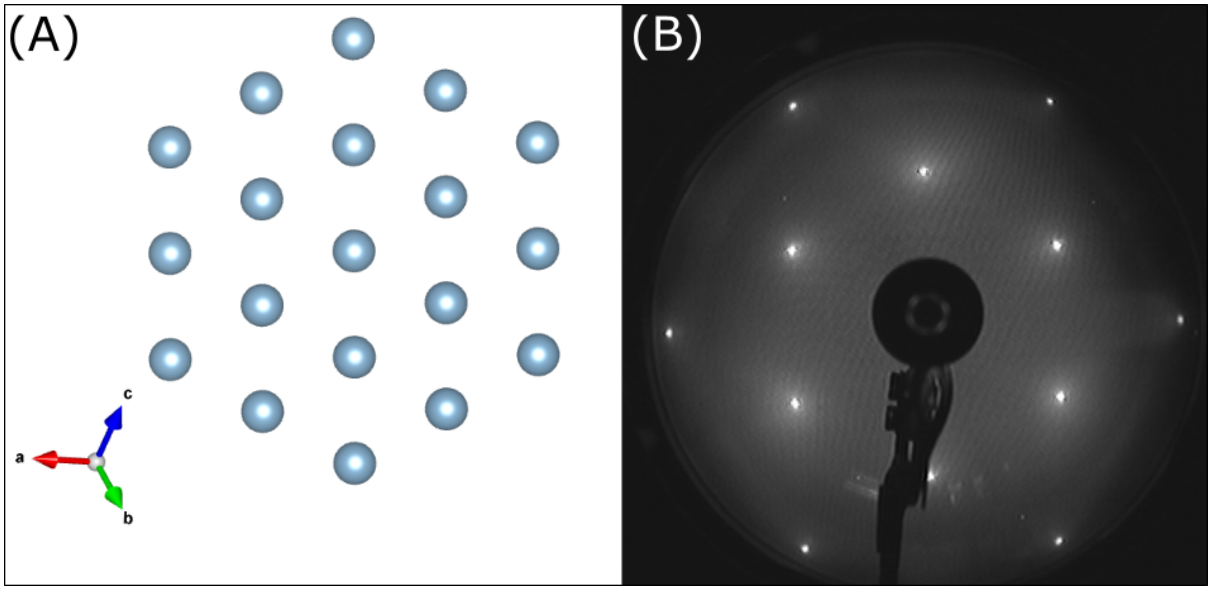

Figure 5.2: (A) The Model of Al (111) showing the surface unit cell. (B) LEED image of Al (111) at 74 eV with Bragg peaks highlighted by white circles.

As no prior LEED analysis had been carried out on Ga_3Ni_2 surfaces, the results were calibrated using LEED images from the Al (111) surface. Figure 5.2 (A) shows the model structure of the Al (111) plane with a hexagonal unit cell and a lattice constant of 2.86 Å.

Figure 5.2 (B) shows a LEED image of the Al (111) surface taken at 74 eV. The expected unit cell can be calculated using Equation 5.1.

$$A = \frac{2\pi}{a * sin(\theta)} \tag{5.1}$$

Where a is the known real-space length of the lattice vector and A is the reciprocal space distance. The reciprocal unit vector is obtained from the LEED pattern.

$$CF = \frac{A}{B} \tag{5.2}$$

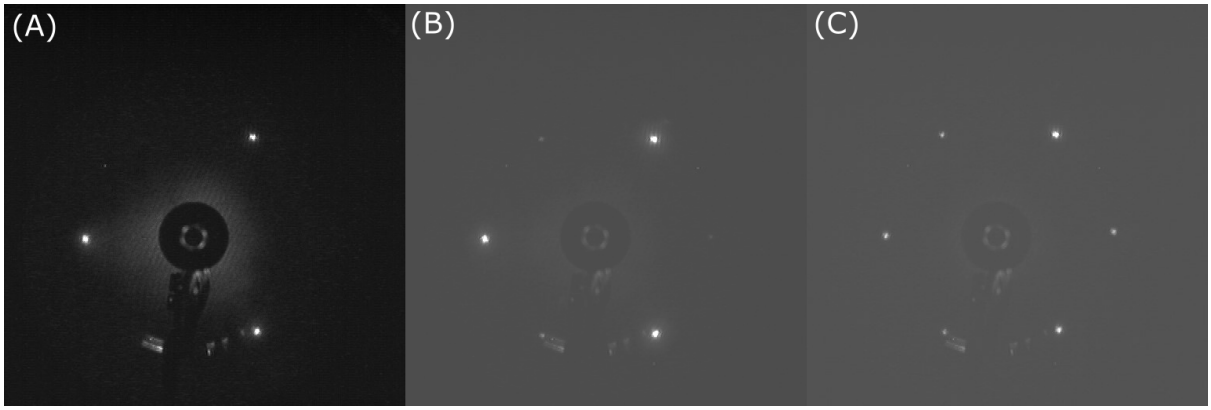

Figure 5.3: LEED patterns for Ga_3Ni_2 (001) surface after sputtering (A) and annealing at 335°C (B) and 525°C (C). The beam energy is 74 eV for all patterns. Spots are highlighted by circles.

CF is the conversion factor that converts the reciprocal unit vector measured from the LEED image, BB, in equation 5.2, into inverse angstroms using the value AA in equation 5.2. By using Al (111), which has a known lattice vector length, aa, we can produce a CF that is usable to convert the reciprocal unit vector for all of the Ga_3Ni_2 surfaces. The CF is sensitive to the beam energy, so it will need to be recalculated for each beam energy used.

With the conversion factor calculated, the next step was to obtain appropriate LEED images from all three of the Ga_3Ni_2 surfaces. For the conversion factor to be applied, the Ga_3Ni_2 LEED images are recorded at the same distance from the phosphorescent screen. The LEED images were recorded by a permanently mounted camera kept in darkness at a fixed point from the phosphorescent screen.

To compare the LEED patterns to the model structure, we first present the atomic structure of the (001) plane in Figure 5.1. The green spheres represent Ga, and the silver spheres represent Ni. The surface unit cell is a rhombus with a dimension of 4.05 Å as marked in Figure 5.1 (A). Figure 5.3 shows the LEED patterns after sputtering and annealing at different temperatures, all at the same beam energy of 74 eV. Typically, no LEED patterns are expected from the sputtered surface because the process roughens it. However, our data shows a LEED pattern, as seen in Figure 5.3 (A). As expected from the rough surface, the LEED pattern has a high background.

After annealing the surface at 335°C (Figure 5.3 (B)), a sharp hexagonal pattern with a low background can be observed in an energy range of 18 - 200 eV. Higher annealing temperatures do not cause any further change in the LEED patterns. The dimensions of the unit cell recorded from the LEED pattern, when converted from reciprocal into real space, match the dimensions of the unit cell from the model, confirming that the surface corresponds to a bulk truncation. The segregation of Ga to the surface has not influenced the surface symmetry.

Surface Structure by STM

Step Terrace Morphology

STM images of the surface were taken after annealing at different temperatures, starting at 335°C and going up to a maximum of 525°C. No steps or terraces were observed until annealing at 450°C, where clearly defined step edges became visible. An STM image taken after annealing at 525°C is shown in Figure 5.4 (A), which shows large flat terraces.

The step heights were analysed from STM images recorded within the annealing temperature range of 450°C to 525°C. Height histograms in the vicinity of a step edge were used to determine the step height. An example of a height histogram is shown in Figure 5.4 (B). STM images from six different areas of the surface, after different preparation cycles, were analysed. In total, 110 steps were measured over an area of 760 μm^2, with three average step heights observed: 5.1 Å, 1.8 Å, and 3.8 Å with the error being the standard error of the mean. The 5.1 Å high steps were found most frequently (94%), while 1.8 Å and 3.8 Å steps were rarely observed (3% each). The highest step is composed of the two smaller steps as shown in Figure 5.4 (C).

Large white spots can be seen mostly at the step edges and a few in the middle of the terraces (Figure 5.4 (A)). These spots protrude from the surface at a height of a few nm. It is unlikely that these spots are due to surface contamination, as XPS results showed no contaminants on the surface. They could be due to segregated Ga collecting on the surface in random clusters, as these clusters were observed throughout the surface. Alternatively, these could be leftover Ga_3Ni_2 that did not diffuse onto the step edges or into the surface during surface preparation.

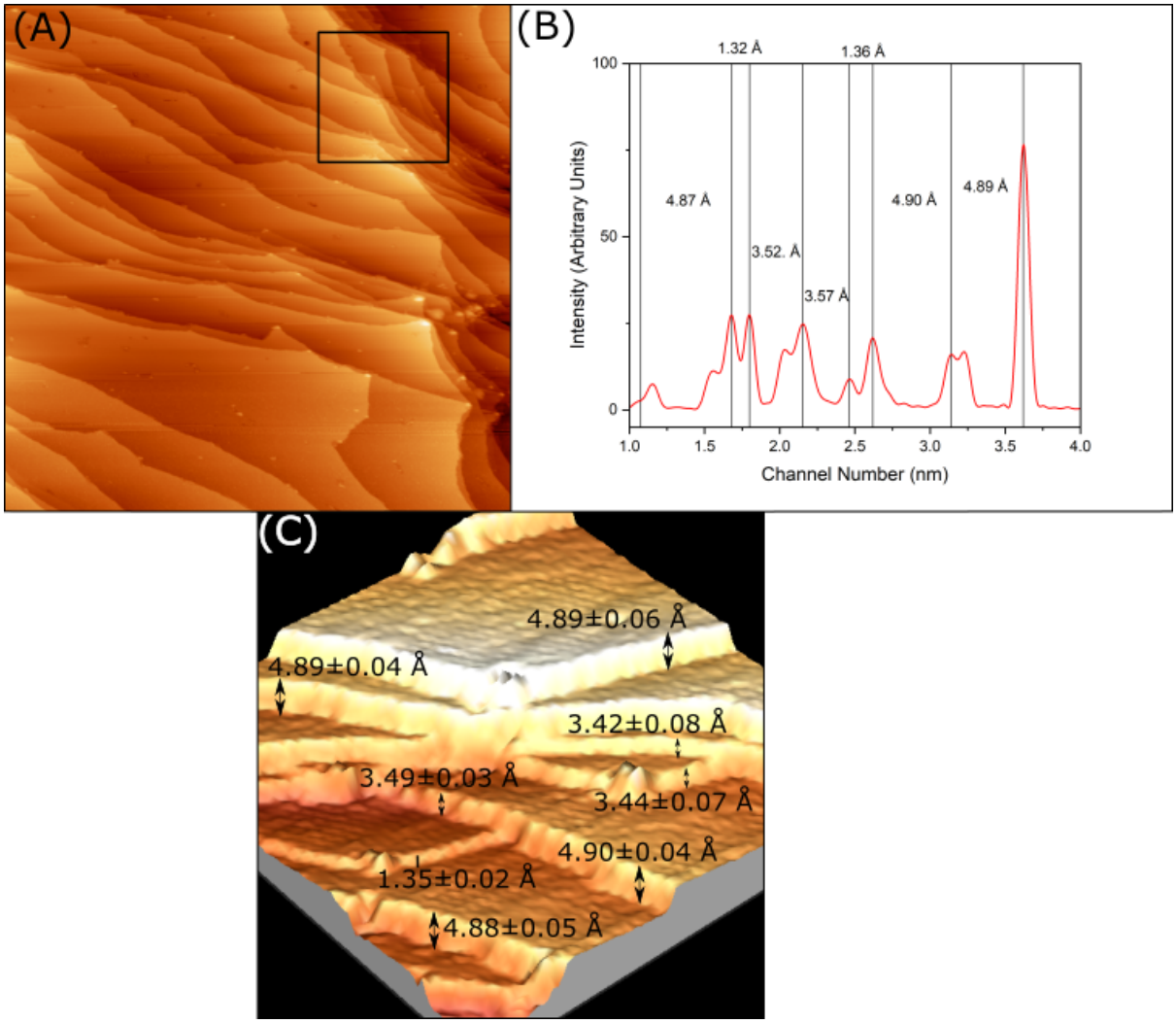

Figure 5.4: (A) A 400×400 nm^2 STM image from the (001) surface. (B) Height histogram from the section of (A) marked by the black square, showing three different step heights (4.89 Å, 1.35 Å and 3.51 Å). The histogram underwent 3-point levelling to reduce the noise present, producing cleaner peaks. (C) A 3D section of (A) marked by the black square showing the miniature steps that make up the larger steps. The sub-steps are marked and their average heights given, plus error.

Atomic Resolution

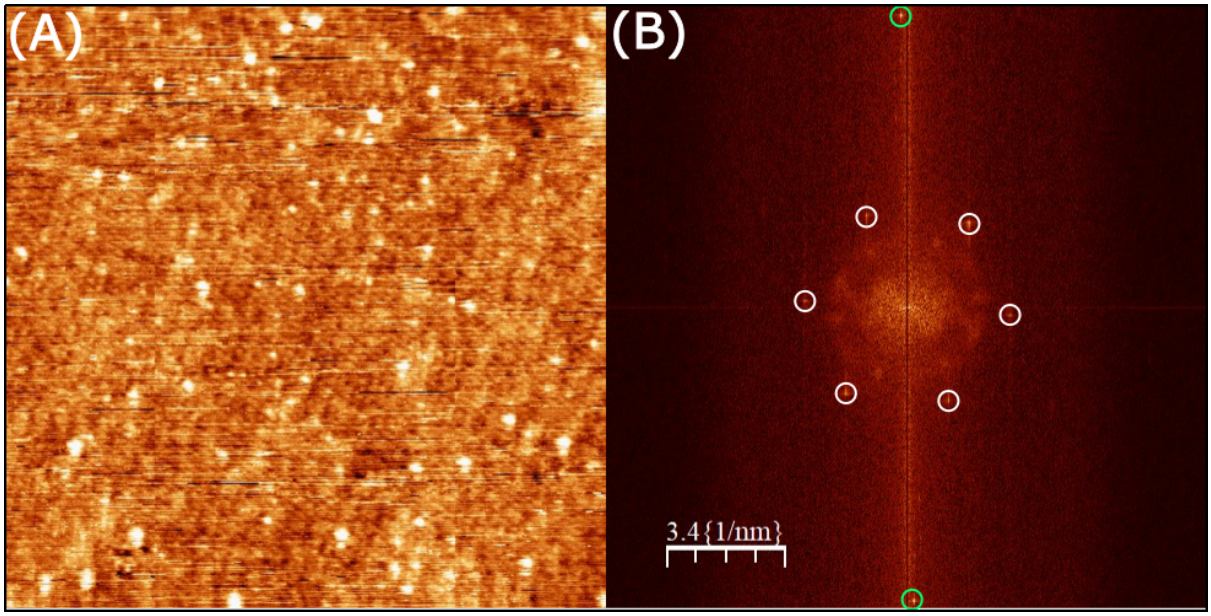

Figure 5.5: (A) 20×20 nm^2 STM image of the Ga_3Ni_2 (001) surface. A row of dots is visible running diagonally across the surface, showing structure on the surface. White patches are randomly dotted over the surface. (B) FFT of (A) with the peaks attributed to the noise highlighted in green and those from the surface in white.

For all of the STM results recorded at the Institut Jean Lamour in Nancy, a 25 *Hz* noise is present due to a standing wave vibration in the building. Each of the chambers is isolated on a concrete block to reduce the effects of noise; however, the 25 *Hz* noise persisted. It was not possible to remove the noise during the measurements. However, during data analysis, the noise could be filtered. Figure 5.5 (B) shows a fast Fourier transformation (FFT) of high-resolution STM images with noise.

The features at the top and bottom of the FFT image are due to the noise. The noise has been filtered from the STM data presented in this section. After selecting a flat section of the (001) surface, decreasing the scan speed, and adjusting the remaining scan parameters to produce an image, the system was left to scan the same window several times to reduce the impact of drift.

Figure 5.5 shows a 20×20 nm^2 STM image from a terrace. Across the centre of the image, the resolution improves due to the tip changes. Large white features with irregular shape and size, similar to the ones seen in Figure 5.4 (A), appear randomly across the image.

Filtering the image by height to select these protrusions did not produce an FFT pattern or a pattern after autocorrelation was performed on these features. The lack of any symmetry present means they are occurring randomly. These white patches are ubiquitous across the entire surface. The FFT of Figure 5.5 shows hexagonal symmetry as expected from the LEED. The lattice constant determined from the FFT was 4.05 Å ± 0.1 Å, which is consistent with the Model structure and LEED results.

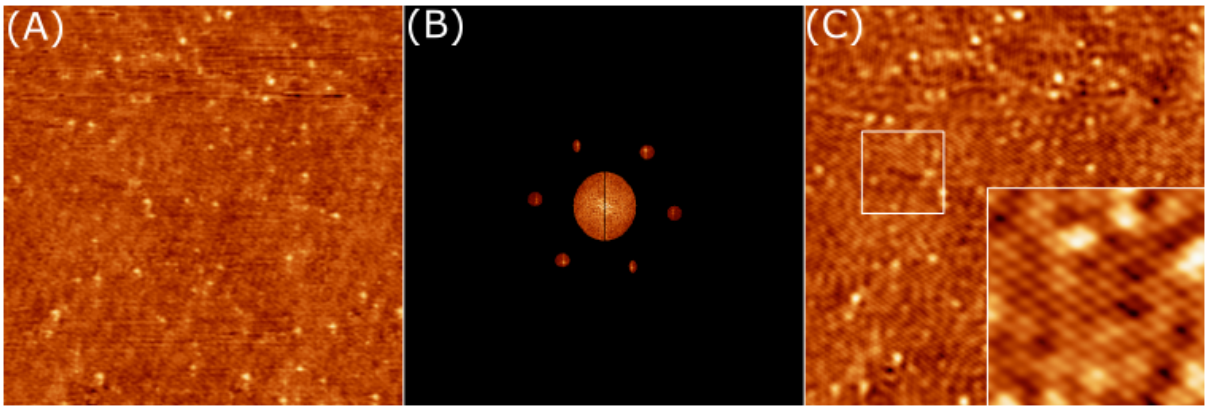

Figure 5.6: (A) The inverse FFT of Figure 5.5 (A). (B) The filtered FFT used to produce (A). All six of the brightest maxima were selected in addition to the background in the centre. (C) The filtered FFT converted back to real space showing the (1×1) structure on the (001) surface.

After filtering the six maxima along with the background from the centre of the FFT, these results were converted back into real space through a reverse FFT to highlight the underlying surface structure. Figure 5.6 (A) shows that after filtering, points can be observed forming hexagons. The average size of the hexagons is 4.0 ± 0.1 Å, which is consistent with the Model values (4.05 Å). After overlaying atoms in the Ni plane from the Model onto a section of the STM image (Figure 5.6 (C)), we were able to observe that the bright features observed in STM matched the position of the Model atoms.

The STM results for the Ga_3Ni_2 (001) sample show three different step heights (5.1 Å, 2.0 Å, and 3.9 Å). The step heights are consistent with the distance between Ni planes from the model, indicating that the surface is Ni-terminated. The atomic resolution observed from the high-resolution images matches the atomic structure in the Ni plane. The STM results are consistent with the LEED, showing a (1×1) pattern.

Weak Superstructure

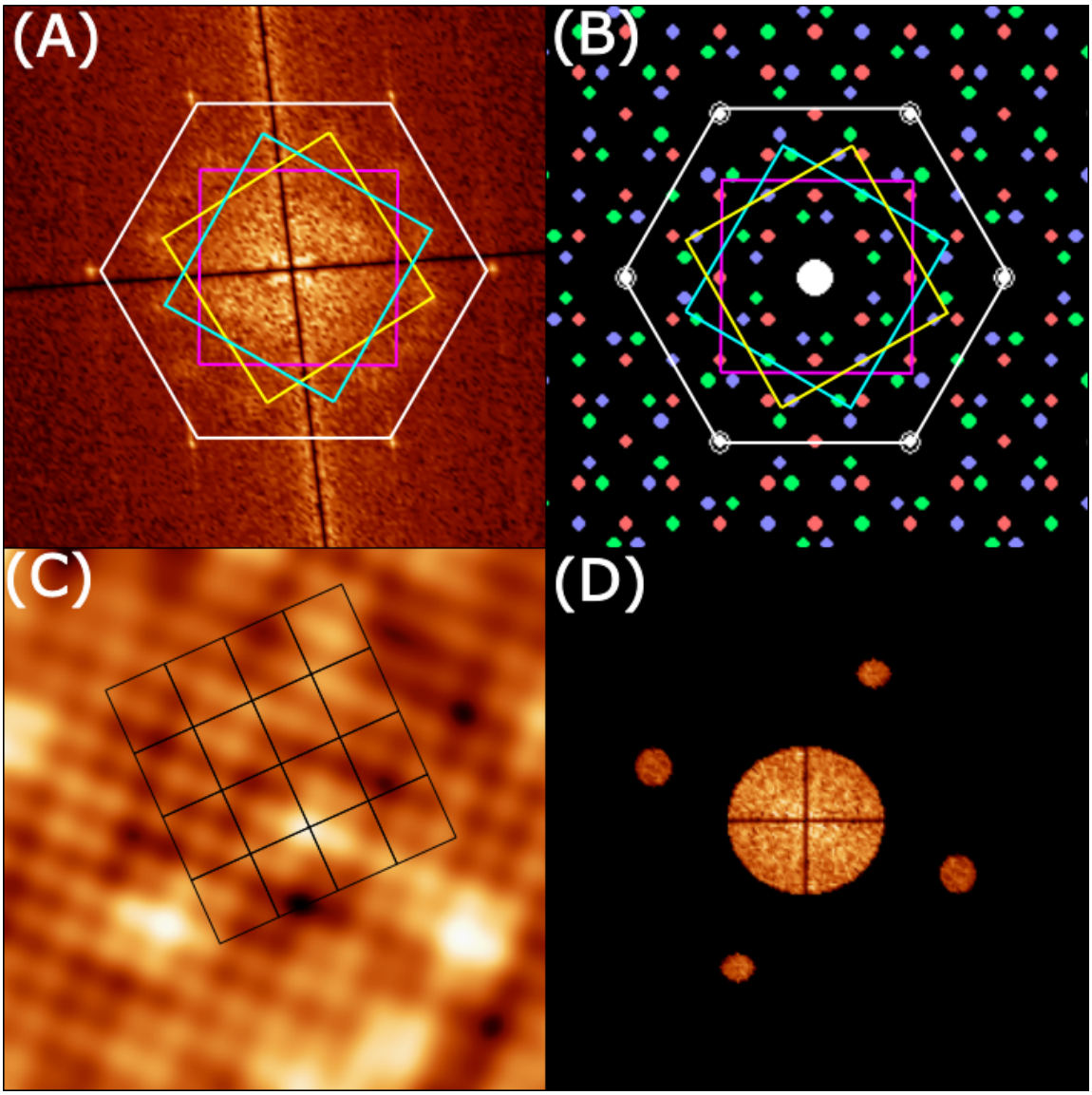

Figure 5.7: (A) The FFT of a high resolution STM image from the (001) surface showing the six bright spots from the (1×1) structure and the twelve diffuse spots resulting from a weak superstructure. (B) The reciprocal space of a three-domain $c(2\sqrt{3} \times 4)$ superstructure, where different colours represent the reciprocal space of three different domains. (C) The inverse FFT of selected superstructure spots shown in (D) with a selected superstructure domain highlighted. (D) The Filtered FFT showing one example of the selected domain.

Figure 5.5 (B) shows the FFT of an STM image from the (001) surface. In addition to the expected peaks from the surface symmetry, there is an inner ring with twelve diffuse spots. These weak spots are highlighted in the magnified FFT in Figure 5.7 (A). These weak spots indicate that a weak superstructure is present on the surface.

Alfahad et al. have shown a superstructure of three domains $c(2\sqrt{3} \times 4)$ on the (001) surface of isostructural In_3Ni_2 [72]. This superstructure was induced by hydrogen present within the UHV chamber. The reciprocal space of this superstructure is shown in Figure 5.7 (A), where the spots in different colours arise from the three different domains. The weak spots observed in the FFT of the STM image match the spots that arise from the $c(2\sqrt{3} \times 4)$ superstructure shown in Figure 5.7 (B). This indicates that our surface also undergoes this superstructure, but the order of the superstructure is very weak.

We also analysed the inverse FFT of each of the three superstructure domains, one example is shown in Figure 5.6 (C), where we can identify a central rectangular unit cell as expected. The dimensions of this unit cell are different from the expected for the $c(2\sqrt{3} \times 4)$ superstructure because we used the second-order spots to calculate the inverse FFT (the first-order spots were not observed in the FFT, Figure 5.7 (D)), and also the superstructure spots are not being fully resolved, which will produce some inaccuracy within the calculations. However, the aspect ratio for the unit cell in the inverse FFT (1.13) closely matches the expected ratio of $\frac{4}{2\sqrt{3}} = 1.16$.

Surface Termination

We will now discuss the possible surface terminations. Three models will be discussed. For this, we present a side view of the (001) surface in Figure 5.8. Model One will explain the surface termination with Ni atoms on the topmost layer bonded to Ga atoms in the layer below (the layers are marked by 1 and 4 in Figure 5.8). In this model, the distance between the Ni atoms on the topmost layer and the Ga atoms in the layer below is 2.61 Å apart; therefore, these atoms are likely to be bonded to each other. Model Two will explain the surface termination with Ga atoms on the topmost layer bonded with the Ni atoms in the layer below (the layers marked by 0 and 3 in Figure 5.8).

The distance between the Ga atoms on the topmost layer and the Ni atoms in the layer below is 2.42 Å so these atoms are likely bonded. Model Three shows the surface termination on the consecutive Ga planes (the layers are marked by 0, 2, and 3 in Figure 5.8). If the surface terminated on plane 2, the Ga atoms from the top layer would be bonded to the Ga atoms in the layer below.

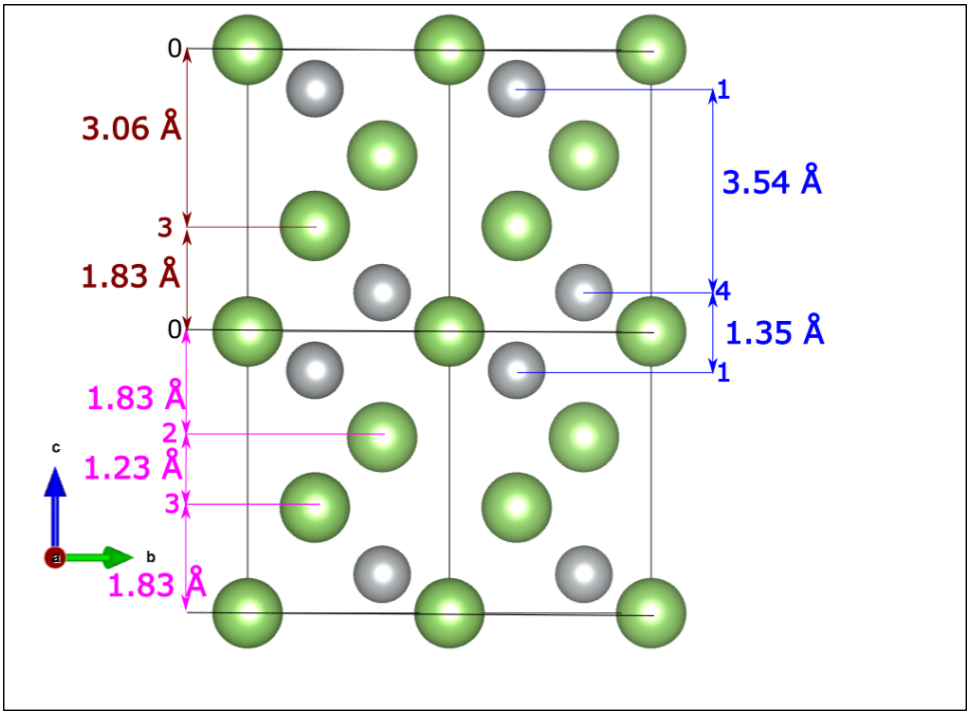

Figure 5.8: The model structure of vertically stacked (001) planes with the three proposed surface termination models, the expected step heights for each model are shown. Model One shows the surface termination with the Ni atoms on the surface, marked by the planes 1 and 4 in blue. Model Two shows the surface termination with Ga atoms on the surface, marked by the planes 0 and 3 in red. Model Three, the Ga surface termination utilises all of the Ga layers, marked by the planes 0, 2 and 3 in magenta.

The step heights expected from Model One are 3.54 Å and 1.35 Å, or their combination, 4.89 Å. These step heights were observed via STM, as shown in Figure 5.4 (C). However, the step heights expected for Model Two (3.06 Å and 1.83 Å) are also close to the measured step heights within experimental errors. Therefore, the Model Two of surface termination is also possible.

We rule out the surface termination with Model Three. If the surface terminated on all three of the consecutive Ga planes, we would expect to see three small steps of 1.83 Å, 1.23 Å, and 1.83 Å appearing consecutively. However these steps were not observed by STM

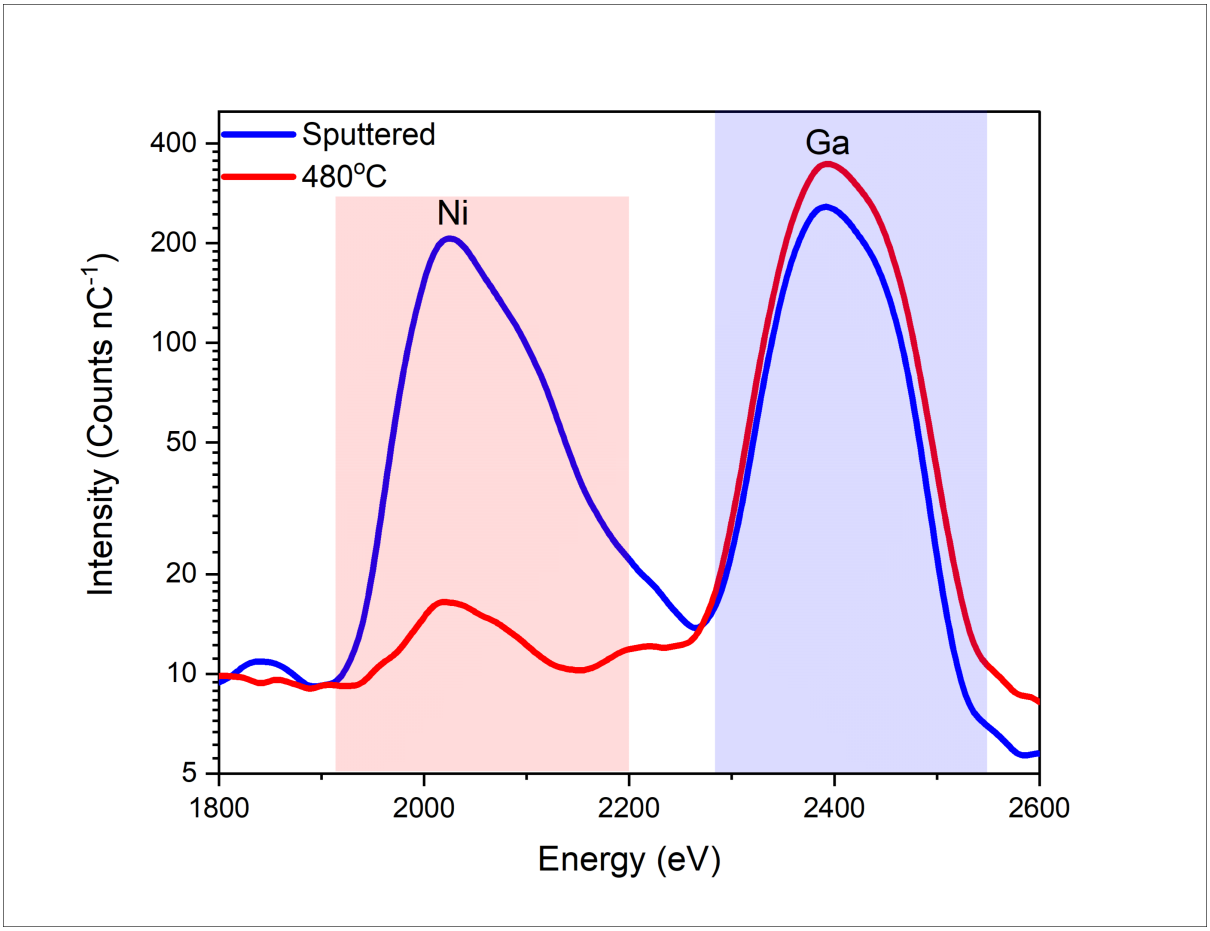

Figure 5.9: LEIS spectra recorded from the Ga_3Ni_2 (001) surface after sputtering and annealing at 480°C. Each peak is highlighted with the corresponding element. The y-axis is set to a natural log scale.

A low-energy ion scattering (LEIS) study was conducted on the (001) surface by Ahowd Alfahad to identify the element(s) present in the topmost atomic layer and thereby determine the most appropriate surface termination model. LEIS employs noble gas ions with energies between 1 and 10 keV. These ions are readily absorbed at the surface, meaning that any detected signal originates exclusively from the outermost atomic layer [142], [143]. Figure 5.9 presents the results of the LEIS measurements on the (001) surface following sputtering and annealing.

After sputtering, the data show approximately equal intensities for Ga and Ni at the surface, indicating that Ga has been removed, consistent with the hypothesis of preferential sputtering of Ga discussed in Chapter 4. Upon annealing to 480°C, the Ni peak decreases, confirming that Ga segregates to the surface, as also observed in Chapter 4. However, the persistence of a notable Ni peak suggests that Ni atoms remain present in

the outermost layer, although Ga is the dominant element. If Model Three were accurate, the topmost Ga atoms would completely block the He^+ ions from reaching the underlying Ni layer, and a Ni peak would therefore not be detected. Therefore, the LEIS results rule out Mode Three, which is consistent with the STM observation.

Model One and Model Two would produce identical surface unit cells, with Ni atoms forming a rhombus of length 4.05 Å in Model One, and Ga atoms with the same geometry in Model Two, as shown in Figure 5.1 (A). This rhombus was observed via STM (Figure 5.6 (C)). Since STM cannot distinguish between Ga and Ni, we are unable to confirm whether Model One or Model Two is correct based on high-resolution STM alone.

Both Model One and Model Two contain bonded Ga and Ni atoms on the surface. The surface stability of other binary intermetallic compounds, such as ZnPd, also suggests that a surface termination with both constituent elements is more stable than a termination with a single element [80]. The presence of Ni on the surface is also important for the catalytic properties of the surface [10].

Between Model One and Model Two, Model Two may be more probable for the following reasons. Ga has a lower surface free energy than Ni [78], making a Ga-terminated surface more stable. Model Two is also consistent with the LEIS results shown in Figure 5.9. With Ga being the dominant element on the topmost layer of the surface, but a notable Ni peak showing that there are Ni atoms present on the surface. Model Two also matches the surface termination of isostructural In_3Ni_2 proposed by Alfahad et al. [72]. Based on STM, LEIS, and DFT calculations of surface free energy, they showed that the surface terminates with In atoms in the topmost layer, bonded with Ni atoms beneath.

5.3.3 Ga_3Ni_2 $(2\bar{1}0)$ surface

Surface Structure by LEED

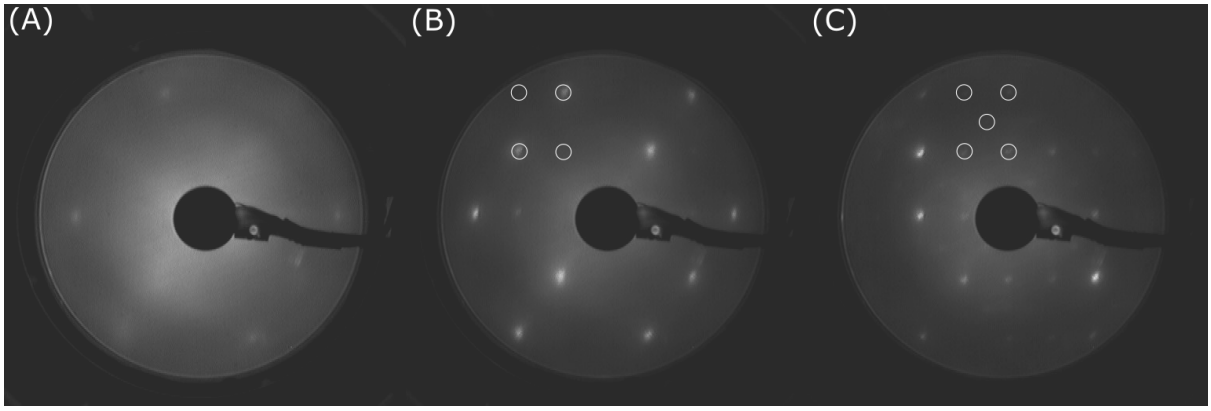

Figure 5.10: LEED patterns for Ga_3Ni_2 $(2\bar{1}0)$ surface after sputtering (A) and annealing at 320°C (B) and 525°C (C). The beam energy is 50 eV for all patterns. The white circles correspond to the (1×1) structure with the cyan circles corresponding to the $c(2 \times 2)$ superstructure.

The LEED patterns were recorded after sputtering and annealing at 320°C and 525°C. Figure 5.1 (C) shows the $(2\bar{1}0)$ surface unit cell. It is rectangular with sides of 7.01 Å and 4.89 Å.

The sputtered surface in Figure 5.10 (A) shows some diffuse Bragg peaks exhibiting rectangular symmetry. The peaks seen in Figure 5.10 (A) are in the same positions as the Bragg peaks seen in the LEED patterns after annealing (Figure 5.10 (B) and (C)).

After annealing to 320°C, the Bragg peaks become sharper, as seen in Figure 5.10 (B), with the additional presence of Bragg peaks previously not observed in Figure 5.10 (A). The surface unit cell matches the model. Background intensity has also decreased at this annealing temperature.

At the highest annealing temperature recorded, 525°C, a new series of Bragg peaks appeared at the centre of each surface unit cell, as shown in Figure 5.10 (C). The reconstruction was identified as $c(2 \times 2)$. A LEED modelling software program, LEEDPat [144], was used to recreate the observed LEED pattern from the given parameters and then construct a superlattice to confirm the type of reconstruction that occurred on the surface.

Figure 5.11 (A) shows an excerpt from the LEEDPat window [144]. In the top left, the Basic 2D lattice section is where the parameters from the Ga_3Ni_2 $(2\bar{1}0)$ model are input. The settings used to produce the model LEED are a Rectangular group with values of a = 7.01 Å and b = 4.89 Å.

After the base lattice was constructed, the superlattice/reconstruction was modelled. The c(2 × 2) superlattice was chosen, as the model LEED results in the bottom right match what was observed in Figure 5.10 (D), with the surface unit cell forming a rectangle with a central peak. The model also calculates the lattice length between the superlattice points, which was consistent with the values measured from the LEED image and from the model shown in Figure 5.11 (B), confirming that a c(2 × 2) reconstruction has occurred.

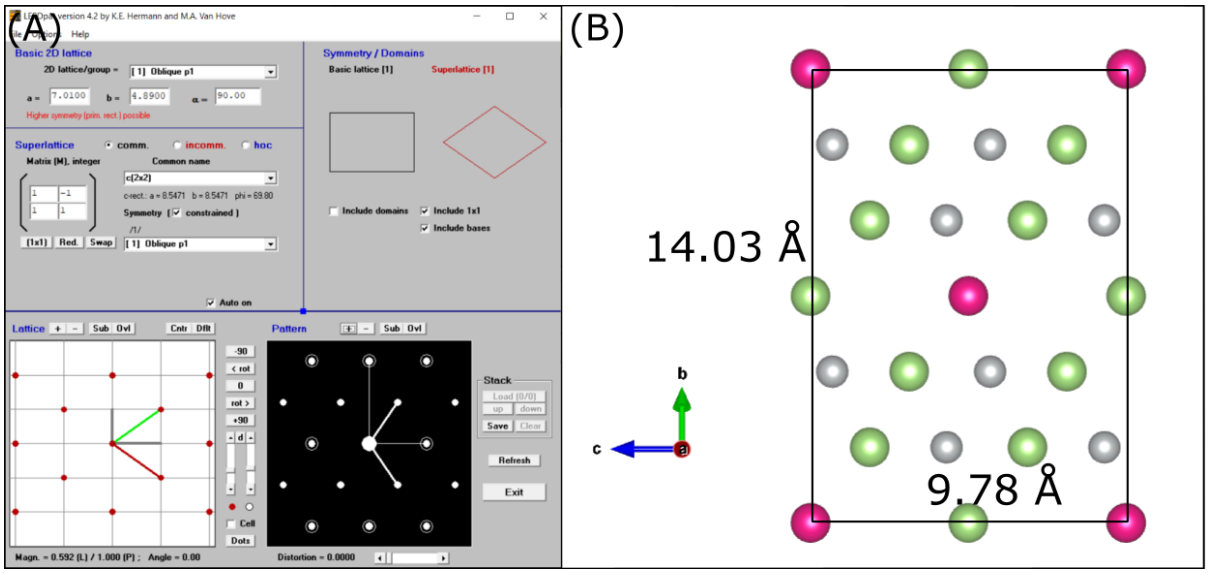

Figure 5.11: (A) The main window from the LEEDPat [144] LEED modelling software shows the input parameters and the type of reconstruction selected, with the real space results on the left and the reciprocal space results on the right. (B) The model $(2\bar{1}0)$ plane with the c(2 × 2) reconstruction highlighted with the purple atoms. The unit cell dimensions are given.

Surface Structure by STM

Step Terrace Morphology

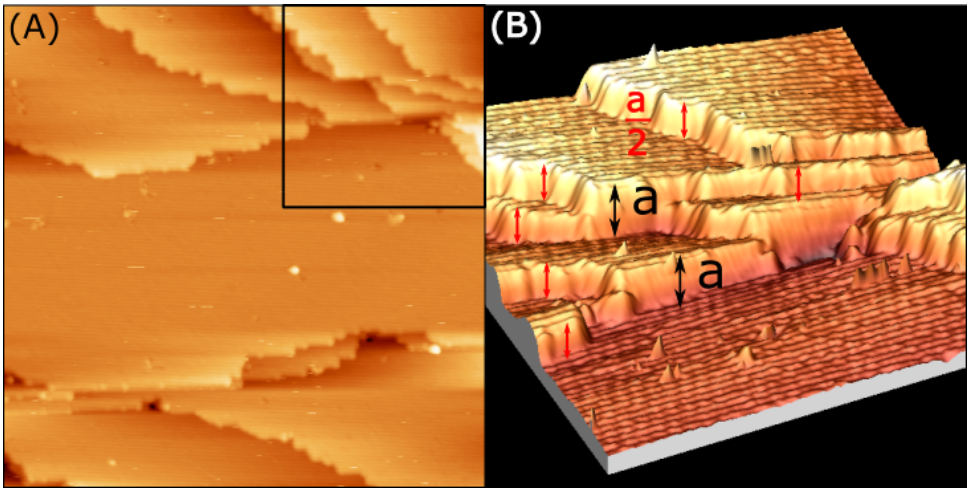

Figure 5.12: (A) 100×100 nm^2 STM image of the Ga_3Ni_2 $(2\bar{1}0)$ surface. (B) The 3D view of the black square in (A). Each plane is labelled with either a red arrow or a black arrow. Black arrows represent the unit cell height a which is 4.05 Å and the red arrows represent $a/2$ which is 2.03 Å.

Large-scale STM images of the $(2\bar{1}0)$ surface were acquired (Figure 5.12 (A)) following annealing at various temperatures between 300°C and 520°C. No step terraces were observed on surfaces annealed below 350°C. At 350°C, step edges and terraces began to appear; however, the terraces remained relatively narrow. To obtain larger terraces, the annealing temperature was increased to 520°C (Figure 5.12).

White protrusions were also observed across the entire surface (Figure 5.12 (A)), similar to those seen on the (001) surface. These protrusions appeared randomly distributed, and filtering the images to isolate these features did not produce a discernible FFT pattern. As discussed in the previous section, these white protrusions are likely attributable to segregated Ga or Ga_3Ni_2 clusters that were not fully incorporated into the surface following sputtering.

According to the model (Figure 5.1 (D)), only a single interplanar spacing (2.03 Å) and its multiples are expected. Using the height histogram and line profile methods described in Section 5.3.2, the step heights were measured to be 2.01 ± 0.1 Å and 4.05 ± 0.02 Å, as shown in Figure 5.4 (B), where only step heights corresponding to a and $a/2$ were observed. These values were determined from measurements of 40 individual step heights across an area of 480 × 480 nm^2 in the STM images.

Atomic Resolution

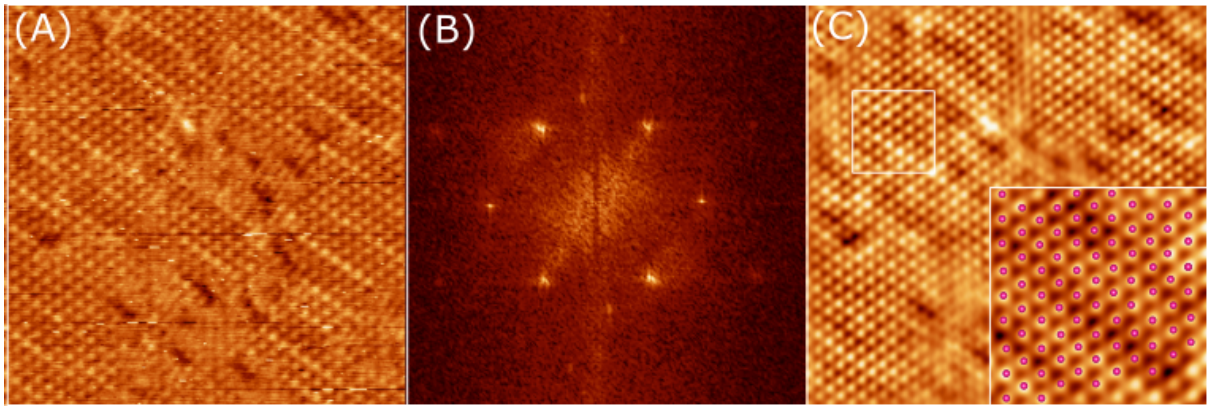

Figure 5.13: (A) 20×20 nm^2 STM image of the Ga_3Ni_2 $(2\bar{1}0)$ surface. A row of dots is visible running diagonally across the surface. White patches are visible and randomly dotted over the surface. (B) FFT of (A) with the spots highlighted by white circles and the surface unit cell outlined with white lines. (C) A model c(2 × 2) reconstruction overlaid onto an inverse FFT of a section of (A).

Figure 5.13 (A) shows a high-resolution STM image of the $(2\bar{1}0)$ surface, where a series of dots forming diagonal rows corresponds to individual atoms. These STM images were obtained after annealing the sample at 500°C, a temperature at which the surface undergoes a c(2×2) reconstruction, as independently confirmed by LEED measurements.

The corresponding FFT, shown in Figure 5.13 (B), displays a central rectangular unit cell, corroborating the c(2×2) symmetry observed in LEED. A primitive unit cell is outlined with a white diamond in Figure 5.13 (B). The lattice constant extracted from the FFT was 8.5 ± 0.1 Å, while direct measurements from the STM image using a line profile tool yielded 8.4 ± 0.1 Å, both consistent with the expected value for a c(2×2) reconstruction (8.5 Å).

To further validate the reconstruction, a structural model of the c(2×2) unit cell was overlaid onto the STM image (Figure 5.13 (C)). The model closely aligns with the positions of the brighter features in the STM data, confirming the presence of the c(2×2) reconstruction on the $(2\bar{1}0)$ surface.

5.3.4 Ga_3Ni_2 (100) surface

Surface Structure by LEED

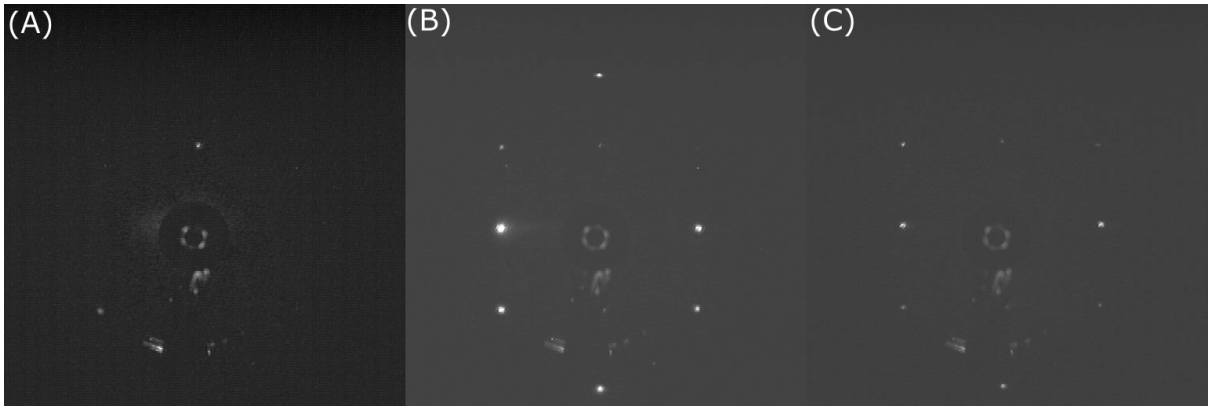

Figure 5.14: LEED patterns for Ga_3Ni_2 (100) surface after sputtering (A) and annealing at 410°C (B) and 494°C (C). The beam energy is 50 eV for all patterns. Spots are highlighted by white circles.

The model of the Ga_3Ni_2 (100) plane, shown in Figure 5.1 (E), displays a rectangular unit cell with sides of 4.05 Å and 4.89 Å. LEED patterns were recorded from the surface after sputtering and annealing at 410°C and 494°C, as shown in Figure 5.14. The LEED pattern after sputtering, Figure 5.14 (A), shows no spots, unlike the (001) surface. Sputtering has roughened the (100) surface too much for any surface symmetries to be observed. After annealing the surface to 410°C, Bragg peaks become visible, displaying a rectangular unit cell across a range of beam energies (20–200 eV).

The dimensions of the surface unit cell measured from the LEED pattern match the unit cell of the model shown in Figure 5.1 (E), suggesting that no reconstruction has occurred. Increasing the annealing temperature has no significant effect on the LEED pattern. As with the (001) surface, the segregation of Ga from the bulk to the surface does not alter the surface symmetry observed.

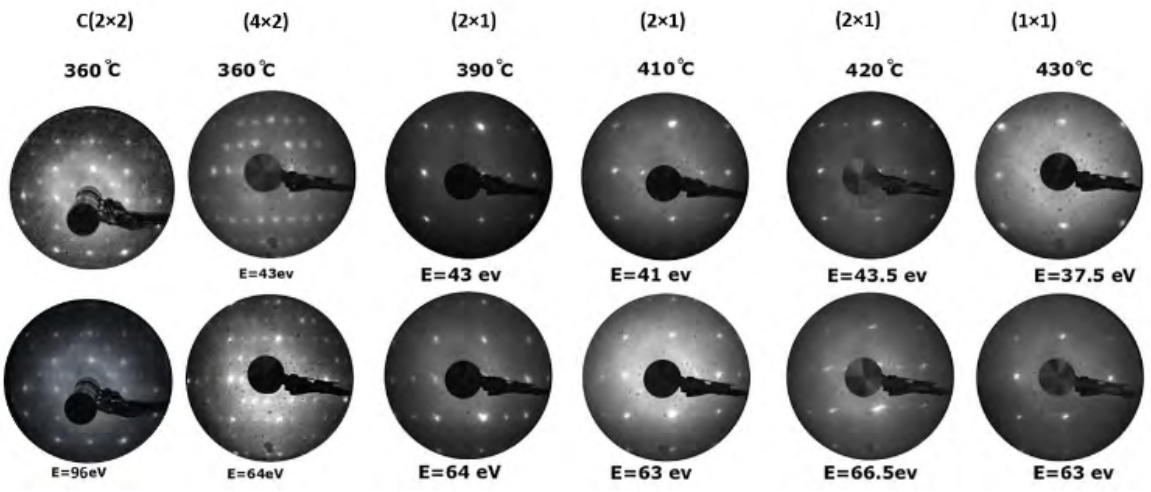

Figure 5.15: The LEED patterns from the Ga_3Ni_2 (100) surface at five different temperatures recorded with a beam energy between 35 - 67 eV. This image is from Dr Ahmna Alofie's thesis [145].

Dr. Amnah Alofie previously performed a LEED study [145] of the (100) surface over a range of annealing temperatures from 360°C to 430°C and recorded a range of reconstructions at the lower annealing temperatures.

Her results match what we observed from our (100) sample, with a (1×1) surface unit cell being observed at temperatures above 410°C. Due to a discrepancy in the emissivity used for temperature recording, we measured a higher temperature than the values quoted in Dr. Amnah Alofie's thesis, which explains the absence of (2×1) reconstruction observed at 410°C.

5.3.5 A Comparison of all Three Ga_3Ni_2 Surfaces

In this section, we will compare all of the results for each of the three Ga_3Ni_2 surfaces, (001), (100) and $(2\bar{1}0)$. Starting with a look at the model for each of the Ga_3Ni_2 surfaces and the differences in the surface structure to explain the difference in the results. Then the individual XPS results for all three surfaces will be compared to show how the preparation conditions have affected each of the surfaces and how segregated Ga has collected on the surface.

Next, we will discuss the LEED results, Sections 5.3.2, 5.3.3 and 5.3.4, and why the $(2\bar{1}0)$ surface was the only one to undergo reconstruction. Then, the STM results will be discussed, and understanding the surface geometry of each sample will offer insights

into the questions raised by the findings of the prior experimental techniques.

Finally, the Ga_3Ni_2 and In_3Ni_2 (001) surfaces will be directly compared to each other. By comparing the surface chemical composition as a function of temperature, surface geometry and symmetry through LEED and oxidation discussed in chapter 6 we can further our understanding of both these samples and what phenomena, such as segregation of the secondary element, Ga/In on the surface, reconstruction on the $(2\bar{1}0)$ surface and a lack of Ni oxides after O_2 exposure, are due to the Al_3Ni_2 family of catalysts and which ones are due to Ga in the intermetallic compound.

Figure 5.1 shows the unit cell of Ga_3Ni_2 followed by a side-on and head-on view of all three surfaces. By adding the bonds between the nearest neighbour atoms, Figure 5.1 shows that the Ni atom is only connected to the nearest Ga atoms. This suggests that the Ni atoms are anchored into the unit cell by the Ga atoms, which encompass the Ni atoms. The site isolation of the Ni atoms from the neighbouring Ni atoms is attributed to the increase in catalytic selectivity [10] of GaNi IMC. Site isolation is present in many IMC from InNi to GaPd [72], [85].

Figure 5.1 (A) shows the (001) surface, which is the only surface to exhibit the buckled planes where the Ga and Ni layers are bonded together. The results from the step height analysis produced two possible options for the surface termination shown in Figure 5.8 either Ga one the surface bonded to Ni, the red distances, or Ni on the surface bonded to Ga atoms in the layer below, the blue distances. LEIS results from Ga_3Ni_3 show both Ga and Ni present on the topmost surface. With Ga having a lower surface free energy than Ni and segregating to the surface observed via XPS in Chapter 4 [92] it was decided that Model Two with Ga atoms on the surface is the expected surface termination matching the isostructural $In-3Ni_2$, which was found to have both In and Ni on the surface via LEIS and though STM and surface energy calculations terminated with In atoms on the surface bonded to the Ni atoms below [72]

The $(2\bar{1}0)$ and (100) surfaces seen in Figure 5.1 (C) and (E) only have Ni on mixed planes, with the (100) surface having a pure Ga plane at the top and bottom of the model unit cell. The (001) surface terminates on the bonded Ga-Ni planes in the centre of the unit cell. The $(2\bar{1}0)$ surface consists of a single mixed plane where the Ni is bound to 2 atoms and a singular Ga in the subsurface.

Each of the three surfaces has slight variations in how the Ga and Ni atoms are bonded. By comparing the results from each of the samples, we can consider whether the change in surface structure is a factor in the differences we observed in how each surface reacts to sputtering and annealing. Each surface terminates on a bonded Ga-Ni plane, which has been observed in In_3Ni_2 [72] though STM and confirmed by surface energy calculations.

Comparison of the LEED results

The XPS results from Chapter 4 showed Ga segregation onto the surface of all three samples. This shift in the atomic composition was thought to affect the surface symmetries observed through LEED. Figure 5.16 shows the LEED results for all three surfaces from sputtered (Figure 5.16 (A), (D) and (G)) and then after annealing at two different temperatures, with the highest temperatures for each surface in the right-hand column. A trend across all three surfaces is seen in Figure 5.16; higher annealing temperatures produce a higher quality LEED image with sharper Bragg peaks and less background. Longer annealing times were used for lower annealing temperatures on the (001) and $(2\bar{1}0)$ surface to see if annealing time would alter the surface symmetry. An increase from 90 minutes to 180 minutes did not affect the quality of the LEED images.

The sputtered results for each of the three surfaces show Bragg peaks, confirming that for the (001) and (100) surfaces, there is significant surface symmetry present after sputtering as the peaks are sharp, and some diffuse Bragg peaks can be seen on the $(2\bar{1}0)$ surface. From the XPS results, Ga is preferentially sputtered from the surface, leaving a more Ni-rich surface. Figure 5.16 (A) shows a triagonal pattern from the (001) surface after sputtering. Increasing the electron energy causes an additional three Bragg peaks to be observed rotated by 60^o. Both sets of peaks together make the expected hexagon shape, which was seen in Figure 5.16 (B) after annealing.

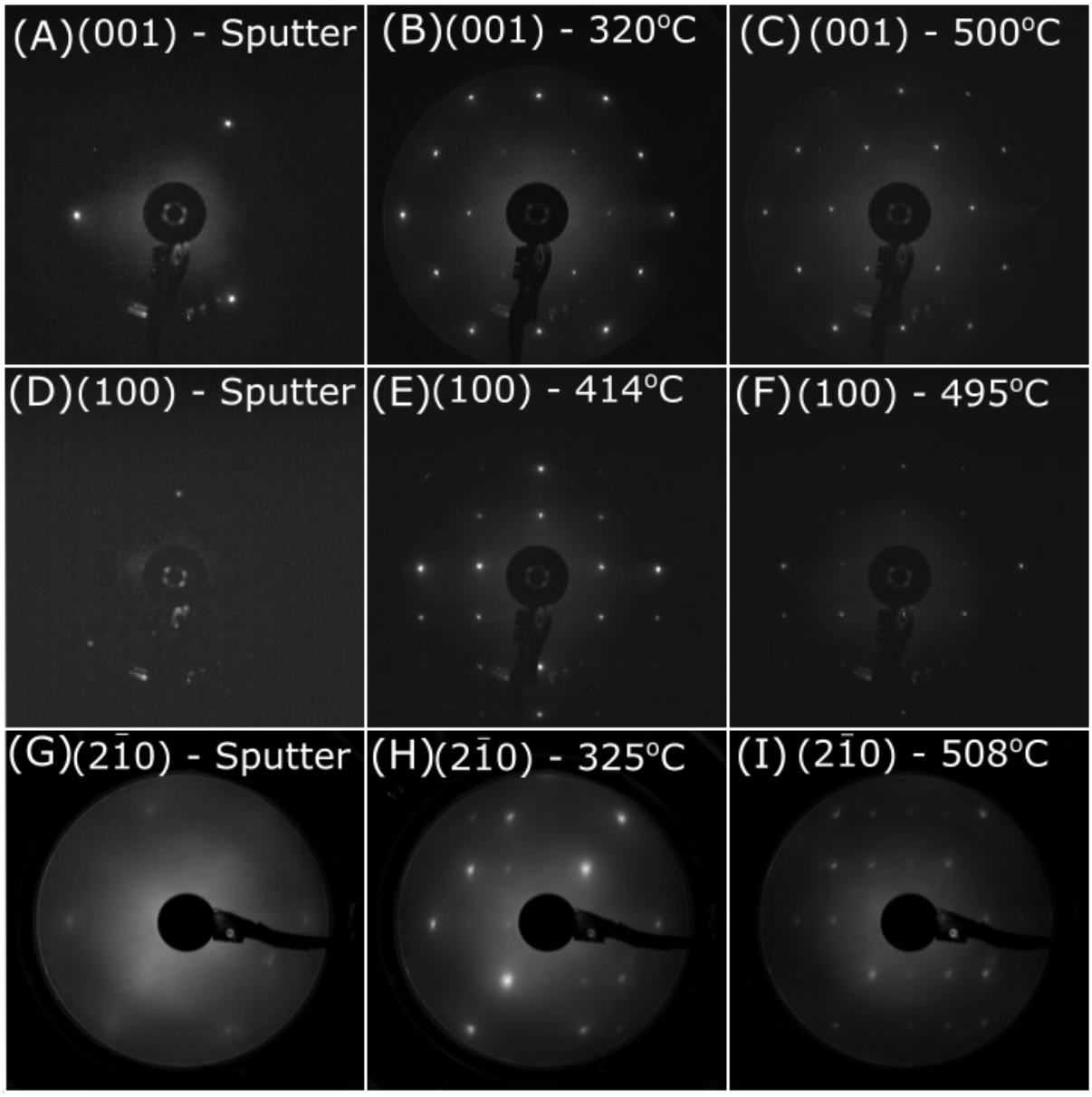

Figure 5.16: A series of LEED images taken from all three surfaces from sputtered to annealed at two increasing temperatures, with the Bragg peaks highlighted. (A), (B) and (C) are from the (001) surface and consist of the sputtered surface. The surface was annealed at 320°C and 500°C, respectively, with the Bragg peaks of interest highlighted in white. (D), (E) and (F) are from the (100) surface and consist of the sputtered surface and the surface annealed at 414°C and 495°C, respectively, with the Bragg peaks of interest highlighted in red. (G), (H) and (I) are from the (2$\bar{1}$0) surface and consist of the sputtered surface, and the surface annealed at 325°C and 508°C respectively with the Bragg peaks of interest highlighted in blue showing the appearance of the c(2×2) reconstruction.

The (100) and (2$\bar{1}$0) surfaces after sputtering, seen in Figure 5.16 (D) and (G), show a similar trend with Bragg peaks being visible. Figure 5.16 (G) shows a large rectangular unit cell, but when converted into real space, the distance would be too small to be any form of real surface structure. After annealing the surfaces in Figure 5.16 (E) and (H), additional Bragg peaks appear as the surface becomes more ordered. Bragg peaks seen from the sputtered LEED images match the position of Bragg peaks seen after annealing the respective surface, suggesting that there is some order present on the sputtered surface. For both the (001) and (100) surfaces at the highest annealing temperatures shown in Figure 5.16 (C) and (F), no reconstruction occurred even with the Ga% exceeding 80% of the surface composition.

The (2$\bar{1}$0) surface underwent c(2×2) reconstruction, observed by the additional Bragg peak and identified through modelling software, once the Ga% on the surface exceeded 60%, Figure 4.7 (A).

At lower Ga%, no reconstruction was observed at any beam energies, showing that this reconstruction was an effect of Ga moving and settling onto the surface. Segregated Ga did not cause a superstructure that could be observed via LEED for the (001) and (100) surfaces.

Comparison of the STM results

Using the results from Chapter 5, we were able to use LEED images to produce surfaces that are ideal for STM images to be recorded. The XPS results in Chapter 4 and Figures 4.7 (A), 4.8 (A), 4.6 (A) show that the Ga % is notably higher than the bulk composition, especially for the (001) surface. In this thesis, we only studied the (001) and the (2$\bar{1}$0) as the (100) surface had been previously studied by Dr Amnah Musaed Alofi [145] at the University of Liverpool.

Both the (001) and (2$\bar{1}$0) surfaces mostly consisted of multiple thin terraces stacked tightly on top of each other at a lower annealing temperature (450^{o}C) with Figure 5.17 (A) and (B) show a wide scan of the (001) and (2$\bar{1}$0) respectively.

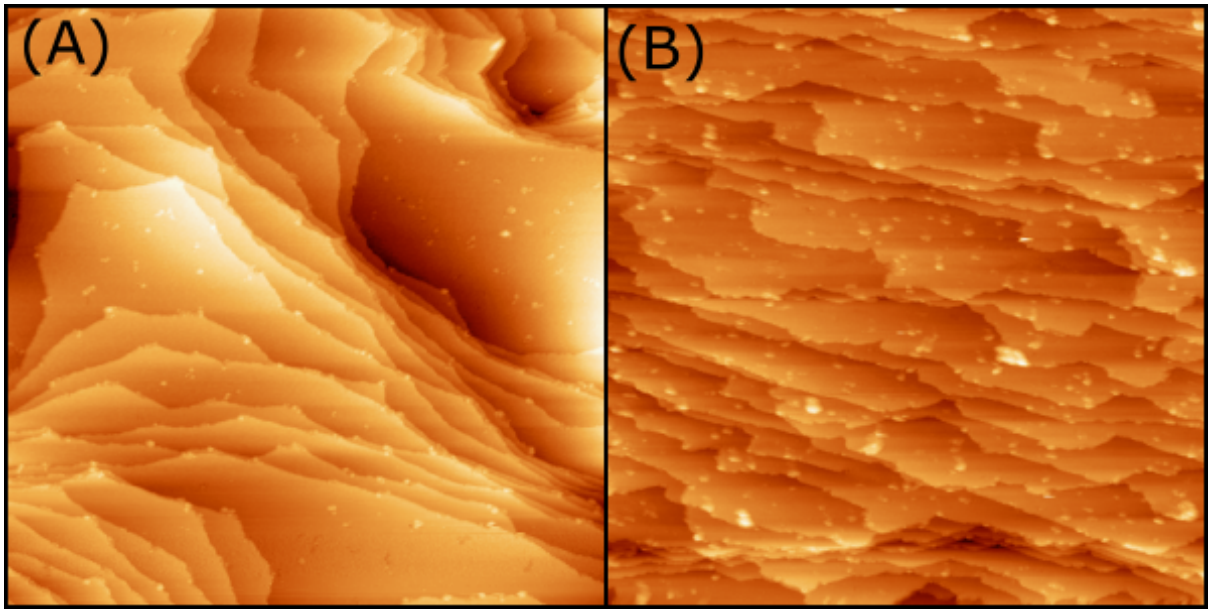

Figure 5.17: (A) A 400×400 nm^2 STM image of the (001) surface. (B) A 100×100 nm^2 STM image of the $(2\bar{1}0)$ surface.

Figure 5.17 (A) shows a mixture of short compact terraces and larger wider terraces in addition to scattering of large white protrusions which can also be seen on the $(2\bar{1}0)$ surface in Figure 5.17 (B) where the protrusions cover all of the steps in large clusters and the step edges are bunched together. Using higher annealing temperatures, larger, flatter terraces were able to form, which can be used for step height analysis. However, the white protrusions remained present.

Figure 5.18 (A) and (B) show 3D images of the (001) and $(2\bar{1}0)$ surfaces which were used to measure the step height and confirm Ni termination for the (001) surface with the presence of the 1.4 Å and 3.5 Å sub-steps. The $(2\bar{1}0)$ surface only had one possible termination plane shown in Figure 5.1 (E), which was consistently observed in Figure 5.18 (B).

Large protrusions that were taller than the surrounding terrace were visible across all of the. These are believed to be large clusters of elemental Ga which have settled on the surface after segregation, as they are randomly dispersed and are not a consistent size or shape. XPS results showed that the surface was only Ga and Ni, with no other elements detected, ruling out contamination as a cause for those.

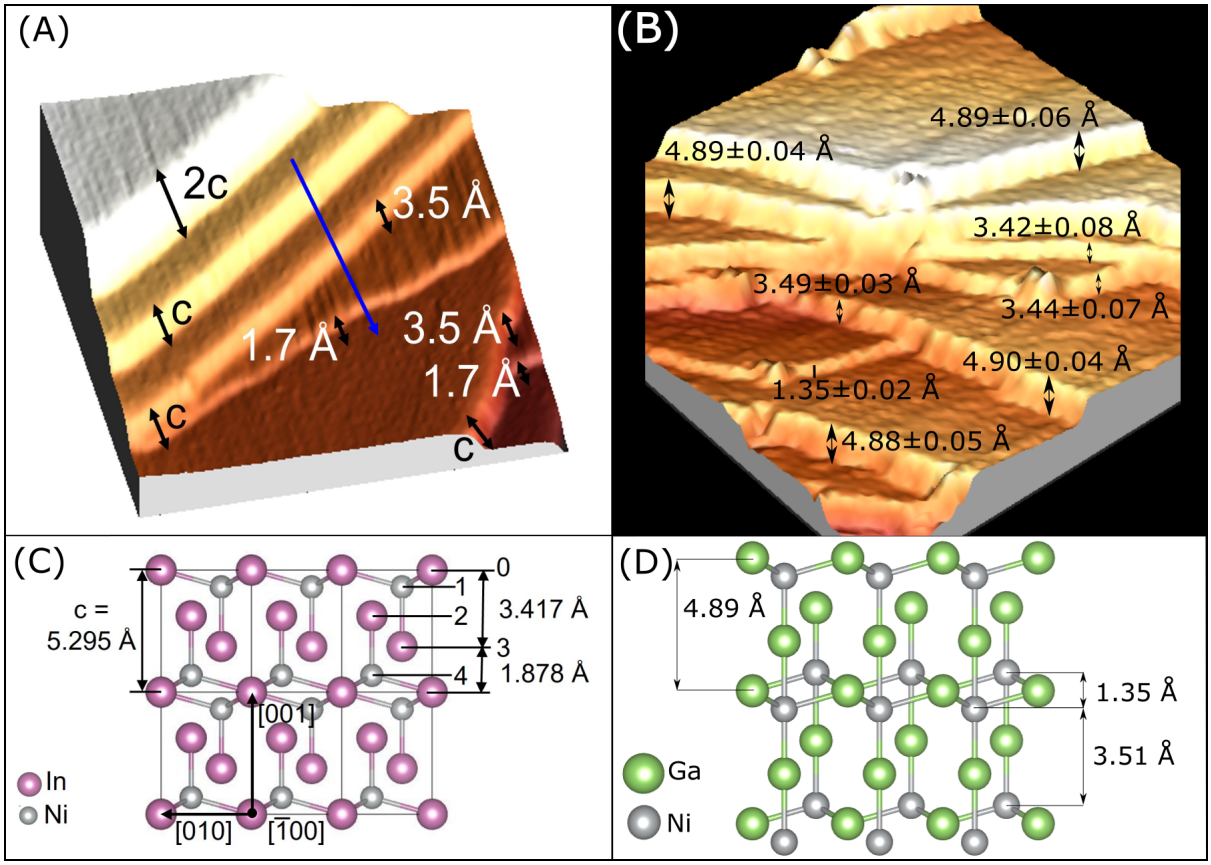

Figure 5.18: (A) A 3D image of the (001) surface with the step heights shown to confirm Ni termination. (B) A 3D image of the $(2\bar{1}0)$ surface with the average step height displayed.

Focusing on a flat section of both surfaces, we were able to resolve atomic structure from both the (001) and $(2\bar{1}0)$ surfaces. Figure 5.19 (A) and (B) both show a clear structure present in particularly with Figure 5.19 (B), where rows of atoms are visible. Figures 5.19 (C) and (D) show the FFT results where both surfaces have had the noise removed to enhance the bright peaks, making them visible.

Both results match the LEED results in Figure 5.16 (C) and (I), with the (001) surface exhibiting (1×1) symmetry and the $(2\bar{1}0)$ surface displaying the c(2×2) reconstruction with the central spot highlighted in Figure 5.19 (D). Figures 5.19 (E) and (F) are Fourier filter images of the (001) and $(2\bar{1}0)$ surfaces, respectively, by selecting the peaks and some of the central noise we have filtered the initial image to only show the periodic parts. This enhances the visible structure seen in Figure 5.19 (A) and (B), which allowed the confirmation of the (1×1) unit cell and the c(2×2) reconstruction.

Figure 5.19 (C) shows the inner ring, which contains twelve spots which correspond to a c($2\sqrt{3} \times 4$) superstructure shown in Figure 5.7. The points are diffuse, suggesting that this superstructure is weak, as it was not observed in the LEED. The c($2\sqrt{3} \times 4$) superstructure matches the one observed from the isostructural In_3Ni_2 (001) surface. Though the superstructure was much more pronounced for In_3Ni_2 [72].

The (100) surface was studied by Dr Alofi at the University of Liverpool and exhibited multiple reconstructions of the surface, which were dependent upon the annealing temperature. With (4×2) and c(2×2) occurring at 366°C and 390°C with a (1×1) surface structure being seen at annealing temperatures $\geq$ 430°C [145]. Each one was confirmed by LEED and STM and matches the $(2\bar{1}0)$ surface, which also showed temperature-dependent surface reconstruction.

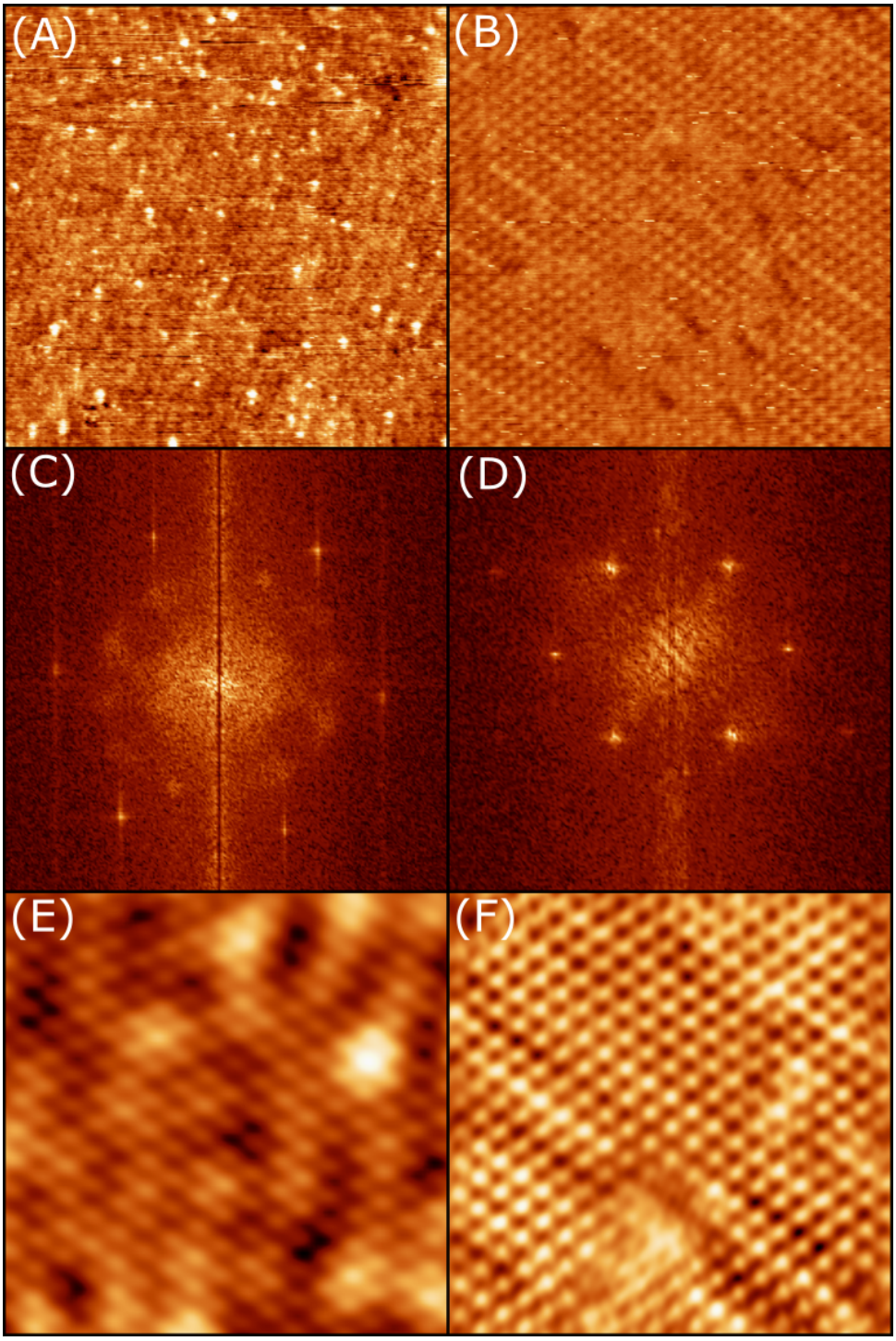

Figure 5.19: STM images of the (001) and (2$\bar{1}$0) surface. (A) 30nm×30 nm^2 section of the (001) surface equalised to highlight surface structure. (B) 35×35 nm^2 section of the (2$\bar{1}$0) surface equalised to highlight surface structure. (C) An FFT of (A) with the noise removed to enhance the peaks and noise. Peaks of interest are highlighted by white circles. (D) An FFT of (B) with the noise removed to enhance the peaks and noise to show the central peak indicative of c(2×2) reconstruction. Peaks of interest are highlighted by white circles. (E) A filtered section of (A) showing atoms forming the (1×1) expected surface structure. (F) A filtered section of (B) showing atoms forming the c(2×2) reconstruction observed through LEED.

Comparison of the (001) surfaces for Ga_3Ni_2 and In_3Ni_2

Three samples of In_3Ni_2 were cut along the same sample planes as the three Ga_3Ni_2 samples are currently being studied by a fellow PhD student at the University of Liverpool. All of the In_3Ni_2 results are attributed to Ahowd Youssef Alfahad [72] By comparing the (001) surface of both Ga_3Ni_2 and In_3Ni_2 we can see how the Ga present within the intermetallic compound affects the (001) surface and which phenomena are intrinsic to the Al_3Ni_2 family of catalysis and which ones can be related to the presence of Ga within the intermetallic compound.

LEED image of the (001) surfaces

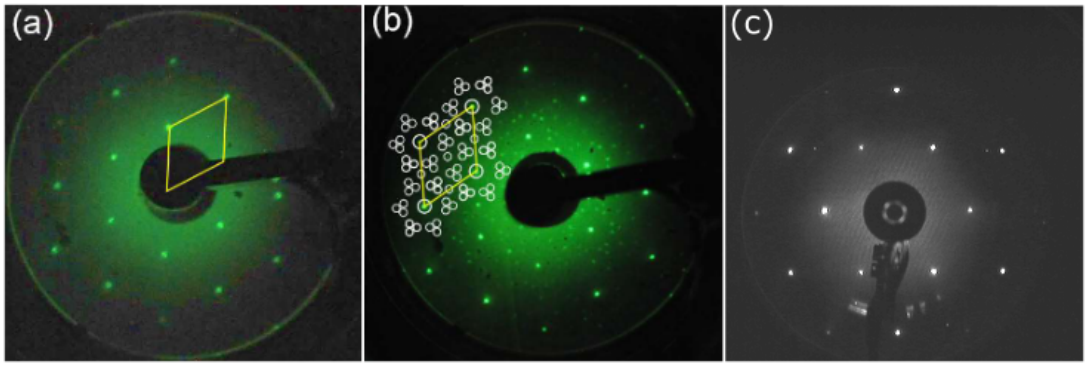

Figure 5.20: The LEED pattern from the (001) surface of In_3Ni_2, after annealing (A) and after hydrogen exposure (B), and Ga_3Ni_2 after annealing over 500°C. (A) and (B) adopted from [72].

Both the (001) surfaces of Ga_3Ni_2 and In_3Ni_2 are isostructural with In_3Ni_2 having a larger unit cell [72]. It was expected that the LEED results would be similar, if not identical, due to both intermetallic compounds exhibiting similar XPS results. Figure 5.20 shows LEED images taken from In_3Ni_2 (001) (A) and (B), and Ga_3Ni_2 (001) (C), after annealing at over 500°C for ninety minutes taken at a beam energy of 100 eV.

Figure 5.20 (A) and (C) show the expected (1×1) hexagonal surface unit cell with the correct dimensions expected from the (001) model for both Ga_3Ni_2 and In_3Ni_2. Figure 5.20 (B) shows a superstructure forming on the In_3Ni_2 (001) surface after exposure to hydrogen after firing the Titanium sublimation pump [72]. A complex c($2\sqrt{3} \times 4$) can be in Figure 5.20 (B).

This phenomenon was not observed with Ga_3Ni_2 even after multiple firings of the TSP no reconstruction occurred. None of the Ga_3Ni_2 samples reacted to the presence of hydrogen within the UHV chamber, even when left for 48 hours. This could suggest that the atoms on the surface, both the Ni from the termination plane and the Ga clusters, are either not susceptible to bonding with the hydrogen released during the TSP cycle or that the hydrogen is bonding to the Ga clusters observed though STM which are randomly distributed across the sample which would shield the surface symmetries from the reconstruction seen in Figure 5.20 (B).

STM of the (001) surfaces

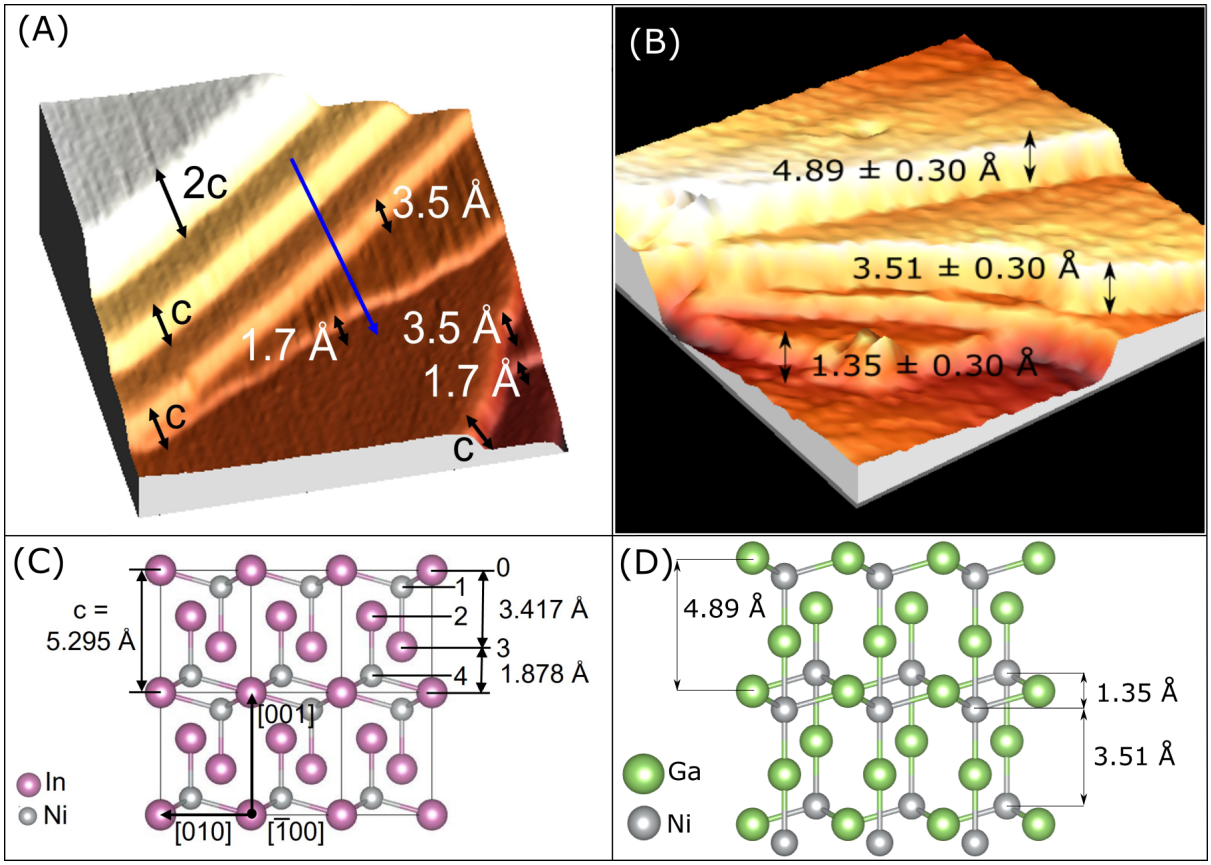

Figure 5.21: 3D STM images of the (001) surface from In_3Ni_2 (A) and Ga_3Ni_2 (B). The model structures of both In_3Ni_2 (C) and Ga_3Ni_2 (D) with the distance between each layer are given.

Figure 5.21 (A) and (B) show a 3D model of STM images from the In_3Ni_2 and Ga_3Ni_2 surfaces respectively. Both intermetallic compounds are mostly composed of larger terrace steps, which are multiples of C, where C is the height of the unit cell. Both intermetallic compounds also had sub-steps from Figure 5.21 (A) are 1.5 Å and 3.7 Å and from Figure 5.21 (B) are 1.4 Å and 3.5 Å

When compared to the model, Figure 5.21 (C) and (D), the sub-steps observed from Ga_3Ni_2 and In_3Ni_2 show that both surfaces are terminated on the bulked planes. These planes are a mixture of bonded Ga/In and Ni, which enhances the stability of the surface. This was confirmed with In_3Ni_2 through surface energy calculations [72].

The other feature observed from the Ga_3Ni_2 (001) surface seen in Figure 5.3.2 was the presence of white clusters over the entire surface. This phenomenon seems to be tied to the segregation of Ga from the bulk to the surface. The In_3Ni_2 (001) surface was not covered in white protrusions comparable to the amount seen on the Ga_3Ni_2 (001) surface. This was expected as Figure 4.9 showed that at similar temperatures the atomic compositions of the surface showed In composing on average 70% of the surface whereas Ga composed 80% of the surface, suggesting that the lower bond energy between Ga - Ni compared to In - Ni allowed for more Ga to travel from the bulk to the surface and conglomerate [146].

This would be a possible explanation for the differences in how Ga_3Ni_2 and In_3Ni_2 behaved during STM imaging. Ga_3Ni_2 was difficult to obtain STM images from with tip quality rapidly fluctuating and degrading as it scanned any of the Ga_3Ni_2 surfaces which could be caused by an excess of weakly bonded elemental Ga on the surface. In_3Ni_2 (001) was easier to obtain images from once the parameters discussed in [72] were found. After similar preparation using the same STM equipment, the only difference was the lack of these white clusters of material covering the surface of the In_3Ni_2 sample.

5.4 Summary

In this chapter, we discussed the LEED and STM results from all three high symmetry surfaces of Ga_3Ni_2, compared them to each other and compared the isostructural In_3Ni_2 (001) and Ga_3Ni_2 (001) surfaces to observe the surface atomic structure.

The LEED images for the (001) surface as shown in Figure 5.3.2 (C) show a clear (1×1) surface unit cell which was also observed in the FFT of the STM image of the (001) surface as seen in Figure 5.5 (B). By filtering the six bright spots and performing an inverse FFT, we were able to see the periodic structure in real space as shown in Figure 5.6 (B) and (C), which matched the (1×1) surface unit cell from the model. A weak $c(2\sqrt{3} \times 4)$ superstructure was observed in the FFT images, highlighted in Figure 5.7 (A), as faint spots within an inner ring. Three domains were found and, when converted into real space, formed a centred unit cell with the expected aspect ratio when compared to the model. This superstructure was also observed on the In_3Ni_2 (001) surface.

Step height analysis for the (001) surface showed the presence of two distance substeps, as shown in Figure 5.4 (C), which were used to identify how the surface terminates. Three models were considered for the surface termination. The model with Ga on the surface bonded to the Ni in the layer below fits the results we have obtained from the step height analysis and the LEIS results shown in Figures 5.4 (C) and 5.9.

The LEED images for the $(2\bar{1}0)$ showed (1×1) surface unit cell when annealing at 320°C and c(2×2) reconstruction after annealing at higher annealing temperature 525°C. The c(2×2) was observed in both the FFT and real space as shown in Figure 5.13. The step height analysis showed only two recorded step heights as shown in Figure 5.12 (B), a and $a/2$, where a is the height of the unit cell 4.05 Å. This was expected from the model seen in Figure 5.1 (D) as the $(2\bar{1}0)$ is composed of one mixed Ga and Ni plane separated by $a/2$.

The LEED results for the (100) surface show a (1×1) surface unit cell which matches the previous results obtained by Dr Alofi in her study of the (100) surface at higher annealing temperatures [145].

Comparing the isostructural Ga_3Ni_2 and In_3Ni_2 (001) surfaces we were able to confirm both surfaces exhibit the $c(2\sqrt{3} \times 4)$ superstructure with the superstructure being stronger on the In_3Ni_2 surface as it was able to be detected from the LEED pattern as shown in Figure 5.20. Figure 5.21 (A) and (B) show the step heights observed for both In_3Ni_2 and Ga_3Ni_2 respectively, both show the presence of substeps which were used to propose that the surface terminates on a mixed plane with the secondary element on the surface, Ga or In, bonded to the Ni atoms in the layer below. Surface energy calculations alongside LEIS studies on the In_3Ni_2 (001) surface confirmed that In atoms are on the surface and bonded to the Ni atoms in the subsurface [72].

Chapter 6

Surface Oxidation Studied by XPS

6.1 Introduction

This chapter presents an XPS study of the oxidation behaviour of Ga_3Ni_2 (001). The air-exposed results shown in Chapter 4 indicate that Ga oxidises and forms a layer on the surface. By exposing the (001) sample to controlled amounts of oxygen, it is possible to observe the transition from a clean surface to an oxygen-saturated surface. Most industrial heterogeneous catalysts operate in environments where oxygen is present, making it essential to understand how the surface reacts to oxygen.

Prior research on the effect of oxidation on the catalytic properties of powdered Ga_3Ni_2 [10] shows the formation of a surface layer of Ga oxide(s) with minimal Ni present. Intermetallic Ga, with a shoulder from Ga oxide(s), and Ni are visible 5nm below the surface, with less Ga oxide(s) observed deeper down [10], as shown in Figure2.15 from Chapter 2. This reduces the effectiveness of the surface as a catalyst, but understanding how the surface reacts to oxygen and how it oxidises could not be achieved using a powdered sample.

6.2 Experimental Details

A single-grain sample of Ga_3Ni_2 was grown via the Czochralski method [30] and cut to expose the (001) surface. The surface was polished using decreasing grain sizes of diamond paste (6 μm to 0.25 μm), after which further cleaning was carried out through cycles of sputtering (Ar^+, thirty minutes, 2 keV, drain current 6μA) and annealing (500°C, ninety minutes). XPS was used to check whether the surface was contaminant-free before oxidation.

The oxidation experiment was performed at the University of Liverpool using an Al K_α source. After cleaning, the surface was dosed with pure oxygen (99.5%) at exposures of 2 L, 11 L, 101 L, 1033 L and 13,265 L at room temperature (One Langmuir (L) of exposure is defined as one second of exposure to 1.3×10^{-6} mbar).

6.3 Results and Discussion

Below, we describe the changes in the core levels of Ga, Ni, and O of the (001) surface after exposing the surface to oxygen at different doses of O_2 and compare them to the clean surface results. All of these results were recorded at the University of Liverpool, in the Stephenson Institute for Renewable Energy.

6.3.1 The Clean Surface

From prior experiments on the (001) surface, we were able to determine that the surface is sufficiently cleaned after two cycles of sputtering and annealing at temperatures around 500°C. This was confirmed by analysing the entire XPS spectrum for Ga_3Ni_2 to check for any contamination. Figure 6.1 (A) shows the entire eV range for the (001) surface after several cycles of sputtering and annealing at 520°C. Multiple peaks can be observed, and each was identified by comparing the position of each peak to literature values of known metallic elements [126].

After the surface had been exposed to air, oxygen, carbon, and nitrogen peaks were observed, as shown in Figure 6.1 (D). O 1s at 532 eV, N 1s at 398 eV, and C 1s at 284 eV. After sputtering and annealing, each of these peaks was removed from the blue spectrum, showing that they were removed from the surface of the sample. A small peak is seen at 531 eV, close to the O 1s peak; this is an overlap with a Ga Auger peak when using an Al Kα source. Using an Mg Kα source would cause an Ni Auger peak to overlap at the same point. Two Gaussian peaks were fitted to both the Ga $2p_{1/2}$ and Ga $2p_{3/2}$ peaks to ensure that any secondary or tertiary oxide peaks were not present on the clean surface.

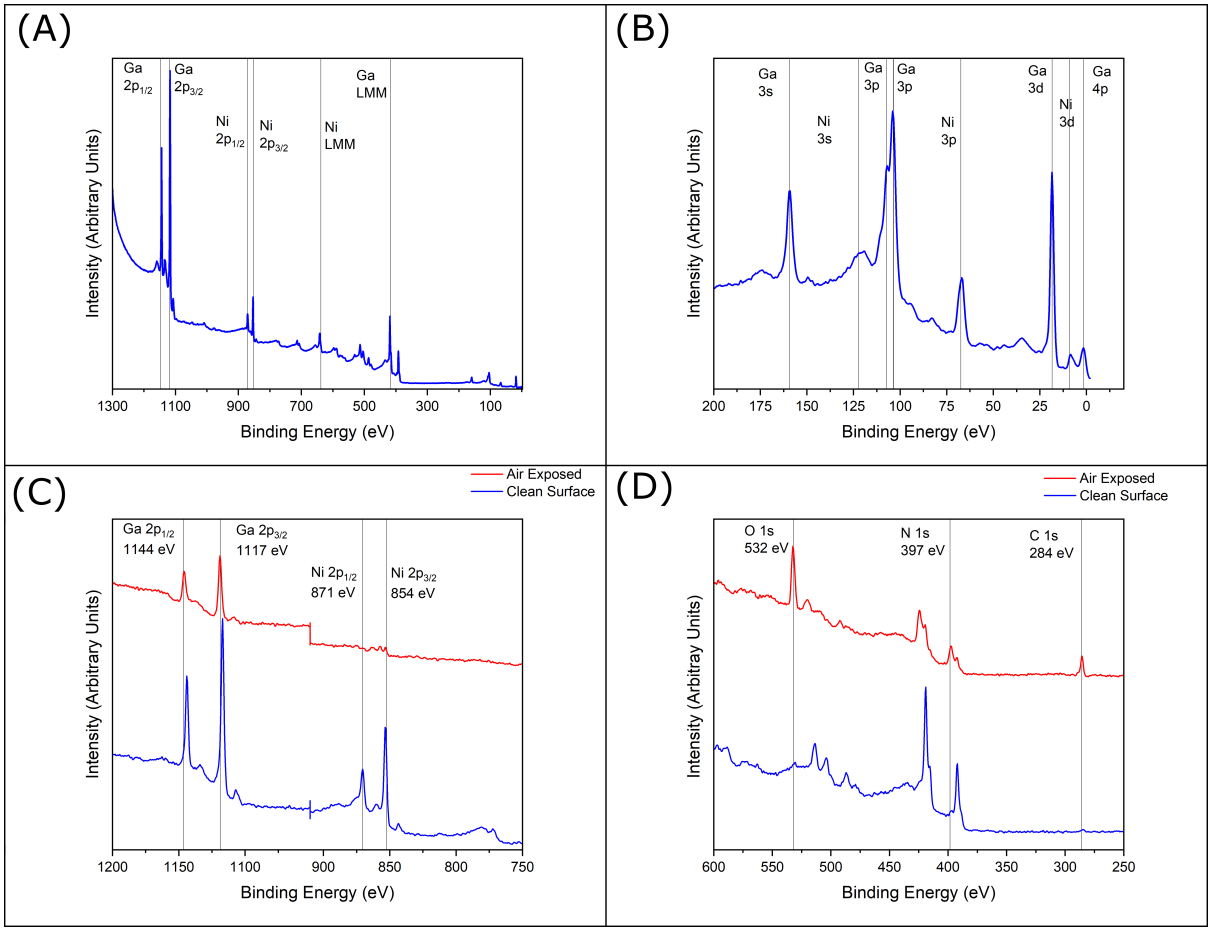

Figure 6.1: The wide XPS scan of the (001) surface after being annealed at 520°C. (A) The entire spectrum of the (001) surface in 0.5 eV steps with the key peaks highlighted and labelled. (B) Shows the 200 - 0 eV range in 0.5 eV steps with each key peak identified. (C) The Ga and Ni peaks after air exposure and cleaning to show the effects on the elements observed. (D) The contamination peaks after air exposure and cleaning, that C, N and O are all removed after sputtering and annealing.

After confirming that the key contaminants were not present on the surface, each peak was identified. Figure 6.1 (A) shows that all of the large peaks could be matched to either Ga or Ni, with Figure 6.1 (B) focusing on the lower energy range, confirming that all the peaks present below 200 eV can be matched to either Ga or Ni.

This confirmed that the surface was clean and ready for the oxidation study, as well as the steps required to reverse the oxidised surface to a clean state when needed. The following section will break down the effects of increasing exposure on the (001) surface, starting with Ga, followed by Ni.

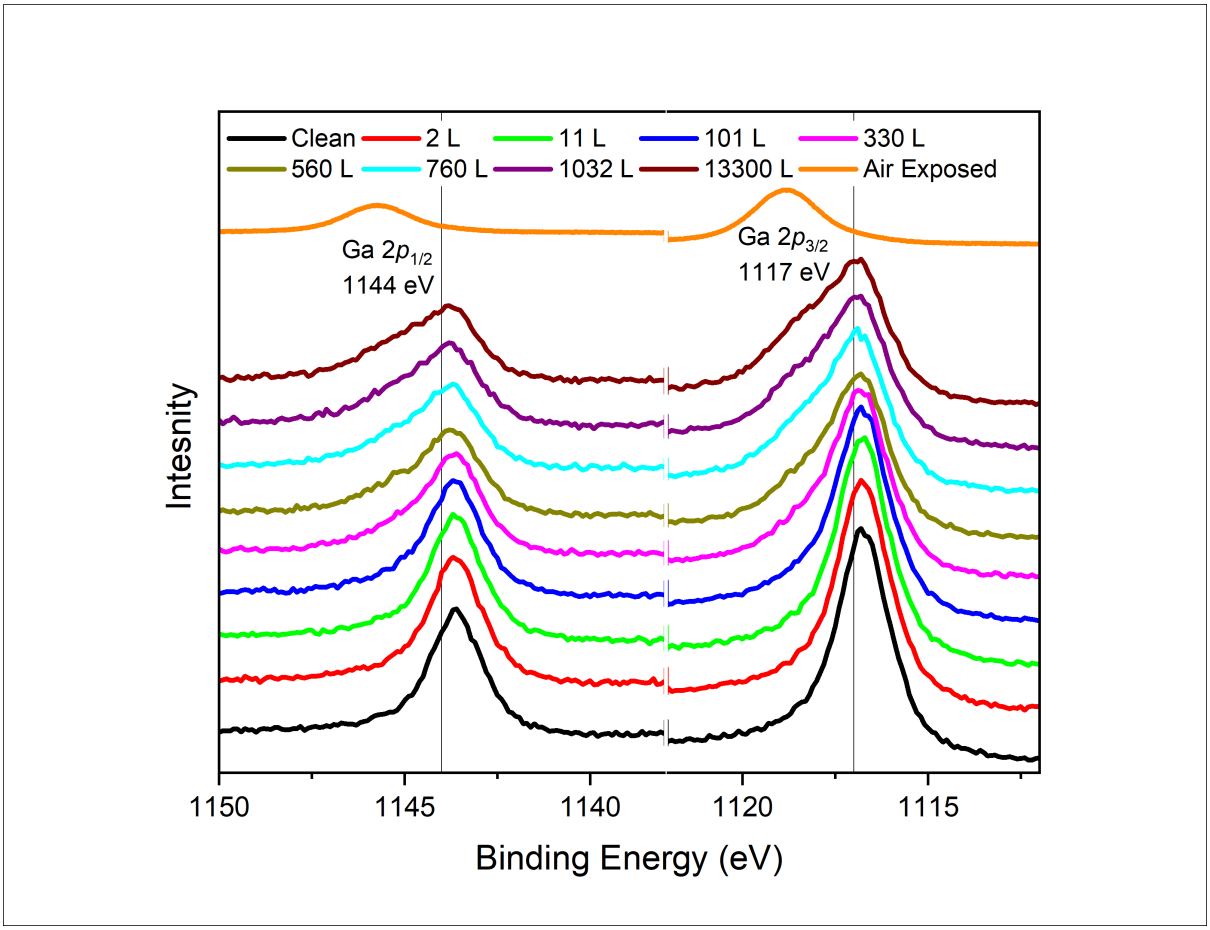

Figure 6.2: XPS spectra of the Ga $2p_{1/2}$ and Ga $2p_{3/2}$ as O_2 exposure was increased, for the Ga_3Ni_2 (001) surface prepared by annealing at 571°C. The formation of a shoulder towards higher binding energy can be observed at higher exposures. Vertical lines mark the binding energy of elemental Ga $2p_{1/2}$ and Ga $2p_{3/2}$ adopted from [125], [126].

6.3.2 Effects on the Gallium Peaks

Figure 6.2 shows the Ga 2p1/2 and Ga 2p3/2 XPS peaks from the clean, oxygen-dosed, and air-exposed surfaces. The clean surface results for the Ga 2p1/2 and Ga 2p3/2 peaks were recorded after sputtering and annealing the surface to 571°C. After exposing the surface to oxygen between 2 and 1001 L, the position and shape of the peaks do not change. At 1033 L, both the Ga 2p1/2 and Ga 2p3/2 peaks begin to show the formation of a shoulder at higher binding energy due to the increasing presence of Ga2O3 on the surface. Once 13,300 L was reached, the shoulder on the 2p1/2 and 2p3/2 peaks becomes more pronounced, showing an increase in the Ga2O3 2p peaks, as seen in Figure 6.2.

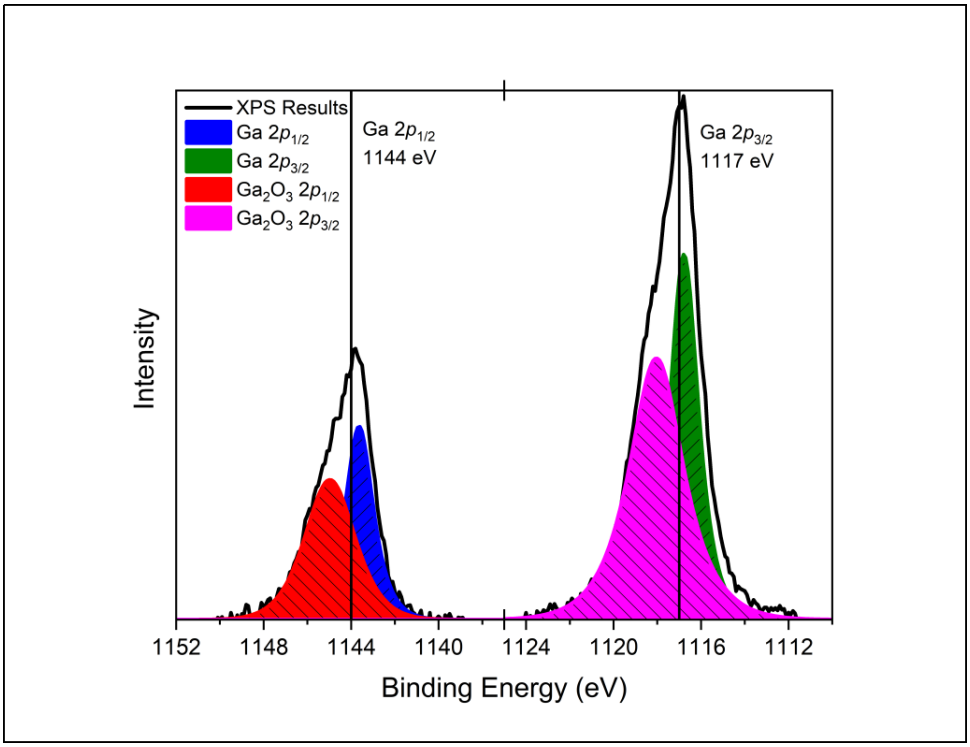

Figure 6.3: XPS spectra from the Ga_3Ni_2 (001) surface after exposure to O_2 (13300 L). The binding energy for elemental Ga has been highlighted, the binding energy was taken from [125]. The Ga peaks required two peaks to fit one from intermetallic Ga and the other from Ga in Ga_2O_3.

Peak	Core Level (eV)				
	Intermetallic Ga	Ga in Ga_2O_3	Air Exposed	Elemental Ga [147]	Ga_2O_3 [126]
$2p_{1/2}$	1116.78	1118.02	1118.8	1117	1119
$2p_{3/2}$	1143.78	1145.08	1145.8	1144	1146

Table 6.1: The extracted peak positions for the intermetallic Ga peaks, the Ga in Ga_2O_3 at 13300 L compared to the literature values for both elemental Ga [147] and Ga_2O_3 [126].

To extract information about the formation of the oxide peak from the XPS, the FWHM and the position of the Ga $2p1/2$ and Ga $2p3/2$ peaks were recorded and locked. As the position and shape of these peaks do not change, with the separation between the peaks being 27 eV, only the intensity of the peak is expected to change as exposure increases.

As the oxide peak forms, it changes in FWHM, position, and intensity to fit the associated $2p$ peak as the exposure increases, as shown in Figure 6.4. The presence of additional oxides, such as Ga2O3, Ga2O, GaO, and GaO_2, are the possible oxidation states.

Figure 6.4 (A) shows the FWHM of the $Ga2O_3$ $2p$ peaks as a function of exposure. The results start at 330 L and show a decrease in the FWHM as exposure increases, in line with the air-exposed results. This is expected as the peak increases in intensity, becoming easier to resolve with a reduced FWHM. As the oxide peak increased in intensity, it began to move away from the intermetallic Ga $2p$ peak, as seen in Figure 6.4 (B). Starting at 330 L, with the formation of the oxide peak, both of the oxide $2p$ peaks move further away from the Ga $2p$ peak as exposure increases.

The reduction in FWHM and the increase in separation between the oxide and intermetallic Ga peaks are expected as exposure increases. As the oxide peak increased in intensity, the peak became easier to resolve, reducing the width of the peak and shifting it to a higher binding energy, eventually reaching the position and FWHM seen in the air-exposed peak (Figure 6.3).

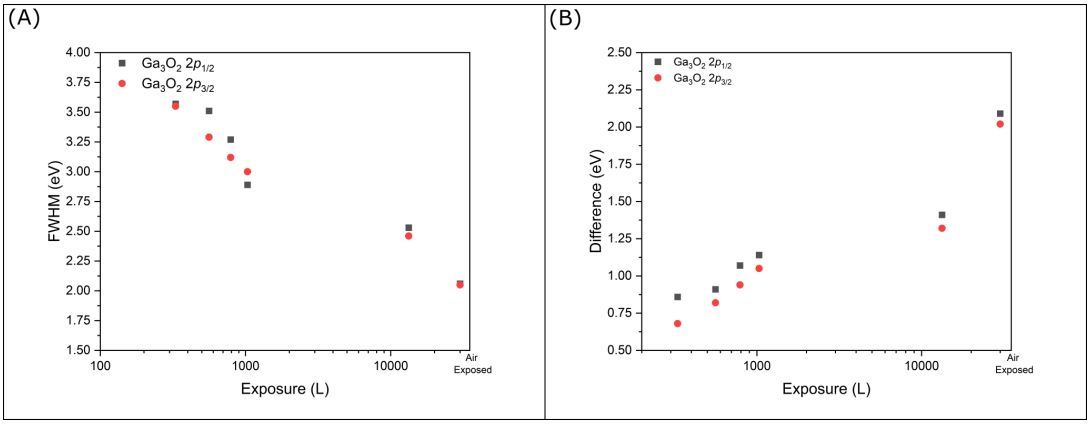

Figure 6.4: (A) The FWHM of the Ga oxides $2p_{1/2}$ and Ga oxides $2p_{1/2}$ as a function of O_2 exposure. (B) The peak position of the Ga oxides $2p_{1/2}$ and Ga oxides $2p_{1/2}$ as a function of O_2 exposure.

As the intensity of the Ga $2p1/2$ and Ga $2p3/2$ peaks could change during the fitting process, we were able to calculate the changes in the atomic composition of the Ga $2p$ peaks, as seen in Figure 6.5. Between 0 and 11 L, no oxide peaks are observed, with a slight presence of Ga oxides at 101 L. However, the 1.46% for Ga oxide is too small to confirm the presence. At 330 L, a shoulder is observed in Figure 6.2, which is due to the increase in Ga oxide observed (25%), with the amount of oxide present increasing with O2 dosing. At 13,300 L, the oxide peak becomes dominant, composing 52% of all Ga observed. When saturated, the oxide peak, predominantly $Ga2O_3$, composes 94% of the peak, after air exposure.

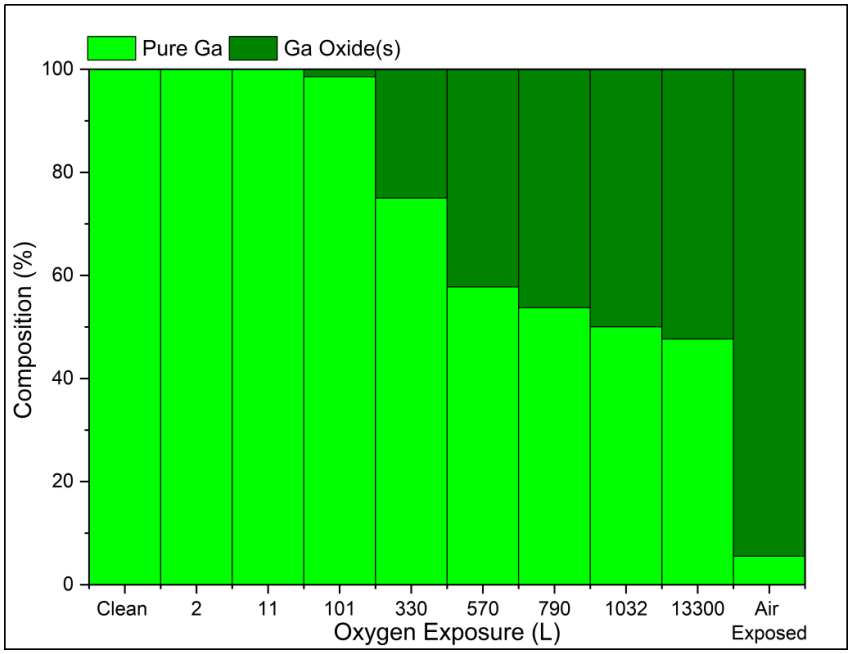

Figure 6.5: The composition of the Ga $2p_{1/2}$ and Ga $2p_{3/2}$ peaks from the (001) surface as exposure to O_2 increases taken from XPS results. The intermetallic Ga peaks and the Ga in Ga_2O_3 are labelled.

Exposure	Ga (%)	Ga Oxide (%)
Clean	100.0	0.0
2.0	100.0	0.0
11.0	100.0	0.0
101.0	98.5	1.5
330.0	75.0	25.0
570.0	57.8	42.2
790.0	53.7	46.3
1032.0	50.0	50.0
13300.0	47.7	52.3
Air Exposed	5.6	94.5

Table 6.2: The atomic composition determined using the $2p$ peaks as exposure to O_2 increases extracted from the XPS spectra.

6.3.3 Effects on the Nickel Peaks

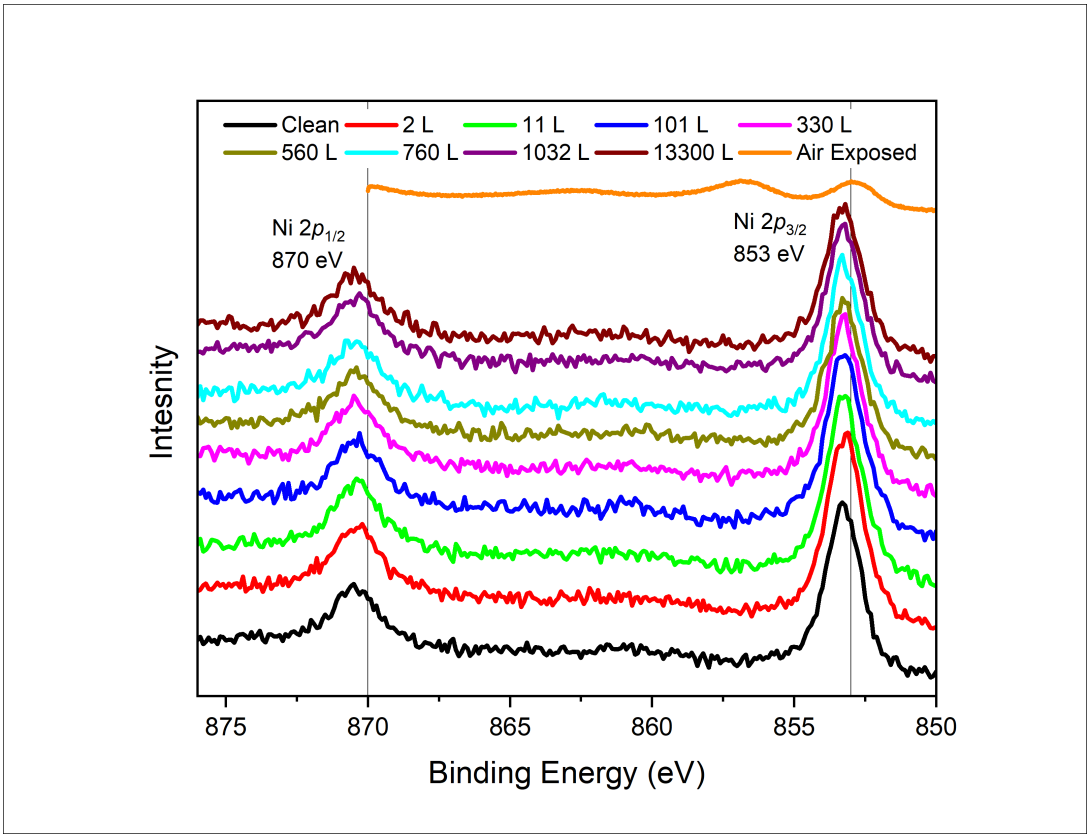

Figure 6.6: XPS spectra of the Ni doublet peak as O_2 exposure is increased.

Both the Ni 2p1/2 and Ni 2p3/2 peaks, as seen in Figure 6.6, show no changes in peak position and shape. There is no occurrence of a secondary peak with exposure to oxygen up to 13,300 L, suggesting that Ni is inert to O_2, as expected from data analysis of the air-exposed sample from Chapter 4.

As exposure increased, the area of the Ni peaks recorded from the surface of the sample decreased (Table 6.3). The decrease was due to the formation of Ga2O3 on the surface. As this oxide layer thickened, the Ni peak count continued to reduce.

The core-level shifts observed from the clean surface results show electron charge transfer from Ni to Ga. The intermetallic Ga peak has shifted 0.3 eV to a lower binding energy compared to elemental Ga (Table 6.1). The intermetallic Ni peak has shifted 0.2 eV to a higher binding energy from elemental Ni (Table 6.3). This suggests that the Ni is donating electrons to Ga when in the Ga_3Ni_2 intermetallic compound, and this is confirmed by DFT.

Exposure	Binding Energy (eV)		FWHM		Intensity (Arb Units)	
(L)	Ni $2p_{1/2}$	Ni $2p_{3/2}$	Ni $2p_{1/2}$	Ni $2p_{3/2}$	Ni $2p_{1/2}$	Ni $2p_{3/2}$
560°C	870.4	853.2	1.7	1.4	4862.3	11647.1
2.0	870.3	853.2	2.1	1.5	6907.5	14201.4
11.0	870.3	853.2	1.9	1.5	6290.6	13812.0
101.0	870.4	853.2	1.8	1.5	5296.8	13063.8
330.0	870.4	853.2	2.0	1.4	5789.4	11848.9
561.0	870.4	853.2	1.9	1.4	5262.7	10874.9
790.0	870.3	853.2	2.0	1.4	5497.0	10923.7
1032.0	870.3	853.2	1.8	1.4	5200.1	10966.6
13300.0	870.4	853.3	2.2	1.6	5153.4	10749.7
Air Exposed	0.0	852.8	0.0	1.6	0.0	2010.4

Table 6.3: Peak position, FWHM and the intensity of the Ni $2p_{1/2}$ and Ni $2p_{3/2}$ XPS spectrum after increasing exposure O_2.

6.3.4 Effects on the Total Atomic Composition

Using the survey scans, the atomic composition was calculated as a function of oxygen exposure and shown in Figure 6.7. By tracking the surface composition of Ga, Ni, and O as the surface was dosed, we could observe how the O $1s$ peak formed. The air-exposed results contained C and $Ni(OH)_2$.

The clean surface shows a Ga percentage of 86%. As the exposure increased, the Ga component in green decreased to 26% at 13,300 L. The percentage of Ni in blue decreased from 14% to 10% at 13,300 L. In addition to the Ga oxide, we detected pure oxygen on the surface. The amount of pure oxygen increased to 31% of the surface composition at 13,300 L. The air-exposed results show the percentages of Ga, Ni, and pure oxygen to be 0.5%, 0.4%, and 47%, respectively, with a large carbon contamination of 44%. The notable change in the Ga oxide to Ga ratio when exposed to air was expected, as the sample was exposed to air at atmospheric pressure, saturating all the Ga on the surface. The presence of water vapour is key for the formation of the hydroxide.

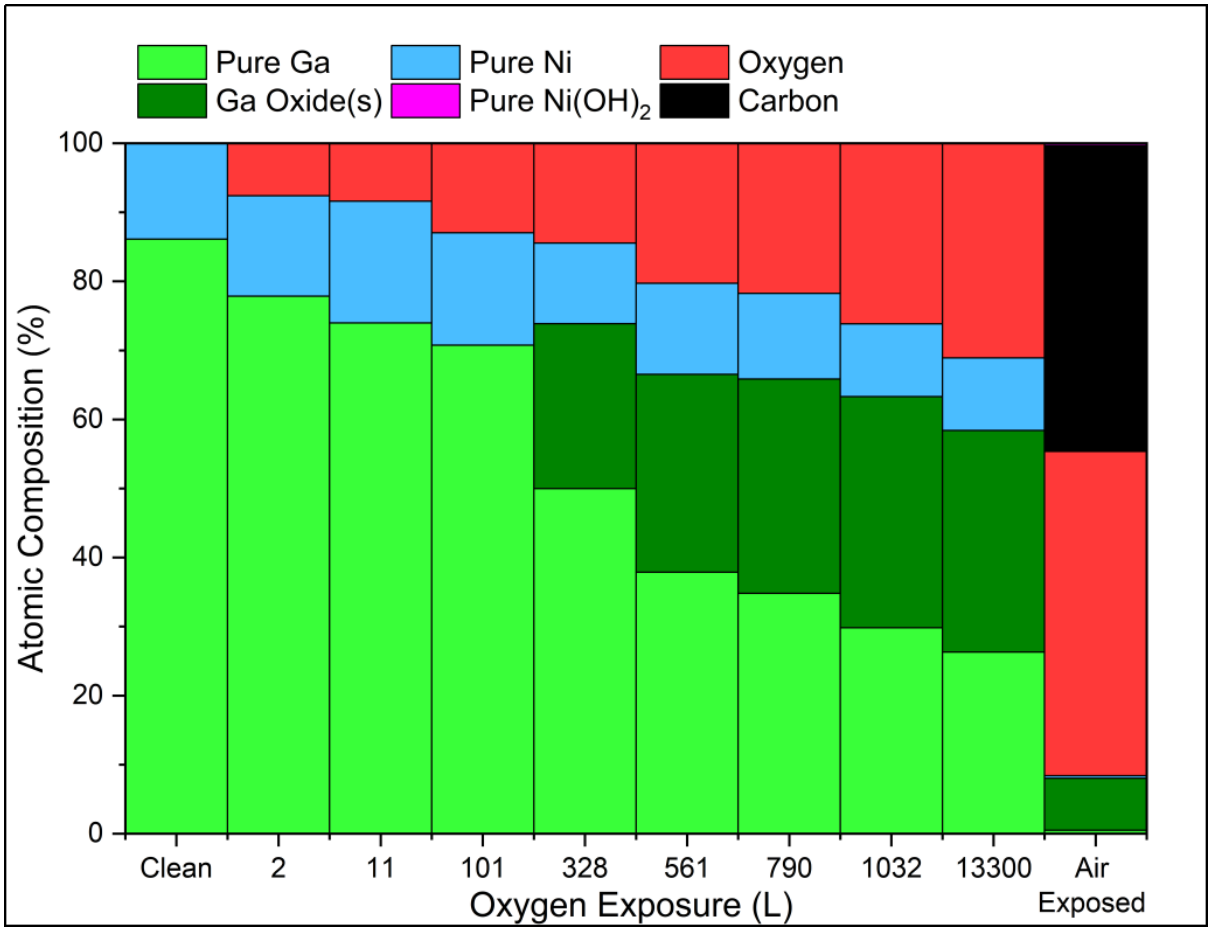

Figure 6.7: The atomic composition of the surface as a function of O_2 exposure showing all the key elements, Ga, Ni, O, C and $Ni(OH)_2$.

6.3.5 Comparison of Oxidation on Ga_3Ni_2 and In_3Ni_2.

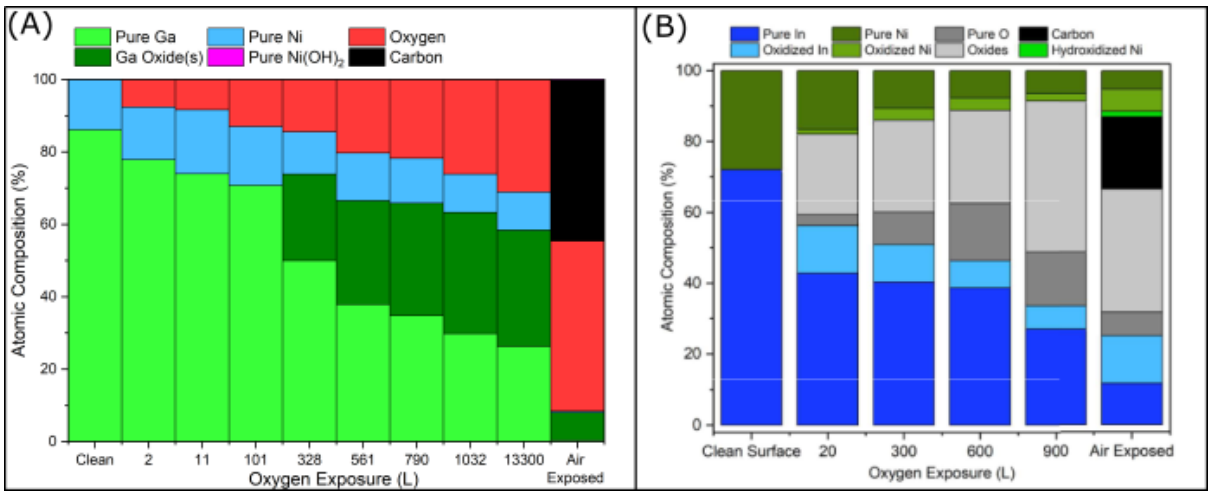

Figure 6.8: The atomic composition as a function of oxygen exposure for Ga_3Ni_2 (A) and In_3Ni_2 (B). (B) is adopted from [72].

As with Ga_3Ni_2, In_3Ni_2 has industrial applications, meaning that it will be used in an environment where oxygen is present. Both the (001) surfaces of Ga_3Ni_2 and In_3Ni_2 have large quantities of the secondary metal present on the surface. Chapter 6 discussed how Ga was the sole element that oxidised on the surface as oxygen exposure increased.

Figure 6.8 shows how both samples were affected by oxygen exposure. Starting from the clean surface, both samples have a surface composition which is dominated by Ga or In above the bulk composition.

As O_2 exposure on the In_3Ni_2 increases, both the In and Ni begin to form oxides. In oxides are the most abundant oxides on the surface at all levels of exposure. Unlike Ga_3Ni_2, the Ni on the surface is oxidising with a clear Ni oxide bar visible at 300 L and more. Both Ga_3Ni_2 and In_3Ni_2 have a presence of Ni hydroxide at air exposure.

With both Ga_3Ni_2 and In_3Ni_2 having oxides forming at 300 L the lack of Ni oxide from Ga_3Ni_2 compared to In_3Ni_2 is a notable change. Both Ga_3Ni_2 and In_3Ni_2 appear to oxidise at a similar rate as the % of Ga, In and Ni are close for equivalent levels of exposure however the amount of oxygen in much higher in the Ga_3Ni_2 results.

After exposure to air at atmospheric pressure, no Ni or elemental Ga was found from the Ga_3Ni_2 sample, unlike with In_3Ni_2, where all constituent elements were able to be resolved. This is due to the Ga being more susceptible to bonding with oxygen from the atmosphere, rapidly forming a layer of oxide from the surface, suppressing the amount of Ni% present, unlike In_3Ni_2.

Both surfaces show the presence of $Ni(OH)_2$ after air exposure but not after exposure to pure O_2 at any amount of exposure. This confirms that the presence of O_2 and H_2 in the UHV chamber is not enough to cause a hydroxide formation, which only occurred after exposure to air at atmospheric pressure.

6.4 Summary

In this chapter, we analysed the change in peak position, shape, and atomic composition of the key elements of the Ga_3Ni_2 (001) surface upon dosing with oxygen using XPS.

The XPS results after exposing the surface to pure oxygen in a controlled environment show the formation of an oxide layer, predominantly composed of Ga2O3 with other oxides being present on the surface. Ni was unaffected by the increase in exposure, aside from a decrease in intensity due to the formation of the Ga oxide. We also compared the results to the air-exposed surface and found that the maximum exposure used (13300 L) had not saturated the surface.

Hydrogen gas is present in the chamber, undetectable via mass spectrometer, which, alongside the oxygen present during exposure, contributes to the formation of Ni hydroxide within the chamber. At the larger exposure amounts, there was no trace of the hydroxide peak, suggesting that water vapour is required to form the hydroxide, which the (001) surface would have been exposed to during air exposure.

The XPS results from this study match aspects of the XPS results from a prior oxidation study of Ga_3Ni2 [10]. Both observed that a surface layer of Ga oxide(s) had formed while reducing the amount of Ni recorded through XPS. The prior research focused on the effects of O2 exposure on the catalytic properties of powdered Ga_3Ni_2 and did not show the surface chemical composition as a function of dosing.

In contrast, we were able to observe the formation of the oxide(s) on the surface. The reduction in catalytic activity observed by Dr Magdalena Wencka is due to the formation of the Ga oxide(s) layer, which reduces the concentration of Ni atoms, the catalytically active element, on the surface. This was corrected by heating the sample to 600°C, where the oxide(s) evaporated, and the surface reconstructed to a more energetically favourable composition akin to the bulk [10].

Further oxidation studies are required on the Ga_3Ni_2 (100) and Ga_3Ni_2 ($2\bar{1}0$) surfaces to observe if there are any changes due to the change in surface orientation. In particular, the Ga_3Ni_2 ($2\bar{1}0$) surface is composed of both Ga and Ni, whereas the other two surfaces are only composed of one element.

Another avenue would be to use angle-resolved XPS to observe how the atomic concentration at the surface changes with different surface sensitivities to see if the Ga oxide(s) peak became more pronounced as the XPS scans became more surface-sensitive.

One final area of study would be confirming the result from *"The effect of surface oxidation on the catalytic properties of Ga_3Ni_2 intermetallic compound for carbon dioxide reduction."* by Dr Magdalena Wencka [10], in which the oxide layer was evaporated off after annealing to 600°C. This was not studied during the oxidation project due to the risk of severe surface damage at those temperatures.

Chapter 7

Valence Band Structure

7.1 Introduction

This chapter presents the study of the valence band structure of Ga_3Ni_2, investigated using ultraviolet photoelectron spectroscopy (UPS) and supported by density of states (DoS) calculations based on density functional theory (DFT), in collaboration with a research group from Tribhuvan University, Nepal. As this work represents the first UPS investigation of the Ga_3Ni_2 surface, comparing the experimental spectra with theoretical DoS calculations provides critical insight into the electronic structure near the Fermi level.

Valence Band Structure

The valence band corresponds to the outermost electron orbitals in a material. Upon excitation, valence electrons can transition to the conduction band and move freely within the solid, as illustrated in Figure 7.1 [148]–[150]. As the most weakly bound electrons, valence electrons are also those that participate in catalytic reactions. Understanding the orbital character near the Fermi level is essential, particularly in identifying which atomic species dominate the electronic structure [151]. Experimental UPS spectra near the Fermi level are compared with DoS calculations to validate the theoretical predictions, including the total and orbital-resolved contributions.

The density of states (DoS) quantifies the number of electronic states per unit energy interval as a function of energy. In this work, DoS calculations were performed using density functional theory (DFT), a quantum mechanical method widely used to model the ground-state electronic properties of materials [152], [153]. These calculations provide a detailed description of the orbital contributions to the electronic structure of the Ga_3Ni_2 intermetallic compound.

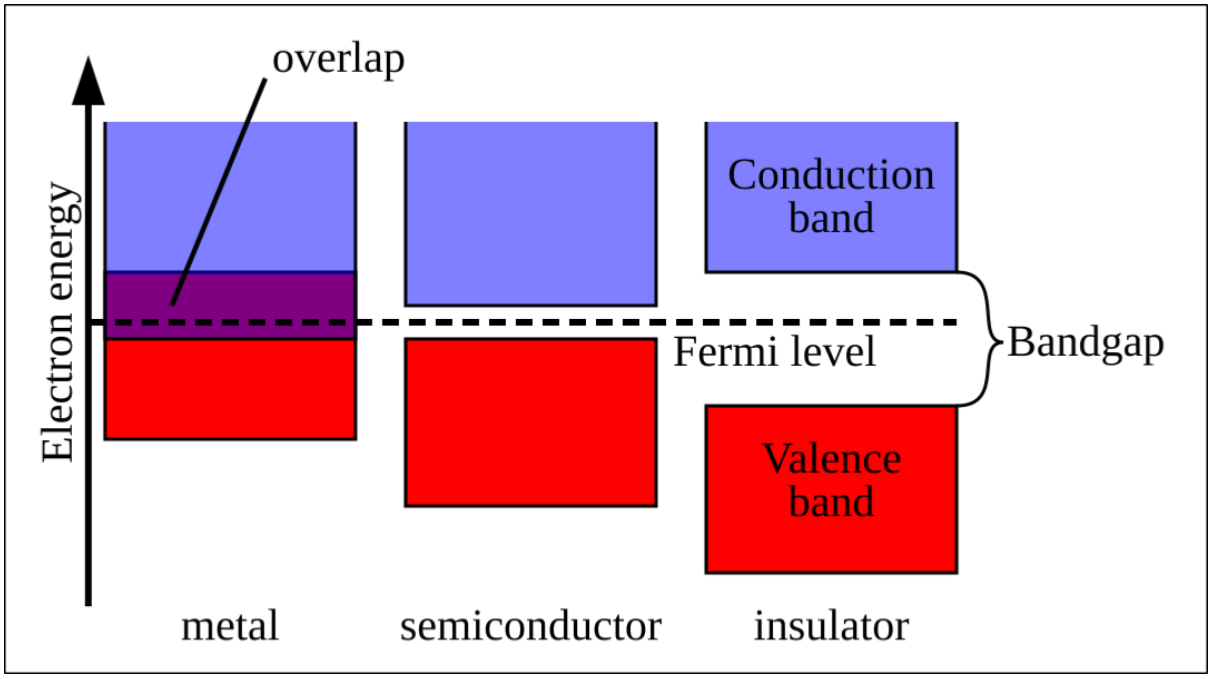

Figure 7.1: Schematic illustration of the valence and conduction bands in insulators, metals, and semiconductors. The Fermi level corresponds to the highest occupied electronic state at absolute zero [154].

7.2 Experimental Details

A single-crystal sample of Ga_3Ni_2 was grown using the Czochralski method [10]. The sample was oriented along the (001) surface, sectioned, and polished sequentially with diamond paste down to a final grain size of 0.25 μm. Surface cleaning was performed in an ultrahigh vacuum (UHV) chamber (base pressure: 2×10^{-10}mbar) using multiple sputtering (Ar^+, 2keV, 6 μA, 30minutes) and annealing cycles (407°C, 90minutes). The sample temperature was monitored using an optical pyrometer with an emissivity setting of 0.2. Post-treatment, no surface contamination was detected by X-ray photoelectron spectroscopy (XPS). However, gallium enrichment was observed after annealing, with the surface composition showing 73% Ga compared to the expected 60% from the bulk stoichiometry. The structural quality of the surface was confirmed to be bulk-terminated based on low-energy electron diffraction (LEED) and scanning tunnelling microscopy (STM) measurements.

UPS measurements were carried out using a He_1 radiation source (photon energy: 21.2 eV) at normal emission. During all UPS experiments, the helium partial pressure was maintained at 7×10^{-8} mbar. The Fermi level was calibrated by recording the UPS spectrum from a tantalum (Ta) strip electrically connected to the sample.

7.3 Results and Discussion

7.3.1 UPS Results

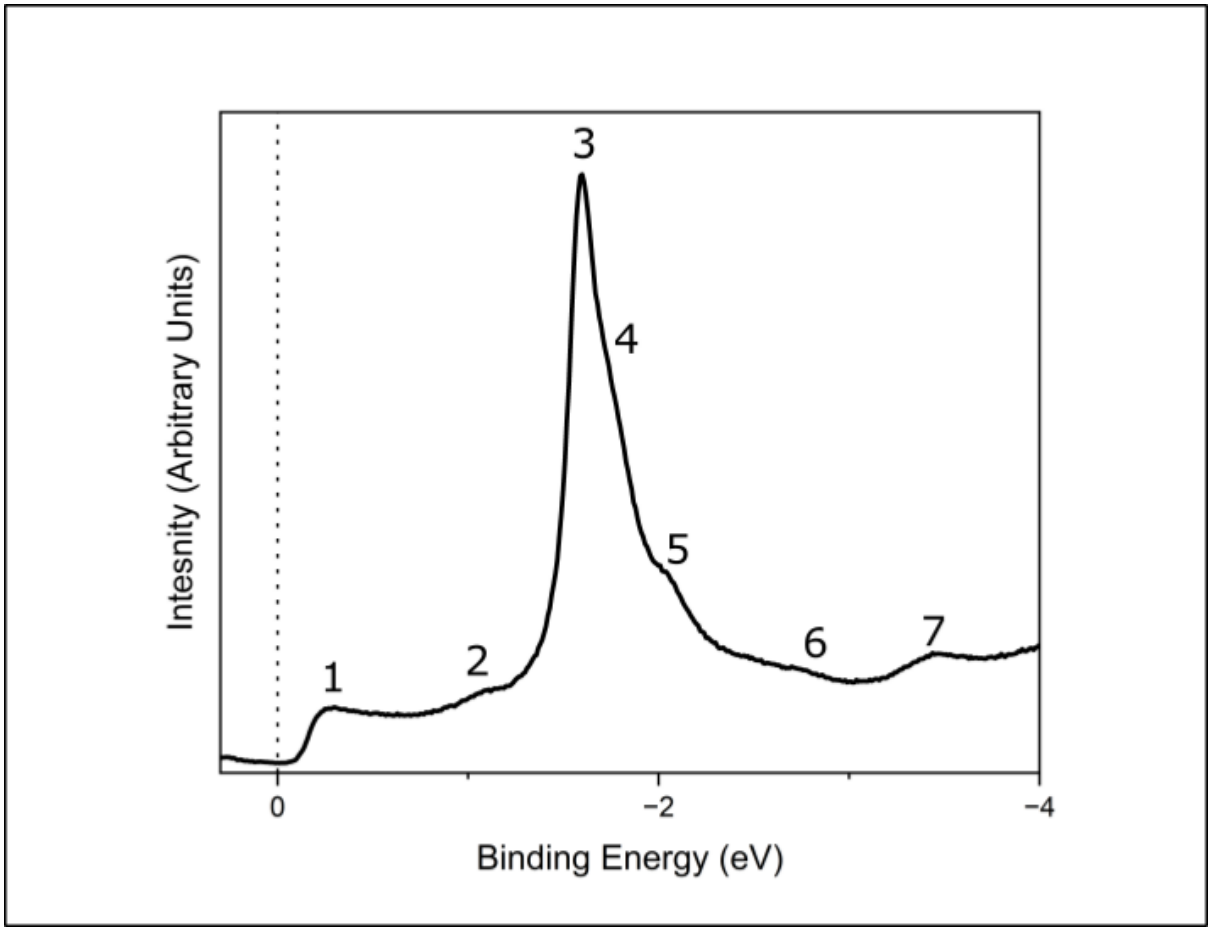

Figure 7.2: UPS spectrum of the $Ga_3Ni_2(001)$ surface after annealing at 414°C for ninety minutes, taken using a He_2 source, with the Fermi edge marked by a vertical dotted line.

The UPS spectrum obtained from the surface after sputtering and annealing is shown in Figure 7.2. A vertical dotted line marks the Fermi edge. A hump is visible around −0.3 eV (marked as 1), and a plateau extends up to −0.8 eV, indicating an appreciable density of states. Between −0.8 eV and −1.1 eV, a weak peak is observed (marked as 2).

A dominant peak appears at −1.50 eV (marked as 3), with two shoulders located around −1.6 eV (marked as 4) and −1.9 eV (marked as 5). Another broad, shallow peak can be discerned between −2.0 eV and −3.0 eV (marked as 6), followed by a peak at −3.3eV (marked as 7). All peaks are summarized in Table7.1.

Peaks	Binding Energy (UPS)	Binding Energy (DFT)	Contribution
Fermi Level	0	0	Ni *d*, Ga *p*, Ni *p*
1	-0.30	-0.30	Ni *d*, Ga *p*, Ni *p*
2	-1.00	-1.02	Ni *d*
3	-1.50	-1.56	Ni *d*, Ga *p*, Ni *p*
4	-1.60	-1.60	Ni *d*
5	-2.30	-1.98	Ni *d*, Ga *p*, Ni *s*
6	-2.80	-2.78	Ni *d*, Ga *p*
7	-3.20	-3.20	Ga *p*, Ni *p*, Ni *s*

Table 7.1: A table showing the peak position of each key feature from the UPS results and the corresponding feature from the DFT calculation (Figure 7.3). The contribution columns show the orbital contributions of each feature in order of largest contributor to smallest.

7.3.2 Comparison of UPS with the DoS Calculations

Figure 7.3 compares the UPS data to the partial and total density of states (DoS). At the Fermi energy, marked by the dashed line, the Ni *d*, Ga *p*, and Ni *p* orbitals contribute. The Ni *d* orbital is the dominant contributor across all regions, followed by the Ga *p* orbital and then the Ni *p* orbital. Peak 1 is mainly contributed by the Ni *d* orbital, with significant contributions from the Ga *p* and Ni *p* orbitals. Peak 2 is solely contributed by the Ni *d* orbital, with no significant contributions from other orbitals. Peaks 3 and 4, separated by 0.04 eV, show different dominant contributions: Peak 3 exhibits a significant contribution from the Ga *p* orbital, while Peak 4 shows contributions from the Ni *d* and Ni *s* orbitals. Peak 5, like Peak 2, is solely contributed by the Ni *d* orbital. Peak 6 shows contributions from both Ni *d* and Ga *p* orbitals. Finally, Peak 7 is dominated by the Ga *p* orbital, with some contribution from Ni *d* as well.

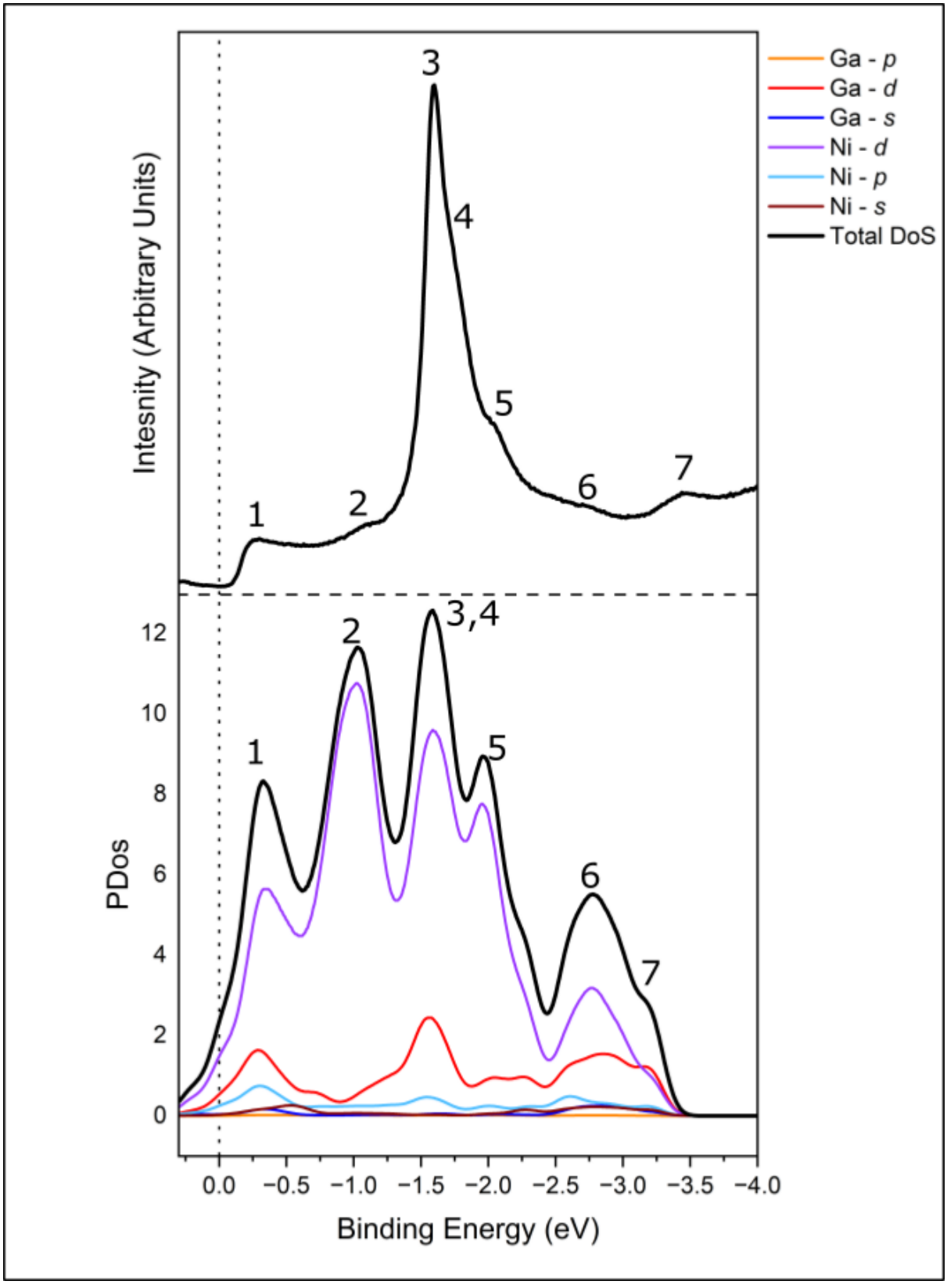

Figure 7.3: The UPS spectrum from Figure 7.2 (upper), the total DoS calculations (Lower). Each peak has been labelled, and the Fermi edge is denoted by a vertical dashed line. Both of the graphs have the same X-axis range (-4 eV to 0.25 eV).

All peaks observed in the total density of states were matched to features present in the UPS results shown in Figure 7.2. From the individual orbital contributions, the Ni d orbital is the dominant contributor to all peaks, followed by Ga p and Ni p orbitals. The substantial contribution from Ni is expected, as Ni acts as the catalytic agent in this intermetallic compound.

On either side of the Fermi edge, contributions from Ga and Ni orbitals—specifically Ni d and Ga p—are present, suggesting that there is no bias dependency. This observation is consistent with the STM results presented in Chapter 5, where the Ga_3Ni_2 (001) surface showed no bias dependency during scanning.

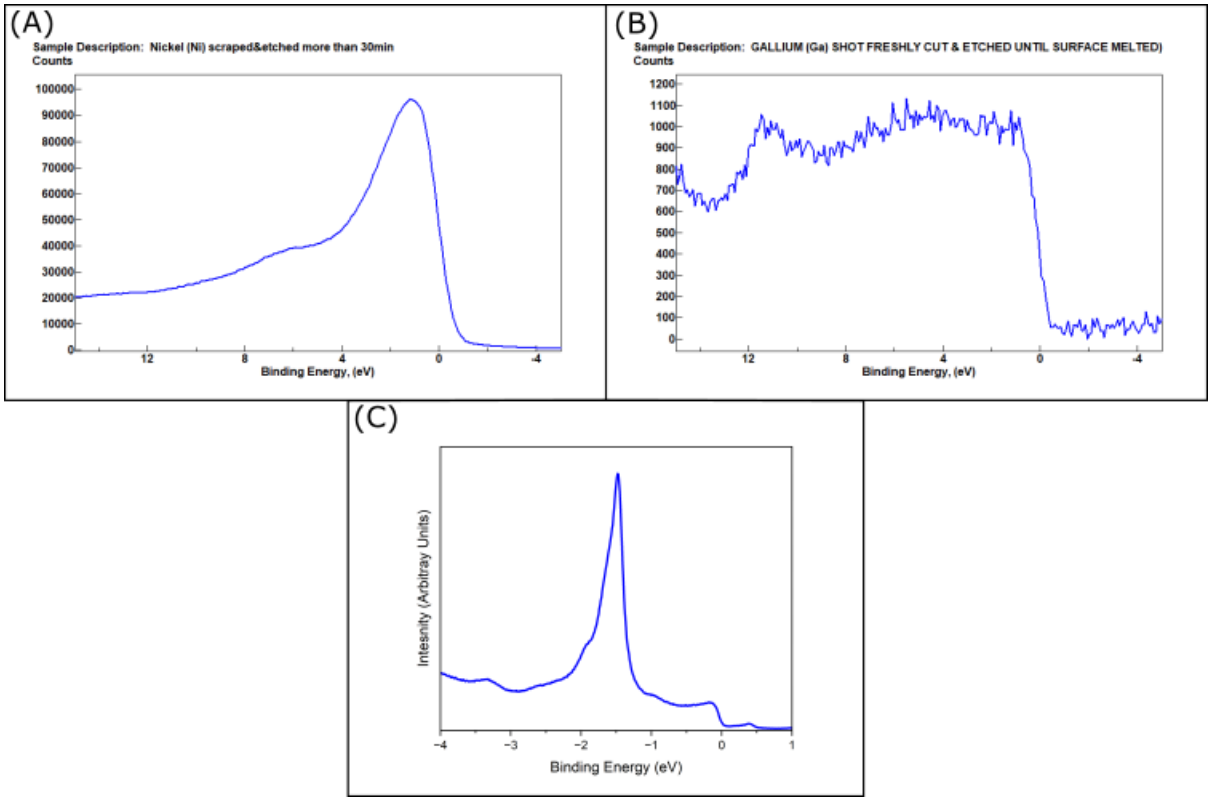

Figure 7.4: Three UPS spectra for (A) Elemental Ni, (B) Elemental Ga and (C) the Ga_3Ni_2. (A) and (B) are from The XPS Library with both samples being scraped and etched, while (C) is from the UPS study performed on Ga_3Ni_2.

The UPS results for Ga_3Ni_2 show that Ni is the dominant elemental contributor to the spectra, as seen in Figure 7.4(C) and corroborated by the DoS in Figure 7.3. Figure 7.4(A) shows the UPS spectrum for elemental Ni [155], while Figure 7.4(B) shows the UPS spectrum for elemental Ga.

The Ni spectrum displays a singular peak beginning just below the Fermi level and extending up to 4 eV, leading to a secondary hump that tapers off after 8 eV. The Ga spectrum shows a sudden increase at the Fermi edge, followed by a relatively flat region from 0.5 eV to 8 eV, with a distinct peak appearing between 10 and 11 eV.

When comparing the Ga_3Ni_2 spectrum to the spectra of its constituent elements, the Ni peak from Figure 7.4(A) can clearly be discerned. In both cases, the peak appears approximately 1.5 eV away from the Fermi edge, and the secondary hump after the main peak is similarly observed in both Ni and Ga_3Ni_2 spectra.

The Ga spectrum exhibits no discernible peaks within the energy range relevant for Ga_3Ni_2, but it may explain the plateau observed in the Ga_3Ni_2 spectrum between 0 eV and -1 eV, as the Ga spectrum shows a substantially lower number of counts compared to the Ni spectrum.

7.4 Summary

It was known from the STM results for the (001) surface (Chapter 5) that the topmost surface contains both Ga and Ni, as shown by the XPS results in Chapter 4. This is expected from the model shown in Figure 2.14(A), where the Ni atoms are bonded to Ga atoms in the layer below. The large contributions from both the Ni d and Ni p orbitals are expected, as Ni is the key catalytic agent in this intermetallic compound due to its ability to rupture C–C double bonds [156], which is vital for methanol steam reforming, discussed in Chapter 2 [157].

Using the same probing depth calculation as for the XPS results in Chapter 4, the probing depth is approximately $3 \times \lambda$, where λ is the photoelectron inelastic mean free path [132]. For the kinetic energy range of the UPS spectrum, 20–25eV, the probing depth was calculated to be between 3.2 and 3.9nm, confirming that the UPS results are surface sensitive. Further UPS studies are planned for all three samples. The $(2\bar{1}0)$ and (001) surfaces will be studied to observe any significant differences between a purely Ni-terminated plane ((001)) and mixed termination planes ($(2\bar{1}0)$ and (100)). Another study will involve annealing the (001) surface at lower temperatures to achieve bulk composition, to observe whether Ga segregation affects the UPS spectra.

Chapter 8

Summary and Outlook

8.1 Conclusions and Further Studies

The work undertaken for this thesis aims to develop our understanding of the three surfaces of the intermetallic compound Ga_3Ni_2. This was accomplished by utilising an array of surface analysis techniques to examine the surface chemical composition and surface geometry of the (001), (100), and $(2\bar{1}0)$ surfaces of Ga_3Ni_2.

As there was no prior research on the surface of Ga_3Ni_2, it was crucial to develop optimal surface preparation conditions. This is addressed in Chapters 4 and 5, which discuss changes in surface chemical composition and surface symmetry as a function of temperature. The results showed that higher annealing temperatures produced LEED images with sharper Bragg peaks and a reduced background, suggesting that the Ga_3Ni_2 surface requires elevated annealing temperatures to produce larger terraces and cleaner STM images. Longer annealing times were tested but yielded no significant improvements compared to increasing the annealing temperature. Further studies could involve extending the annealing time to confirm these findings.

In Chapter 4, the surface chemical composition of all three Ga_3Ni_2 surfaces was monitored after sputtering and annealing. Initial results showed that Ga was preferentially sputtered from the surface due to its lower surface free energy compared to Ni. This was true for all three surfaces, although to varying extents, attributed to differences in the composition of each surface. Similar results, where the heavier element was preferentially sputtered from the surface, were also observed in In_3Ni_2 and Ag-Yb-In [72], [137], supporting the validity of these findings.

After annealing, Ga segregated from the bulk to the surface, as shown by the increase in Ga concentration with increasing annealing temperature in Figures 4.6 (A), 4.7 (A), and 4.8 (A). A similar trend was also observed in In_3Ni_2 [72].

At the annealing temperatures required to achieve ideal LEED images, Ga had segregated from the bulk to the surface in excess of the bulk composition for all three surfaces. Angle-dependent XPS results showed that Ga and Ni were evenly distributed among the topmost layers as Ga migrated from the bulk to the surface.

Further study into these three samples would involve using a laser probe to record lower annealing temperatures than those measurable with the optical pyrometer, in order to identify the transition temperature for the (001) and (100) surfaces, and to plot the temperature at which the Ga percentage exceeds the bulk value for the $(2\bar{1}0)$ surface. A comprehensive temperature analysis of the surface chemical composition would help to understand the parameters required to induce Ga migration to the surface. Additionally, a study of the surface chemical composition of Al_3Ni_2, as Ga_3Ni_2 is a part of this family of catalysts, would provide insights into how Ga in the intermetallic compound affects the increase in Ga

Chapter 5 discusses the surface symmetries and images recorded via LEED and STM, respectively. Ideal LEED images were obtained at higher annealing temperatures; increasing the annealing time further produced no observable changes. Sharper Bragg peaks and reduced background noise were seen for the (100) and (001) surfaces, while the $(2\bar{1}0)$ surface underwent a c(2×2) reconstruction. This reconstruction was observed in STM images of the $(2\bar{1}0)$ surface, where the reconstructed unit cell was visible without enhancements.

The (001) surface exhibited a (1×1) unit cell, as expected from the LEED results. Wide-area scans of the (001) surface revealed multiple terrace step heights, confirming a buckled termination plane consisting of both Ga and Ni. Research conducted on In_3Ni_2 (001) produced the same conclusion of preferential sputtering and surface segregation of the secondary element, confirming that the surface contained a mixture of both elements [72].

Both the (001) and $(2\bar{1}0)$ surfaces were covered with clusters of material, presumed to be excess Ga segregated from the bulk. Further studies would aim to determine optimal conditions to inhibit the formation of these white clusters, thereby improving the consistency and quality of STM imaging, as achieved with In_3Ni_2.

These clusters appear to be loosely bound to the surface and can migrate to the STM tip during scanning. Depositing O2 or C60 onto each surface and observing the resulting behaviour would enhance surface studies of these three samples.

Chapter 6 examined the effect of exposing the Ga_3Ni_2 (001) surface to increasing amounts of oxygen. Ga on the surface rapidly oxidised, forming a top layer, as evidenced by the emergence of a Ga oxide shoulder that developed into a secondary peak, and the concurrent reduction of the Ni peak—with no Ni oxide peak recorded or observed as exposure increased. This behaviour is distinct from that of In_3Ni_2, where Ni oxide formation was observed.

The oxidation results of Ga_3Ni_2 aligned with those from a previous study on powdered oxidised Ga_3Ni_2, where Ga formed surface oxides and the amount of observable Ni decreased with exposure [10]. Our results provided further insight into how this oxide layer develops as a function of pure O_2 exposure.

Exposing the (100) and $(2\bar{1}0)$ samples to oxygen should be a priority for future studies to complete the oxidation profile of Ga_3Ni_2. Additionally, performing angle-dependent XPS on each oxidised surface would confirm the formation of the Ga oxide layer and identify the O_2 dose required to fully cover the surface. Finally, analysis of the O *1s* peak as the O_2 dose increases would offer valuable information on how, or whether, oxygen bonds to the Ga_3Ni_2 surface.

Chapter 7 was carried out in collaboration with Tribhuvan University, Nepal, which provided the density of states (DOS) calculations. These were used to fit the UPS results to the total and partial DOS, confirming that Ni is the dominant orbital contributor near the Fermi level. This finding was expected, as discussed in Chapter 2, where many other intermetallic compounds show the catalytically active element contributing the most to the density of states at the Fermi level. Further studies on the UPS of Ga_3Ni_2 should focus on the (100) and $(2\bar{1}0)$ samples to assess how different surface structures influence the UPS results.

Further studies on Ga_3Ni_2 that would complement the results presented in this thesis have been discussed at the end of each summary section. In summary, the surface of Ga_3Ni_2 has exhibited many interesting behaviours that warrant further investigation. Additional surface analysis techniques, such as atomic force microscopy or low-temperature STM, could be employed to reduce the movement of elemental Ga on the surface, which currently makes reliable STM imaging of Ga_3Ni_2 challenging.

Secondly, a LEED I–V study to quantify the atomic positions within each surface would offer new insights into the structure of these complex samples. Finally, a study of the surface of Al_3Ni_2 would contribute to a comprehensive understanding of the Al_3Ni_2 family of intermetallic compounds and how the presence of Al, Ga, or In influences the surface's response to sputtering, annealing, and oxidation.

Bibliography

[1] M. Armbrüster, R. Schlögl, and Y. Grin, "Intermetallic compounds in heterogeneous catalysis: A quickly developing field," *Science and Technology of Advanced Materials*, vol. 15, no. 3, 2014.

[2] M. Armbrüster, M. Behrens, K. Föttinger, *et al.*, "The intermetallic compound ZnPd and its role in methanol steam reforming," *Catalysis Reviews*, vol. 55, no. 3, pp. 289–367, 2013.

[3] A. Tsai, S. Kameoka, and Y. Ishii, "PdZn = Cu: Can an Intermetallic Compound Replace an Element?" *Journal of the Physical Society of Japan*, vol. 73, no. 12, pp. 3270–3273, 2004.

[4] C. Quilis, N. Mota, E. Millán, B. Pawelec, Y. Navarro, and M. Rufino, "Application of intermetallic compounds as catalysts for the selective hydrogenation of CO_2 to methanol," *ChemCatChem*, vol. 16, no. 14, 2024.

[5] A. Álvarez, A. Bansode, A. Urakawa, *et al.*, "Challenges in the greener production of formates/formic acid, methanol, and DME by heterogeneously catalyzed CO_2 hydrogenation processes," *Chemical Reviews*, vol. 117, no. 14, pp. 9804–9838, 2017.

[6] W. Sachtler and R. Van Santen, "Surface composition of binary alloys," *Applications of Surface Science*, vol. 3, no. 2, pp. 121–144, 1979.

[7] J. Hagen, "Industrial Catalysis: A Practical Approach," *John Wiley & Sons*, 2015.

[8] A. McNaught, A. Wilkinson, *et al.*, "Compendium of Chemical Terminology," *Blackwell Science Oxford*, vol. 1669, 1997.

[9] D. Goodman, "Model catalysts: From extended single crystals to supported particles," *Surface Review and Letters*, vol. 02, no. 01, pp. 9–24, 1995.

[10] M. Wencka, J. Kovač, V. Dasireddy, *et al.*, "The effect of surface oxidation on the catalytic properties of Ga_3Ni_2 intermetallic compound for carbon dioxide reduction," *Journal of Analytical Science and Technology*, vol. 9, pp. 1–10, 2018.

[11] K. Molcanov and V. Stilinovic, "Chemical crystallography before X-ray diffraction," *Angew. Chem., Int. Ed*, vol. 53, no. 3, pp. 638–652, 2014.

[12] D. Sands, "Introduction to Crystallography," *Courier Corporation*, 1993.

[13] R. Soni, R. Rana, and S. Godara, "Characterization Tools and Techniques for Nanomaterials and Nanocomposites," in *Nanomaterials and Nanocomposites*, CRC. Press, 2021, pp. 61–83.

[14] C. Kittel and P. McEuen, "Introduction to Solid State Physics," *John Wiley & Sons*, 2018.

[15] S. Kubba, "LEED Practices, Certification, and Accreditation Handbook," *Butterworth-Heinemann*, 2009.

[16] E. Maciá and M. de Boissieu, *Complex metallic alloys: Fundamentals and applications*, 2011.

[17] E. Belin-Ferré, "Properties and applications of complex intermetallics," *World Scientific*, vol. 2, 2009.

[18] A. Deschamps, F. Tancret, I. Benrabah, F. De Geuser, and H. Van Landeghem, "Combinatorial approaches for the design of metallic alloys," *Comptes Rendus. Physique*, vol. 19, no. 8, pp. 737–754, 2018.

[19] T. Yang, B. Cao, T. Zhang, *et al.*, "Chemically complex intermetallic alloys: A new frontier for innovative structural materials," *Materials Today*, vol. 52, pp. 161–174, 2022.

[20] Z. Zhang, H. Tang, and Z. Xu, "Fatigue database of complex metallic alloys," *Scientific Data*, vol. 10, no. 1, p. 447, 2023.

[21] T. Umemura, K. Sato, Y. Kusaka, and H. Satoh, "Palladium," in *Handbook on the Toxicology of Metals*, Elsevier, 2022, pp. 649–662.

[22] M. Armbrüster, "Intermetallic compounds in catalysis. A versatile class of materials meets interesting challenges," *Science and Technology of Advanced Materials*, vol. 21, no. 1, pp. 303–322, 2020.

[23] S. Furukawa and T. Komatsu, "Intermetallic compounds: Promising inorganic materials for well-structured and electronically modified reaction environments for efficient catalysis," *ACS Catalysis*, vol. 7, no. 1, pp. 735–765, 2017.

[24] A. Dasgupta and R. Rioux, "Intermetallics in catalysis: An exciting subset of multimetallic catalysts," *Catalysis Today*, vol. 330, pp. 2–15, 2019.

[25] B. Johansson, L. Nordström, O. Eriksson, and M. Brooks, "Magnetism in rare-earth metals and rare-earth intermetallic compounds," *Physica Scripta*, vol. 1991, no. 39, 1991.

[26] R. Cava, H. Takagi, H. Zandbergen, *et al.*, "Superconductivity in the quaternary intermetallic compounds $LnNi_2B_2C$," *Nature*, vol. 367, no. 6460, pp. 252–253, 1994.

[27] M. Conrad, B. Harbrecht, T. Weber, D. Jung, and W. Steurer, "Large, larger, largest - A family of cluster-based tantalum copper aluminides with giant unit cells. II. the cluster structure," *Structural Science*, vol. 65, no. 3, pp. 318–325, 2009.

[28] C. Dong, H. Ma, H. Ma, and Y. Wang, "Nucleation and growth of intermetallic compounds on the prefabricated Cu_6Sn_5 layer," *Materials Chemistry and Physics*, vol. 296, 2023.

[29] M. Hahne and P. Gille, "Single crystal growth of the intermetallic compound InPd," *Journal of Crystal Growth*, vol. 401, pp. 622–626, 2014.

[30] M. Wencka, M. Pillaca, and P. Gille, "Single crystal growth of Ga_3Ni_2 by the Czochralski method," *Journal of Crystal Growth*, vol. 449, pp. 114–118, 2016.

[31] G. Gottstein, "Physikalische grundlagen der materialkunde," *Springer-Verlag*, 2013.

[32] S. Brühne, R. Sterzel, E. Uhrig, C. Gross, and W. Assmus, "Medium range real atomic structure of face-centred icosahedral $Ho_9Mg_{26}Zn_{65}$," *Zeitschrift für Kristallographie-Crystalline Materials*, vol. 219, no. 5, pp. 245–258, 2004.

[33] D. Shechtman and I. Blech, "The microstructure of rapidly solidified Al_6Mn," *Metallurgical Transactions A*, vol. 16, pp. 1005–1012, 1985.

[34] B. Luisa, "Handbook of Convex Geometry," *Elsevier*, 2014.

[35] J. Bamberg, G. Cairns, and D. Kilminster, "The crystallographic restriction, permutations, and goldbach's conjecture," *The American Mathematical Monthly*, vol. 110, no. 3, pp. 202–209, 2003.

[36] L. Bursill and P. Ju Lin, "Penrose tiling observed in a quasi-crystal," *Nature*, vol. 316, no. 6023, pp. 50–51, 1985.

[37] W. Steurer, "Quasicrystals: A primer," *Foundations of Crystallography*, vol. 53, no. 4, pp. 526–526, 1997.

[38] J. Wisniak, "The history of catalysis from the beginning to nobel prizes," *Educación Química*, vol. 21, no. 1, pp. 60–69, 2010.

[39] T. Soderberg, "Organic chemistry with a biological emphasis volume i," *Chemistry Publications 1*, 2019.

[40] L. Lloyd, "Handbook of industrial catalysts," *Springer Science & Business Media*, 2011.

[41] D. Trimm, "The design of industrial catalysts," *US. Department of Energy Office of Scientific and Technical Information*, 1989.

[42] S. Shikha, "Designing clusters for efficient catalytic activity at a realistic condition from first-principle simulations," *Delhi: Indian Institute of Technology Delhi*, 2020.

[43] R. Schlögl, "Heterogeneous catalysis," *Angewandte Chemie International Edition*, vol. 54, no. 11, pp. 3465–3520, 2015.

[44] C. Friend and B. Xu, "Heterogeneous catalysis: A central science for a sustainable future," *Accounts of Chemical Research*, vol. 50, no. 3, pp. 517–521, 2017.

[45] A. Glazer, "Crystallography: A very short introduction," *Oxford University Press*, vol. 469, 2016.

[46] K. Sytwu, M. Vadai, and J. Dionne, "Bimetallic nanostructures: Combining plasmonic and catalytic metals for photocatalysis," *Advances in Physics: X*, vol. 4, no. 1, 2019.

[47] A. Iandelli and A. Palenzona, "Crystal chemistry of intermetallic compounds," *Handbook on the Physics and Chemistry of Rare Earths*, vol. 2, pp. 1–54, 1979.

[48] K. Taylor, "Automobile catalytic converters," *Springer*, 1984.

[49] C. Luengo, A. Cabrera, H. MacKay, and M. Maple, "Catalysis of carbon monoxide and carbon dioxide methanation by $CeAl_2$, $CeCo_2$, $CeNi_2$, Co, and Ni," *Journal of Catalysis*, vol. 47, no. 1, pp. 1–10, 1977.

[50] K. Nozawa, N. Endo, S. Kameoka, A. Tsai, and Y. Ishii, "Catalytic properties dominated by electronic structures in PdZn, NiZn, and PtZn intermetallic compounds," *Journal of the Physical Society of Japan*, vol. 80, no. 6, 2011.

[51] A. Ranjekar and G. Yadav, "Steam reforming of methanol for hydrogen production: A critical analysis of catalysis, processes, and scope," *Industrial & Engineering Chemistry Research*, vol. 60, no. 1, pp. 89–113, 2021.

[52] P. Villars and K. Cenzual, "CuTi crystal structure: Datasheet from Pauling File multinaries edition - 2022," *Springer Materials*, 2023.

[53] W. Tyson, "Surface energies of solid metals," *Canadian Metallurgical Quarterly*, vol. 14, no. 4, pp. 307–314, 1975.

[54] M. Friedrich, D. Teschner, A. Knop-Gericke, and M. Armbrüster, "Influence of bulk composition of the intermetallic compound ZnPd on surface composition and methanol steam reforming properties," *Journal of Catalysis*, vol. 285, no. 1, pp. 41–47, 2012.

[55] G. Weirum, M. Kratzer, H. Koch, *et al.*, "Growth and desorption kinetics of ultrathin Zn layers on Pd (111)," *The Journal of Physical Chemistry C*, vol. 113, no. 22, pp. 9788–9796, 2009.

[56] H. Koch, I. Bako, G. Weirum, M. Kratzer, and R. Schennach, "A theoretical study of Zn adsorption and desorption on a Pd (111) substrate," *Surface Science*, vol. 604, no. 11, pp. 926–931, 2010.

[57] J. Osswald, R. Giedigkeit, R. Jentoft, *et al.*, "Palladium-gallium intermetallic compounds for the selective hydrogenation of acetylene: Part I: Preparation and structural investigation under reaction conditions," *Journal of Catalysis*, vol. 258, no. 1, pp. 210–218, 2008.

[58] A. Borodziński and G. Bond, "Selective hydrogenation of ethyne in ethene-rich streams on palladium catalysts. part 1. effect of changes to the catalyst during reaction," *Catalysis Reviews*, vol. 48, no. 02, pp. 91–144, 2006.

[59] A. Bos and K. Westerterp, "Mechanism and kinetics of the selective hydrogenation of ethyne and ethene," *Chemical Engineering and Processing: Process Intensification*, vol. 32, no. 1, pp. 1–7, 1993.

[60] W. Sachtler, "Chemisorption complexes on alloy surfaces," *Catalysis Reviews*, vol. 14, no. 1, pp. 193–210, 1976.

[61] M. Krajči and J. Hafner, "The (210) surface of intermetallic B20 compound GaPd as a selective hydrogenation catalyst: A DFT study," *Journal of Catalysis*, vol. 295, pp. 70–80, 2012.

[62] K. Kovnir, M. Armbrüster, D. Teschner, *et al.*, "In situ surface characterization of the intermetallic compound PdGa – a highly selective hydrogenation catalyst," *Surface Science*, vol. 603, no. 10, pp. 1784–1792, 2009.

[63] J. Osswald, K. Kovnir, M. Armbrüster, *et al.*, "Palladium gallium intermetallic compounds for the selective hydrogenation of acetylene: Part ii: Surface characterization and catalytic performance," *Journal of Catalysis*, vol. 258, no. 1, pp. 219–227, 2008.

[64] J. Ledieu, É. Gaudry, L. Loli, *et al.*, "Structural investigation of the (010) surface of the $Al_{13}Fe_4$ catalyst," *Physical Review Letters*, vol. 110, no. 7, 2013.

[65] M. Armbrüster, K. Kovnir, M. Friedrich, *et al.*, "$Al_{13}Fe_4$ as a low-cost alternative for palladium in heterogeneous hydrogenation," *Nature Materials*, vol. 11, no. 8, pp. 690–693, 2012.

[66] V. Singh, M. Krajčí, S. Sarkar, *et al.*, "Electronic structure of β-Al_3Mg_2 and $Al_{13}Fe_4$ complex metallic alloys," *Physical Review B*, vol. 105, no. 20, 2022.

[67] A. Darmawan, M. Aziz, M. Ajiwibowo, M. Biddinika, K. Tokimatsu, and B. Lokahita, "Integrated ammonia production from the empty fruit bunch," *Innovative Energy Conversion from Biomass Waste*, vol. 3, p. 149, 2022.

[68] I. Iavicoli, L. Fontana, A. Bergamaschi, *et al.*, "Palladium: Exposure, uses, and human health effects," in *Encyclopedia of environmental health*, Elsevier Inc., 2011, pp. 307–314.

[69] Z. Khan, K. Ahmad, T. Ahmad, *et al.*, "Evaluation of nickel toxicity and potential health implications of agriculturally diversely irrigated wheat crop varieties," *Arabian Journal of Chemistry*, vol. 16, no. 8, 2023.

[70] E. Meloni, M. Martino, and V. Palma, "A short review on Ni based catalysts and related engineering issues for methane steam reforming," *Catalysts*, vol. 10, no. 3, 2020.

[71] I. January, "Euromat. 2007 - european congress on advanced materials and processes," *Int J Mat Res (formerly Z. Metallkd)*, 2006.

[72] A. Alfahad, V. Singh, E. Gaudry, *et al.*, "Atomic structure, chemical composition, and oxidation behavior of the (001) surface of Ni_2In_3 intermetallic catalyst," *Physical Review Materials*, vol. 9, no. 3, 2025.

[73] S. Anil, S. Indraja, R. Singh, S. Appari, and B. Roy, "A review on ethanol steam reforming for hydrogen production over Ni/Al_2O_3 and Ni/CeO_2 based catalyst powders," *International Journal of Hydrogen Energy*, vol. 47, no. 13, pp. 8177–8213, 2022.

[74] J. Guo, Z. Wang, J. Li, and Z. Wang, "In - Ni intermetallic compounds derived from layered double hydroxides as efficient catalysts toward the reverse water gas shift reaction," *ACS Catalysis*, vol. 12, no. 7, pp. 4026–4036, 2022.

[75] G. Onyestyák, S. Harnos, A. Kaszonyi, M. Štolcová, and D. Kalló, "Acetic acid hydroconversion to ethanol over novel InNi / Al_2O_3 catalysts," *Catalysis Communications*, vol. 27, pp. 159–163, 2012.

[76] W. Liu, L. Li, S. Lin, *et al.*, "Confined Ni-In intermetallic alloy nanocatalyst with excellent coking resistance for methane dry reforming," *Journal of Energy Chemistry*, vol. 65, pp. 34–47, 2022.

[77] P. Gille, "Single crystal growth of intermetallics by the Czochralski method," *De Gruyter*, pp. 61–90, 2019.

[78] L. Vitos, A. Ruban, H. Skriver, and J. Kollár, "The surface energy of metals," *Surface Science*, vol. 411, no. 1-2, pp. 186–202, 1998.

[79] M. Hochstrasser, A. Atrei, B. Bolliger, R. Eismann, M. Erbudak, and D. Pescia, "The structure of Fe on Al (001)," *Surface Review and Letters*, vol. 5, no. 05, pp. 1007–1014, 1998.

[80] M. Lowe, A. Al-Mahboob, D. Ivarsson, *et al.*, "Atomic structure of different surface terminations of polycrystalline ZnPd," *Physical Review Materials*, vol. 8, no. 10, 2024.

[81] F. Studt, I. Sharafutdinov, F. Abild-Pedersen, *et al.*, "Discovery of a Ni-Ga catalyst for carbon dioxide reduction to methanol," *Nature Chemistry*, vol. 6, no. 4, pp. 320–324, 2014.

[82] E. Maxted, "The poisoning of metallic catalysts," in *Advances in Catalysis*, vol. 3, Elsevier, 1951, pp. 129–178.

[83] H. Okamoto, "Ga - Ni (Gallium - Nickel)," *Journal of Phase Equilibria and Diffusion*, vol. 31, pp. 575–576, 2010.

[84] P. Tomaszewski, "Jan Czochralski—father of the Czochralski method," *Journal of Crystal Crowth*, vol. 236, no. 1-3, pp. 1–4, 2002.

[85] M. Wencka, J. Schwerin, M. Klanjšek, *et al.*, "Physical properties of the $GaPd_2$ intermetallic catalyst in bulk and nanoparticle morphology," *Intermetallics*, vol. 67, pp. 35–46, 2015.

[86] T. Schuelke and T. Grotjohn, "Diamond polishing," *Diamond and Related Materials*, vol. 32, pp. 17–26, 2013.

[87] L. Bochang, W. Yibo, L. Zhengdong, *et al.*, "Gallium oxide (Ga_2O_3) heterogeneous and heterojunction power devices," *Fundamental Research*, vol. 5, no. 2, pp. 804–817, 2023.

[88] G. Somorjai and Y. Li, "Introduction to surface chemistry and catalysis," *John Wiley & Sons*, 2010.

[89] D. Holkeboer, D. Jones, F. Pagano, and D. Santeler, "Vacuum technology and space simulation," *NASA*, 1966.

[90] K. Oura, V. Lifshits, A. Saranin, A. Zotov, and M. Katayama, "Surface science: An introduction," *Springer Science & Business Media*, 2013.

[91] E. Vacuum, *Bakeout Pressure Against Time*, https://www edwardsvacuum com/en-uk/knowledge/applications/three-factors-to-consider-when-performing-a-system-bake-out, Accessed: (26/06/2024), 2024.

[92] L. Feldman and J. Mayer, "Fundamentals of surface and thin film analysis," *Pearson*, 1986.

[93] P. Sigmund, "Theory of sputtering. 1. sputtering yield of amorphous and polycrystalline targets," *Physical Review*, vol. 184, no. 2, 1969.

[94] H. Sharma, M. Shimoda, S. Ohhashi, and A. Tsai, "First UHV surface studies of single-grain icosahedral Ag-In-Yb quasicrystal," *Philosophical Magazine*, vol. 87, no. 18-21, pp. 2989–2994, 2007.

[95] T. Kato, K. Morimoto, K. Isogai, M. Kato, T. Fukushima, and R. Fukuda, "Development of efficient thermionic energy converter," in *Functionally Graded Materials 1996*, Elsevier, 1997, pp. 661–666.

[96] C. Davisson and L. Germer, "The scattering of electrons by a single crystal of nickel," *Nature*, vol. 119, no. 2998, pp. 558–560, 1927.

[97] J. Cowley, "Electron diffraction techniques," *Oxford University Press*, vol. 2, 1992.

[98] M. Seah and W. Dench, "Quantitative electron spectroscopy of surfaces: A standard data base for electron inelastic mean free paths in solids," *Surface and Interface Analysis*, vol. 1, no. 1, pp. 2–11, 1979.

[99] G. Binnig and H. Rohrer, "Scanning tunneling microscopy," *Surface Science*, vol. 126, no. 1-3, pp. 236–244, 1983.

[100] M. Nasrollahzadeh, M. Sajadi, M. Atarod, M. Sajjadi, and Z. Isaabadi, "An introduction to green nanotechnology," *Academic Press*, vol. 28, 2019.

[101] F. Trixler, "Quantum tunnelling to the origin and evolution of life," *Current Organic Chemistry*, vol. 17, no. 16, pp. 1758–1770, 2013.

[102] D. Damjanovic, "Ferroelectric, dielectric and piezoelectric properties of ferroelectric thin films and ceramics," *Reports on Progress in Physics*, vol. 61, no. 9, 1998.

[103] P. Hansma and J. Tersoff, "Scanning tunneling microscopy," *Journal of Applied Physics*, vol. 61, no. 2, pp. 1–24, 1987.

[104] G. Binnig and H. Rohrer, "Scanning tunneling microscopy—from birth to adolescence," *Reviews of Modern Physics*, vol. 59, no. 3, 1987.

[105] I. Horcas, R. Fernández, J. Gómez-Rodríguez, J. Colchero, J. Gómez-Herrero, and A. Baro, "WSXM: a software for scanning probe microscopy and a tool for nanotechnology," *Review of Scientific. Instruments*, 2007. DOI: 101063/12432410.

[106] D. Nečas and P. Klapetek, "Gwyddion: An open-source software for SPM data analysis," *Central European Journal of Physics*, 2012. DOI: 102478/s11534-011-0096-2.

[107] P. Sutter, "Scanning tunneling microscopy in surface science," *Science of Microscopy*, pp. 969–1024, 2007.

[108] R. Hamers and D. Padowitz, "Methods of tunneling spectroscopy with the stm," *Scanning Probe Microscopy and Spectroscopy: Theory, Techniques, and Applications*, vol. 2, 2001.

[109] M. Le Ster, S. Pawłowski, I. Lutsyk, and P. Kowalczyk, "Fourier transform-based post-processing drift compensation and calibration method for scanning probe microscopy," *Ultramicroscopy*, vol. 263, 2024.

[110] H. Habibullah, "30 years of atomic force microscopy: Creep, hysteresis, cross-coupling, and vibration problems of piezoelectric tube scanners," *Measurement*, vol. 159, 2020.

[111] Myscope, *Scanning probe & atomic force microscopy*, `https://myscope.training/SPM-Scanner-artefacts`, 2025.

[112] J. Gan and X. Zhang, "A review of nonlinear hysteresis modeling and control of piezoelectric actuators," *AIP Advances*, vol. 9, no. 4, 2019.

[113] S. Klassen, "The photoelectric effect: Reconstructing the story for the physics classroom," *Science & Education*, vol. 20, pp. 719–731, 2011.

[114] J. Mulligan, "Heinrich hertz and the development of physics," *Physics Today*, vol. 42, no. 3, pp. 50–57, 1989.

[115] D. Patton, "Roentgen and the "new light" i. roentgen and lenard," *Investigative Radiology*, vol. 27, no. 6, pp. 408–414, 1992.

[116] E. Rothwell and M. Cloud, "Electromagnetics," *CRC. press*, 2018.

[117] M. Planck, "Über das gesetz der energieverteilung im normalspektrum," *Springer*, pp. 178–191, 1978.

[118] A. Einstein, "On a heuristic viewpoint concerning the emission and transformation of light," *Annalen der Physik*, vol. 17, no. 6, pp. 132–148, 1905.

[119] K. Mitchell, "The theory of the surface photoelectric effect in metals—i," *Proceedings of the Royal Society of London. Series A*, vol. 146, no. 857, pp. 442–464, 1934.

[120] C. Tusche, Y. Chen, C. Schneider, and J. Kirschner, "Imaging properties of hemispherical electrostatic energy analyzers for high resolution momentum microscopy," *Ultramicroscopy*, vol. 206, 2019.

[121] J. Czochralski, "Ein neues verfahren zur messung der kristallisationsgeschwindigkeit der metalle," *Zeitschrift für physikalische Chemie*, vol. 92, no. 1, pp. 219–221, 1918.

[122] P. Tomaszewski, "Jan Czochralski father of the Czochralski method," *Journal of Crystal Growth*, vol. 236, no. 1-3, pp. 1–4, 2002.

[123] P. Gille and B. Bauer, "Single crystal growth of $Al_{13}Co_4$ and $Al_{13}Fe_4$ from Al-rich solutions by the Czochralski method," *Crystal Research and Technology: Journal of Experimental and Industrial Crystallography*, vol. 43, no. 11, pp. 1161–1167, 2008.

[124] C. Schmetterer, H. Flandorfer, C. Lengauer, J. Bros, and H. Ipser, "The system Ga–Ni: A new investigation of the Ga-rich part," *Intermetallics*, vol. 18, no. 2, pp. 277–285, 2010.

[125] B. Crist, "Handbooks of monochromatic XPS spectra," *John Wiley & Sons*, 2019.

[126] B. Crist, "Handbook of monochromatic XPS spectra: The elements of native oxides," *John Wiley & Sons*, 2000.

[127] A. Mansour and C. Melendres, "Characterization of α - $Ni(OH)_2$ by XPS," *Surface Science Spectra*, vol. 3, no. 3, pp. 255–262, 1994.

[128] J. Scofield, "Hartree-slater subshell photoionization cross-sections at 1254 eV and 1487 eV," *Journal of Electron Spectroscopy and Related Phenomena*, vol. 8, no. 2, pp. 129–137, 1976.

[129] S. Tanuma, C. Powell, and D. Penn, "This software provides facilities to determine the inelastic electron mean free paths by the Tanuma Powell and Penn algorithm," *Surf Interf Analysis*, 1994.

[130] S. Tanuma, C. Powell, and D. Penn, "Calculations of electron inelastic mean free paths for 14 organic compounds over the 50-2000 eV range," *Surface and Interface Analysis*, vol. 21, no. 3, pp. 165–176, 1994.

[131] J. Carrazza and V. León, "A general and simple approach for the determination of energy analyser transmission functions," *Surface and Interface Analysis*, vol. 17, no. 5, pp. 225–229, 1991.

[132] S. Villaseca, J. Ledieu, L. Serkovic, *et al.*, "Structural investigation of the (001) surface of the Al_9CO_2 complex metallic alloy," *The Journal of Physical Chemistry C*, vol. 115, no. 30, pp. 14 922–14 932, 2011.

[133] C. Fadley, R. Baird, W. Siekhaus, T. Novakov, and S. Bergström, "Surface analysis and angular distributions in X-ray photoelectron spectroscopy," *Journal of Electron Spectroscopy and Related Phenomena*, vol. 4, no. 2, pp. 93–137, 1974.

[134] C. Fadley, "Angle-resolved X-ray photoelectron spectroscopy," *Progress in Surface Science*, vol. 16, no. 3, pp. 275–388, 1984.

[135] C. Yuen, B. Unal, D. Jing, and P. Thiel, "Weak bonding of Zn in an Al-based approximant based on surface measurements," *Philosophical Magazine*, vol. 91, no. 19-21, pp. 2879–2888, 2011.

[136] R. Kelly and D. Harrison, "A summary of the theory of the preferential sputtering of alloys," *Materials Science and Engineering*, vol. 69, no. 2, pp. 449–455, 1985.

[137] H. Sharma, P. Nugent, T. Noakes, *et al.*, "Medium energy ion scattering (MEIS) study from the five-fold surface of icosahedral Ag-In-Yb quasicrystal," in *Journal of Physics: Conference Series*, IOP Publishing, vol. 809, 2017.

[138] K. Eldressi, H. Eltawahni, M. Moradi, E. Twiname, and R. Mistler, "Energy effects in bulk metals," in *Reference Module in Materials Science and Materials Engineering*, Elsevier, 2019.

[139] Z. Duan, J. Zhong, and G. Wang, "Modeling surface segregation phenomena in the (111) surface of ordered Pt_3Ti crystal," *The Journal of Chemical Physics*, vol. 133, no. 11, 2010.

[140] T. Owolabi, K. Akande, and S. Olatunji, "Estimation of the atomic radii of periodic elements using support vector machine," *IJAIST*, vol. 28, no. 28, pp. 39–49, 2014.

[141] D. Tandon, E. Hippo, H. Marsh, and E. Sebok, "Surface topography of oxidized hopg. by scanning tunneling microscopy," *Carbon*, vol. 35, no. 1, pp. 35–44, 1997.

[142] H. Brongersmal and P. Mu, "Analysis of the outermost atomic layer of a surface by low-energy ion scattering," *Surface Science*, vol. 35, pp. 393–412, 1973.

[143] C. Cushman, P. Brüner, J. Zakel, *et al.*, "Low energy ion scattering (LEIS). a practical introduction to its theory, instrumentation, and applications," *Analytical Methods*, vol. 8, no. 17, pp. 3419–3439, 2016.

[144] K. Hermann and M. Van Hove, "LEEDpat, version 4.2," *Fritz Haber Institute: Berlin*, 2015.

[145] A. Alofi, "Surfaces of Complex Metallic Alloys and their Adsorption Properties," Ph.D. dissertation, University of Liverpool, 2023.

[146] R. Sanderson, "Chemical bonds and bonds energy," *Elsevier*, vol. 21, 2012.

[147] J. Chastain and R. King Jr, "Handbook of X-ray photoelectron spectroscopy," *Perkin-Elmer Corporation*, vol. 40, no. 221, 1992.

[148] H. Li, B. Li, Y. Zou, *et al.*, "Modulating valence band to enhance the catalytic activity of Co-Cr-B/NG for hydrolysis of sodium borohydride," *Journal of Alloys and Compounds*, vol. 924, 2022.

[149] P. Chen, T. Du, H. Jia, *et al.*, "A novel Bi_2WO_6/Si heterostructure photocatalyst with fermi level shift in valence band realizes efficient reduction of CO_2 under visible light," *Applied Surface Science*, vol. 585, 2022.

[150] K. Lee, T. Kim, T. Kim, J. Lee, and S. Yu, "Enhancement of TOC removal efficiency of sulfamethoxazole using catalysts in the radiation treatment: Effects of band structure and electrical properties of radiocatalysts," *Separation and Purification Technology*, vol. 312, 2023.

[151] I. Bidermane, I. Brumboiu, R. Totani, *et al.*, "Atomic contributions to the valence band photoelectron spectra of metal-free, iron and manganese phthalocyanines," *Journal of Electron Spectroscopy and Related Phenomena*, vol. 205, pp. 92–97, 2015.

[152] M. Orio, D. Pantazis, and F. Neese, "Density functional theory," *Photosynthesis research*, vol. 102, pp. 443–453, 2009.

[153] L. Bartolotti and K. Flurchick, "An introduction to density functional theory," *Reviews in Computational Chemistry*, pp. 187–216, 1996.

[154] E. Myasnikov and A. Myasnikova, "Band theory of semiconductors and autolocalization of electrons," *Physics Letters A*, vol. 286, no. 2-3, pp. 210–216, 2001.

[155] B. Crist, "The XPS library website: A resource for the XPS community including-the XPS library of information, XPS spectra-base having over 70,000 monochromatic XPS spectra, and spectral data processor," *Journal of Electron Spectroscopy and Related Phenomena*, vol. 248, 2021.

[156] J. Llorca, V. Corberán, N. Divins, R. Fraile, and E. Taboada, "Hydrogen from Bioethanol," *Renewable Hydrogen Technologies*, pp. 135–169, 2013.

[157] S. Ali, M. Zagho, M. Al-Marri, Y. Arafat, and M. Khader, "Development of nickel-based catalysts for methane steam reforming," in *Proceedings of the 4th International Gas Processing Symposium*, Elsevier, 2015, pp. 111–116.

In this section I will list all of the conferences I attended during this PhD.

Conferences

- ECMetAC Days 2020 online (Poster Presentation)
- ECMetAC Days 2022 in Split (Oral Presentation)
- IOP Surface Science Day 5 2023 (Attended)
- IOP Surfaces Summer School 2022 (Attended)

Publications

- Valence band characteristics of Ni_2Ga_3 Intermetallic Compound Studied by Density Functional Theory and Ultraviolet Photoelectron Spectroscopy. (Yet to be published)